## *Seismolosical studies of magma injection processes: volcano monitoring and imaging of magma chambers*

Konstantinou, Konstantinos I.

# Seismological Studies of Magma Injection Processes: Volcano Monitoring and Imaging of Magma Chambers

Konstantinos I. Konstantinou

A thesis submitted for the degree of

Doctor of Philosophy



Department of Geological Sciences

University of Durham

April 2001

# Declaration

This dissertation describes my own work, except where acknowledgement is made in the text, and is not substantially the same as any work that has been, or is being submitted to any other university for any degree, diploma or other qualification.

K. I. Konstantinou April 2001

**...I shall arise from my enmarbled sleep**
**and from my mystic tomb I shall come forth.**
**To open wide the bricked-up golden gate;**
**And victor over the Caliphs and the Tsars,**
**hunting them beyond the Red Apple Tree,**
**I shall seek rest upon my ancient bounds.**

From *'The King's flute'* by Kostis Palamas

# Seismological Studies of Magma Injection Processes: Volcano Monitoring and Imaging of Magma Chambers

Konstantinos I. Konstantinou

## Abstract

The processes associated with magma injection at shallow depths within the crust have been the topic of many geophysical studies, some investigating the seismicity that accompanies volcanic activity and others attempting to map the subsurface extent and geometry of the resulting magma bodies. The aim of this study is to obtain a better understanding of these processes by investigating the nature of seismic signals that accompany volcanic eruptions and by seismically imaging a magma body beneath a mid-ocean ridge, both located on, or adjacent to Iceland.

The seismic phenomena associated with the 1996 Vatnajökull subglacial eruption in central Iceland, have been studied using data recorded by both temporary (HOTSPOT) and permanent (SIL) seismic networks. These networks comprise 60 broadband and short-period three-component seismographs and cover most parts of the country. Two very active volcanic systems, Bárdarbunga and Grimsvötn, are situated underneath the Vatnajökull ice cap. The volcanoseismic signals recorded there were categorised according to their waveform shape and frequency content, into three groups: (a) low-frequency events (1-2 Hz); (b) mixed-frequency events (1-4 Hz); and (c) volcanic tremor. The eruption was preceded by intense seismic activity which began with a $M_w = 5.6$ earthquake located at the Bárdarbunga volcanic system. The epicentres of the earthquake swarm that followed the $M_w = 5.6$ event initially delineated the Bárdarbunga caldera rim and then migrated towards Grimsvötn, to a place where a fissure was later observed. Pre-eruptive tremor started at least two days before the eruption as a harmonic signal around five narrow frequency bands (0.5-0.7, 1.6, 2.2, 2.8 and 3.2 Hz). Co-eruptive tremor started as a broadband, continuous signal which evolved into low-amplitude background tremor interrupted by high-amplitude, cigar-shaped bursts. Further analysis revealed that continuous tremor and the cigar-shaped bursts had all the characteristics of low-dimensional chaotic signals. Geophysical and geochemical evidence suggest that a lateral migration of magma from Bárdarbunga facilitated the rupture of the roof of a magma chamber, situated at the fissure area, which subsequently erupted as tephra on the glacier.

The second phase of the RAMESSES (Reykjanes Ridge Axial Melt Experiment: Structural Synthesis from Electromagnetic and Seismics) experiment involved the acquisition of multichannel seismic reflection data from 39 along- and across-axis lines shot over the magmatically active 57°45'N axial volcanic ridge. The data from one along-axis line were processed using a variety of techniques that mainly aimed at reducing the large amount of coherent noise present, a result of scattered energy at the rough seabed. The final processsed section revealed a number of reflection events that could be interpreted as intra-crustal reflections, originating from the interface between pillow lavas and sheeted dykes, and from the top part of a thin melt lens.

# Acknowledgements

Unfortunately I cannot say, as many other PhD students do in their acknowledgements section, that I have enjoyed all of my time in Durham. However, this doesn't mean that I don't have to thank people that throughout this period of three and a half years helped, supported and accompanied me through the highs and lows of a PhD course. Therefore, thanks are due to:

- Neil Goulty for being a dedicated supervisor and teacher, always being available to help and give his scientific expertise - but above all for being a good friend at difficult times.
- Christine Peirce for taking me as her PhD student, giving me the RAMESSES data to work on (and thus allowing me to continue my PhD) and guiding me through all the curiosities of ProMAX (which are quite a lot!). Furthermore I should thank her for providing the funds for me to attend the 1999 AGU meeting and covering the costs involved in the reproduction of the colour figures in the Vatnajökull paper.
- Vera Schlindwein for being an 'auxiliary' supervisor, for always boosting my morale and for some nice wine sessions, when we were discussing about everything else except from geophysics. Vielen Dank Vera!
- Matt Pritchard and Zhijun Du for the computational help they gave me during my early days in Durham.
- The PIs of the HOTSPOT project G. Nolet, W. J. Morgan, G. R. Foulger, B. R. Julian, R. Stefánsson, that helped collecting the Vatnajökull eruption data. In particular I would like to thank Guust Nolet for carefully reading the draft of the Vatnajökull paper and providing many useful comments.
- All past and present office mates and fellow PhD students for offering me their friendship and help when needed, including: Rashmin, David, Anthony, Alex and Chris.
- Eddie Huijbens for making life at Parsons Field House less boring, much more interesting and full of unexpected events - I could certainly say that Eddie is the best flatmate I had throughout the entire period of my stay in Durham.

Last but not least, I would like to thank my family not only for providing me with the means to study abroad, but also for supporting me during this period.

# Contents

# List of figures

# List of tables



# List of additional material

A large scale plot of the final processed seismic section of Line 37 and a reprint of the following paper, which is based on the results described in this thesis, are contained in a separate envelope.

Konstantinou, K. I., Nolet, G., Morgan, W. J., Allen, R. M., Pritchard, M. J., 2000. Seismic phenomena associated with the 1996 Vatnajökull eruption, central Iceland, J. Volcanol. Geotherm. Res., 102, 169-187.

# Chapter 1

# Mid-ocean ridges, Iceland and the Vatnajökull area

## 1.1 Introduction

The process of magma injection at shallow depths within the crust has been the topic of many geophysical studies, either from the viewpoint of seismicity associated with volcanic activity or attempts to map the subsurface extent and geometry of the resulting magma bodies. Mid-ocean ridges are most attractive targets for trying to image magma bodies because of the on-going crustal accretion processes and the applicability of a wide range of controlled source seismic methods. Iceland on the other hand provides a unique opportunity to study volcanic eruptions, and the seismic phenomena accompanying them, because of the large number of active volcanoes present there. This dissertation contains a study of the seismic phenomena associated with the 1996 Vatnajökull eruption in central Iceland and an attempt to image, using multichannel reflection data, the magmatic system beneath an axial volcanic ridge located at 57°45'N on the Reykjanes Ridge, part of the Mid-Atlantic Ridge south of Iceland. In this chapter an introduction of the geological and tectonic setting of the areas studied is presented together with a summary of previous geophysical investigations that have taken place.

## 1.2 Mid-ocean ridges

### *1.2.1 Oceanic crust*

The majority of currently available knowledge about the main components of the oceanic crust comes from geophysical investigations and the study of ophiolite sequences which are thought to represent ancient oceanic crust. Hill (1957) and

Raitt (1963) originally modelled the oceanic crust to consist of three main layers of constant seismic velocity and density. According to the nomenclature proposed by Houtz & Ewing (1976) and Bratt & Purdy (1984), layer 1 represents the shallowest layer consisting of deep sea sediments; layer 2 comprises intrusive and extrusive volcanic rocks; layer 3 consists of massive gabbro; layer 4, which is identified by seismologists as the uppermost mantle, consists of peridotite. More recently layers 2 and 3 have been further subdivided to other components (2A, 2B, 2C, 3A, 3B) based on changes in their vertical velocity gradient that indicate the presence of first or second order boundaries. A summary of the now widely accepted layered structure of the oceanic crust is shown in Fig. 1.1 and this scheme will be used throughout this thesis.

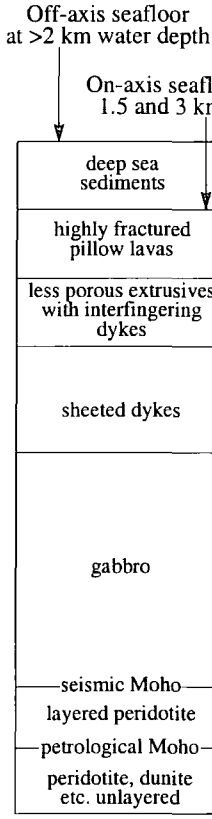


| | typical ophiolite | | oceanic crust | | |
|---|---|---|---|---|---|
| | thickness (km) | velocity (km s$^{-1}$) | thickness (km) | velocity (km s$^{-1}$) | velocity gradient (s$^{-1}$) |
| layer 1 | ~0.3 | - | 0.5 | ~2.0 | - |
| layer 2A | 0.3-0.7 | 3.3 | 0.5 | 2.5-4.5 | 5 |
| layer 2B | | | 0.5 | 4.5 | 0 |
| layer 2C | 1.0-1.5 | 4.1 | 1.0 | 4.5-6.5 | 1 |
| layer 3A | 2.0-5.0 | 5.1 | 1.0 | 6.5-6.8 | 0.1 |
| layer 3B | | | 2.0 | 6.8-7.0 | |
| layer 4 | | 2.5-4.2 | | 8.0+ | 0.03 |

Figure 1.1: The composition and physical properties of the oceanic crust based on ophiolite studies and seismic data (after Brown & Mussett, 1981; Bratt & Purdy, 1984; Navin, 1996).

### *1.2.2 The magmatic system of mid-ocean ridges*

After the introduction of the theory of plate tectonics and seafloor spreading, mid-ocean ridges have been widely recognised as sites of crustal accretion (e.g. Vine, 1966; Cann, 1974; Macdonald, 1982; Fowler, 1990). The seafloor morphology of mid-ocean ridges around the world (Fig. 1.2) shows a degree of correlation between the spreading rate and the crustal structure, indicating that accretionary processes may strongly be influenced by the spreading rate. A topic of on-going research, as well as debate among ridge researchers, is the presence, extent and geometry of magma bodies beneath mid-ocean ridges. Early models of magma chambers based on studies of ophiolite sequences predicted an 'onion-shaped' magma body of large width (Fig. 1.3a) filled with molten material. The inclusion of energy conservation and thermal considerations (conductive and convective cooling) in this model altered substantially this geometry (Fig. 1.3b). However, geophysical observations have provided evidence for small sill-like melt bodies, overlying sub-circular low velocity zones of partially molten rock instead of the anticipated large, essentially molten reservoirs (Fig. 1.3c).

Current understanding of the crustal structure of mid-ocean ridges for different spreading rates can be summarised as follows:

**Fast spreading ridges.** Full spreading rates greater than 90 mm $yr^{-1}$. A fast spreading ridge whose segments have been studied extensively, is the East Pacific Rise (EPR) (e.g. at 9°N, 13°N and 17°N - Detrick *et al.,* 1987; Vera *et al.,* 1990; Christenson *et al.,* 1994; Collier & Singh, 1997; The MELT seismic team, 1998). These studies have revealed a total crustal thickness of 6-7 km, with layer 2A exhibiting high attenuation ($Q \sim$ 10-20) and porosity ($>$ 20%) but low velocity ($\sim$ 2.5 km $s^{-1}$) which increases to 5 km $s^{-1}$ when layer 2B is reached. Axial magma chambers have been imaged as thin (10-100 m) and narrow (1-2 km) lenses underlain by bell-shaped or sub-circular low velocity zones (LVZ), which probably represent regions filled with crystallised material and a small percentage of melt (Fig. 1.4a).

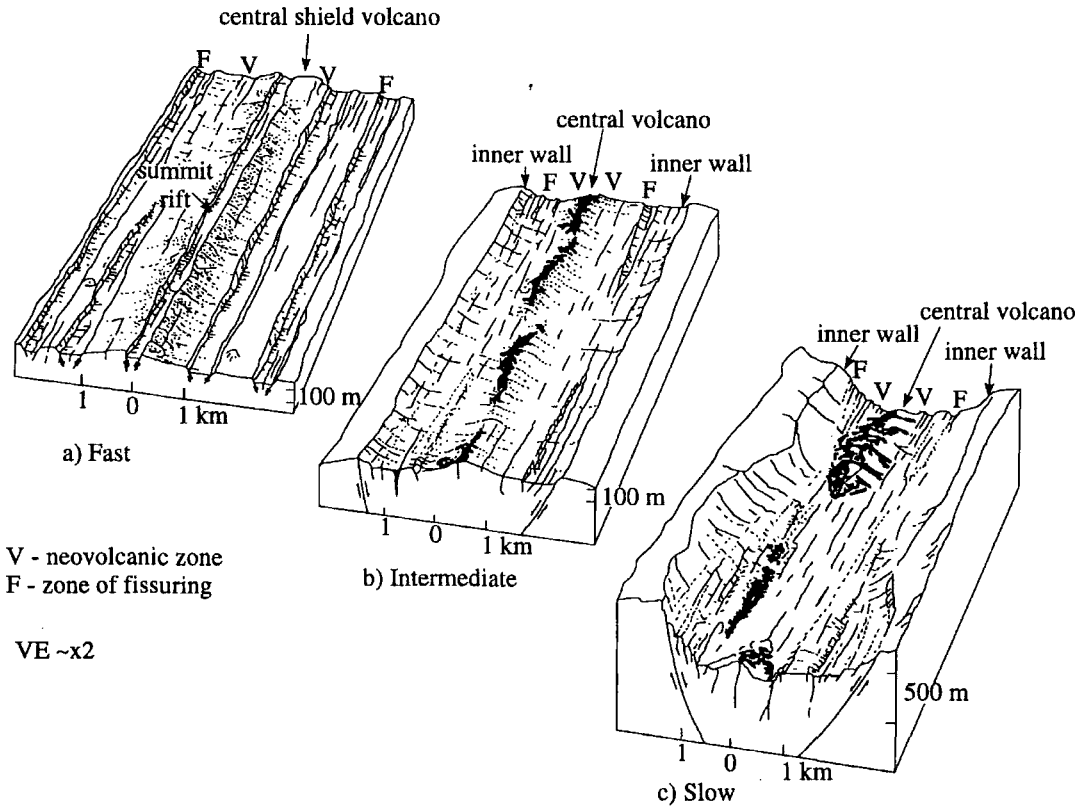


Figure 1.2: Schematic illustrations of the axial seabed morphology at fast, intermediate and slow spreading ridges. The central volcano is continuous at fast rates (a), moderately continuous with *en enchelon* offsets at intermediate rates (b) and highly discontinuous at slow rates (c). Note the different vertical scales (after Macdonald, 1982; Navin, 1996).

**Slow spreading ridges.** Full spreading rate less than 50 mm $yr^{-1}$. The Mid-Atlantic Ridge (MAR) is a typical example of a slow spreading ridge and few parts of it have been studied in detail seismically (Purdy & Detrick, 1986; Detrick *et al.*, 1990; Calvert, 1995; Sinha *et al.*, 1998). While crustal thickness appears to lie in the same range as the other ridge types, there is controversy over the existence or not of an axial magma chamber. A detailed description of the geophysical study of the Reykjanes Ridge at 57°45'N (Navin *et al.*, 1998; Sinha *et al.*, 1998) that provides the first unequivocal evidence for such a magma chamber (Fig. 1.4b) will be given in the next section.

**(a) Geological models**

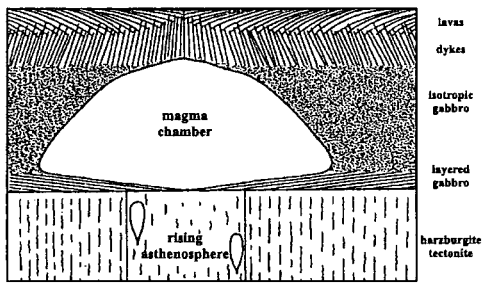


Cann (1974)

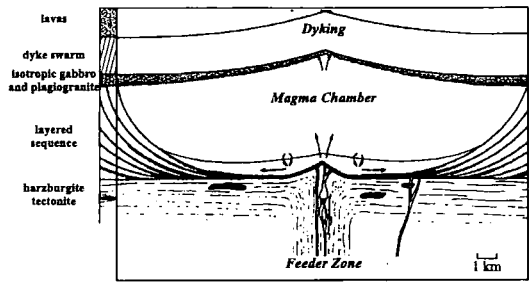


Smewing (1981)

**(b) Thermal models**

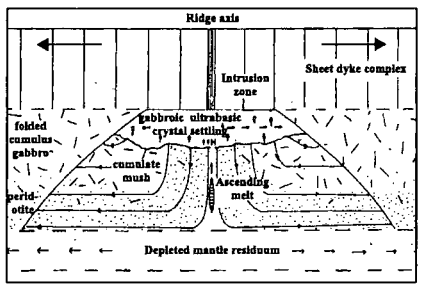


Sleep (1975)

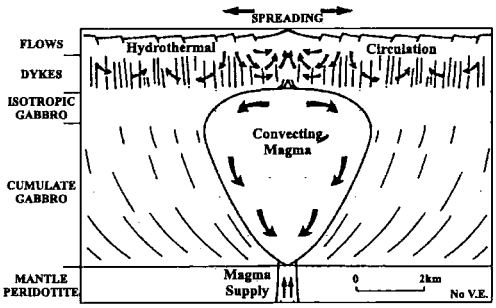


Wilson *et al.* (1988)

**(c) Integrated geophysical models**

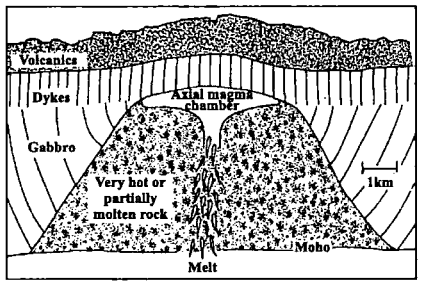


Macdonald (1989)

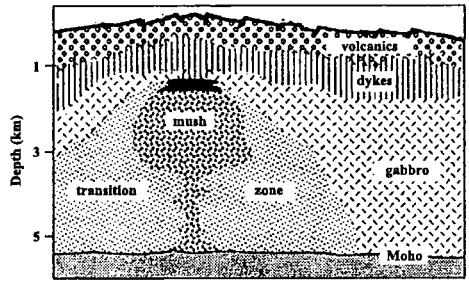


Sinton and Detrick (1992)

Figure 1.3: Across-axis magma chamber models. (a) Geological models based on theoretical models of the processes taking place at mid-ocean ridges and the interpretation of gabbro layering and genesis of the Oman ophiolite. (b) Thermal models based on energy conservation and conductive/convective cooling. (c) Intergrated geophysical models combining recent seismic observations of the geometry of the melt and underlying low velocity zone at the East Pacific Rise with previous geological and thermal models.

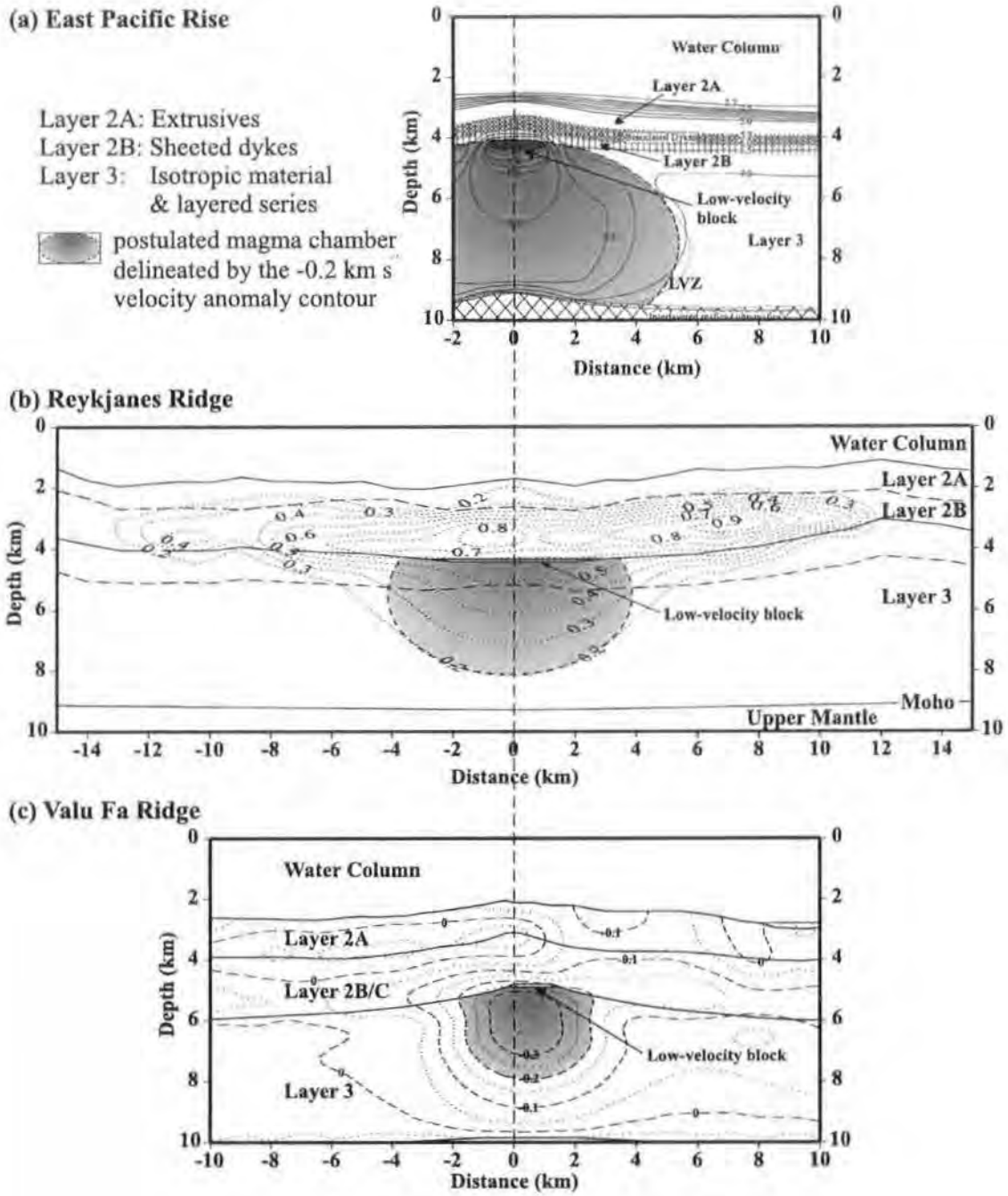


Figure 1.4: A comparison of the crustal structure found at fast, slow and intermediate spreading ridges. The spreading axis are located at 0 km model offset and subcrustal magma chambers are delinated by the 0.2 km $s^{-1}$ velocity anomaly contour. (a) EPR crustal structure at 9°30'N (after Vera *et al.*, 1990). (b) Reykjanes Ridge crustal structure at 57°45'N (after Navin *et al.*, 1998). (c) Valu Fa Ridge crustal structure at 22°26'N imaging a LVZ body (after Turner, 1998).

**Intermediate spreading ridges.** Full spreading rate between 50-90 mm $yr^{-1}$. Two of the most well studied intermediate spreading ridges are the Valu Fa Ridge (Morton & Sleep, 1985-first imaging of a melt lens; Collier & Sinha, 1990; Turner *et al.*, 1999) and the Juan de Fuca Ridge (Morton *et al.*, 1987; Rohr *et al.*, 1988; Christeson *et al.*, 1993; Cudrak & Clowes, 1993). The crustal structure of these ridges has many similarities with that found in EPR, however the crust appears to be thicker (6-8 km). Some of these studies have failed to image a LVZ underneath the melt region (cf. Fig. 1.4c for an exception) which may be partly explained by a diminished magma supply at the time of the study.

### *1.2.3 Geophysical studies at slow spreading ridges*

The absence of a substantial magma body beneath slow spreading ridges was widely accepted for many years (e.g. Keary & Vine, 1990). This argument was supported by a number of studies showing that: (a) the centroid depths of earthquakes observed at slow spreading ridges imply that the axial crust is brittle to 8 km depth (Huang & Solomon, 1988); (b) sub-axis propagating S waves were observed indicating that there was no significant body of partial melt underneath (37°N and 45°N - Fowler, 1976; 1978); and (c) a multichannel reflection survey at the most hydrothermally active area presently known along the MAR (23°20'N), failed to identify an intra-crustal reflector that could be associated with a magma body (Detrick *et al.*, 1990).

Based on the observations mentioned above Sinton & Detrick (1992) suggested an interpretive model of a magma chamber beneath a slow spreading ridge such as the MAR (Fig. 1.5). The main feature of this model is the lack of an eruptable magma lens because of a low magma supply from the mantle. Magma injection episodes are considered to take place sporadically, forming only small sill-like bodies that crystallise very quickly. If the model proposed by Sinton & Detrick (1992) is

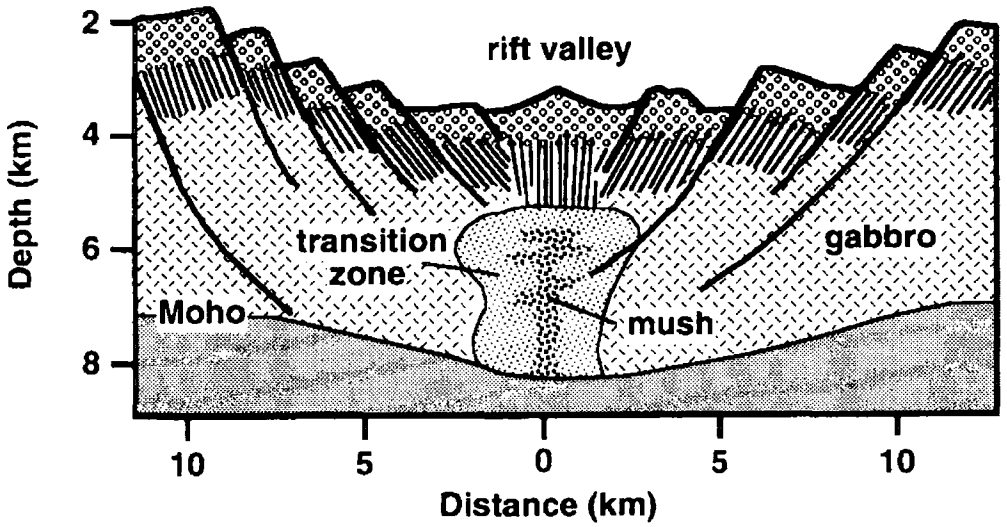


Figure 1.5: Model of the magmatic system beneath a slow spreading ridge based on geophysical and petrological constraints. A dyke-like mush zone is envisioned beneath the rift valley, forming small sill-like intrusive bodies which progressively crystallise to form oceanic crust. Faults bordering the rift valley may root in the brittle-ductile transition within the partially molten magma chamber. Eruptions will be closely coupled in time to injection events of new magma from the mantle (from Sinton & Detrick, 1992).

correct such magma bodies are, therefore, likely to be ephemeral features beneath slow spreading ridges.

However, more recent studies suggest that the crustal structure and processes of crustal accretion at slow spreading ridges are broadly similar to those at fast spreading ridges, differing only in the temporal stability of magma chambers. Calvert (1995) reprocessed the dataset obtained by Detrick *et al.* (1990) and after suppressing the high-amplitude coherent noise generated at the seafloor, he observed a low-amplitude reflector at a depth 1-2 km beneath the seabed and interpreted it as corresponding to the roof of a small magma chamber.

A much more detailed study of the slow spreading ridge at 57°45'N on the Reykjanes Ridge (Fig. 1.6) took place as part of the RAMESSES (Reykjanes Ridge

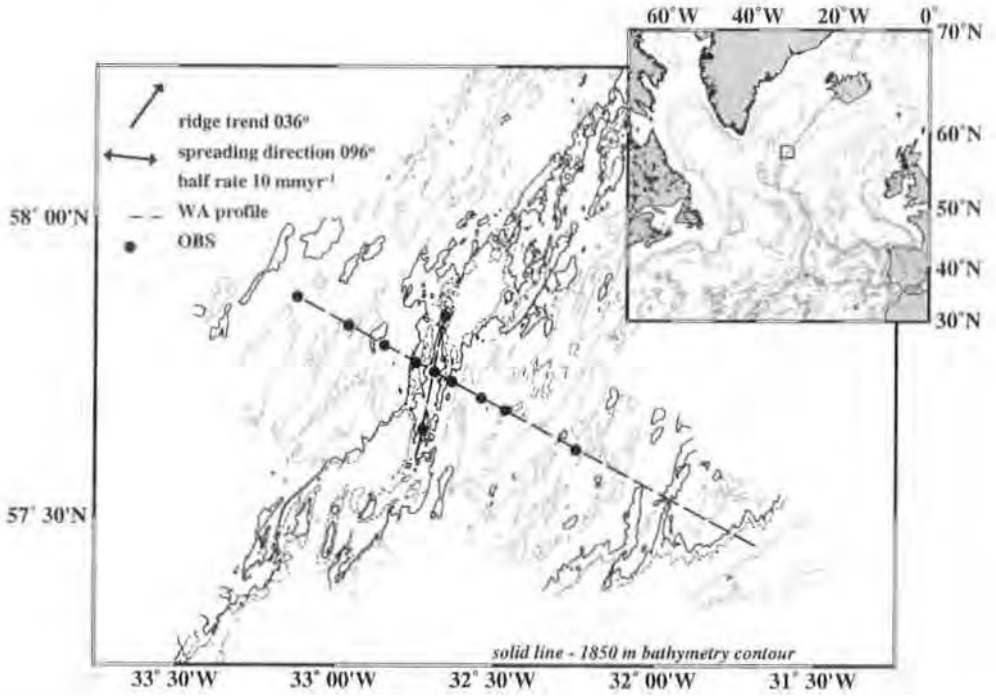


Figure 1.6: Map showing the RAMESSES study area and the corresponding bathymetry (C. Peirce, pers. comm. 2000). Solid lines indicate the position of wide-angle refraction/normal-incidence reflection profiles shot and black dots represent the position of ocean bottom seismometers. The inset map shows the bathymetry of the North Atlantic region and position of the study area (solid box).

Axial Melt Experiment: Structural Synthesis from Electromagnetic and Seismics) experiment (Sinha *et al.*, 1998). The aim of this project was to conduct an integrated geophysical study of a carefully selected, magmatically active axial volcanic ridge (AVR) segment that comprise this system. The survey consisted of three major components: wide-angle seismic profiles along and across the AVR, together with coincident seismic reflection profiles; controlled source electromagnetic sounding and magnetotelluric sounding. Supplementary datasets included swath bathymetry, gravity and magnetics.

Ray-trace modelling of the along and across-axis wide-angle seismic data revealed an axial LVZ in layer 3 beneath the AVR, which extends to a depth of 8 km and has a width of about 8 km (Fig. 1.7) (Sinha *et al.*, 1998; Navin *et al.*, 1998). This LVZ was interpreted to be the main body of the magma chamber containing a low percentage of melt and was shown to be overlain by an axial low velocity block at a depth 2.5 km beneath the seafloor, with a nominal thickness of 100 m and P wave velocity 3.0 km $s^{-1}$. This modelling was supported by reversed polarity reflection events identified along-axis (Inglis, 1995; Navin *et al.*, 1998) and forward modelling of coincident controlled source electromagnetic data showing a low resistivity ($\sim$ 1 $\Omega$m) anomaly within layer 3 (MacGregor *et al.*, 1998). The RAMESSES experiment was the first large scale geophysical study of an AVR segment at a slow spreading ridge. Its findings put forward the idea that crustal accretion at slow spreading ridges involves the presence of magma chambers similar to those found at intermediate and fast spreading ridges, although they seem to be short-lived rather than steady-state features.

## 1.3 Iceland

### *1.3.1 Tectonic setting and geological background*

Iceland lies on the Mid-Atlantic Ridge and is the result of the interaction of the spreading plate boundary and a mantle hotspot which together, have formed a large volcanic pile and unique on-land exposure of an accretionary plate boundary. The hotspot is thought to be a thermal anomaly within the mantle causing mantle melting beneath Iceland, the formation of a partial melt zone within the asthenosphere and updoming of the asthenosphere. The hotspot is believed to have migrated eastwards relative to the North American plate over the last 70 Ma emerging from beneath eastern Greenland at about 36 Ma and now considered to be situated at 64°N 16°W beneath Iceland (Lawver & Müller, 1994). This eastwards migration is also the reason why the plate boundary within Iceland is now offset by about 150 km to the east of the main trend of the Mid-Atlantic Ridge. Spreading along the

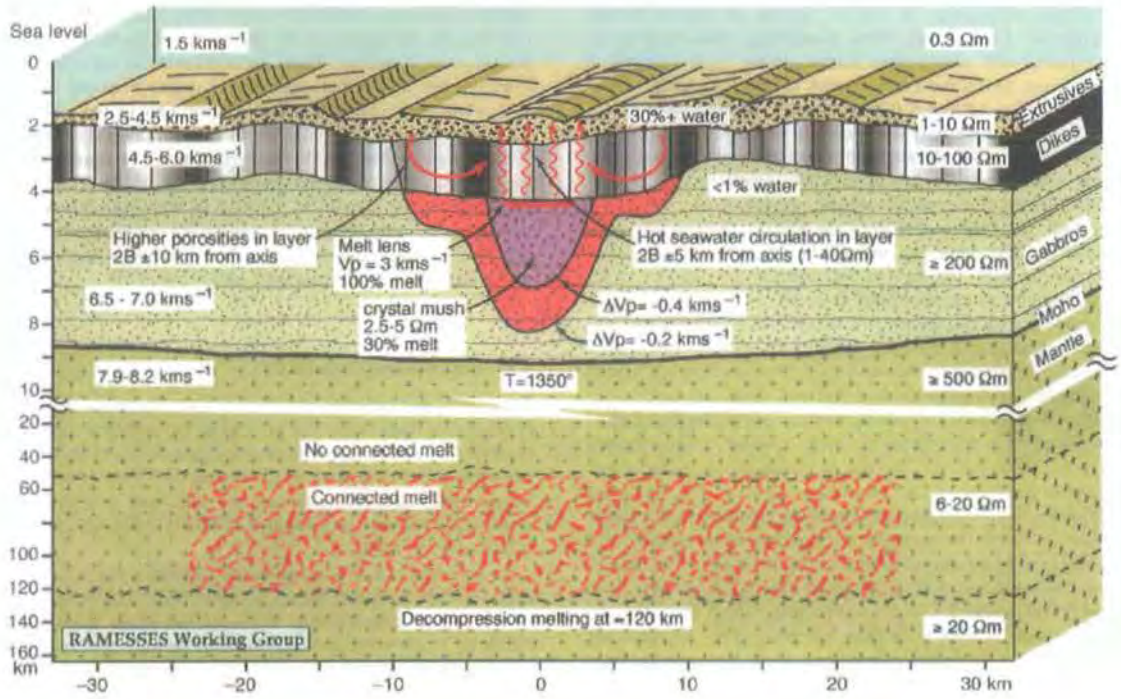


Figure 1.7: Inferred structural cross-section through the 57°45'N AVR, based on a synthesis of the results from the wide-angle and reflection seismic and controlled source electromagnetic components of the RAMESSES experiment. The seafloor bathymetry and the positions of the seismic layer boundaries are quantitatively accurate and are based on swath bathymetry data and seismic modelling. Similarly, estimates of seismic velocities, electrical resistivity, porosity, melt content and temparature are quantitative estimates based on observational data and modelling. Note that a 10:1 break in scale occurs at a depth of 10 km below sea level (from Sinha *et al.*, 1998).

Mid-Atlantic Ridge in Iceland occurs at a rate of 18 mm $y^{-1}$ (DeMets *et al.*, 1994).

The oldest exposed rocks in Iceland date from about 16 Ma and are probably underlain by rocks that date from at least 26 Ma (Bott, 1985). Tholeiitic basalts of Tertiary age in the east and northwest form about 50% of the surface area of Iceland. Most of the basalts dip gently towards the centre of the island, with the steepest dips (up to 10°) found at the lowest stratigraphic levels. Individual units tend to thicken downdip and most of them have originated from central volcanoes, the majority of which are now extinct and eroded (Walker, 1974). The extinct central volcanoes exhibit major geothermal alteration with dyke swarms and usually large intrusive bodies of gabbro or granophyre that represent solidified magma chambers.

During the last 700,000 years (upper Pleistocene) volcanic and tectonic activity has been concentrated along the plate boundary, which comprises the neovolcanic zones and two transform zones (Fig. 1.8). In the north, the Tjörnes Fracture Zone (TFZ) connects the Kolbeinsey Ridge north of Iceland to the Northern Volcanic Zone (NVZ). South of 65°N the plate boundary is split into the Western Volcanic Zone (WVZ) and the Eastern Volcanic Zone (EVZ). The South Iceland Seismic Zone (SISZ) joins the southern ends of the WVZ and EVZ. At its western end the SISZ meets the WVZ and the Reykjanes Peninsula at the Hengill triple junction.

There are two neovolcanic flank zones, one at Snæfellsness and the other south of the EVZ, that have only been volcanically active since the Plio-Pleistocene. These zones are characterised by a transition to alkali lava types and large cone-shaped or elongated central volcanoes. They have much less extensional faulting and graben formation than the other volcanic zones and their volcanic products lie unconformably on older, often eroded, rocks.

### *1.3.2 Seismicity*

Almost all seismic activity within Iceland occurs along the plate boundary (Einarsson, 1991). The largest earthquakes in historical times had magnitudes up to 7.1

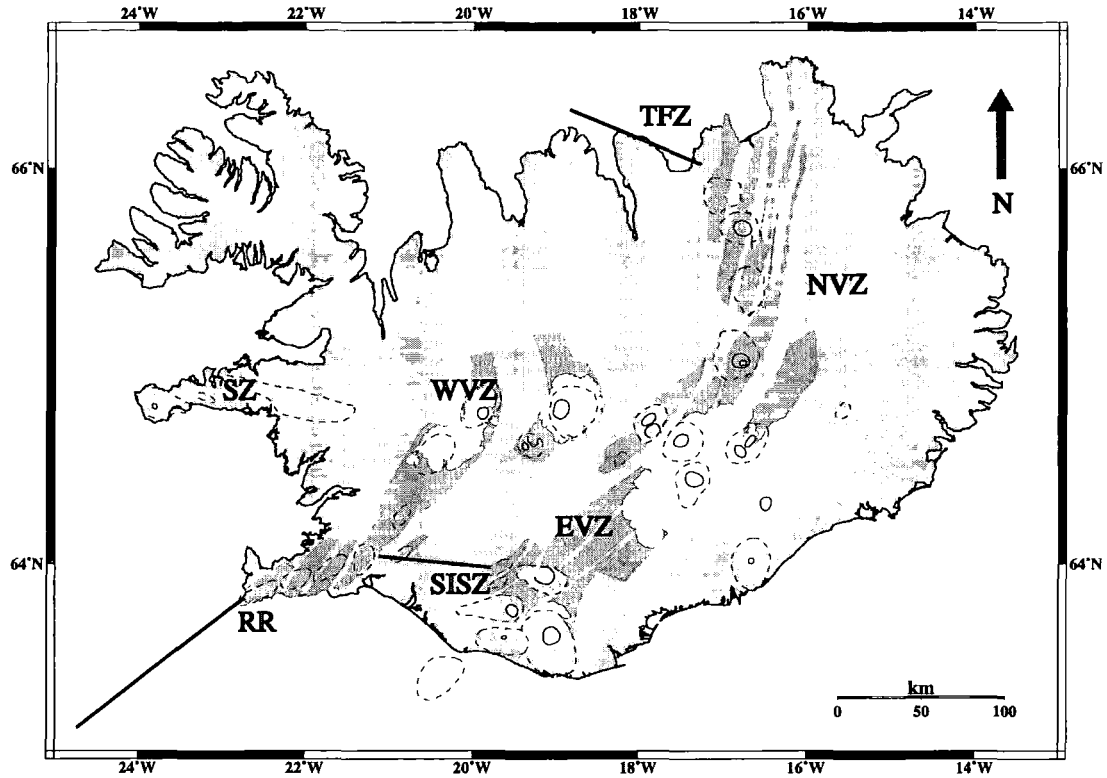


Figure 1.8: The plate boundary and volcanic systems in Iceland. NVZ: Northern Volcanic Zone, EVZ: Eastern Volcanic Zone, WVZ: Western Volcanic Zone, SISZ: South Iceland Seismic Zone, RR: Reykjanes Ridge, SZ: Snæfellsness Zone, TFZ: Tjörnes Fracture Zone. Solid lines represent outlines of calderas, dashed lines represent outlines of central volcanoes and thick black lines indicate main fracture zones. The white areas indicate permanent glaciers, of which Vatnajökull in the centre, is the largest.

and occurred in the SISZ and the TFZ (Stefánsson *et al.*, 1993). In the neovolcanic zones three types of seismicity are generally identified: small magnitude activity in geothermal areas that is continuous on a daily basis; tectonic earthquakes that often occur in swarms and are sometimes associated with rifting episodes; and volcanic earthquakes associated with major eruptions. The latter type of seismicity is common at volcanoes such as Krafla (in the NVZ), Katla (in the EVZ) and the volcanoes underneath the Vatnajökull ice sheet.

### *1.3.3 Crustal structure*

Early seismic refraction work in Iceland led to two possible interpretations of the Icelandic crust: (a) a 'thick crust' model consisting of three layers with a total thickness of 28 km and the deepest layer having a seismic velocity 7.4 km $s^{-1}$ (Båth, 1960); and (b) a 'thin crust' model consisting of two layers with a total thickness of 10 km underlain by a half-space that has a seismic velocity of 7.4 km $s^{-1}$ (Tryggvason, 1962). During the late 1960s and early 1970s a more detailed study of the Icelandic crust was conducted by Pálmason (1971). After interpreting the results of 80 refraction profiles shot around Iceland (some of them unreversed), Pálmason (1971) divided the crust into three layers comprising the upper and lower crust. The fourth layer was a half-space with an anomalously low velocity of 7.4 km $s^{-1}$ and was thus characterised as the 'anomalous mantle'.

For many years Pálmason's model was used to represent Iceland's crustal structure. The RRISP (Reykjanes Ridge Iceland Seismic Profile) experiment (Angeheister *et al.*, 1980; Gebrande *et al.*, 1980) conducted in the late 1970s supported the interpretation made by Pálmason for a thin crust, since the results showed that the crustal thickness lies in the range of 10-15 km (Fig. 1.9a). However, it was noted that should the 7.0-7.4 km $s^{-1}$ layer be taken as part of the lower crust, the depth to the Moho would be approximately 30 km.

The first serious doubt about the validity of the thin crust model was put forward by Bjarnason *et al.* (1993) after the interpretation of data obtained during the SIST (South Iceland Seismic Tomography) experiment. Strong wide-angle reflections from several shots, were interpreted as reflections from the Moho at 20-24 km depths with an apparent sub-Moho velocity of 7.7 km $s^{-1}$ and lower crustal velocities of 7.2-7.25 km $s^{-1}$ (Fig. 1.9b). In the light of these new results, Menke *et al.* (1996) studied the RRISP data and reinterpreted them to give a crustal thickness of 30-35 km. Menke *et al.* (1995) also measured values of the seismic Q factor for rays turning between 12-20 km depth beneath the WVZ and found them to be of the order of several hundred, suggesting a lower crust consisting mainly of gabbro having a temperature

of 700-775 °C.

Further evidence for a thick crust was provided by the ICEMELT experiment (Darbyshire *et al.,* 1998). This refraction profile was 310 km long and traversed Iceland from the Skagi peninsula on the north coast to the southeast coast and crossing over the Vatnajökull glacier (Fig. 1.9c). The crustal thickness was found to be 25 km at the north end of the profile, increasing to 38-40 km beneath southern central Iceland. The P wave velocities in the upper crust were estimated to vary between 3.2 to 6.4 km $s^{-1}$, while the velocity in the lower crust, at a depth of 24 km, was found to be 7.2 km $s^{-1}$. Calculated values of the Poisson ratio of the order of 0.26-0.27 were considered as an indication that the crust is well below the solidus temperature.

In contrast to the results obtained by the seismic experiments, which show no velocity inversions with depth, a number of studies of the electrical resistivity structure beneath Iceland (Beblo & Björnsson, 1980; Beblo *et al.,* 1983; Hersir *et al.,* 1984; Eysteinsson & Hermance, 1985) indicate the existence of a high-conductivity layer at varying depth (10-25 km) that could be attributed to partial melt. This apparent contradiction between the results obtained by the different geophysical methods probably indicates that there is still a fair degree of uncertainty in our knowledge of the nature of the crust beneath Iceland.

### *1.3.4 Structure of volcanic systems*

Volcanic systems in Iceland usually consist of a central volcano and a fissure swarm cutting across it roughly parallel to the volcanic zone. Many of these volcanic systems have also developed a collapse caldera. The fissure swarms are between 5-20 km wide and 40-100 km long (Gudmundsson, 1995), and are characterised by normal faulting during subsurface lateral magma excursions from the central volcano and fissure eruptions when these excursions reach the surface.

Studies of extinct volcanic systems have revealed the presence of sheet swarms

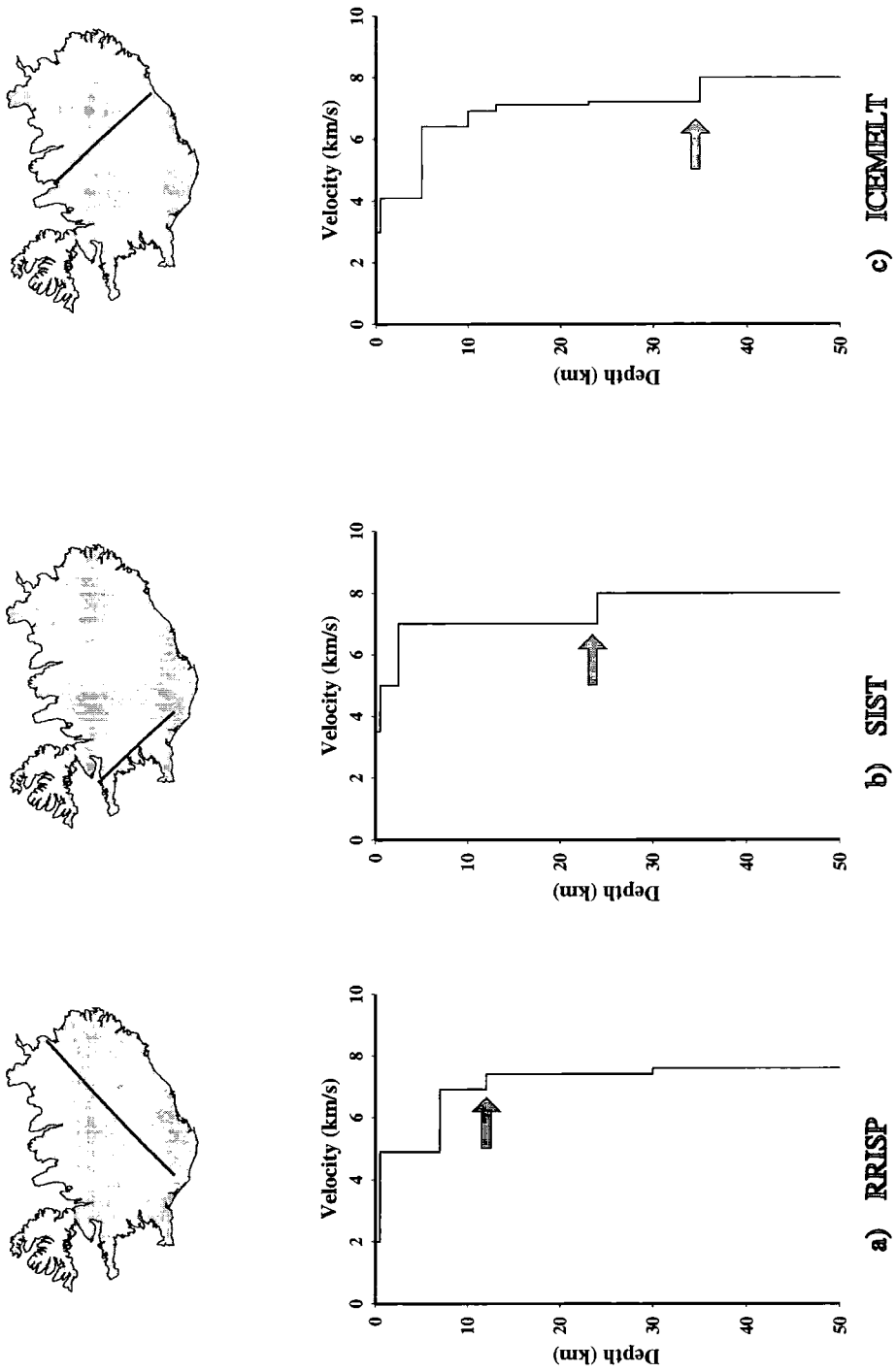


Figure 1.9: P wave velocity profiles obtained from interpretation of data collected during (a) the Reykjanes Ridge Iceland Seismic Profile experiment (after Gebrande *et al.*, 1980), (b) the South Iceland Seismic Tomography experiment (after Bjarnason *et al.*, 1993) and (c) the ICEMELT experiment (after Darbyshire *et al.*, 1998). The black arrows indicate the Moho depths as interpreted in each study, while the thick black lines on the maps of Iceland indicate the position of the profile in each experiment.

confined to the extinct central volcanoes and dyke swarms occurring outside being approximately 50 km long and 5-10 km wide. The sheet swarms are normally circular or slightly elliptical with a radius of several kilometres, while the dykes are subparallel and subvertical. Gudmundsson (1995) suggested that the dyke swarms are supplied with magma from deep-seated reservoirs, probably located at the crust-mantle boundary, and that the sheet swarms are mainly fed from shallow (1-3 km), crustal magma chambers (Fig. 1.10).

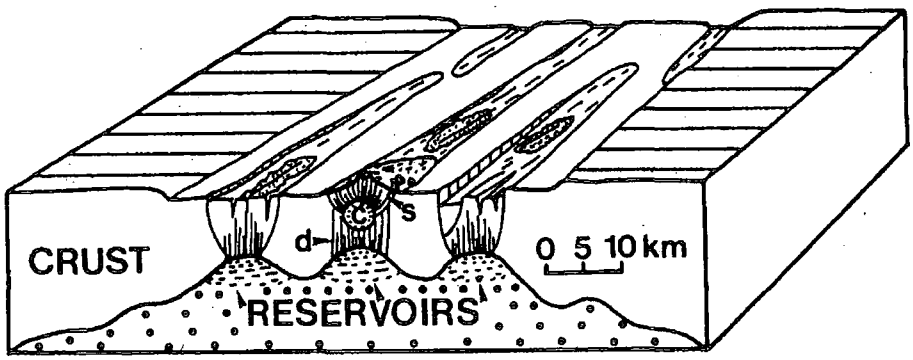


Figure 1.10: Schematic illustration of the proposed magma reservoirs below the volcanic systems of the rift zone in Iceland. The reservoirs are semi-ellipsoidal, dome-shaped top regions of the partially molten mantle beneath the rift zone. The reservoirs are separated by regions of thicker crust, so that the magma in each reservoir may evolve independently of the magmas in the neighbouring reservoirs. The infrastructure of the volcanic system in the centre is marked by dykes (d), inclined sheets (s) and a crustal magma chamber (c) that feeds a central volcano, whereas the other systems represent the regions outside the central volcanoes. The scale is approximate (from Gudmundsson, 1995).

Only a few geophysical studies have tried to image magma chambers in the Icelandic crust, therefore the exact shape, size, location and stability of such magma bodies remain uncertain. Einarsson (1978) used local recording of seismicity to delineate a body causing a shadow zone for S waves, at depths between 3-7 km within the Krafla caldera. However, uncertainties in event locations and ray geometry made it impossible to recover details about the shape of this body. Gudmundsson *et al.* (1994) performed a 2-D seismic undershooting experiment at Katla volcano (in the

EVZ) and observed large localised traveltime anomalies of the order of 0.4 s. After forward modelling of the anomalies, Gudmundsson *et al.* (1994) interpreted them as being caused by a shallow ($\sim$ 3 km depth), elliptical, magma chamber having an estimated volume of 10 km$^3$.

## 1.4 The Vatnajökull area

### *1.4.1 Geology, tectonics and previous geophysical studies*

The Vatnajökull glacier, located in central Iceland, is Europe's largest glacier and its northwest part (Fig. 1.11) is also suggested by geophysical (Einarsson, 1954; Tryggvason *et al.*, 1983) and geochemical studies (Sigvaldasson *et al.*, 1974), as the centre of the Icelandic hotspot. The fact that the area is covered by a thick ice layer and that it is tens of kilometres away from the inhabited south coast has made it difficult to resolve structural details of the volcanic systems that lie underneath the ice cap. Two of these volcanic systems, responsible for much of the observed activity, are Bárdarbunga and Grimsvötn. Each is characterised by an elliptical caldera and it is generally believed that the fissure swarms that appear outside the ice cap are connected to these volcanic systems (Sæmundsson, 1979, 1980; Jakobsson, 1979, 1980).

Most of the geophysical studies undertaken to date have focused on the area around Grimsvötn, mainly because of the frequent eruptions occurring there and the observed high geothermal heat flux. Seismic reflection surveys (Joset & Holtzscherer, 1954; Gudmundsson, 1989) have revealed an ice thickness of 240-260 m and a permanent subglacial caldera lake covering an area of 10 km$^2$ with a water depth of 40-90 m. The caldera floor was found to be covered by sediments in the northern and eastern parts and with lava flows in its southern part (Fig. 1.12) (Gudmundsson, 1989). Large piles of hyaloclastite rocks, formed by the interaction of hot lava with ice, surround the northern and southern flanks of the caldera.

Gudmundsson & Milsom (1997) conducted a gravity and magnetic survey in the

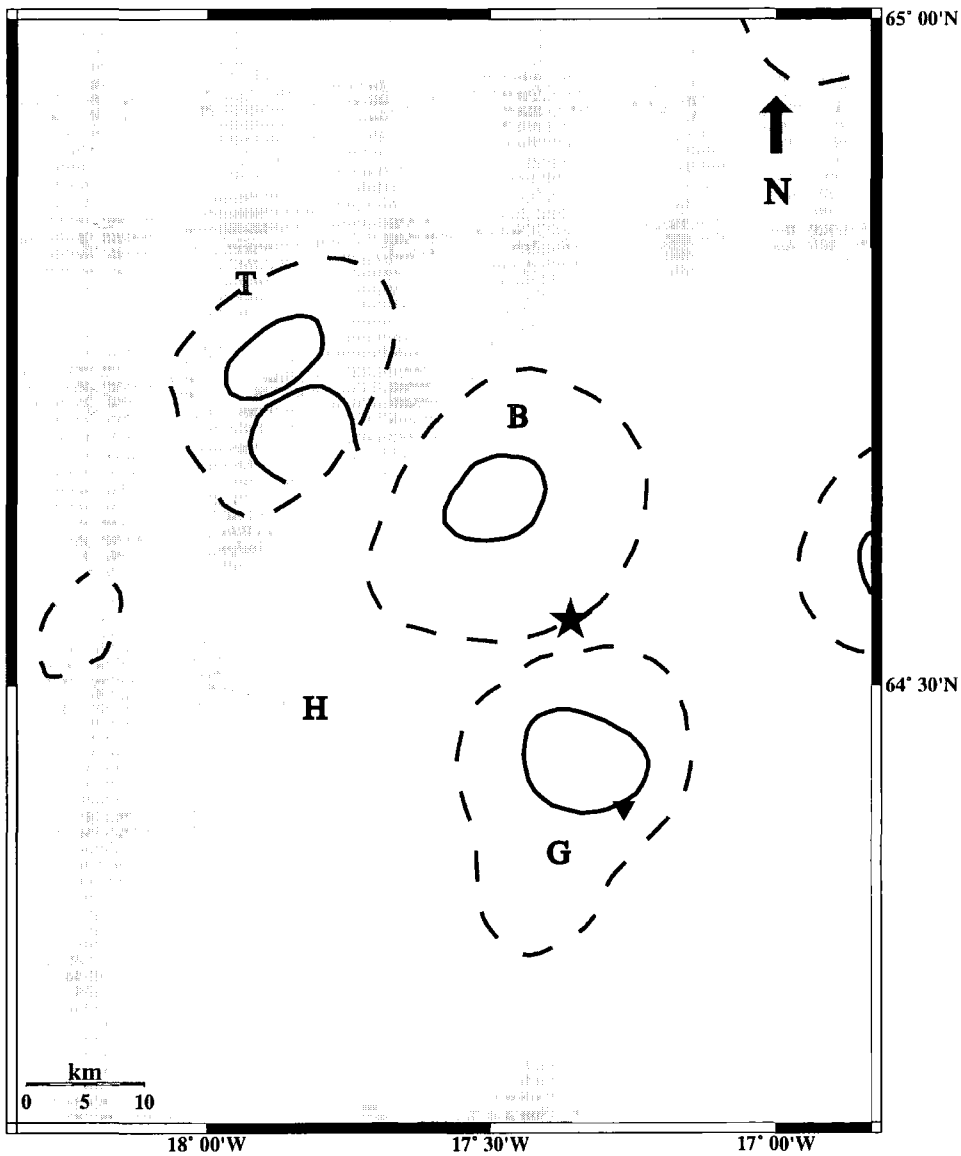


Figure 1.11: The northwest part of the Vatnajökull glacier and corresponding volcanic systems. T: Tungafellsjökull. B: Bárdarbunga. H: Hamarinn. G: Grimsvötn. Solid lines indicate outlines of calderas, while dashed lines indicate outlines of central volcanoes. The star shows the site of the 1938 eruption and the inverted triangle the site of 1934 and 1983 eruptions.

area that covers the Grimsvötn caldera. Analysis of the gravity data revealed a Bouguer gravity high of the order of 20 mGal that roughly coincided with a broad magnetic low, which also exhibited superimposed short-wavelength magnetic highs. Forward modelling of the gravity and magnetic fields revealed a dense body ($\rho$ = 2.95-3.0 Mg $m^{-3}$) ranging from 4 km depth to the surface, under the flanks of the caldera, which has been interpreted as a gabbroic intrusion and variable magnetisation in the uppermost 1-2 km of the crust, probably reflecting variations in hydrothermal alteration. Gudmundsson & Milsom (1997) also noted that the data are consistent with, but do not require, a 10 $km^3$ molten magma chamber occupying the uppermost 1.5 km of the crust beneath the caldera.

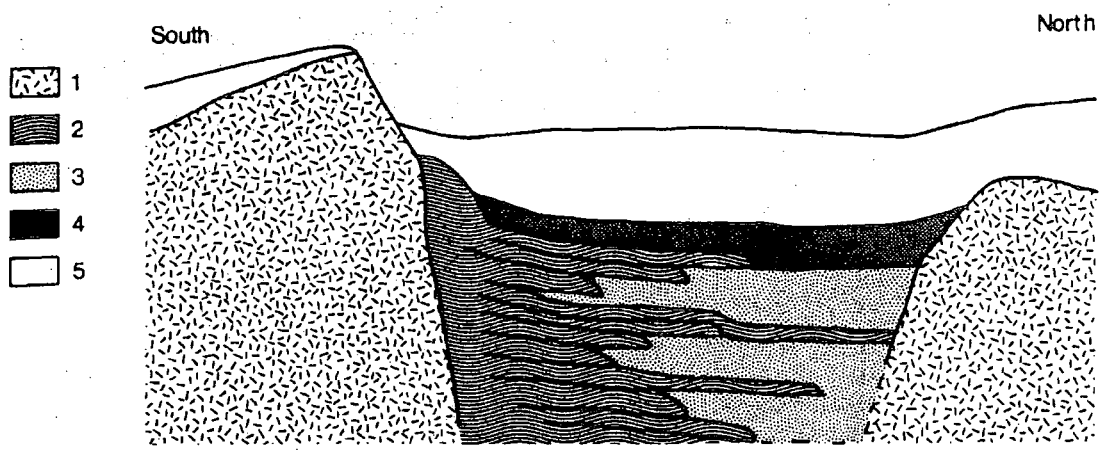


Figure 1.12: Schematic cross-section of the infill of the Grimsvötn caldera. Figure is not to scale. Lava flows and sills are believed to constitute the major part of the infill in the southern part of the caldera but sediments have accumulated in the northern part. 1: Hyaloclastite rocks. 2: Lava flows and shallow intrusions. 3: Sediments. 4: Water. 5: Ice. (from Gudmundsson, 1989).

### *1.4.2 Volcanism and related seismicity*

Over the last 1100 years the volcanoes beneath Vatnajökull are believed to have erupted 80 times, with 63 eruptions considered as certain, of which the number of

eruptions at Grimsvötn has been estimated between forty and fifty (Gudmundsson & Björnsson, 1991). During the last century Grimsvötn has erupted six times (Table 1.1), including the latest eruption on December 18, 1998, after the large eruption in 1996. Most of the information that we have about the eruptive activity in Grimsvötn come from aerial photographs of the area. Such observations show openings in the ice surface or depressions in the ice at the eruption site, filled with meltwater produced by the interaction of magma with ice. Accumulation of meltwater in the Grimsvötn caldera and its subsequent drainage underneath the glacier to the south coast has caused in the past catastrophic floods, that are described in the literature with the term 'jökulhlaup' (meaning flooding from the glacier). However, jökulhlaups cannot be considered as definite indicators of eruptions, since the high geothermal heat flux may also cause excessive production of meltwater (Björnsson, 1988).

**Table 1.1** Eruptions in the Grimsvötn area over the last century (after Gudmundsson & Björnsson, 1991)

| Year | Duration | Associated phenomena | Volume erupted ($km^3$) |
|---|---|---|---|
| 1934 | $\geq$ 2 weeks | Depressions in the ice, jökulhlaup | 0.03-0.04 |
| 1938 | 1-5 weeks | 7-8 km fissure, jökulhlaup | 0.3-0.5 |
| 1983 | 5-6 days | Depression in the ice | 0.01 |
| 1984 | 1 hour? | Volcanic tremor recorded | ? |
| 1996 | 2 weeks | 9 km fissure, jökulhlaup | 0.4 |
| 1998 | 10 days | Depressions in the ice | ? |

The first eruption in Grimsvötn to be detected by an increase in the level of seismicity was that of 1983, when a seismic network of 35 stations throughout the country became fully operational. This eruption was preceded by an intense earthquake swarm (Fig. 1.13), believed to have been caused by the failure of the magma chamber walls and subsequent migration of magma in the surface (Einarsson & Brandsdóttir, 1984). Volcanic tremor was also recorded and it was most intense

during the first 12 hours of the eruption. Unfortunately, since the seismograms were recorded on paper, it has not been possible to conduct a spectral analysis of the observed signals. Tremor was observed again one year later, on August 21, 1984 for only one hour and was interpreted as a small eruption that did not reach the surface of the ice (Björnsson & Einarsson, 1990).

Unlike Grimsvötn, Bárdarbunga was identified as an active volcano only recently, when aerial photographs revealed its elliptical caldera (Einarsson, 1991). There are no historical records of volcanic activity at Bárdarbunga, even though tephrochronological and geochemical studies suggest that it may have been active in the early centuries of historical times (Larsen, 1984). Since 1974 the Bárdarbunga area has been the centre of unusual seismic activity with the occurrence of ten large earthquakes ($M_w \geq 5.1$), the latest having occurred prior to the large volcanic eruption in September 1996 (Einarsson, 1991; Nettles & Ekström, 1998). The epicentres are located around the Bárdarbunga caldera (Fig. 1.14) and their focal mechanisms appear to deviate strongly from the conventional double-couple source model.

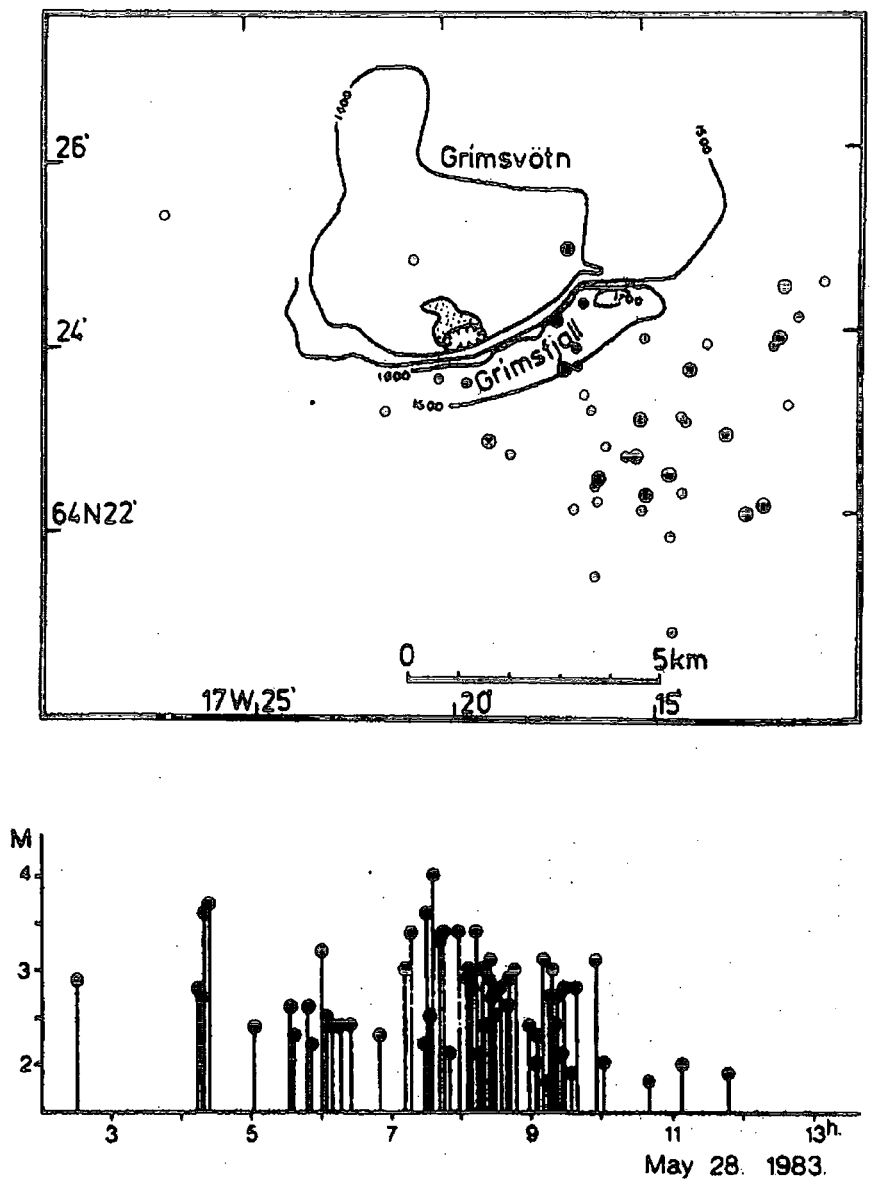


Figure 1.13: Epicentral map of the earthquake swarm that preceded the eruption on May 28, 1983. The arrival times for each event were read from paper records with an accuracy of $\pm$ 0.1 s and located using the HYPOINVERSE software. Standard error of the epicentral locations shown is better than 3 km. The time history of the swarm (coda magnitude versus time) is shown in the lower part of the figure (after Brandsdóttir & Einarsson, 1984).

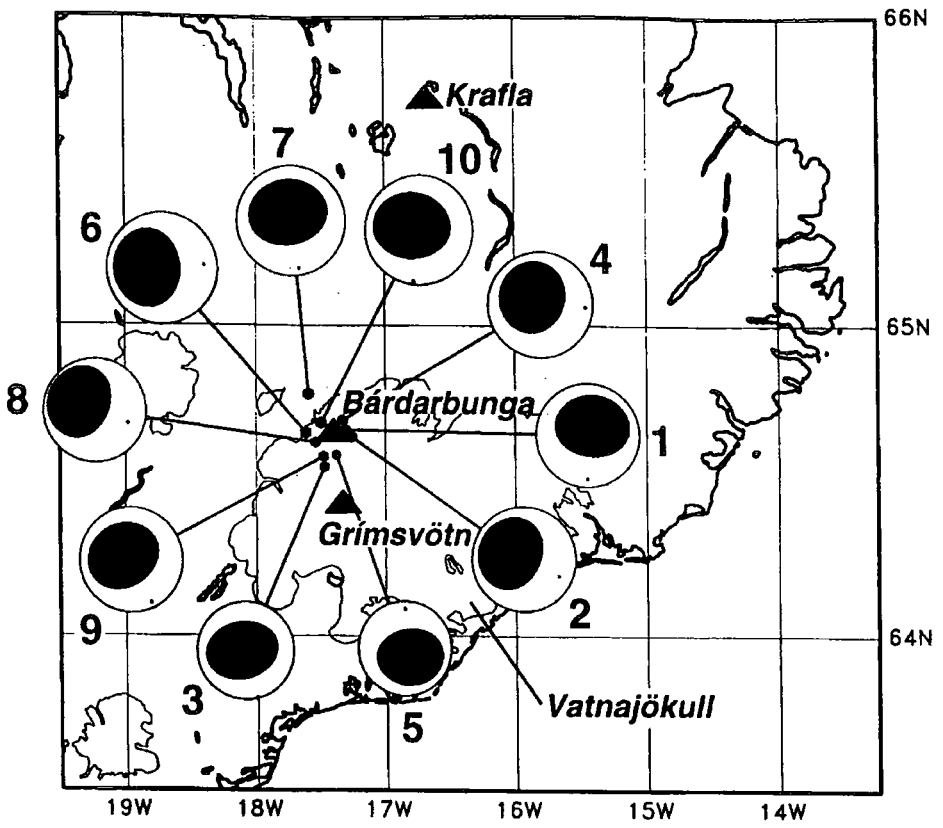


Figure 1.14: CMT solutions for the 10 earthquakes in the Harvard catalog which are located near Bárdarbunga volcano. The earthquakes are highly non-douple-couple and have vertical T axes, indicative of horizontal compression, despite their location in an extensional tectonic setting. Event 1: July 27, 1976 $M_w = 5.4$ depth 5.8 km. Event 2: December 28, 1977 $M_w = 5.4$ depth 4.5 km. Event 3: June 22, 1979 $M_w = 5.2$ depth 5.1 km. Event 4: August 12, 1980 $M_w = 5.4$ depth 4.2 km. Event 5: February 3, 1989 $M_w = 5.1$ depth 6.7 km. Event 6: September 15, 1990 $M_w = 5.6$ depth 4.0 km. Event 7: September 26, 1992 $M_w = 5.6$ depth 4.2 km. Event 8: June 22, 1993 $M_w = 5.4$ depth 3.3 km. Event 9: May 5, 1994 $M_w = 5.4$ depth 3.9 km. Event 10: September 29, 1996 $M_w = 5.6$ depth 3.6 km (from Nettles & Ekström, 1998).

## 1.5 Aims of this study

The overall objective of this study is to obtain a better understanding of the processes that are related to magma injection and emplacement in the earth's crust, by investigating the seismic signals that accompany such processes and by seismically imaging a magma body. In particular the following aspects will be addressed:

- Volcanic earthquakes recorded during the 1996 Vatnajökull eruption will be located and classified into specific groups. A description of the seismicity and the course of events during the main phase of the eruption will be given, while possible scenarios explaining the physical mechanism of the eruption will be presented.
- Volcanic tremor signals will be studied using both traditional spectral methods and methods from the discipline of nonlinear dynamics. The results obtained will be compared with those published for volcanic tremor recorded elsewhere and will be used to infer a possible source model involving magma flow.
- Seismic reflection data from the RAMESSES experiment phase two, will be processed in order primarily to investigate different processing methods and find an optimum processing procedure that will enhance the data as much as possible and then try to image the along-axis magmatic system of a slow spreading mid-ocean ridge.

## 1.6 Summary and structure of this dissertation

Mid-ocean ridges are now widely recognised as the sites of crustal accretion. Even though the oceanic crust has been found to be suprisingly uniform, the existence, geometry and extent of magma chambers beneath mid-ocean ridges with different spreading rates is a topic of active research and debate. The interaction of the Mid-Atlantic Ridge with a mantle hotspot is responsible for the formation of Iceland. The crustal structure of Iceland is not well understood, however recent studies point

to the possibility of a thick crust ($\sim$ 30 km) exhibiting strong lateral variations. The volcanic systems on Iceland are mostly located along the neovolcanic zone and consist of a central volcano with a collapse caldera and a fissure swarm, fed by shallow ($\sim$ 1-3 km), elliptical-shaped magma chambers. In particular, the Bárdarbunga and Grimsvötn volcanic systems, which lie underneath the Vatnajökull glacier in central Iceland, are responsible for frequent eruptions and the generation of large earthquakes ($M_w \geq 5.1$) that seem to have non douple-couple source mechanisms.

In this chapter the main areas of study have been described and previous geological and geophysical studies conducted have been summarised.

Chapter 2 describes data acquisition and the procedure followed for the location and classification of the volcanoseismic events recorded during the 1996 Vatnajökull eruption. A summary of the course of events during the eruption and its relation to the seismicity is also presented.

Chapter 3 gives a detailed review of volcanic tremor as recorded at volcanoes around the world, including the nature of its wavefield and models that have been proposed in order to explain its source mechanism.

Chapter 4 analyses the available volcanic tremor signals from the 1996 Vatnajökull eruption, first by a study in the time and frequency domain and then by using tools and methods from the discipline of nonlinear dynamics.

Chapter 5 describes the processing scheme applied to multichannel reflection data acquired during the RAMESSES phase two project along-axis at the 57°45'N axial volcanic ridge in an effort to image its magmatic system.

Chapter 6 contains a discussion of the possible physical mechanisms of the Vatnajökull eruption and the description of a physical model that could explain the excitation of the observed tremor. Also discussed is the interpetation of the reflection events observed on the along-axis reflection profile at the 57°45'N axial volcanic ridge.

# Chapter 2

# Seismicity and course of events during the 1996 Vatnajökull eruption

## 2.1 Introduction

In the summer of 1996 the HOTSPOT seismic network (Fig. 2.1) was installed on Iceland as a joint project between Princeton and Durham Universities, the Icelandic Meteorological Office and the US Geological Survey. The primary purpose of the project was to obtain high quality data of local and teleseismic events in order to study crustal and mantle structure. A secondary objective was to complement the existing permanent seismic network SIL (South Iceland Lowlands) in monitoring the volcanic and high seismicity zones. To date the research that has been carried out using data from HOTSPOT includes investigations of the crustal structure using receiver functions (Du & Foulger, 1999), attenuation tomography and surface waves (Allen *et al.*, 1999) and a large scale tomographic study of the mantle beneath Iceland using teleseismic events (Pritchard, 2000). This chapter describes the classification and location of volcanic earthquakes recorded by HOTSPOT and SIL during the main phase (September 29th-October 6th) of the 1996 Vatnajökull eruption.

## 2.2 Data acquisition

HOTSPOT consisted of 30 seismic stations each comprising a broadband, three-component seismometer supplied by the IRIS-PASSCAL instrument pool and a REFTEK Data Acquisition System (DAS) which recorded data to 0.66-1.2 Gbyte hard disks. The seismographs were equipped with three different types of sensors (CMG-3T, CMG-40T, CMG-3ESP), differing only slightly in their response to low frequencies and in their susceptibility to higher frequency noise. Factors such as

local sources of noise (roads, generators, rivers etc.), site geology and accessibility played a major role in determining the location of each station. The fact that the interior of Iceland is uninhabited and considerably more difficult to access than the coastal areas, due to poor road and weather conditions, meant that careful planning was required for servicing each of the stations installed there. Disks with the largest capacity were, therefore, used for stations that were difficult to access, such as station HOT23 installed on a rock outcrop on the Vatnajökull glacier. This minimised the number of servicing and maintenance visits to approximately one every 4 months for these stations, while in stations where accessibility was relatively easy maintenance was carried out monthly.

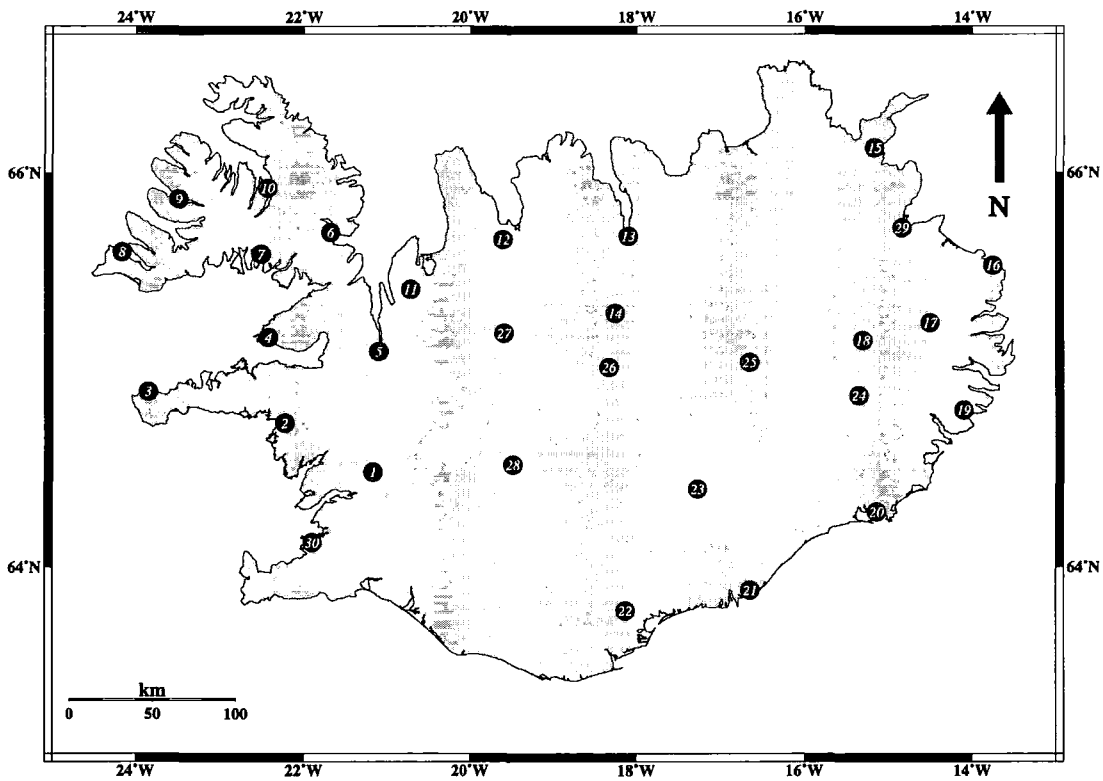


Figure 2.1: The HOTSPOT seismic network. Black numbered dots indicate the locations of seismic stations. White areas indicate permanent glaciers.

Whenever possible stations were installed in a sheltered location, such as a farm-house or a wooden hut, and normally placed directly on bedrock or on concrete floors underlain by bedrock. If this was not possible the instrument was put inside a concrete-bottomed pit constructed by the field party which included two large

inverted buckets as the vault walls. Power to the instrument was supplied by 60 Ahr lead-acid battery packs and/or 30 Watt solar panels for stations far away from inhabited areas, and by continuous mains power when that was available. Time corrections to the internal DAS clocks were calculated from the timing signal broadcast by the Global Positioning System (GPS) satellites and all stations were equipped with an antenna in order to be able to receive it. A detailed description of the instrumentation, station installation and maintenance procedures can be found in Pritchard (2000).

Data extraction from the field disks was performed at the project headquarters in the Icelandic Meteorological Office, using computer hardware supplied by IRIS-PASSCAL, which included two Sun workstations, three 9 Gbyte disks and 4-mm DAT tapedrives. The data blocks written by the DAS were converted into Miniseed format using the program *ref2mseed* and stored in files kept on the workstations' disks. After a visual quality control of randomly chosen files, the data were dumped to DAT tapes and distributed to the institutes participating in the project.

## 2.3 The data related to the 1996 eruption

The dataset used to study the 1996 Vatnajökull eruption covers the period from the onset of the seismic activity on September 28th, either in the form of volcanic tremor or earthquake swarms, until October 13th which marks the end of the main phase of the eruption (Einarsson *et al.*, 1997). During that time all HOTSPOT stations were operational, recording continuously with a sampling interval of 20 samples $s^{-1}$, except from station HOT26 which was down due to power failure. Station HOT23 was the closest ($< 10$ km) station to the eruption site and provided valuable records of volcanic tremor that occurred before and after the eruption.

First, data were read from the DAT tapes and stored in separate directories for each day named `E1996.xxx`, where `xxx` was a three digit number indicating the corresponding Julian day with subdirectories for each station (e.g `E1996.273/HOT23`).

Each datafile was in Miniseed format and contained 20 minutes of data, with a naming convention `96.xxx.ab.cd.ef.yyy.z.m`, where `xxx` is the Julian day, `ab, cd, ef` was the starting hour, minute and second for each file, `yyy` was the DAS number and `z` the component number (4 for the vertical, 5 for NS and 6 for EW).

## 2.4 Processing of the HOTSPOT data

### *2.4.1 Description of seismic signals recorded*

#### *2.4.1.1 Classification schemes used for volcanoseismic signals*

The variety of seismic signals generated during volcanic eruptions has prompted researchers to find ways to categorise them, making their study easier as well as more systematic. Minakami (1960) was the first to propose a way of classifying volcanoseismic signals based on their waveform appearance and frequency content. Minakami (1960) characterised high-frequency (1-15 Hz) earthquakes as 'A-type'; low-frequency earthquakes (1-5 Hz) as 'B-type'; earthquakes caused by an explosive eruption as 'explosion earthquakes'; and persistent ground vibrations as 'volcanic tremor'. This classification scheme has been used quite extensively for seismic signals originating at volcanoes around the world (e.g. Tsuruga *et al.*, 1997; Sherburn *et al.*, 1999).

The development of models that describe the source processes of volcanic earthquakes (Chouet, 1986; 1992) as well as the more thorough understanding of propagation effects has led many authors to propose alternative classification schemes based on the inferred source mechanism for each event (e.g. Power *et al.*, 1994). In general it is believed that impulsive P onsets and a high-frequency content indicate that shear failure of rock due to excessive fluid pressure is the dominant source process. Emergent P onsets and a low-frequency content may indicate fluid-flow processes as a possible source. McNutt (1996) highlighted the uncertainties arising from such an approach and suggested instead a classification in terms descriptive of the frequency content of each signal. Table 2.1 gives a comparison of the different

terminology that is currently used.

**Table 2.1** Classification schemes used for volcanoseismic signals.

| **Latter (1979)** | **Power *et al.* (1994)** | **McNutt (1996)** |
|---|---|---|
| Tectonic, volcanotectonic | Volcanotectonic | High-frequency |
| Volcanic | Long-period | Low-frequency |
| Medium-frequency | Hybrid | Mixed-frequency |
| Volcanic explosion | Explosion | - |
| Volcanic tremor | Volcanic tremor | Volcanic tremor |

### *2.4.1.2 Classification of the Vatnajökull signals*

It is common practice in seismic monitoring of active volcanoes to place all available instruments as close as possible to the eruption site, in order to avoid distortions of the recorded waveforms due to propagation through heterogeneous structures that usually characterise volcanic areas. However, the HOTSPOT network was not designed for monitoring volcanic activity and the only station close to the site of the 1996 Vatnajökull eruption that could be used for signal classification was HOT23. An additional problem was that most of the data were contaminated with ocean microseismic noise (by far the commonest source of noise on Iceland), an almost monochromatic signal with a frequency of 0.3 Hz. Highpass filtering at 0.5 Hz usually solves this problem, but leaves open the question of whether some signals contain energy in the same frequency range as ocean microseismic noise.

Initially, data from station HOT23 were visually inspected using the program *pql* provided by the IRIS-PASSCAL software library. *pql* runs in the X-windows and enables the user to view a number of traces at a time on the screen, to filter them (using a built-in Butterworth filter) or to select any trace and view its amplitude spectrum as a linear, semilogarithmic or logarithmic plot. Even though *pql* is easy

to use because of its graphics interface, it does not have the ability to create complicated plots of traces alongside their spectra, that can be subsequently converted to postscript files. The latest version of the Seismic Analysis Code (SAC2000) software package (Goldstein *et al.*, 1998) contains this option and such plots can be created by means of macros that contain SAC commands. Therefore, the data were converted from Miniseed to AH ('ad-hoc') format using the program *ms2ah*, and from AH to SAC format using the program *ah2sac*, both provided by the AH software library.

The files containing three-component seismograms for each earthquake were first viewed on screen, using the `plot1` SAC command and an analysis window centred on the event was chosen. The SAC macro *do_spectra* was then used to highpass filter the three-component traces at 0.5 Hz, then to apply a Hanning window to each trace, to calculate its spectrum and to plot the results creating also a SAC graphics file. The program *sgftops*, which is part of the SAC package, was used to convert the file to postscript. Hardcopies of all events were obtained and chronologically ordered, so that direct comparisons could be made. Since no information about the source processes of these events was available in advance, the classification scheme suggested by McNutt (1996) was preferred and will be used hereafter in this thesis. The characteristics found in each group are:

**Low-frequency events.** The waveform is characterised by an emergent onset of the P wave and a lack of clear S phases (Fig. 2.2). The coda decays very slowly with time, increasing the duration of the signal up to one minute. The energy in the spectrum is mostly in the range 0.5-2 Hz, with multiple sharp peaks. In many cases, two or more of these events are clustered together forming a continuous wavetrain.

**Mixed-frequency events.** The waveform is characterised by a high frequency, impulsive P wave onset and the lack of an S phase, followed by a coda that decays almost exponentially with time (Fig. 2.3). There is considerable energy in the range 1-2 Hz, but energy at higher frequencies is also present.

**Volcanic tremor.** Following the start of the eruption, wavetrains with small amplitudes form continuous tremor. Bursts with larger amplitudes and variable duration are superimposed upon it (Fig. 2.4). Energy is concentrated in the frequency range 0.5-3.9 Hz. A detailed analysis of volcanic tremor signals will be presented in Chapter 4.

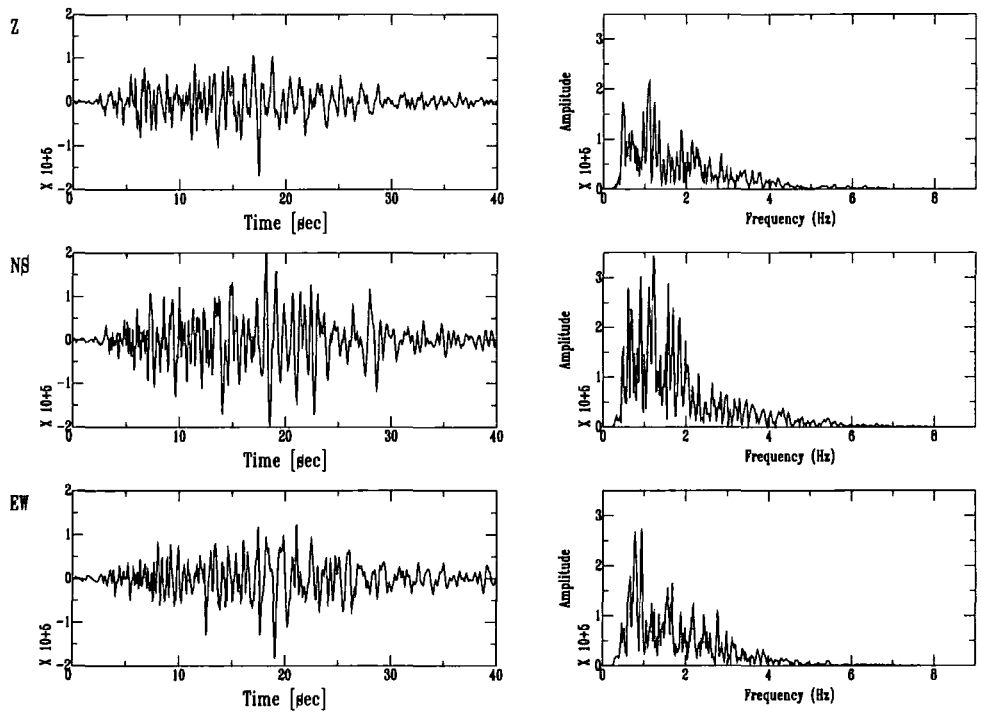


Figure 2.2: Velocity waveforms and amplitude spectra of a low-frequency event recorded after the onset of the eruption at station HOT23. The amplitude scales are normalised to the largest value of the three components.

## *2.4.2 Location of events recorded by HOTSPOT*

### *2.4.2.1 Phase picking procedure*

Data files covering the period September 28th until October 6th were converted from Miniseed to AH format, split into five minute segments for every station and a list file of the pathnames for each of these segments created using Bourne-shell scripts

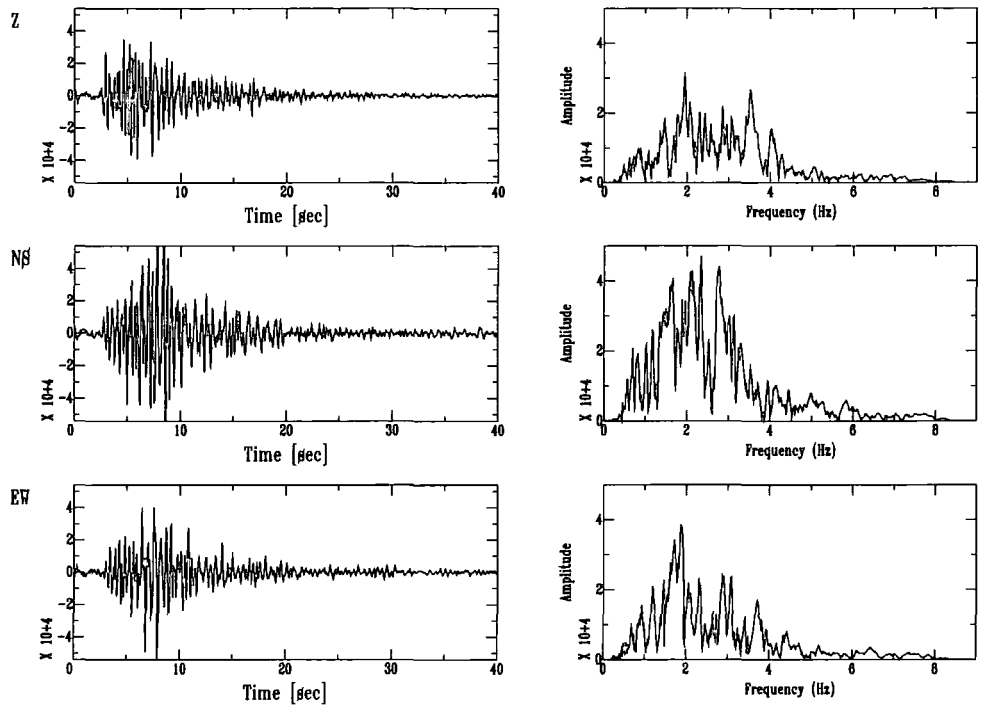


Figure 2.3: Velocity waveforms and amplitude spectra of a mixed-frequency event, recorded before the onset of the eruption.

written by B. R. Julian. List files were named `xxx.ab.cd.ef.list`, where `xxx` corresponds to the Julian day number, and `ab, cd, ef` the starting hour, minute and second of each segment. The picking program *epick* (B. R. Julian pers. comm., 1998) was called with the command

```
epick -l listfile
```

and displayed on the screen a number of three-component traces at a time.

The nature of the volcanic earthquakes precluded the picking of S phases, so the bulk of the picks were made using P onsets on the vertical component traces. A typical picking procedure started by identifying an event recorded by at least five stations, with a good azimuthal coverage around the eruption site and with

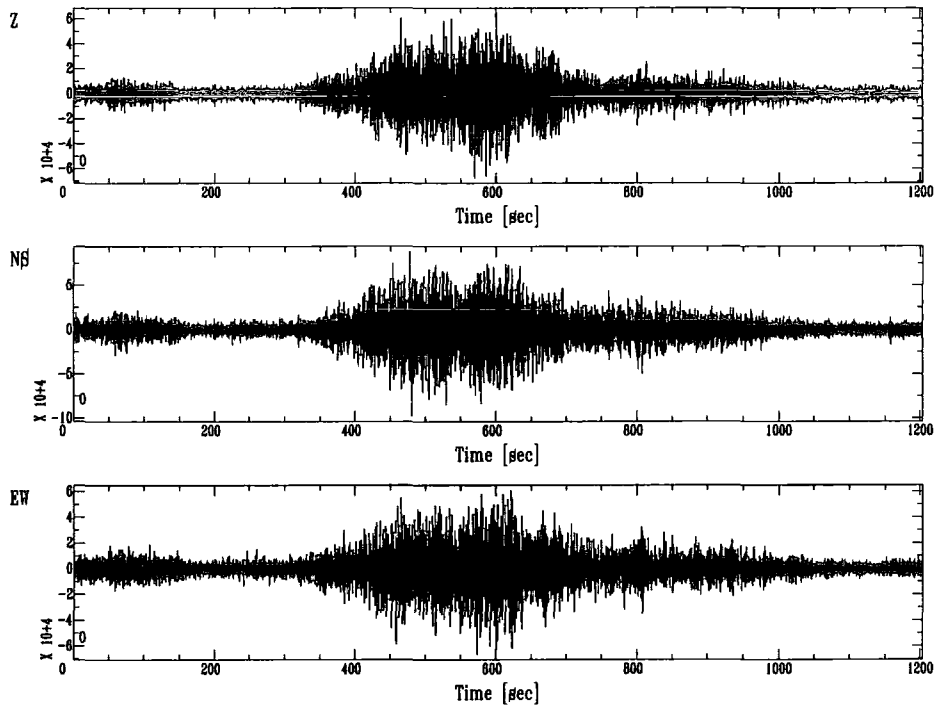


Figure 2.4: Velocity waveforms of high-amplitude tremor superimposed on the background tremor, recorded after the onset of the eruption.

high signal-to-noise ratio. Once a station was selected for picking, *epick* plotted the three-component seismograms in a new window (Fig. 2.5) and enabled the user to magnify or filter the data displayed using a built-in, three-pole Butterworth filter. Normally at this stage traces were highpass filtered at 0.5 Hz to remove any ocean microseismic noise present. Once a pick was made it was assigned a quality value, which was 1 or 2 in most cases, using a value of 0 as best quality and 4 as worst. The information associated with each pick (picked station, time to the nearest millisecond, phase identification label, pick quality) was then written automatically to a binary file which had the same root name with the list file and the suffix 'ep' appended at the end, e.g. `xxx.ab.cd.ef.ep`. In total 339 earthquakes were picked in this way for the period of nine days.

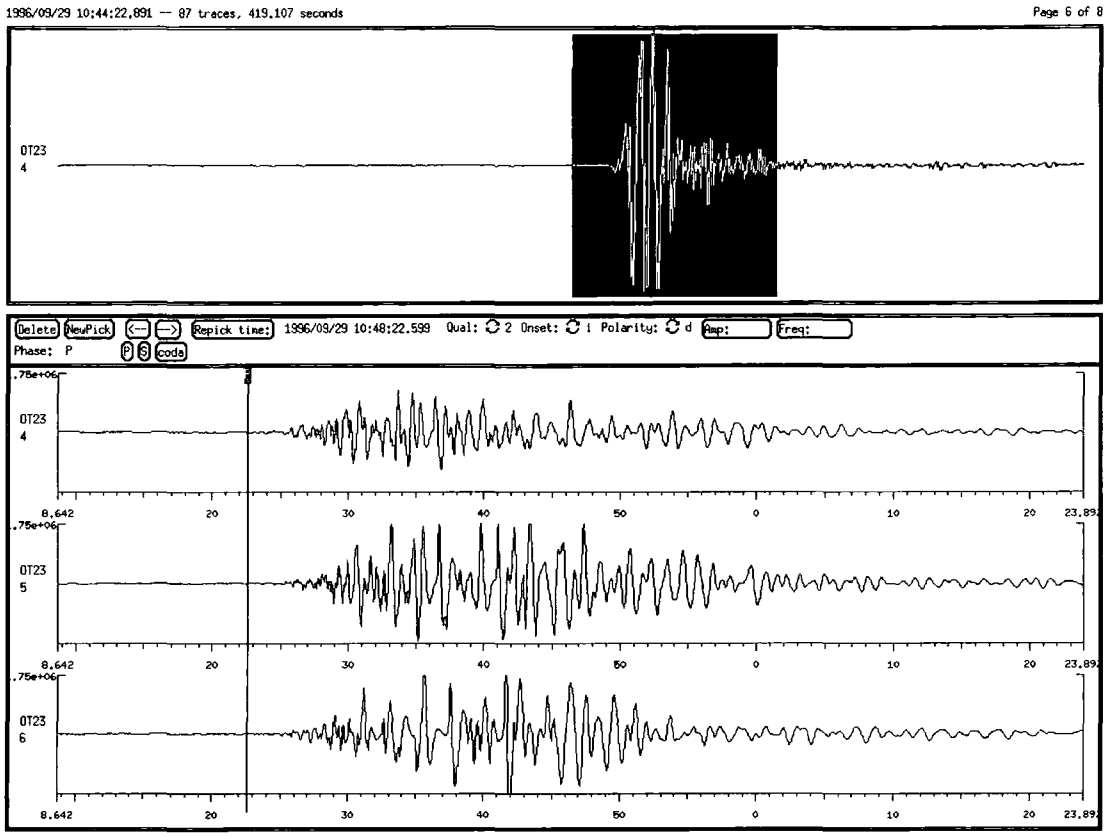


Figure 2.5: Picking window of the program *epick*. The event highlighted is the $M_w$ 5.6 earthquake that initiated the seismic activity prior to the eruption.

### *2.4.2.2 Clock corrections*

The corrections applied by the GPS receiver to the internal DAS clock were written to a separate log file for each station. Graphical representations of the amount of clock drift versus time were then obtained in order to assess the performance of the clock in each station. Throughout the period that the HOTSPOT network was operational, it was found that the largest amount of clock drift at any station did not exceed ± 50 ms (Pritchard, 2000). In particular, for the period September 28th-October 6th for which the volcanic earthquakes were picked, the amount of drift in most HOTSPOT stations was of the order of ± 5 ms. Taking into account that the picking accuracy for impulsive, mixed-frequency events was approximately one

sample and for low-frequency events five samples, it was not considered necessary to apply any clock corrections to the data.

### *2.4.2.3 Event location procedure*

The locations of events picked were obtained using the program *qloc* (B. R. Julian, pers. comm. 1998), which performs an iterative, damped inversion of P and S wave arrival times to minimise the sum of squared travel-time residuals. The initial epicentral location assumed by *qloc* for any event coincides with the position of the station that has the earliest arrival time and a hypocentral depth of 3 km. Subsequent iterations first correct the epicentral location and then find a depth that gives the best fit to the observed travel times.

The one-dimensional velocity model used for all locations presented in this thesis (Table 2.2) is also used for routine location of local events by the Icelandic Meteorological Office (G. Gudmundsson pers. comm., 1998) and is based on the results of the tomographic study of Iceland published by Bjarnason *et al.* (1993). The operation of *qloc* is controlled by the Bourne-shell script *eloc* which reads the binary pick files created by *epick*. The output of *eloc* is an ASCII list giving the best fit epicentre and hypocentre location together with the residuals obtained from each station. Relative locations using the master event method were also obtained and are shown in Appendix C.

As in previous studies of the seismicity of the Vatnajökull area (Einarsson & Brandsdóttir, 1984), difficulties were encountered in constraining the hypocentral locations for a large number of events. The main reason for this is the poor knowledge of the strongly heterogeneous Icelandic crust, which is not easily accommodated by a one-dimensional velocity model. A secondary reason is the lack of clear S phases from most of the events. Taking into account the thinning of the upper crust beneath Vatnajökull, as indicated by seismic refraction studies (Darbyshire *et al.*, 1998), it was decided to include in this study only those hypocentres which are

**Table 2.2** Crustal model used to locate events.

| Layer thickness (km) | P wave velocity (km $s^{-1}$) |
|---|---|
| 1.00 | 3.53 |
| 2.00 | 4.47 |
| 3.00 | 5.16 |
| 4.00 | 5.60 |
| 6.00 | 5.96 |
| 9.00 | 6.50 |
| 20.00 | 6.73 |
| 32.00 | 7.20 |
| 90.00 | 7.40 |

located no deeper than 8 km.

### *2.4.3 Course of events and distribution of seismicity*

At 10:48 hours GMT on the morning of September 29th, an earthquake of magnitude $M_w = 5.6$ took place near the northern rim of the Bárdarbunga caldera (Fig. 2.6). It was followed by a swarm of other earthquakes about twenty minutes afterwards. All of these earthquakes may be characterised as low-frequency events and their epicentres delineate the caldera rim. Between 14:10 and 17:20 hours, the activity decreased but resumed again in the evening of the same day. This time the epicentres were located to the southeast of the Bárdarbunga caldera and 15 km away from the area where the seismic activity first started. The spectra of these events exhibit energy at higher frequencies but their coda decay slowly, similar to those of low-frequency events.

In the early hours of the morning the seismic activity continued at the same

area, slowly migrating southwards towards Grimsvötn during the day (Fig. 2.7). The resulting earthquake cluster that is formed is elongated in the northnortheast-southsouthwest direction and covers the same area where the eruptive fissure and depressions on the ice were observed later. Meanwhile the Bárdarbunga area was relatively quiet, with only a few events occurring at the northeast caldera rim. Almost all of these earthquakes are mixed-frequency events, and have a coda decaying exponentially with time. Later that evening (22:00) continuous volcanic tremor became visible above the ambient background noise at the nearest station (HOT23), indicating that the subglacial eruption was imminent.

On October 1st, the activity persisted in the northern part of Grimsvötn, forming a smaller elongated cluster of epicentres, while at the same time another cluster formed at the northeast part of the Bárdarbunga area (Fig. 2.8). Early in the morning of that day, the fissure and depressions in the ice were observed from an aeroplane. Most of the earthquakes recorded subsequently are typical low-frequency events, superimposed on the background tremor. On October 2nd, the eruption broke through the ice and became subaerial, but the seismic activity decreased considerably. The Grimsvötn area was quiet and most of the events were located in the northeast part of the Bárdarbunga caldera (Fig. 2.9). On subsequent days (October 3rd-6th) low-frequency events continued to take place in the northeast of Bárdarbunga and inside its caldera. However, a small number of earthquakes were located to the north and inside the Tungafellsjökull volcanic system, up to 20 km away from the Bárdarbunga caldera (Fig. 2.10). Cross-sections of the hypocentres for the whole period are shown in Fig. 2.11. Table 2.3 gives a summary of the evolution of the sequence of events described in this section.

**Table 2.3** Summary of the course of events during the Vatnajökull eruption (all times shown are GMT).

| Date | Time | Event |
|---|---|---|
| September 29th | 10:48 | Large Bárdarbunga earthquake |
| September 29th | 11:10 | Occurrence of episodic swarm |
| September 29th | 14:10 | Seismic activity decreases |
| September 29th | 17:20 | Seismic activity resumes southeast of Bárdarbunga |
| September 30th | - | Seismic activity migrates slowly towards Grimsvötn |
| September 30th | 22:00 | Onset of continuous volcanic tremor |
| October 1st | - | Onset and evolution of subglacial eruption |
| October 2nd | Afternoon | Eruption becomes subaerial and tephra is deposited on the glacier |
| October 3rd-6th | - | Seismic activity occurring at Bárdarbunga and Tungafellsjökull |
| October 13th | - | End of the main phase of the eruption |

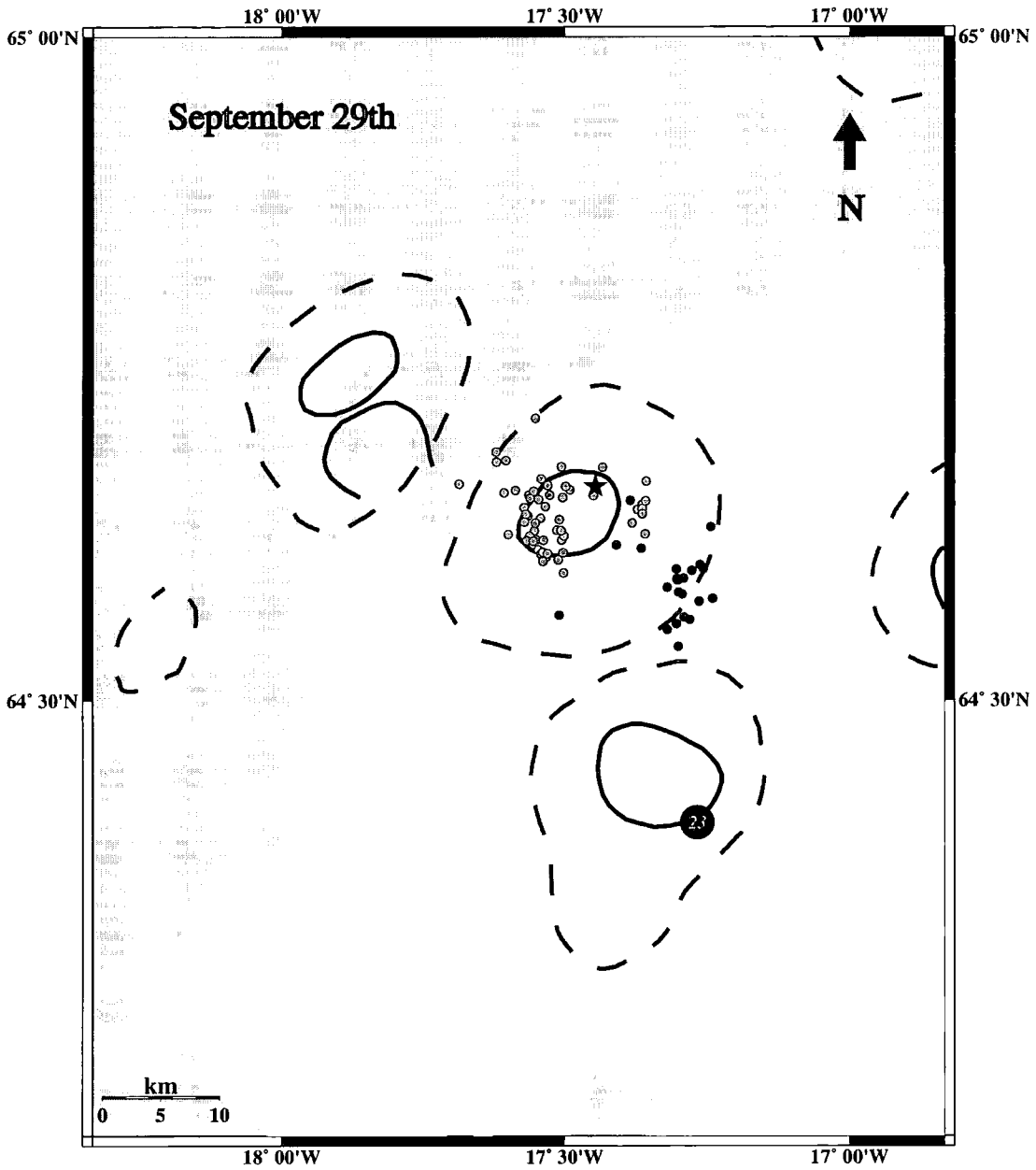


Figure 2.6: Events located for September 29th. The star indicates the epicentre of the magnitude $M_w = 5.6$ event at Bárdarbunga. The grey circles indicate epicentres of low-frequency events, while the black indicate epicentres of mixed-frequency events.

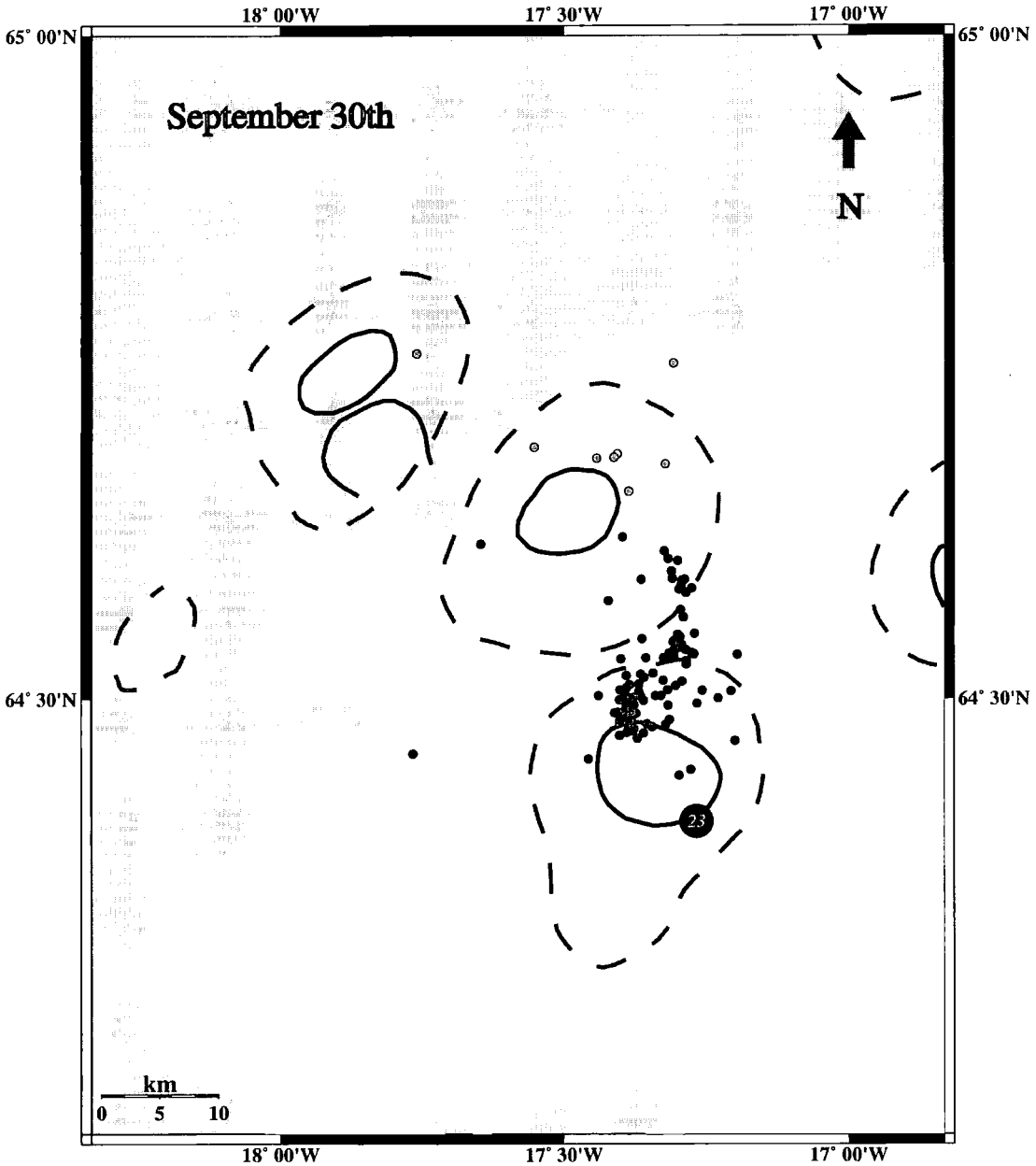


Figure 2.7: Same as in Fig. 2.6 for September 30th.

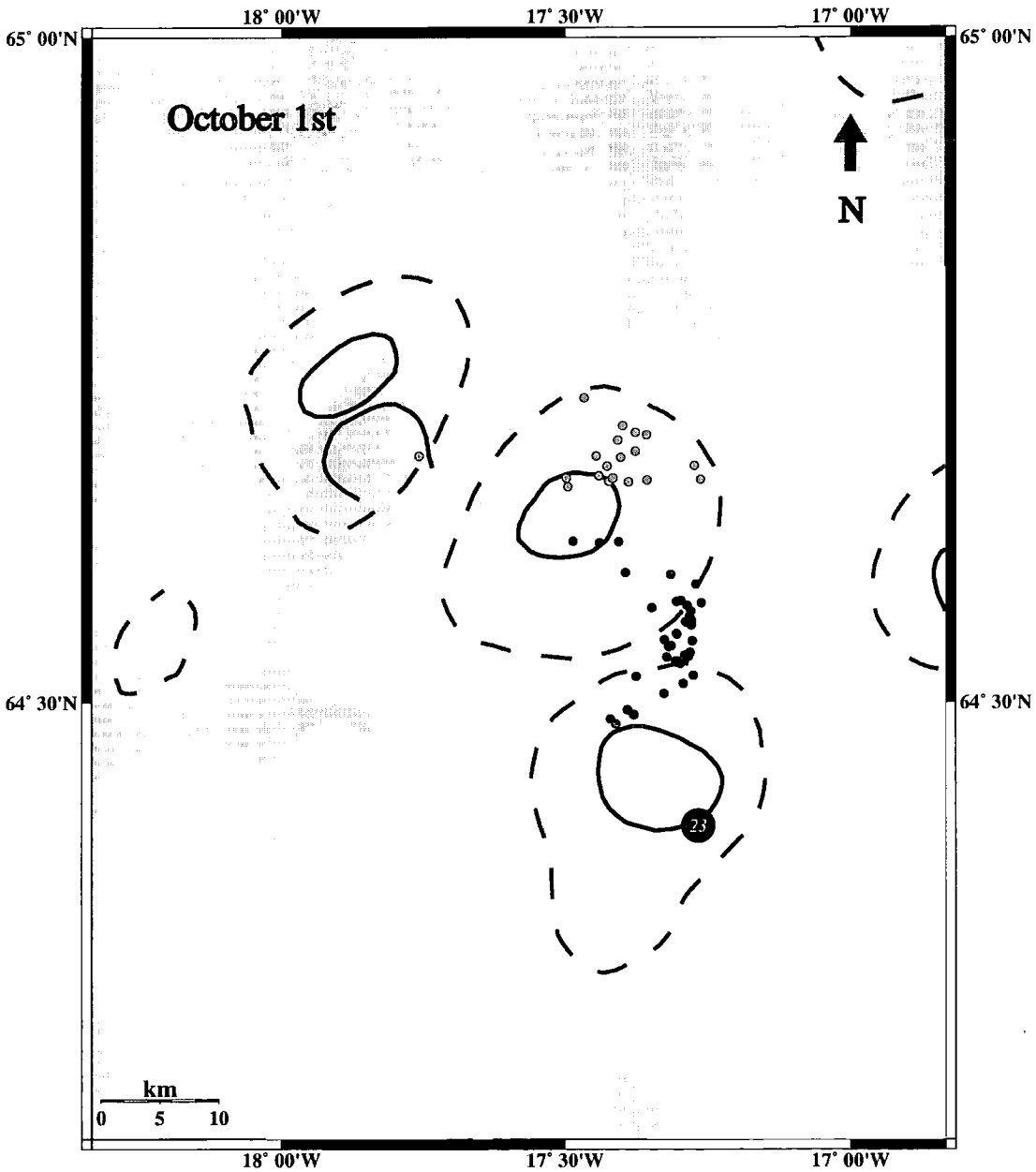


Figure 2.8: Same as in Fig. 2.6 for October 1st.

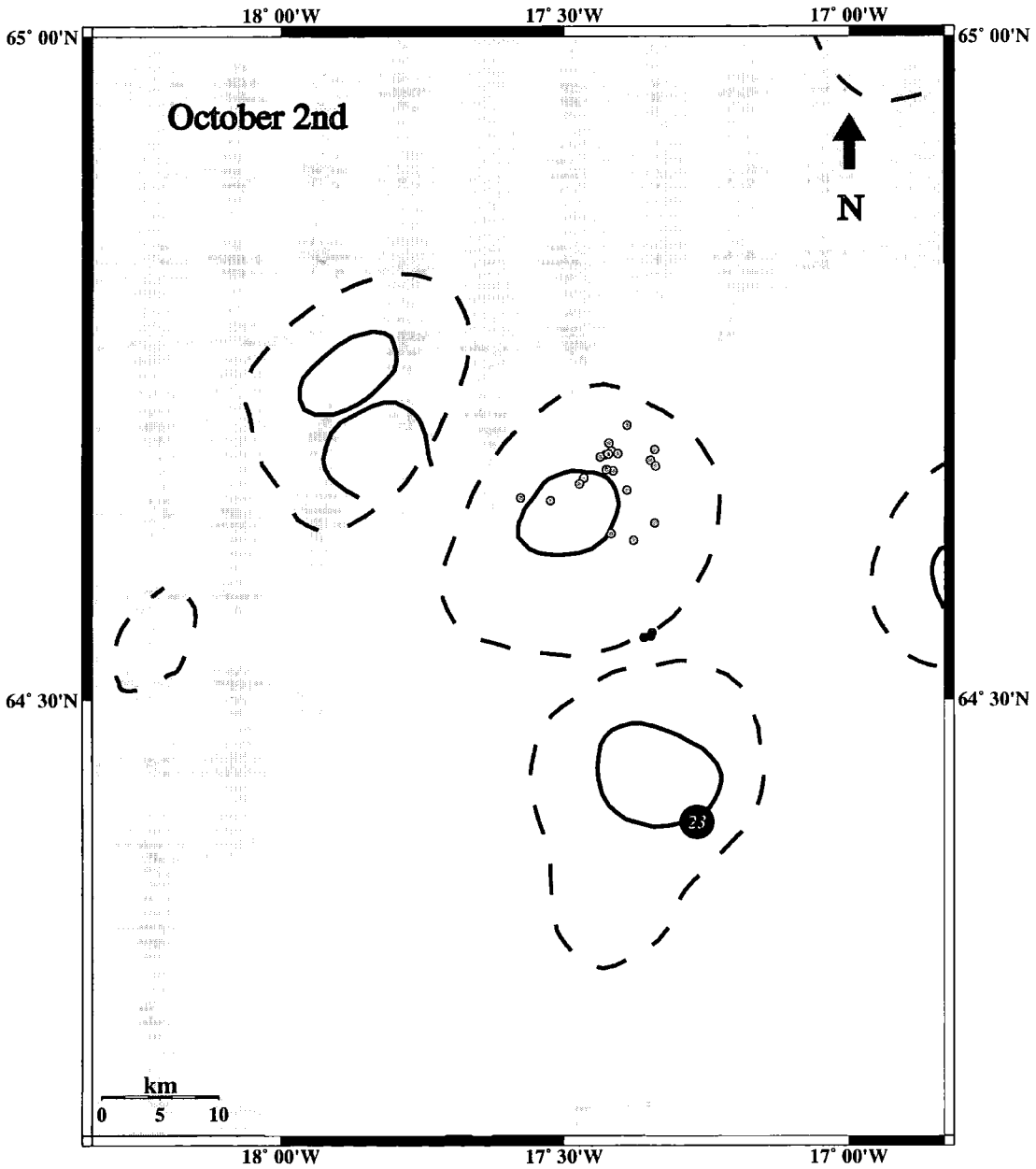


Figure 2.9: Same as in Fig. 2.6 for October 2nd.

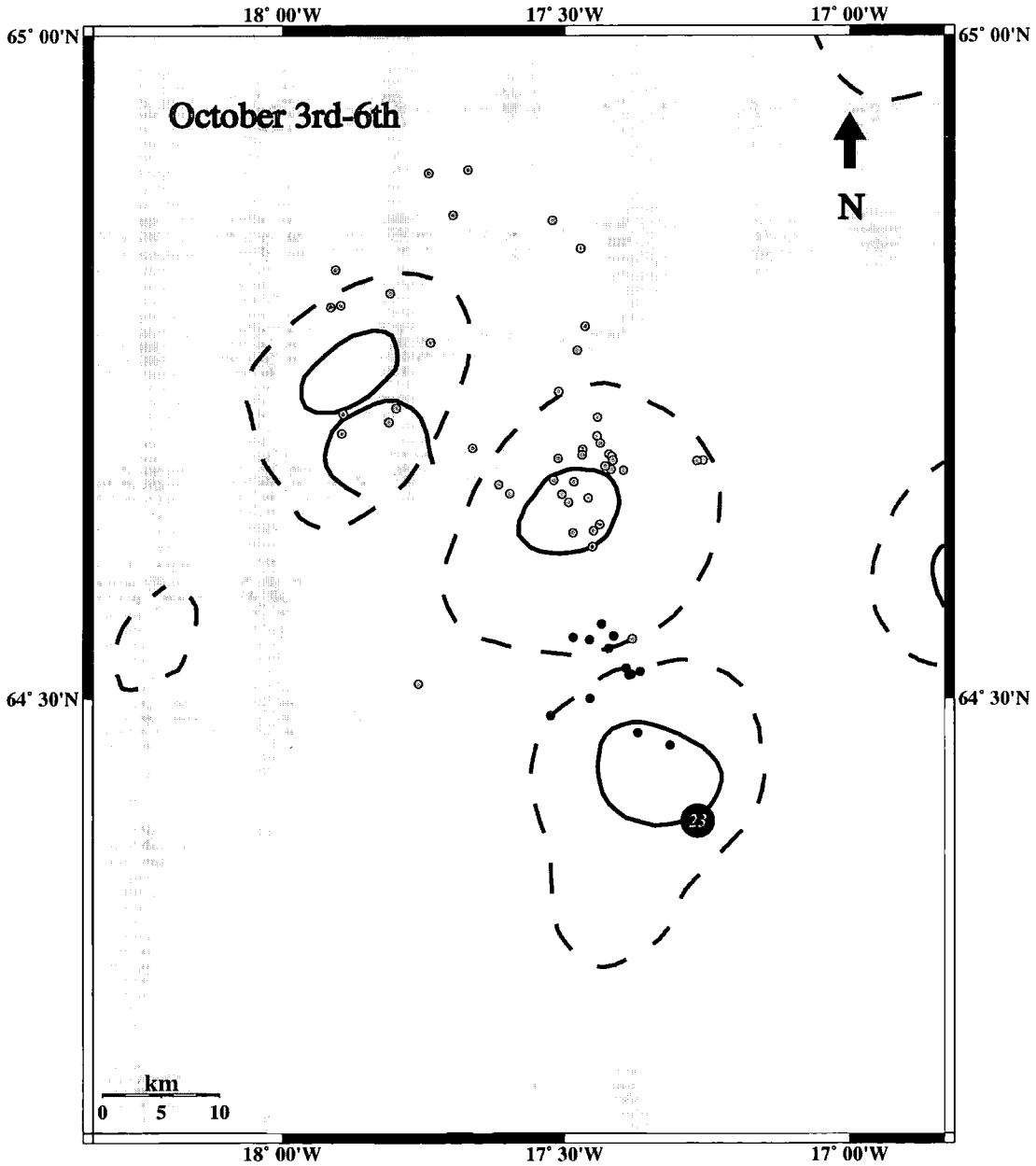


Figure 2.10: Same as in Fig. 2.6 for October 3rd-6th.

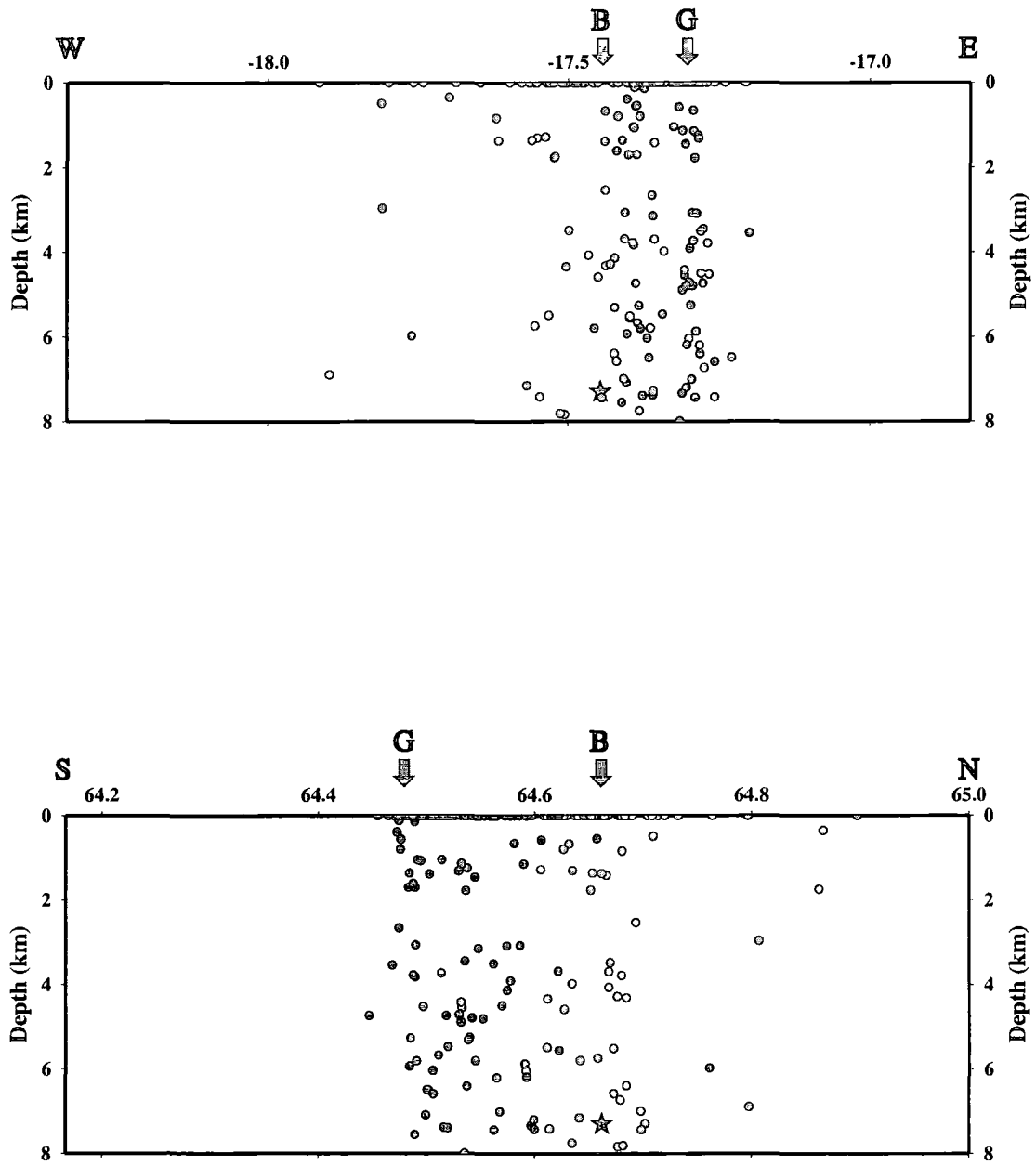


Figure 2.11: East-west and north-south depth cross-sections of events for the period September 29th-October 6th. Symbols as in Fig. 2.6. B: Bárdarbunga. G: Grimsvötn.

## 2.5 Processing of the SIL data

### *2.5.1 The SIL network*

The SIL network (Stefánsson *et al.*, 1993) was first operated by the Icelandic Meteorological Office as part of an earthquake prediction project, covering parts of the south coast of Iceland where the seismic hazard is highest. Initially it consisted of eight stations equipped with broadband seismometers. After financial support was provided by the research council of the Nordic countries, the network was expanded to other parts of Iceland where destructive earthquakes are likely to occur, such as the Tjörnes fracture zone in the north. The SIL network now consists of 33 stations, 24 of which are equipped with broadband instruments, while the rest have short period sensors (Fig. 2.12). Even after this expansion, however, large parts of the country still have no seismic station coverage.

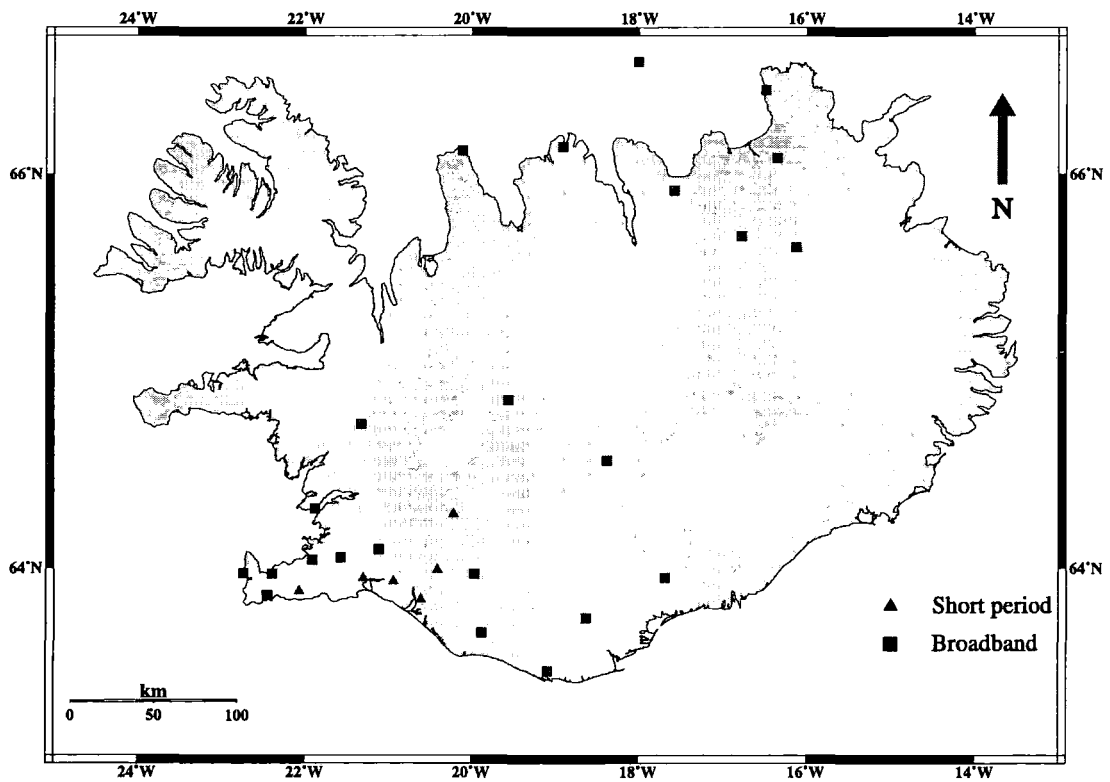


Figure 2.12: Locations of the SIL seismic stations.

Each SIL station is equipped with a three-component sensor and an acquisition system consisting of a 16-bit gain-ranging digitiser, a GPS clock and a 32-bit UNIX computer connected by X25 telephone link to the Icelandic Meteorological Office's headquarters in Reykjavik. Data are initially sampled at 400 samples $s^{-1}$ and then filtered and resampled at 100 samples $s^{-1}$ for local events or 20 samples $s^{-1}$ for teleseismic events. A phase detection system has been implemented based on simple signal-to-noise ratio characteristics. The detected signal is scanned to obtain its exact onset time and a phase-log entry is written, containing information such as maximum amplitude, azimuth and spectral parameters. The phase-log is relayed by telephone link to Reykjavik, where association of phase-logs from different stations is made automatically. Relevant sections of waveform data are then requested from each station, are manually picked and then located by the staff of the Icelandic Meteorological Office.

### *2.5.2 SIL data associated with the eruption*

Files containing arrival times and location information from the SIL stations were obtained from a public directory at the web page http://www.vedur.is of the Icelandic Meteorological Office. All local events are archived according to their year, month, day of occurrence in subdirectories for every 5 minutes of real time: e.g. `1996/abc/xx/hh:mm:ss` where `abc` is the first three letters for each month, `xx` is a two digit number representing the day and `hh:mm:ss` indicates starting hour, minute and second of the 5 minute segment. A typical SIL pickfile is shown in Appendix E. Figs. 2.13 and 2.14 show the spatio-temporal distribution of epicentres and depth cross-sections of events as determined by the Icelandic Meteorological Office for the whole period of the eruption (September 29th-November 4th). Each event is scaled according to its local magnitude, which is calculated using an empirical formula suggested by Tryggvason (1973). It is evident, bearing in mind the geometry of the SIL network and the crustal model limitations discussed previously, that epicentre and hypocentre locations may be quite inaccurate.

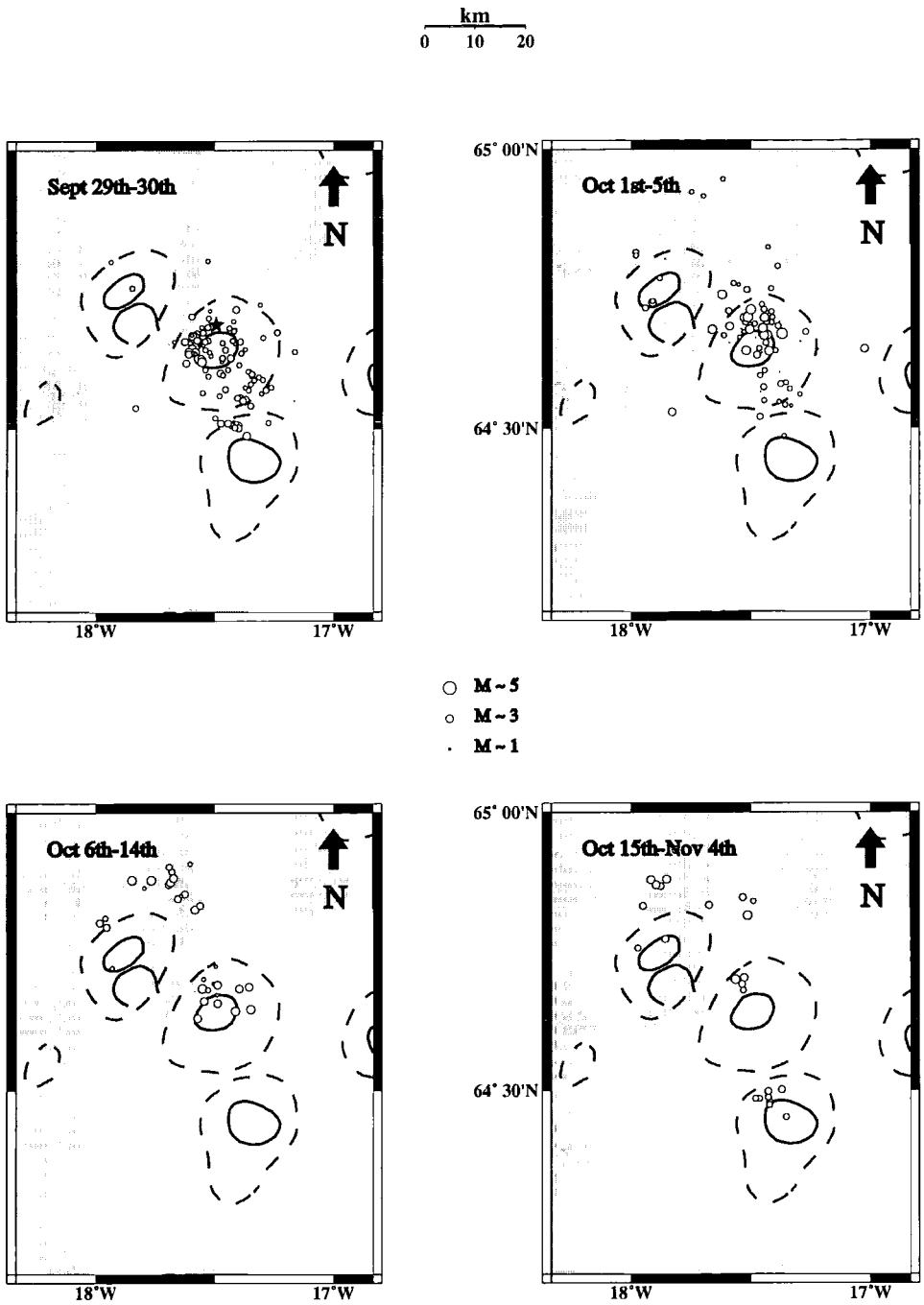


Figure 2.13: Epicentres of events associated with the 1996 Vatnajökull eruption located by the SIL network. The star indicates the large Bárdarbunga event.

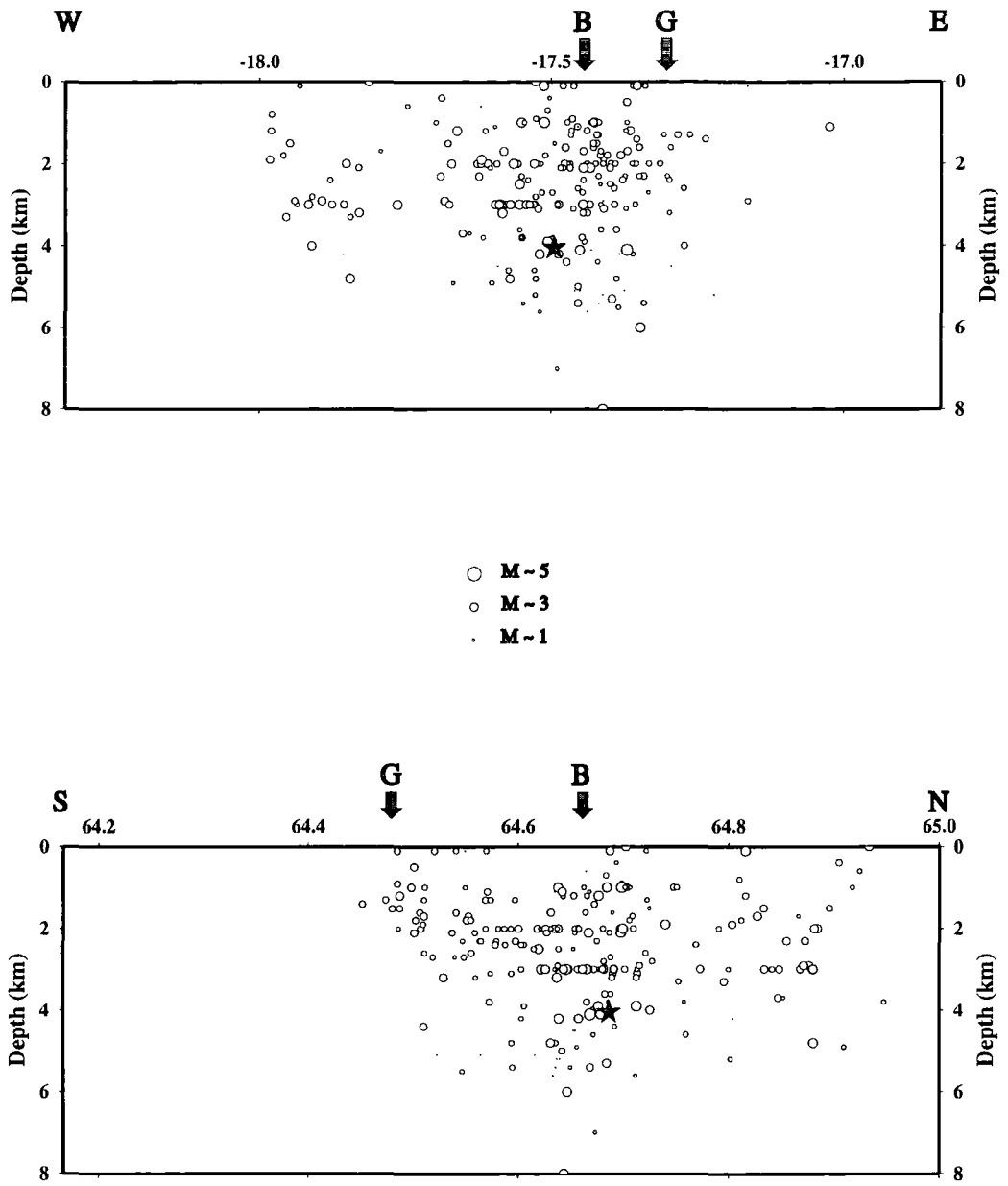


Figure 2.14: East-west and north-south depth cross-sections of all events shown in Fig. 2.13. B: Bárdarbunga. G: Grimsvötn. Note how many hypocentres tend to cluster in straight lines, indicating the difficulty in obtaining a correct value for the depth.

### *2.5.3 SIL database discrepancies*

During the process of identifying events that were recorded by both the HOTSPOT and SIL networks during the period September 29th until October 6th for relocation purposes, a number of discrepancies were found. The most serious of these concern events that are present in the SIL database with an epicentre-hypocentre location and calculated local magnitude, that are not present in the HOTSPOT dataset (Fig. 2.15). Less serious discrepancies reflect events that appear to have been picked at many SIL stations but are visible only at two HOTSPOT stations (HOT23-HOT25), or events whose origin time is up to 13 seconds late with respect to the first arrival at the closest HOTSPOT station to the eruption site (HOT23). A catalogue of all these discrepancies is given in Appendix D. Even though this catalogue has been sent to the Icelandic Meteorological Office, the reason for these discrepancies (up to the time of the writing of this thesis) still remains unknown.

### *2.5.4 Relocation procedure using HOTSPOT and SIL data*

Arrival times of 154 SIL events that could be found in the HOTSPOT dataset were used for relocation using data from both networks. The SIL pickfiles were converted from ASCII to the binary format required as input by *qloc*, using the program *sil2ep*, written by the author of this thesis. *sil2ep* processes an arbitrary number of files specified as command line arguments and writes the binary format in separate files for each event, using the name of the SIL pickfile with the suffix 'ep' appended at the end. All arrival times for the SIL events have been corrected for any clock drift. The arrival times (HOTSPOT & SIL) of all 154 events were concatenated together and located manually using the command

```
cat (HOTSPOT picks) (SIL picks) | eloc
```

in order to be able to check in every case the consistency of the new location for each event. The results were then written to separate files for each day. The minimum

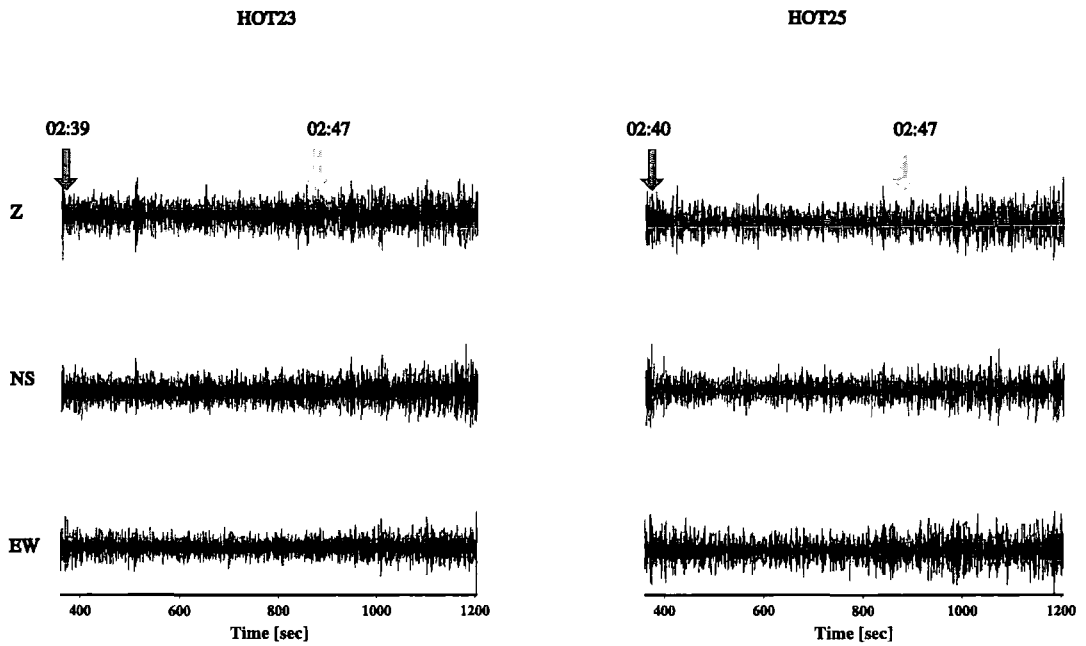


Figure 2.15: An example of a 'missing' SIL event. The SIL database has an entry on October 2nd for an event with an origin time 02:47:23 (GMT), an epicentre at latitude 64.67219°N and longitude 17.52927°W, hypocentral depth 4.611 km, and local magnitude 1.26. No such event is recorded by either of the two HOTSPOT stations closest to the eruption site. Traces have been highpass filtered at 0.5 Hz to remove oceanic microseisms. Black arrows show the starting time of the window, grey arrows show the origin time of the event.

number of SIL picks found for an event was 4, therefore a minimum number of 9 (HOTSPOT & SIL) picks were used for each relocation.

The relocation maps (Fig. 2.16) show, for most cases, a difference in the epicentre locations obtained from HOTSPOT data of $\pm$ 1 km during the first days of the eruption. This difference tends to increase during the following days and the events that exhibit the largest differences from the initial HOTSPOT locations are mostly small, low-frequency events with very emergent P onsets. The event detection performance for the two networks is shown in Fig. 2.17 for the whole period that the Vatnajökull area was seismically active.

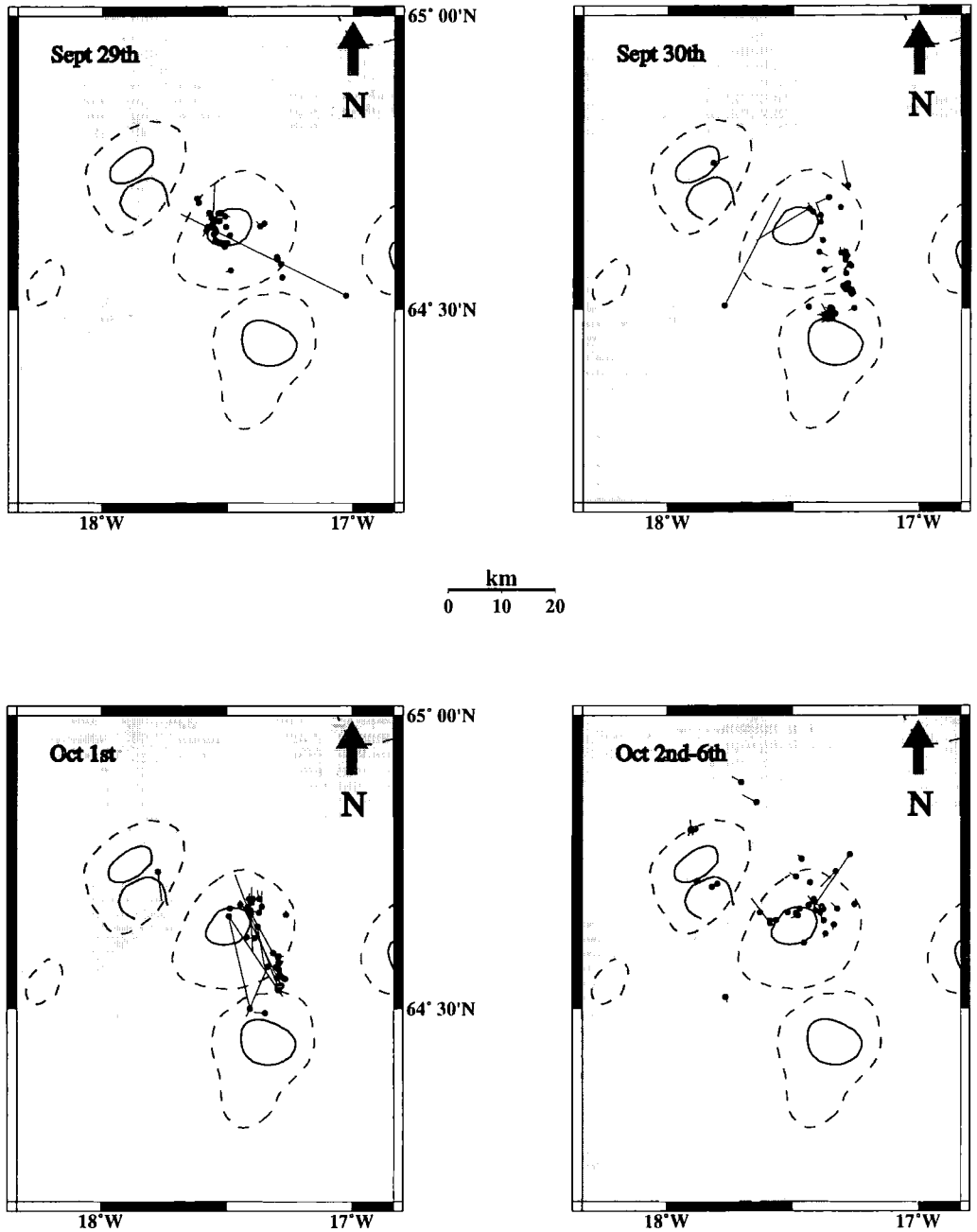


Figure 2.16: Events relocated using both HOTSPOT and SIL arrival times. The relocation vector has a direction from the location obtained with HOTSPOT arrival times to the new location obtained using both HOTSPOT and SIL arrival times (black circle).

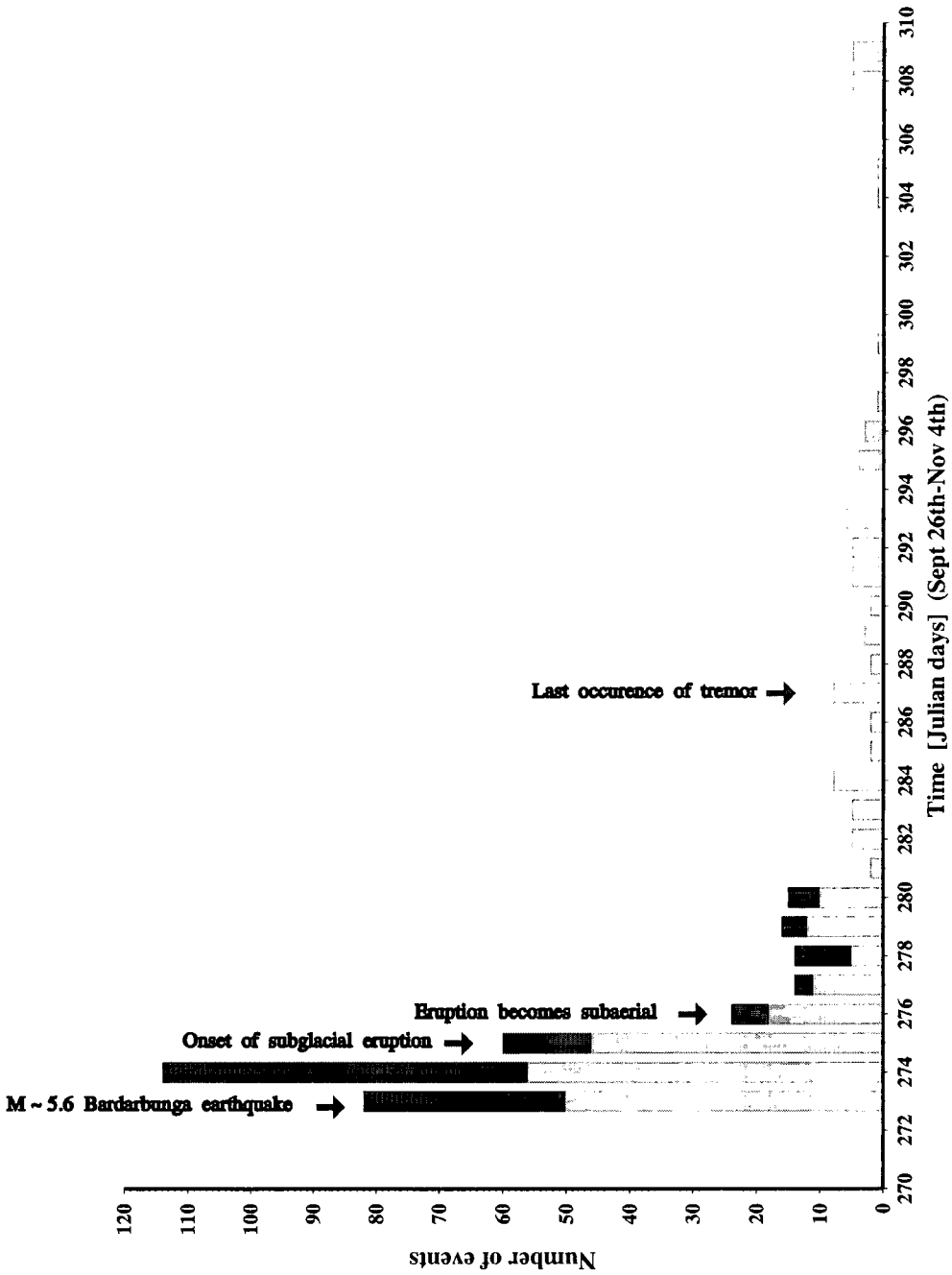


Figure 2.17: Distribution of located events during the whole period of the eruption. Black bars: events located using only HOTSPOT data. Grey bars: events located using only SIL data.

## 2.6 Summary

During late September 1996 a major eruption took place at the northwest part of the Vatnajökull glacier in central Iceland. The eruption was preceded by intense seismic activity which began with a $M_w = 5.6$ earthquake two days previously. The volcanoseismic phenomena associated with the eruption were recorded on both temporary (HOTSPOT) and permanent (SIL) seismic networks, covering most parts of the country. The events recorded by HOTSPOT were categorised according to their waveform shape and frequency content, into three groups: (1) low-frequency events (1-2 Hz); (2) mixed-frequency events (1-4 Hz); and (3) volcanic tremor. Arrival times picked at HOTSPOT stations were used to locate 339 events for the period September 29th-October 6th. The epicentres of the earthquake swarm that followed the $M_w = 5.6$ event initially delineated the Bárdarbunga caldera rim and then migrated towards Grimsvötn, to the place where a fissure was later observed. Over the following days the activity declined and most earthquakes were observed inside the Bárdarbunga caldera and at distances 20 km away, at the Tungafellsjökull volcanic system. Arrival times picked at SIL stations were obtained in order to relocate the events using data from both networks. However, due to a number of discrepancies found in the SIL database this was possible for only 154 events. The relocation shows that, at the onset of the seismic activity, the shift from the initial location obtained by HOTSPOT arrival times is of the order of 1 km. As the activity proceeds, the events become smaller with more emergent onsets, introducing larger picking errors and consequently larger epicentral shifts.

# Chapter 3

# Volcanic tremor: a review

## 3.1 Introduction

Since the beginning of seismic observations near active volcanoes by Omori in 1910, interest in the study of a particular type of seismic signal called volcanic tremor, that occurs prior to and after eruptions, has been growing steadily. The quest for insight into the processes that take place during eruptions, as well as the social benefits stemming from their forecasting in densely populated volcanic areas, are the primary reasons for such a growth (Aki, 1992). However, from a quite early stage seismologists realised that the study of volcanic tremor is far more complicated than the study of signals generated by sources such as shear faulting or man-made explosions.

Trying to analyse and understand the physical mechanism of the source of tremor has proved to be a very difficult task. Complexities arise from the fact that a volcano essentially represents the place of interaction between materials of different physical properties: magmatic fluids, the surrounding bedrock and exsoluted gases when ascending magma reaches shallow depths in the crust. Thus a number of candidate mechanisms or even a combination of them may be generating volcanic tremor. Depending on the eruptive activity of the volcano, flow regime and chemical composition of magma, the characteristics of these sources may be expected to change in time and/or space. These factors allow constraints to be placed upon the applicability of each proposed mechanism for individual volcanoes and indicate that there may not be a stationary, unique source even within the same volcano (McNutt, 1986; Yamaoka *et al.*, 1991; Sherburn *et al.*, 1999).

Another area of difficulty is the uncertainty regarding the relationship between tremor and the different kinds of volcanic earthquakes that occur during eruptions.

The observation that low-frequency earthquakes have similar waveforms and spectra to volcanic tremor led researchers to believe that tremor may be a superposition of such events (Fehler, 1983). However, this proposition has not resolved the problem of what common source mechanism generates both phenomena. Furthermore, it is well known that very different physical processes in a volcano may produce quite similar results (Schick, 1992). This has also been confirmed by theoretical modelling in the frequency domain of observed spectra of tremor and low-frequency events where it was found that many physical mechanisms could explain them equally well (Nishimura *et al.*, 1995). This chapter covers a review of the methods and source modelling that have been used to study and explain characteristics of volcanic tremor recorded at a number of volcanoes worldwide (Fig. 3.1).

## 3.2 The nature of volcanic tremor

Volcanic tremor can be formally defined as a persistent seismic signal that is observed only near active volcanoes, lasting from several minutes to several days, preceding and/or accompanying most volcanic eruptions (Fehler, 1983; Julian, 1994; Ripepe, 1996; Métaxian *et al.*, 1997). In most classification schemes (section 2.4.1.1) the term 'volcanic tremor' is being used in order to describe tremor signals of varying amplitude and duration. Other terms and modifiers have also been used which characterise the appearance of the signal in the time or frequency domain (Table 3.1). In order to avoid confusion throughout this chapter only the general term 'volcanic tremor' will be used to describe all such signals.

The majority of volcanic tremor waveforms have emergent onsets to the extent that picking of first arrivals is almost impossible and travel-time location methods used for earthquakes cannot be applied (Hofstetter & Malone, 1986). However, there are notable exceptions with clear impulsive onsets (Kilauea-Aki & Koyanagi, 1981; Mt. St Helens-Fehler, 1983) (Fig. 3.2) that have made it possible to locate the source of tremor, e.g. at Kilauea at a depth of about 40 km. Observations regarding the relation of tremor amplitude to the intensity of the eruptive activity are mixed.

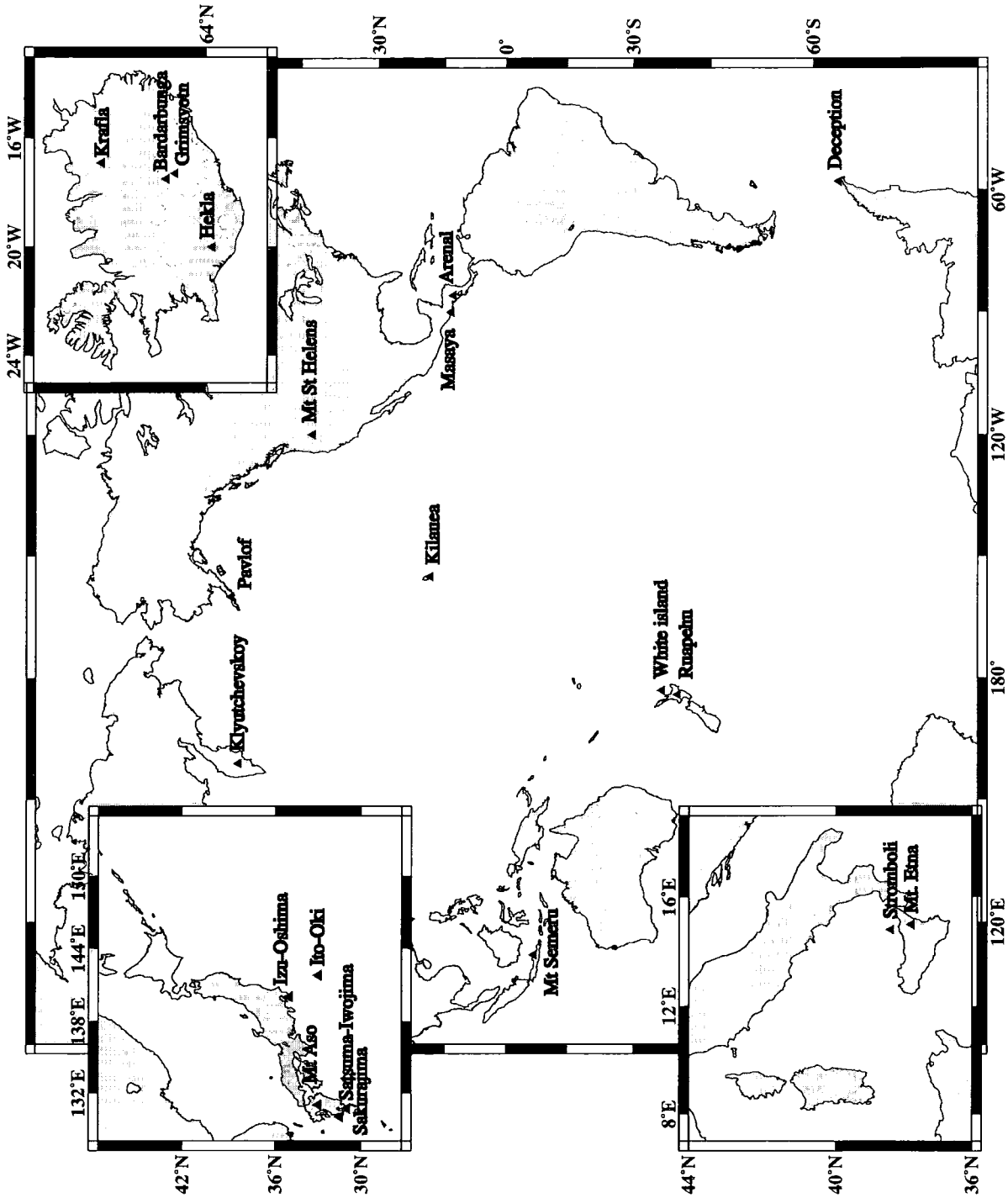


Figure 3.1: Location of volcanoes where the tremor occurrences discussed in the text were recorded.

**Table 3.1** Terms/modifiers used to characterise volcanic tremor.

| Term | Domain | Description | Example |
|---|---|---|---|
| Harmonic | Frequency/Time | Multiple peaks with a fundamental frequency and harmonics | Mt. Semeru |
| Monochromatic | Frequency/Time | Spectrum consisting of only one sharp peak | Ruapehu |
| Banded | Time | Tremor bursts that resemble stripes or bands on a seismogram | Pavlof |
| Spasmodic | Time | Continuous tremor with large amplitude variations | Krafla |
| Tremor storm | Time | Small duration tremor bursts | Mt. Etna |

In many cases an increase in tremor amplitude coincides with visual observations of strong lava fountaining or dome building (Pavlof-McNutt, 1986; Kilauea-Dvorak & Okamura, 1985; Hekla-Brandsdóttir & Einarsson, 1992). However, in other cases no relationship between superficial activity and amplitude could be identified suggesting that the temporal variations in the amplitude are a function of the flow rate of magma at great depths within the crust (Kilauea-Ferrazzini & Aki, 1992).

In the frequency domain tremor signals show a great variation in their spectral content and appearence. As will be discussed in detail later (section 3.3.1.2), this variation may be attributed either to source or path/attenuation effects associated with the propagation of the waves through strongly heterogeneous volcanic structures. The power in the spectrum is often concentrated in the band between 0.5-7

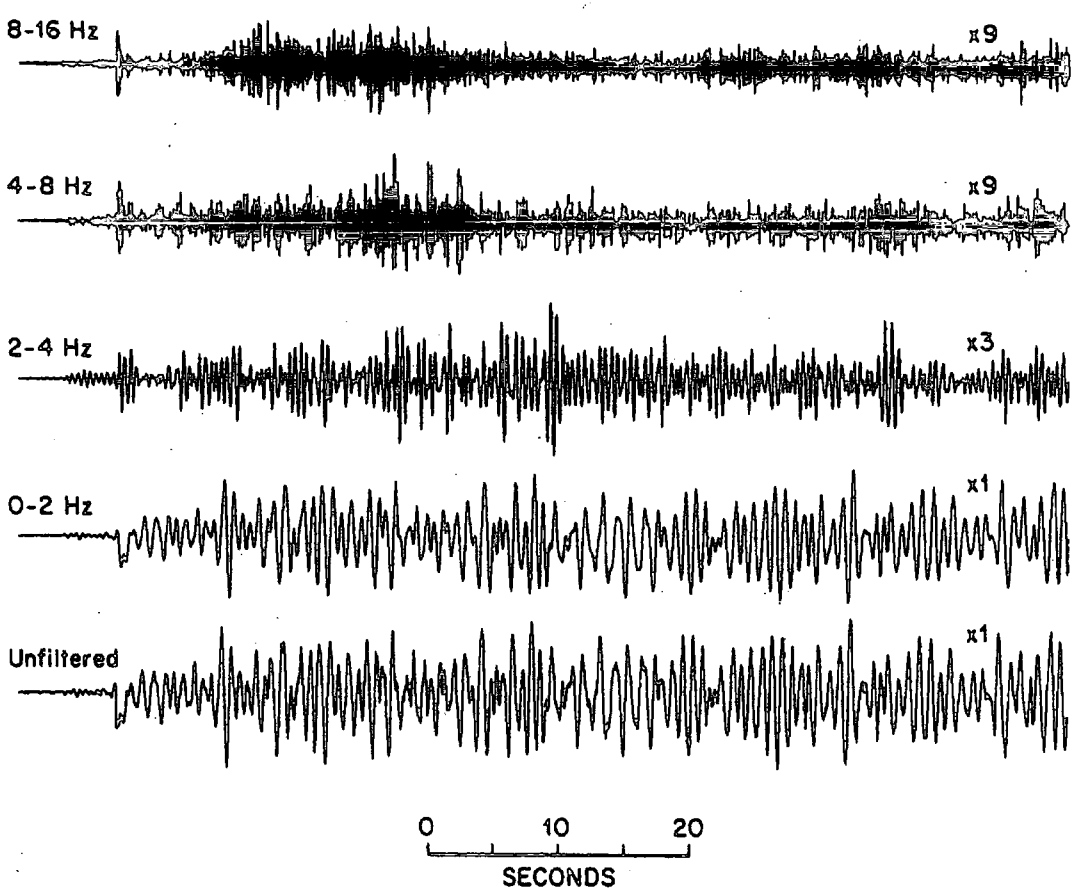


Figure 3.2: Velocity waveform of a tremor episode with impulsive onset, recorded during the 1980 eruption of Mt. St Helens and filtered traces (from Fehler, 1983).

Hz, taking into account the influence of different instrument responses on the calculated spectrum. The use of broadband seismometers has also revealed the existence of volcanic tremor at frequencies as low as 0.1 Hz (Mt. Etna-Seidl *et al.*, 1981; Mt. Aso-Kawakatsu *et al.*, 1994). The shape of the spectrum is usually dominated by one or more sharp peaks that represent either a fundamental frequency with harmonics (Fig. 3.3) or a random distribution of peaks (Fig. 3.4). Temporal variations in the frequency content of tremor have also been observed and it is believed that they reflect source effects (Klyutchevskoy-Gordeev *et al.*, 1990; Sakurajima-Tsuruga *et al.*, 1997).

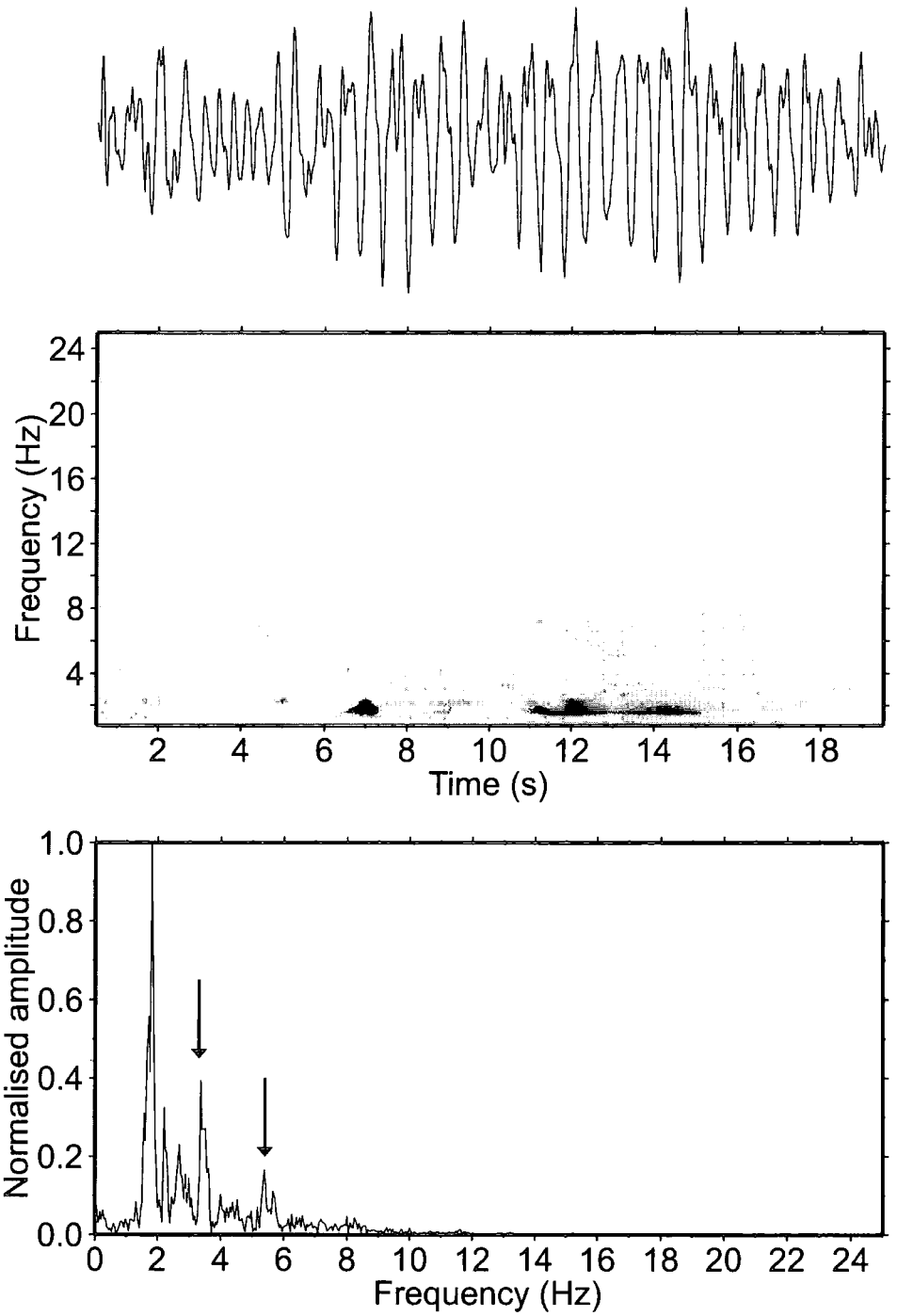


Figure 3.3: Velocity waveform, spectrogram and amplitude spectrum of 20 seconds of tremor recorded at White Island. Dark shades in the spectrogram indicate high energy and light shades low energy. Harmonics are marked with arrows. This kind of tremor is rare at White Island and occurs during periods when there is no eruptive activity (from Sherburn *et al.*, 1998).

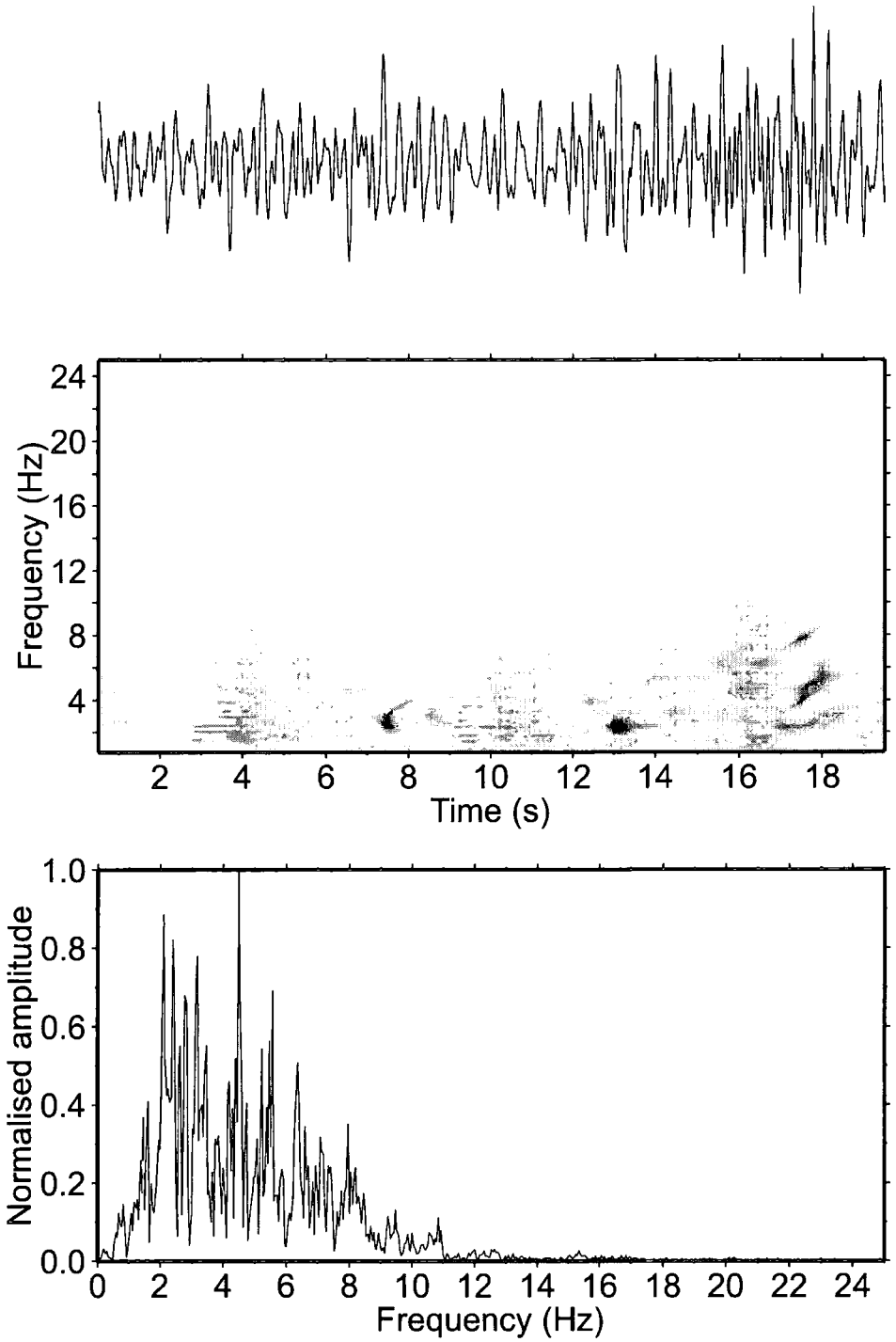


Figure 3.4: Velocity waveform, spectrogram and amplitude spectrum of 20 seconds of broadband tremor recorded at White Island. The shades in the spectrogram are as in Fig. 3.3. In contrast to the tremor shown in the previous figure, broadband tremor is very common at White Island and usually accompanies volcanic activity (from Sherburn *et al.*, 1998).

Unlike the study undertaken in the frequency domain, the study of the properties of the wavefield (wave types, polarisation, phase velocities) has not been so thorough, either due to the lack of digital three-component data or poor station coverage/network geometry in the studied areas. In most cases the wavefield consists of Rayleigh and Love waves (Kilauea-Ferrazzini *et al.*, 1991; Mt. Etna-Ereditato & Luongo, 1994 and Wegler & Seidl, 1997) and is strongly influenced by path effects. There are also a few studies that indicate a mixed composition of the wavefield with the presence of both body and surface waves (Deception Island-Almendros *et al.*, 1997). Other studies focus on data from local arrays, by using the polarisation properties of the wavefield in order to calculate the backazimuth of the propagating waves and estimate the location of the source (Kilauea-Ferrazzini *et al.*, 1991; Masaya-Métaxian *et al.*, 1997).

## 3.3 Methods of analysis applied to volcanic tremor

### *3.3.1 Spectral analysis*

#### *3.3.1.1 Methods of spectral estimation*

In most studies of volcanic tremor the estimation of frequency content has been one of the primary tools for investigating the nature of the signal. However, any method used for the calculation of the spectrum should be able to cope successfully with a number of characteristics not present in other seismic signals. Firstly, tremor can persist for long periods of time resulting in the accumulation of large volumes of data that have to be analysed. Secondly, it may exhibit strong temporal variations in amplitude and/or frequency content that should be monitored, as they are of importance for source modelling and eruption forecasting. Thirdly, the calculated spectrum may have multiple sharp peaks around narrow frequency bands, in which case a high degree of resolution is required in order to resolve the individual frequencies.

One of the first spectral methods to be applied to digital tremor data was the

direct segment method (Båth, 1974). With this method the long tremor time series is divided into shorter non-overlapping segments and the spectrum is calculated for each segment by means of a Fast Fourier Transform (FFT). The final spectral estimate is then the average of all the individual spectra. This method has been applied to volcanic tremor recordings from Mt. St Helens (Fehler, 1983; Hoffstetter & Malone, 1986). The method has the advantage that it enhances the spectral peaks that are common to every time segment and suppresses those generated by random noise. A similar method for real-time spectral estimation of tremor data has been implemented at the Ruapehu volcano observatory (Hurst, 1985), where average spectra are calculated over successive 3 min intervals with a frequency resolution of 0.1 Hz in the band between 0.05 and 4.04 Hz (Sherburn *et al.*, 1999).

In order to detect temporal changes in the frequency content of the signal a direct comparison of the averaged spectra should be performed. Such a comparison of spectra from different time periods is feasible only when the volume of data is relatively small and when the observed variations are larger than the ambient noise levels. A better way of detecting temporal variations is by incorporating in the display all of the variables that are likely to change (time, frequency, amplitude). This is accomplished by creating a spectrogram (Fig. 3.5), which is a two-dimensional representation of the variations in spectral amplitude and frequency of the observed signal as time elapses. The calculation of the spectrogram can be achieved by moving a sliding window over the whole length of the time series and estimating the spectrum by performing an FFT for overlapping positions of the window (e.g. Mt. Semeru-Schlindwein *et al.*, 1995; White Island-Sherburn *et al.*, 1998).

The resolution of the spectrum obtained by using an FFT algorithm is proportional to the reciprocal of the window length chosen for the analysis. In order to increase the spectral resolution more than it is possible with the FFT, the Maximum Entropy Method (MEM) (Burg, 1967) has been applied in a number of cases (Pavlof-McNutt, 1986; Izu-Oshima-Yamaoka *et al.*, 1991; Mt. Etna-Seidl *et al.*, 1990). Assuming that the time series is generated by a linear random mechanism

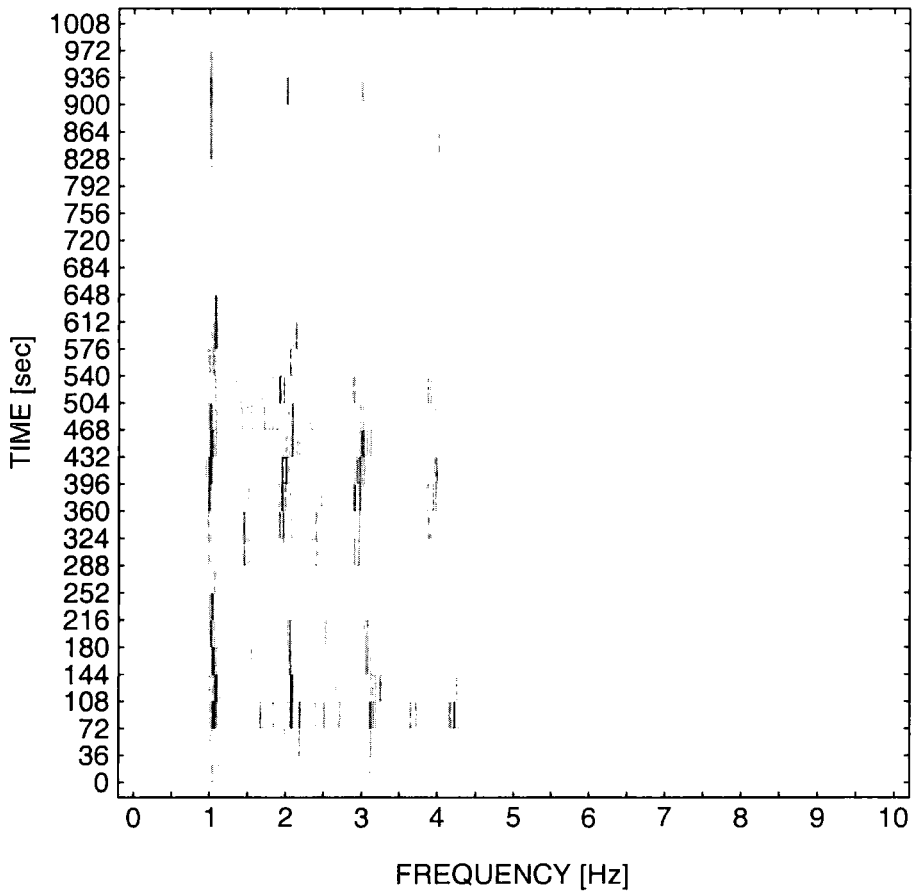


Figure 3.5: Spectrogram of tremor recorded at Mt. Semeru with eight harmonics clearly visible. The vertical axis marks the beginning of every calculation window and dark shades indicate high energy, while light shades low energy. Note how the spectral lines representing each harmonic shift with time keeping the same horizontal distance from each other; this phenomenon, which has been termed 'gliding', was also observed at Arenal volcano by Hagerty *et al.* (2000) (from Schlindwein *et al.*, 1995).

MEM fits to the data, in a least squares sense, an autoregressive process of order $p$ of the form (detailed derivations of these equations can be found in Ulrych & Bishop (1975))

$$y_t = \alpha_1 x_{t-1} + \alpha_2 x_{t-2} + ... + \alpha_p x_{t-p} + r_t \tag{3.1}$$

by applying a prediction filter of length $p$, where $\alpha$ are the filter coefficients calculated by solving the normal equations posed by the least squares problem, $r_t$ is a white noise series with zero mean and $\sigma_a^2$ variance. Then the spectrum of $y_t$ will be estimated by the equation

$$Y(\omega) = \frac{2\sigma_a^2}{|1 - \sum_{i=1}^{M} \alpha_i exp(-i2\pi\omega j)|^2} \tag{3.2}$$

where $\omega$ is frequency and M represents the total number of samples in the time series considered for the analysis. If the selected time window of the data is small enough the MEM will produce a much higher resolution spectrum than the usual FFT methods, otherwise the result will essentially be the same. Table 3.2 gives an account of the different volcanoes where the methods discussed in this section were used, together with some spectral characteristics in each case.

**Table 3.2** Spectral characteristics and methods of spectral analysis applied to volcanic tremor.

| Volcano | Frequency content | Method applied |
|---|---|---|
| Mt. St Helens | 1-2.1 Hz[ab] | Direct segment |
| Pavlof | 0.7-3 Hz[a] | FFT, MEM |
| Kilauea | 1-8 Hz[b] | FFT overlapping windows |
| Klyutchevskoy | 0.5-5 Hz[b] | Direct segment |
| Ruapehu | 2,3,7 Hz[ab] | FFT overlapping windows |
| Mt. Aso | 0.1 Hz | FFT |
| Deception island | 1-8 Hz | FFT overlapping windows |
| Mt. Semeru | 1-5 Hz[ab] | FFT overlapping windows |
| Arenal | 0.9-7.2 Hz[b] | FFT/periodogram |
| White Island | 1-8 Hz[ab] | FFT overlapping windows |
| Stromboli | 0.1-8 Hz | FFT |
| Mt. Etna | 0.25-5 Hz | FFT, MEM |
| Ito-Oki | 1-7 Hz[a] | FFT overlapping windows |
| Izu-Oshima | 0.7-8 Hz | MEM |

[a] Data from short-period sensors were used for the spectral calculations.

[b] Temporal variations in the frequency content observed.

### *3.3.1.2 Identification of source effects from observed spectra*

Any recorded seismic signal can be considered as the result of the consecutive application of a series of linear filters to the original wavelet generated by a source (Lay & Wallace, 1995). This can be represented mathematically by the convolution of one filter with the other in the time domain,

$$W(t) = S(t) * P(t) * R(t) * I(t) \tag{3.3}$$

or the equivalent equation in the frequency domain

$$W(\omega) = S(\omega)P(\omega)R(\omega)I(\omega) \tag{3.4}$$

where W(t) is the recorded waveform, S(t) is the original source wavelet, P(t) represents the filter characteristics due to the propagation of the signal through the earth, R(t) represents filtering effects due to the structure beneath the recording station and I(t) accounts for the filtering due to limited frequency bandwidth of the recording instrument. Hereafter the S(t), P(t) and R(t) filters will be referred to as 'source', 'path' and 'site effects' respectively.

Since, in most cases, the resulting spectrum consists of a series of sharp peaks, a major difficulty is to successfully determine which factors have shaped it. A comparison between tremor and earthquake spectra recorded at the same station is a common method of checking for possible site effects, since they should influence both signals (Mt. St Helens-Fehler, 1983; Kilauea-Goldstein & Chouet, 1994; Deception Island-Almendros *et al.*, 1997). Unfortunately it is far more difficult to find and isolate path effects, mainly because of the limited knowledge of the structure between the source and the receivers in most volcanic areas. If the recording stations are located close together and are azimuthally distributed around the source, similarities in spectra from different stations may be attributed to source effects (Pavlof-McNutt, 1986).

A less empirical approach to resolving the source-path effect separation problem involves the use of spectral ratios for pairs of events recorded at a number of stations (Sakurajima-Tsuruga *et al.*, 1997). The method uses two time windows A and B from a tremor time series that were recorded at several different stations. Based on the assumption that these two events are generated by the same source and at the same hypocentral area, the path and site effects will be the same, thus equation 3.4 will be yielding spectral ratios of the form $S^A(\omega)_i/S^B(\omega)_i$ for the *ith* station. The correlation of the estimated ratios for all stations and for different frequency bands can be checked by performing a statistical covariance analysis, where high correlation coefficients should indicate a common source effect for the two events.

This method may not be always applicable, since the assumptions made for events generated by the same source and at the same depth are not generally valid in every volcanic environment.

The problem of correct identification of specific frequencies as source effects and not as propagational artefacts has been made easier with the widespread use of spectrograms that display any new frequency as it appears. Since the path and site effect factors listed in equation 3.3 behave as linear filters and cannot generate new frequencies to their input signal (Anstey, 1981), these frequencies can only be attributed to a source effect.

### *3.3.2 Study of the wavefield properties*

#### *3.3.2.1 Polarisation analysis*

A further step in the analysis of volcanic tremor is the study of its wavefield and the identification of the types of waves that compose it. The standard method used for such an analysis is that of the covariance matrix (Montalbetti & Kanasewich, 1970; Jurkevics, 1988) which utilises data recorded by one or more three-component seismometers. The method works in the time domain by bandpass filtering the signal around the frequency band of interest and then calculating the covariance matrix for a short, sliding time window along the time series by using the following equation

$$S_{ik} = \frac{\mathbf{X}\mathbf{X}^T}{N} = \frac{1}{N}\sum_{i=1}^{N} x_{ij}x_{ik} \tag{3.5}$$

where $\mathbf{X} = [x_{ij}]$; $i = 1, 2, ...N$; $j = 1, 2, 3$; is the data matrix in one window and $x_{ij}$ is the $ith$ sample of component j, N is the number of samples and T denotes the transpose of $\mathbf{X}$. The estimated covariance matrix $\mathbf{S}$ will be of the form

$$\mathbf{S} = \begin{pmatrix} S_{zz} & S_{zn} & S_{ze} \\ S_{zn} & S_{nn} & S_{ne} \\ S_{ze} & S_{ne} & S_{ee} \end{pmatrix} \tag{3.6}$$

where z, n, e denote the vertical, north-south and east-west components respectively and $S_{ze}$ is the cross-variance of the vertical and east-west components, while $S_{zz}$ is the auto-variance of the vertical component. Solving the eigenvalue problem $(\mathbf{S} - \lambda^2\mathbf{I})\mathbf{u} = \mathbf{0}$ will give the three eigenvalues $(\lambda_1, \lambda_2, \lambda_3)$ and their corresponding eigenvectors $(\mathbf{u}_1, \mathbf{u}_2, \mathbf{u}_3)$. The three principal axes of the polarisation ellipsoid will be given by $\lambda_j\mathbf{u}_j$, with $j = 1, 2, 3$; the eigenvectors are the axis orientations and their lengths are equal to $\lambda_j$ in amplitude units. One non-zero eigenvalue implies a purely rectilinear ground motion, while two non-zero eigenvalues characterise a purely elliptical polarisation. In order to obtain a measure of what kind of motion prevails in the time window the rectilinearity and planarity coefficients are being used, these are given by $1 - (\lambda_2 + \lambda_3)/2\lambda_1$ and $1 - 2\lambda_3/(\lambda_1 + \lambda_2)$ respectively.

The method described above has been used to study the wavefield properties of volcanic tremor from Mt. Etna for a time period spanning six years (1987-1993) during which different kinds of volcanic activity were at work, including periods of quiescence, Strombolian activity or lava fountaining (Ferrucci *et al.*, 1990; Ereditato & Luongo, 1994; Wegler & Seidl, 1997). Polarisation analysis for the whole of this period revealed a persistent pattern of high values for the rectilinearity coefficient with an east-west polarisation, suggesting that the wavefield consists of waves radiated from a vertically extended source aligned in the north-south direction. The dominant wave types have been identified either as P waves (Ferrucci *et al.*, 1990) or as Love/SH waves (Ereditato & Luongo, 1994; Wegler & Seidl, 1997) showing a complicated overlapping pattern. Similar observations have been reported for the tremor wavefield in other volcanoes, such as Arenal where the dominant wave type was identified as S waves by Benoit & McNutt (1997), while Hagerty *et al.* (2000) reported a very complicated composition of the wavefield and were unable to identify any particular wave type.

### *3.3.3 Study of the wavefield and source location using array methods*

#### *3.3.3.1 Method of correlation coefficients*

While polarisation analysis can provide a qualitative picture of the composition of the tremor wavefield (even using data from only one seismometer), array methods can provide a much more detailed knowledge of it, at the expense of having to use more instruments and a specific receiver geometry. Aki (1957) designed and used the method of correlation coefficients in order to identify the predominant wave type of the background seismic noise generated by traffic in Tokyo. The method assumes that the recorded seismic signal is stationary and stochastic in time and space and that it consists mostly of surface waves, implying that the method can resolve wavefield properties generated by shallow sources.

The spatial correlation function is calculated for pairs of receivers, one being at the centre of a semicircular array (reference receiver) and the others at its circumference, covering an azimuth of 0 to $\pi$ degrees. This function is defined as

$$\phi(r,\varphi) =< u(x,y,t).u(x+rcos\varphi, y+rsin\varphi, t) > \tag{3.7}$$

where the angle brackets denote averaging over time $(x, y)$ and $(x+rcos\varphi, y+rsin\varphi)$ are the Cartesian coordinates of the two receivers, $r$ is the distance between them and $\varphi$ is the azimuth of the two receivers measured from the direction of the $x$-axis. Integrating this function for the azimuth range covered by the array will give

$$\bar{\phi} = \frac{1}{\pi}\int_0^{\pi} \phi(r,\varphi)d\varphi \tag{3.8}$$

For a wave with a phase velocity $c(\omega)$ the azimuthally averaged correlation function is related to the power spectrum $\Phi(\omega)$ by the equation

$$\bar{\phi} = \frac{1}{\pi}\int_0^{\infty} \Phi(\omega)J_0[\frac{\omega}{c(\omega)}r]d\omega \tag{3.9}$$

where $J_0$ is the Bessel function of zeroth order. Since in almost all cases one or more specific frequency bands are of interest, filtering the signal through a narrow bandpass filter centred at $\omega_0$, the power spectrum will be $\Phi(\omega) = P(\omega_0)\delta(\omega - \omega_0)$, where $P(\omega_0)$ is the spectral power density of the signal at frequency $\omega_0$ and $\delta$ is the Dirac function. The correlation function will become

$$\bar{\phi}(r, \omega_0) = \frac{1}{\pi} P(\omega_0) J_0[\frac{\omega_0}{c(\omega_0)} r] \tag{3.10}$$

the correlation coefficient $\rho(r, \varphi, \omega_0)$ can then be defined as

$$\rho(r, \varphi, \omega_0) = \frac{\phi(r, \varphi, \omega_0)}{\phi(0, \varphi, \omega_0)} \tag{3.11}$$

the azimuthal average of the correlation coefficients will be equal to

$$\bar{\rho}(r, \omega_0) = J_0[\frac{\omega_0}{c(\omega_0)} r] \tag{3.12}$$

It is possible, therefore, to calculate the correlation coefficients for different values of $\omega$ and azimuth $\varphi$, then fit a Bessel function to the coefficients and recover the phase velocity $c(\omega_0)$ of the recorded waves. By further analysis of the dispersion curves one may obtain the two-dimensional velocity structure beneath the array for depths ranging from 100 m to 1 km. The equations that relate the correlation coefficients with the phase velocities of different wave types (Rayleigh, Love) can be found in Aki (1957; 1959). A contour map of the coefficients versus azimuth and frequency is used in order to determine the backazimuth of the incoming waves (Fig. 3.6). Assuming that a plane wave is propagating at a fixed azimuth $\theta$, the correlation coefficient will be

$$\rho(r, \varphi, \omega_0) = \cos[\frac{\omega_0 r}{c(\omega_0)} \cos(\theta - \varphi)] = \cos[\omega_0 \tau(r, \varphi, \omega_0)] \tag{3.13}$$

where $\tau$ is the time delay between two receivers separated by distance $r$ at an

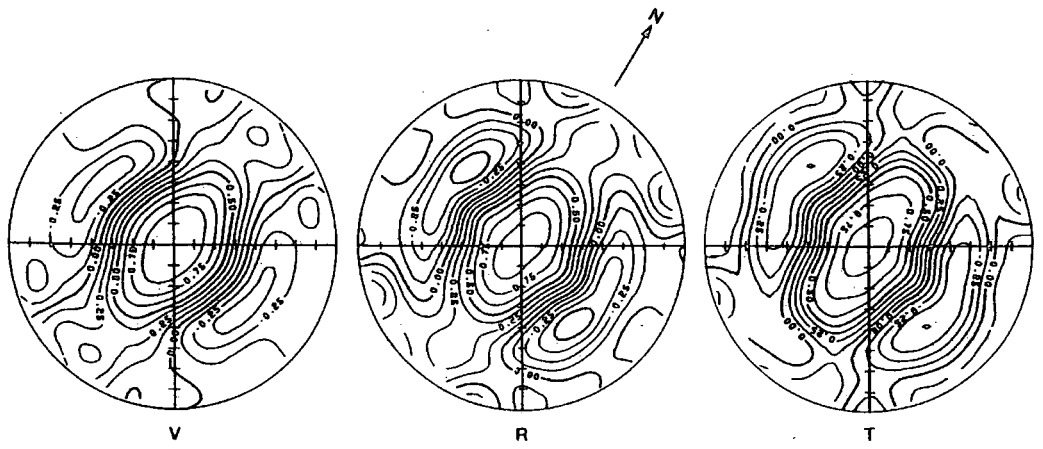


Figure 3.6: Contour maps of the correlation coefficients $\rho(r, \varphi, \omega_0)$ calculated from tremor data recorded at Kilauea (Puu Oo crater) over a window of 180 s. The three plots correspond, from left to right, to the vertical, radial and transverse component. The frequency axis is taken along the radius of the circle with the origin at the centre. Note the rapid decrease of values along the east-west direction, while they remain almost constant along the north-south which is the direction of the propagating waves (from Ferrazzini *et al.*, 1991).

azimuth $\varphi$. In this sense $\rho$ is constant along the wavefront ($\varphi = \theta \pm \pi/2$) and decays in a direction perpendicular to it ($\varphi = \theta$).

Open conduit volcanoes that exhibit either permanent degassing or regular lava fountaining activity are good candidates for applying the correlation method, since the tremor source can be considered to a good approximation as stationary and it is shallow enough to excite sufficient surface waves. The application of the method to three different volcanic systems (Kilauea-Ferrazini *et al.*, 1991; Masaya-Métaxian *et al.*, 1997; Stromboli-Chouet *et al.*, 1998) showed that the recorded waves were coming from the summit crater of each volcano, where most of the activity was visually observed. In the case of Masaya volcano, two arrays were available for the application of the method and the intersection of their backazimuth directions was used to locate the tremor source. Although at Masaya and Stromboli the tremor

wavefield was found to consist of both Rayleigh and Love waves, at Kilauea only Rayleigh waves could be identified after study of their dispersion curves.

### *3.3.3.2 Semblance methods for source location*

A realistic visualisation of the tremor source should not only account for the temporal evolution of its properties, but should also extend spatially over some volume underneath a volcano, thus representing a possible channel geometry over a magma reservoir or hydrothermal fluid circulation through a system of cracks. The methods discussed thus far can pinpoint the area of origin of tremor, but cannot delineate it in three or even two dimensions. Furumoto *et al.* (1990; 1992) attempted to image the source of tremor at Izu-Oshima volcano using a portable array of vertical component seismometers. The array was situated near the crater and recorded tremor during a fissure formation episode. Their approach was to take advantage of the available multichannel data by calculating the semblance (Neidell & Taner, 1971) which is defined as

$$S = \frac{\sum_{j=1}^{L} (\sum_{i=1}^{N} f_{i,j(i)})^2}{N \sum_{j=1}^{L} \sum_{i=1}^{N} f_{i,j(i)}^2} \tag{3.14}$$

where N is the number of stations, $f_{i,j(i)}$ is a seismogram recorded at the $ith$ station, in the $jth$ time sample and $L$ is the number of samples that defines a time window. Assuming that the coherency of the signal is maximised in certain time windows because of phases arriving from a source, it is possible to calculate source-receiver travel times by changing the source location on a 2-D or 3-D grid of nodes and evaluating the semblance for each window specified by these travel times. In this way the spatial distribution of semblance values can be depicted with higher values covering the area of the seismic source.

In the case of Izu-Oshima only the high frequency (5-25 Hz) part of the recorded

tremor was analysed using the method outlined above, as Furumoto *et al.* (1990; 1992) noted that inclusion of larger wavelengths would have resulted in the deterioration of spatial resolution due to the small aperture of the array (500 m). The semblance distribution showed two separate areas with high values inside the caldera, which also coincided with the tips of the fissure that was formed during the eruption. Furumoto *et al.* (1992) suggest that these two source regions are the tips of an expanding crack, formed by magma forcing its way up to the surface. The high-frequency tremor was then interpreted as the result of the brittle fracture of rock owing to fluid-solid interaction as magma is injected into the crack.

An expanded definition of semblance has been used in order to locate the source region of volcanic tremor with a dominant period of 7-10 s (Mt. Aso-Kawakatsu *et al.*, 2000; Stromboli-Chouet *et al.*, 1999). This kind of tremor appears in the time domain more as a swarm of discrete pulses rather than continuous episodes (Fig. 3.7); it occurs even when no signs of volcanic activity are observed and the particle motion indicates a high degree of rectilinearity with a direction pointing from each station to the crater of the volcano. In this case it is reasonable to assume that the source is isotropic, and use the radial component (R) from each station to calculate the semblance, penalising any departure from a pure rectilinear motion (caused by propagation effects) by subtracting the other components (V, T). The semblance will be

$$S = \frac{\sum_{j=1}^{L}[(\sum_{i=1}^{N} R_{i,j(i)})^2 - N(\sum_{i=1}^{N} V_{i,j(i)}^2) - N(\sum_{i=1}^{N} T_{i,j(i)}^2)]}{N \sum_{j=1}^{L} \sum_{i=1}^{N} R_{i,j(i)}^2} \tag{3.15}$$

This definition not only takes advantage of a large number of stations which improves the signal-to-noise ratio, but it also incorporates independent information about the tremor wavefield, such as the rectilinearity. Kawakatsu *et al.* (2000) call this semblance 'waveform semblance' and use it to locate the source region of the long-period tremor (Fig. 3.8) in a similar manner to that of Furumoto *et al.* (1990; 1992).

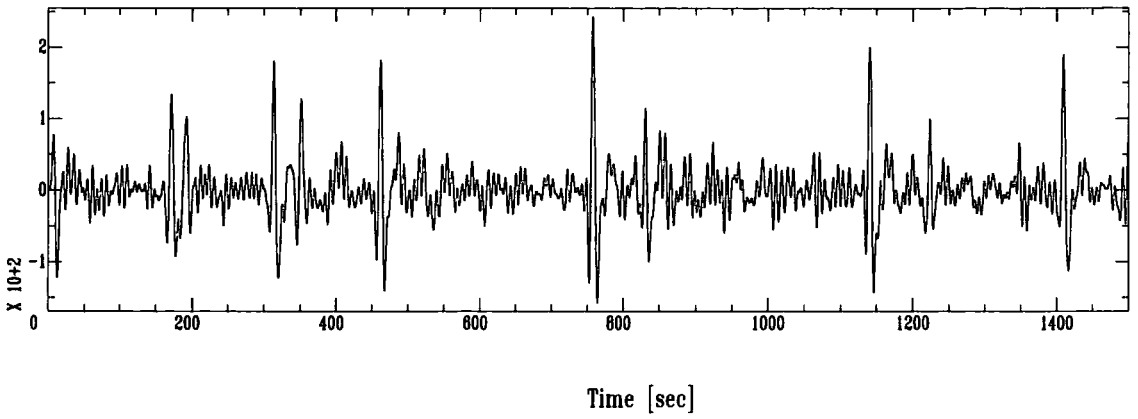


Figure 3.7: Vertical component velocity waveform of long-period tremor recorded at Puu Oo crater, Hawaii. The trace has been bandpass filtered between 0.01-0.1 Hz (T. Bond, pers. comm. 2000).

## 3.4 Visual and acoustic observations related to tremor

An important way of gaining insight into the physical processes that generate tremor and other volcanoseismic phenomena, is the visual monitoring of eruptive activity. Even though a range of different factors may be involved when it comes to a decision for conducting such observations (accessibility to the erupting site, possible danger posed to the lives of the scientific party, use of different type of instruments like video cameras, etc.) the independent information that will be collected may play a significant role in explaining possible physical mechanisms. Detailed visual observations described by Ferrazzini & Aki (1992) during a seismic experiment at Kilauea, combined with instrument recordings, enabled them to distinguish between the different physical mechanisms that generate tremor and spindled-shaped signals called gas-piston events (Swanson *et al.*, 1979). High-amplitude tremor was being recorded during the first month of the experiment and visual observations around the crater indicated lava fountaining activity while glows could be seen at night. A decrease in tremor amplitude marked the onset of gas-piston events reflecting a change in the volcanic activity: the level of the lava lake in the crater started rising, with upwelling domes appearing at the surface of the lake associated with the onset

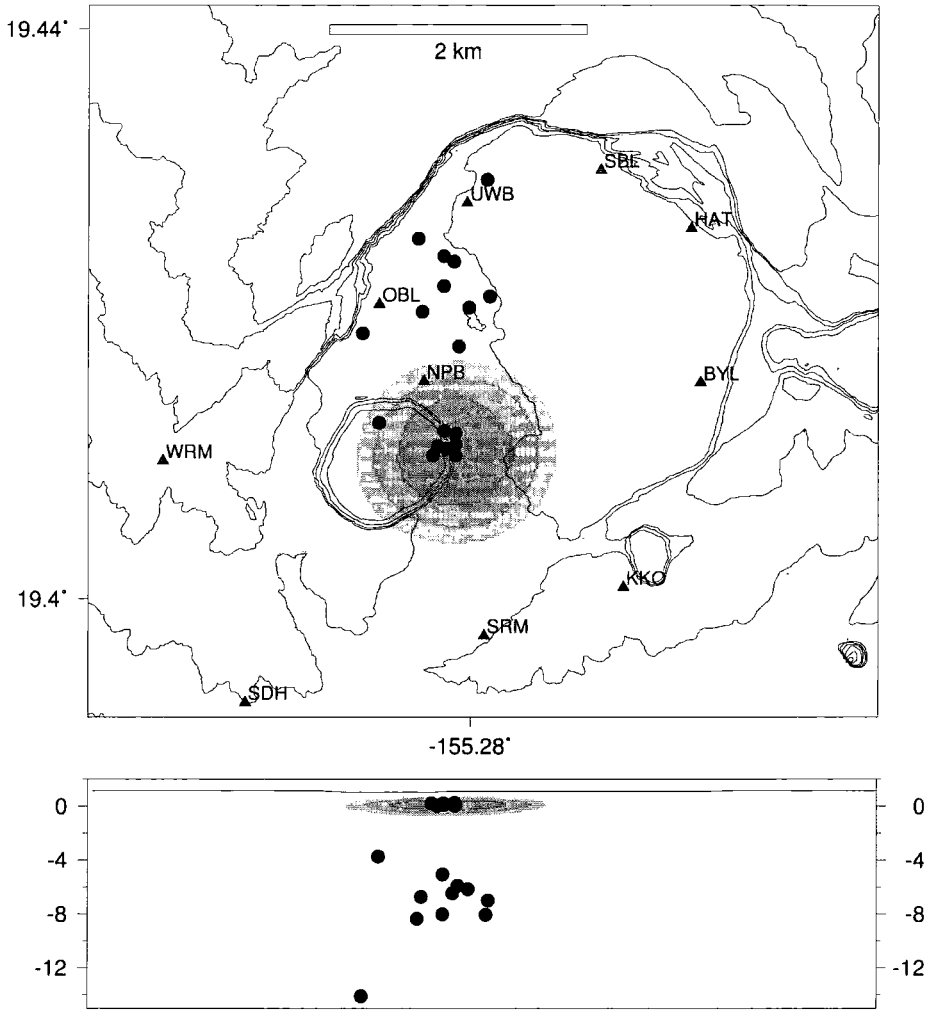


Figure 3.8: Example of location of very long-period tremor using the waveform semblance method, Puu Oo crater, Hawaii. The triangles mark station positions, the filled circles represent peaks of semblance for eighteen located events. The three regions of grey shading represent distribution of semblance, the central and darkest region being that region in which semblance is within three percent of the peak, successively lighter shading marking the sixth and ninth percentile regions. The lower plot is an east-west depth cross-section (vertical scale in kilometers) for the events shown in the top plot (from Bond, 2000).

of bursting of gas bubbles. After that the level of the lake fell, although the same kind of ponding and withdrawal of lava continued in episodic cycles.

Even though it is well known that volcanic eruptions can generate pressure disturbances in the atmosphere with a frequency that can range between $10^{-3}$-20 Hz (Richards, 1963), until recently there has been no systematic recording of temporal variations of these signals near erupting volcanoes. Nowadays the installation of very sensitive microphones that record air-pressure waves with high resolution is an important supplement to the seismic monitoring of active volcanoes (Stromboli-Ripepe *et al.,* 1996; Pavlof-Garcés & Hansen, 1998; Arenal-Garcés *et al.*, 1998; Sakurajima-Garcés *et al.*, 1999). In the case of the Pavlof 1996 eruption, a common pattern of signals was observed consisting of pairs of short duration low-frequency/high-frequency phases on the seismograms superposed on the background tremor (Fig. 3.9), while at the same time explosion sounds were recorded by the microphones.

An explanation for the appearance of these two phases during explosion episodes has been given by Garcés & Hansen (1998), based on the concept of a stratified magma column (Fig. 3.10). This column is assumed to be composed of layers of magma with depth- and time-varying physical properties. While the deepest parts are dense and viscous, exhibiting high sound velocity, the shallower layers are less dense due to an increase in the bubble content owing to degassing that lowers their velocity. A steady flow of magma from a deeper reservoir is not expected to alter the stratification, therefore, the deepest dense layer acts as the area of generation of seismic waves (tremor) that due to the sharp impedance contrast with the upper parts can only propagate in the surrounding bedrock (low-frequency part). A similar process may occur in the shallower layers where metastable gas mixtures of $H_2O$ and $CO_2$ can produce explosions that can only propagate in the atmosphere and then back to the ground (high-frequency air wave). On the other hand, an unstable, turbulent flow of magma can disrupt the stratification and smooth the density contrast between the layer boundaries so that it is possible to have sound waves propagating through the different parts of the magma column. Theoretical

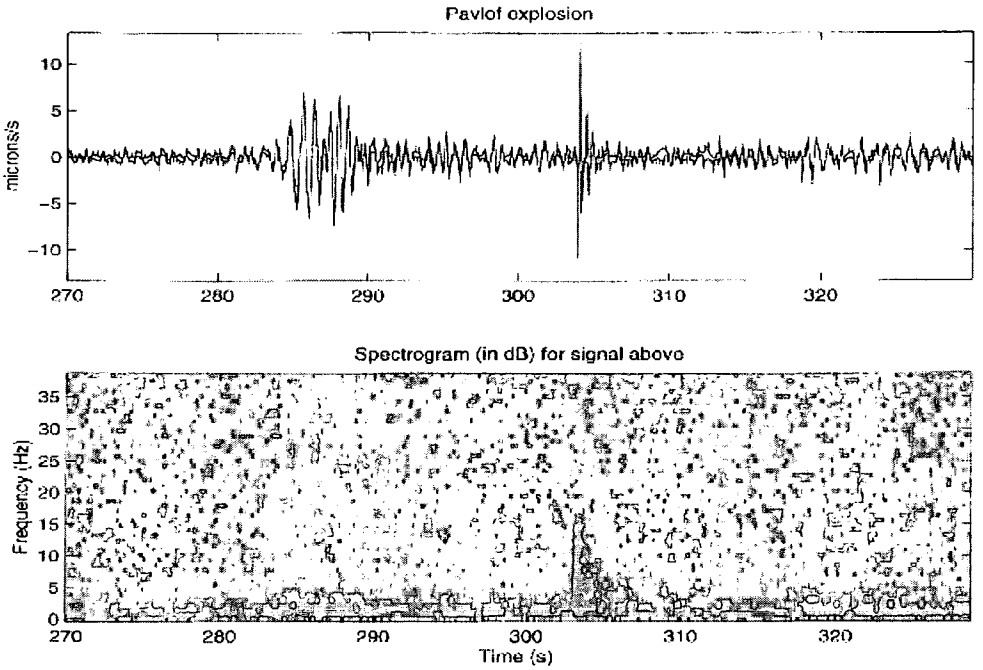


Figure 3.9: Velocity waveform and spectrogram of an explosion signal with a low-frequency/high-frequency pair superposed to the background tremor, recorded during the 1996 eruption of Pavlof. The spectrogram was calculated using a sliding 1.28 s Hanning window with 90% overlap. Dark shades indicate high energy and light shades low energy (from Garcés & Hansen, 1998).

models of these processes have been published by Garcés (1997) and Garcés & McNutt (1997), while results from their direct application to model waveforms of seismoacoustic data acquired during the 1996 eruption of Pavlof volcano have been published recently by Garcés *et al.* (2000). Table 3.3 summarises similar visual as well as acoustic observations reported at volcanoes around the world.

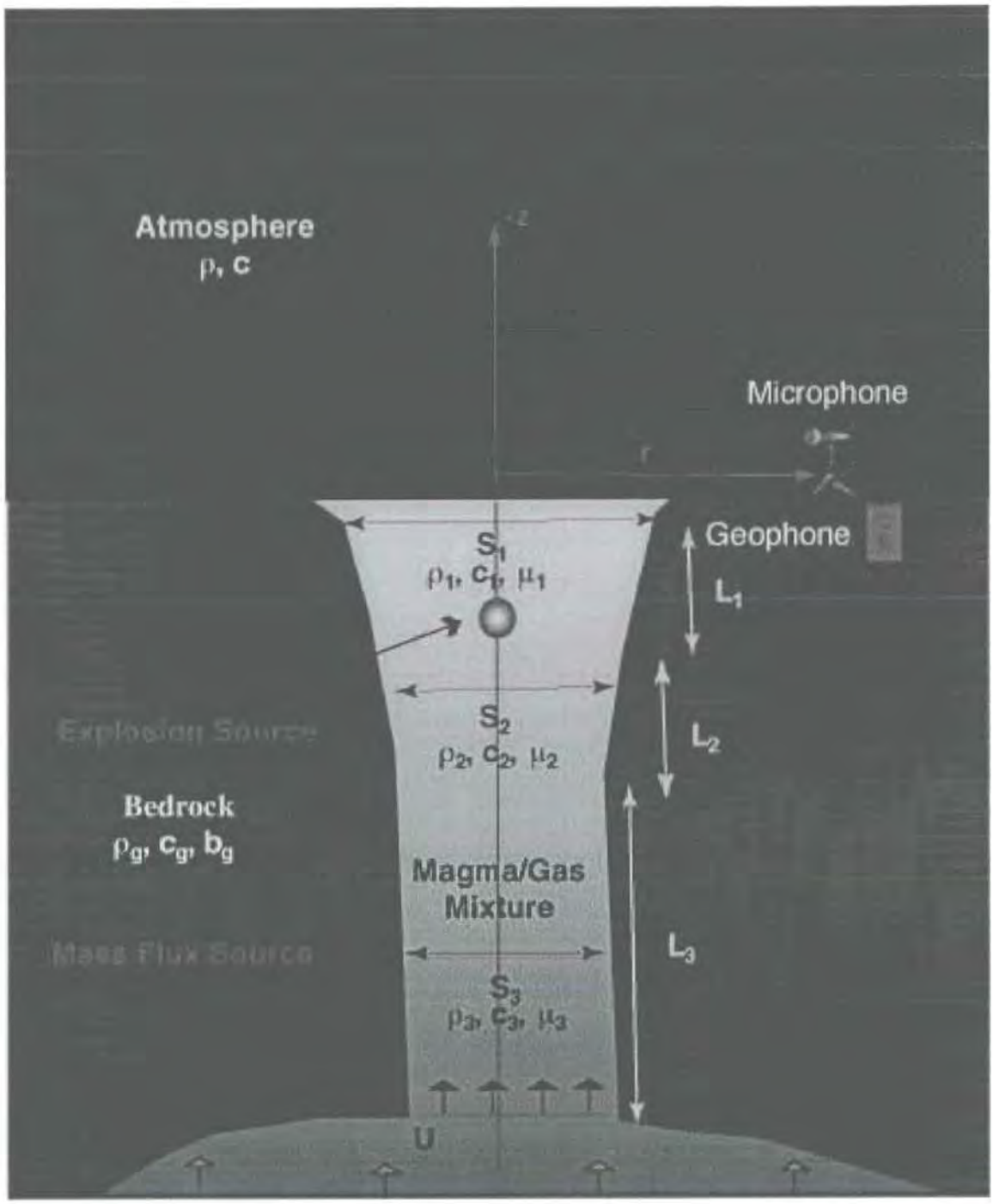


Figure 3.10: A stratified magma column as it was modelled from seismoacoustic signals at Pavlof. The mass flux source is considered to be responsible for the radiation of tremor signals, while the explosive source is generating high-frequency signals similar to those shown in Fig. 3.9, see text for details (from Garcés & Hansen, 1998; Garcés *et al.*, 2000).

**Table 3.3** Reported visual and acoustic observations related to tremor activity.

| Volcano | Visual/acoustic observation |
|---|---|
| Pavlof | Lava fountaining related to high-amplitude tremor |
| Klyutchevskoy | Variation of tremor spectral amplitude envelope whenever the eruptive activity changed |
| Kilauea | Gas-piston events associated with cycles of ponding and withdrawal of lava from the crater followed by high-amplitude tremor |
| Mt. Semeru | Pumping and explosion sounds with durations of 40 s-16 min that coincided with tremor episodes |
| Stromboli | Gas bursts at the top of the magma column coincide with high-amplitude tremor |
| Arenal | Different explosion sounds that are accompanied by ash plumes and precede tremor episodes |
| White Island | Eruptive/intrusive activity always followed by tremor |
| Satsuma-Iwojima | Strong tremor occurring while vent emits high-temperature volcanic gas |

## 3.5 Modelling the source of volcanic tremor

### *3.5.1 Fluid-flow induced oscillations*

The process of how magma ascends from a deep source and moves towards the surface causing an eruption has been studied extensively by many authors and at different scales. On the smallest possible scale magma is considered to flow through the porous matrix of partially molten rock, forming during its ascent shape-preserving (soliton) waves as has been demonstrated analytically (Scott & Stevenson, 1984) and experimentally (Scott & Stevenson, 1986). On a larger scale, the interior of a volcano is modelled as consisting of a shallow magma reservoir fed from a deeper source and a cylindrical-shaped conduit that transports the fluid upwards and may be connected to a network of other conduits (Fedotov, 1981). In general the reservoir is considered to behave elastically under the variable stress conditions imposed by fluid accumulation or outflow. The cylindrical conduit on the other hand is believed to exhibit more complicated, viscous behaviour so that a high driving fluid pressure from below results in deformation being transmitted periodically as expansions or contractions of its walls (Ida & Kumazawa, 1986; Ida, 1996). A mixed visco-elastic response should be expected when the fluid pressure either builds up quickly, forcing the conduit to respond elastically by a fast opening, or fluid pressure is low and viscous deformation prevails (Maeda, 2000).

Several observations made during eruptions suggest a direct link between inward and outward flow of magma from a reservoir and the generation of volcanic tremor. Tilt observations indicate the occurrence of cycles of slow build-up of ground deformation starting as volumetric expansion and terminating with contraction, which are accompanied almost always by tremor episodes (Kilauea-Dvorak & Okamura, 1985; Izu-Oshima-Oikawa *et al.*, 1991; Fukao *et al.*, 1998). The quantitative study of magma flow through a geometrically irregular volcanic conduit poses a difficult numerical problem which requires the formulation and simultaneous solution of a system of partial differential equations describing the flow of the fluid as well as the elastic disturbance being caused by coupling to the surrounding rock (Chouet

& Shaw, 1991). Further complications may arise if the fluid consists of a gas and liquid phase, or if the thickness of the conduit changes in space as well as in time, effectively exhibiting viscous or visco-elastic behaviour. In models of tremor generation involving fluid flow, a number of simplifying assumptions are usually made: (a) the fluid has a constant density and consists of one phase only; (b) the motion occurs in one or two dimensions; and (c) the conduit behaves elastically, while its thickness can only change as a function of time.

Based on these assumptions and using the principles of conservation of mass and momentum for the fluid, Julian (1994) derived a third-order system of nonlinear ordinary differential equations that describe the flow inside a vertically extending crack connecting an upstream and a downstream reservoir (Fig. 3.11). Considering a fluid density and viscosity typical for basaltic melts ($\rho = 2500$ kg m$^{-3}$ and $\eta = 500$ Pa s), a crack 10 m long with a thickness (in equilibrium condition) of 1 m, Julian (1994) solved the system of equations numerically for different values of driving pressure at the lower end of the conduit. In the interval 10-15 MPa, the numerical solutions indicate a cyclic behaviour of continuous increasing and decreasing conduit thickness. According to Bernoulli's theorem the quantity $p + \rho v^2/2$ must remain constant. Therefore, for large flow speeds $v$, the fluid pressure $p$ in the conduit decreases and the walls move towards each other constricting the flow. For the same reason the pressure builds up again forcing the walls apart and results in a fluid-induced periodic oscillation. Oscillations for fluid pressure less than 10 MPa were found to decay quickly in time, resembling to the behaviour of low-frequency earthquakes. For fluid pressure values greater than 15 MPa a large number of subharmonics appears, assuming values that are $\frac{1}{2}, \frac{1}{4}, \frac{1}{8}, \frac{1}{16}...$ of the value of the fundamental period of the oscillation.

This phenomenon, known as 'period doubling cascade', is one of the ways that a system described by a set of nonlinear differential equations may evolve from a periodic, predictable behaviour in the time/frequency domain to a state of nonperiodic and almost noisy looking time series/spectrum, which is termed as chaotic (e.g.

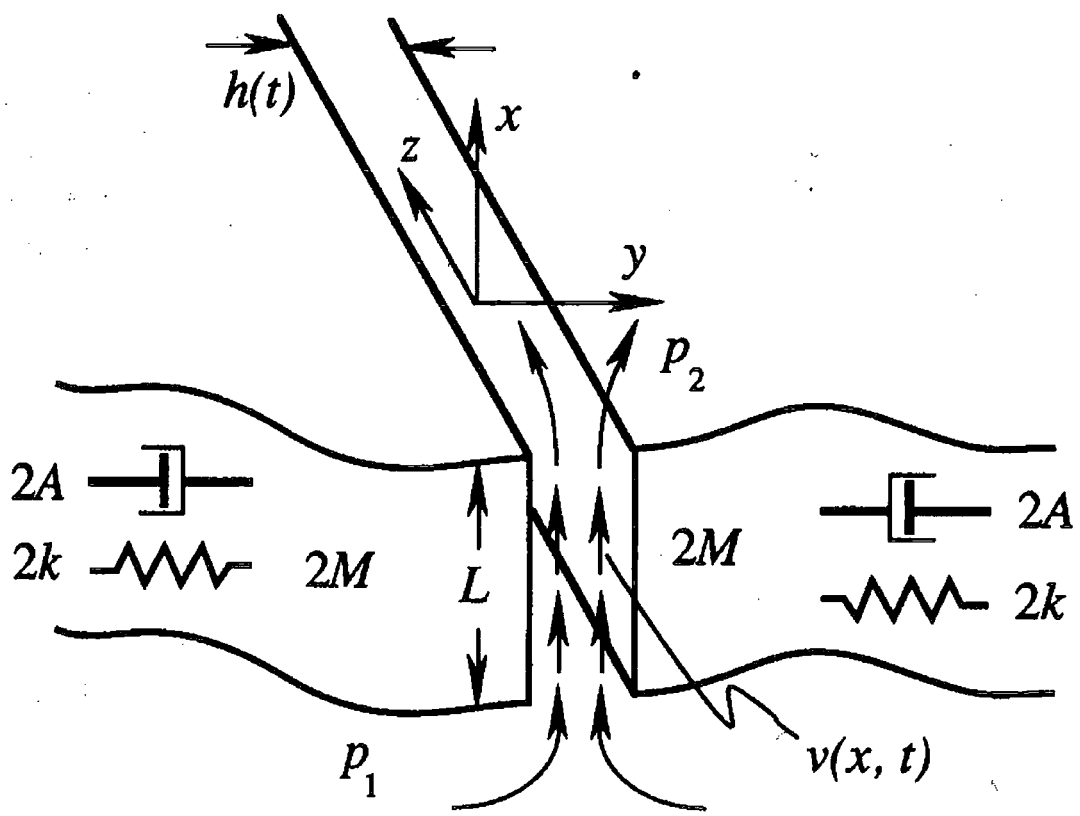


Figure 3.11: Lumped parameter model of the generation of volcanic tremor. Viscous incompressible fluid flows in the $x$ direction from the upstream to downstream reservoir through a channel of length $L$ with imperfectly elastic walls, modelled as movable but undeformable blocks of mass $2M$, stiffness $2k$ and damping constant $2A$ (all measured per unit distance in the $z$ direction). All motion occurs in the $x-y$ plane and it is independent of $z$. The dynamic variables are the channel thickness $h(t)$ and the fluid speed $v(x,t)$ (from Julian, 1994).

Bergé *et al.*, 1986). A plot of the triplet of values $h, v, \dot{h}$ (where $h$ is the conduit thickness and the dot indicates differentation with respect to time), known as the state of the system, reveals sets of orbits that while they diverge exponentially from each other due to sensitivity to initial conditions, they also fold because of dissipation of energy (Fig. 3.12). This stretching and folding process makes them move always within a bounded region of the state space, forming a geometrical object with fractal properties, called a strange attractor. A more detailed discussion of the application of nonlinear dynamics to the study of volcanic tremor and the results obtained will be presented in Chapter 4.

Another type of flow-induced oscillation may occur if the fluid system is suddenly perturbed from its equilibrium state by some external cause, such as fracturing of the surrounding bedrock and formation of a new conduit, or a sudden variation in the fluid supply (St Lawrence & Qamar, 1979; Ferrick *et al.*, 1982). This perturbation will result in the generation of a fluid transient with characteristics that will depend on the physical properties of the fluid, the geometry of the conduit and the boundary conditions. Pressure oscillations caused by the transient will displace the conduit walls generating elastic waves in the surrounding medium. Two parameters that control the frequency response of the system are the characteristic impedance of the fluid $Z_c$ and the orifice impedance $Z_{or}$, defined as

$$Z_c = \frac{\alpha}{gA}, \quad Z_{or} = \frac{2H}{Q} \tag{3.16}$$

where $\alpha$ is the pressure wave speed in the fluid, $g$ is the acceleration due to gravity, $A$ is the cross-sectional area of the conduit, $H$ is the pressure head and $Q$ is the flow rate of the fluid. $Z_{or} > Z_c$ implies a small conduit opening, where a small quantity of fluid may pass through resembling a close pipe system, with frequencies $\omega = n\pi\alpha/2L$, where $L$ is the conduit length and $n = 1, 3, 5...$ . For $Z_{or} < Z_c$ the inverse is true and the system responds as an open pipe with frequencies given by the same equation but $n = 2, 4, 6...$ . A more complicated behaviour is expected if the conduit is a part of an extended network that is believed to exist beneath

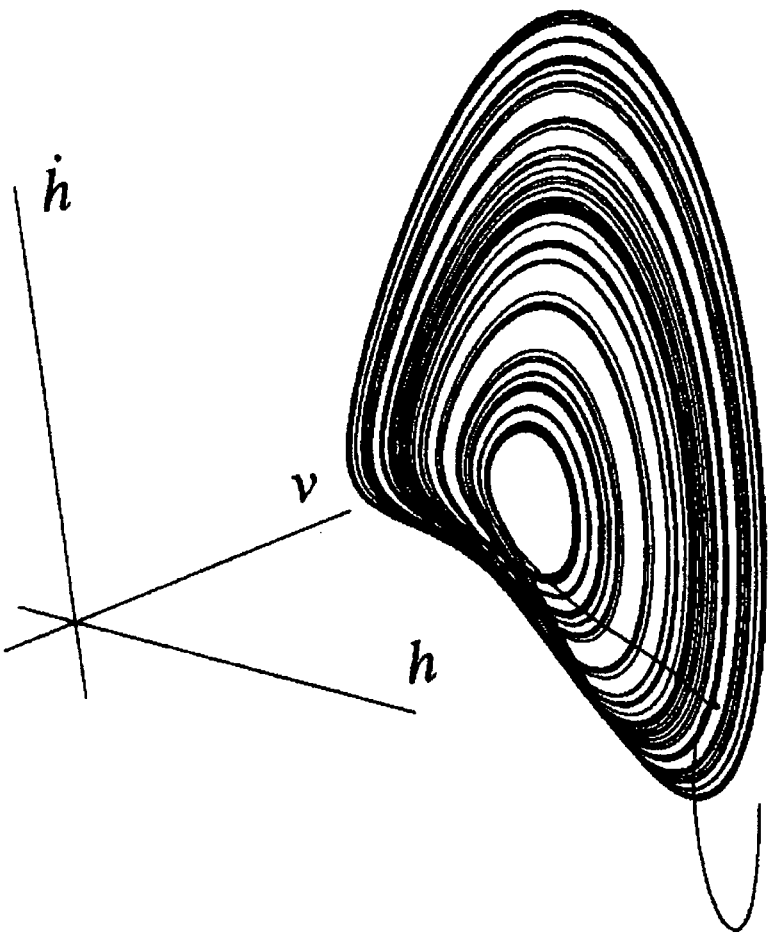


Figure 3.12: Stereoscopic view of orbits in phase space formed by plotting the triplet of values $h, v, \dot{h}$ for a driving pressure of $p_1 = 19.0$ MPa. The resulting geometrical object has a fractal structure and is called a 'strange' attractor. Note the folding of the orbits at the lower part of the plot (after Julian, 1994).

many volcanoes. Energy considerations show that once the system is perturbed it will continue to oscillate, until damped primarily by fluid friction, since dissipation of energy due to the generation of seismic waves is relatively small (Ferrick & St Lawrence, 1984). Similar unsteady flow in conduits followed by tremor-like seismic signals has been reported at a power plant at Oroville, California caused by a faulty valve (Ferrick *et al.*, 1982) and at Tarbela dam, Pakistan, while water was moving through outflow tunnels (McNutt, 1986).

### *3.5.2 Excitation of fluid-filled cracks*

Brittle failure of rock and crack formation inevitably accompany any upward movement of magma during different stages of volcanic activity. The main result of such rock fracturing is the generation of various types of seismic signals, ranging from events that can hardly be distinguished from common tectonic earthquakes to low-frequency events with emergent onsets, absence of clear S wave phases and a slowly decaying coda (Power *et al.*, 1994). Injection of water in hot dry rock has been found to produce seismic signals similar to low-frequency volcanic earthquakes and supports the idea of a source that involves the opening of tensile cracks caused by excess fluid pressure (Bame & Fehler, 1986). The overall similarity of tremor and low-frequency events in the time and frequency domain, notwithstanding their different signal duration has been suggested by many authors to indicate that a common source may be at work; which of the two seismic signals will be generated will depend on the duration of the excitation mechanism (Fehler, 1983; Chouet, 1985; Hofstetter & Malone, 1986; Tsuruga *et al.*, 1997; Almendros *et al.*, 1997).

Volcanic tremor generated at Kilauea during the 1963 eruption was mainly composed of P waves, shared the same source area with the low-frequency earthquakes and was deep enough to assume that its source was related to magma transportation and not degassing processes (Aki *et al.*, 1977; Aki & Koyanagi, 1981). Aki *et al.* (1977) proposed that the observed tremor could be explained by the jerky extension of a chain of cracks (Fig. 3.13) caused by magmatic pressure build-up as magma

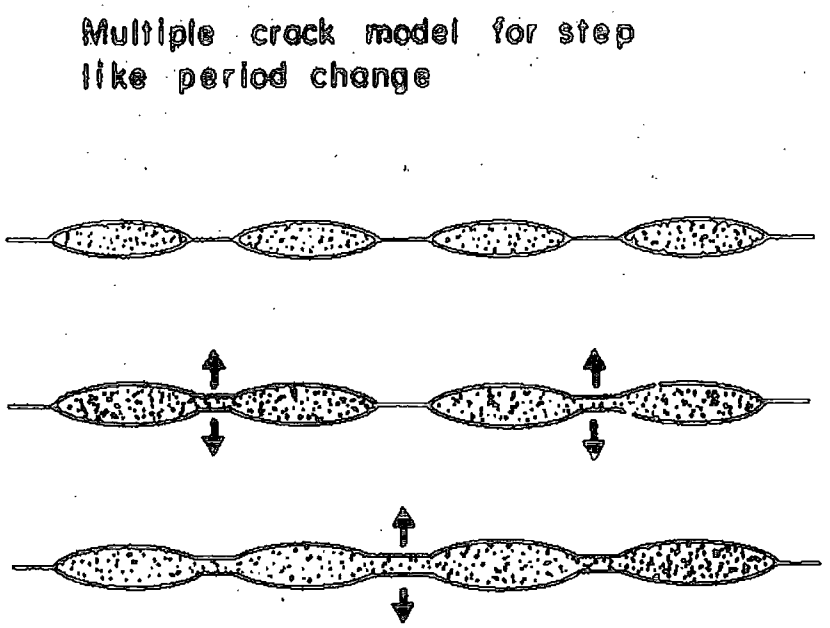


Figure 3.13: Schematic illustration of the multiple crack model used to explain tremor episodes during the 1963 Kilauea eruption. During increased magma transport, the number of cracks participating in the vibration increases, leading to an increase in the tremor period (from Aki & Koyanagi, 1981).

moves away from a deep reservoir beneath the summit of the volcano. The cracks may be arranged in a series and are connected by narrow channels that open when magma pressure reaches a critical value, facilitating the movement of fluid from one crack to the next one. The vibration caused by such a movement was found to have a period proportional to the crack length and an amplitude that depended on the excess pressure and the area of extension.

In order to explain the temporal variations of the frequency content during a tremor episode from higher (5-10 Hz) to lower frequencies (1.5-3 Hz), Aki & Koyanagi (1981) suggested that this process starts with a few cracks generating a signal of small period which increases as more cracks vibrate and the length of the chain gets longer. However, two discrepancies have been pointed out regarding this model.

First, as the length of the chain increases, a systematic lowering of the frequencies of the tremor signal should occur, which was not observed. Second, numerical studies on crack generation and growth show that a tensile stress regime when combined with the fact that the largest part of each crack is expected to be filled with fluid, favours catastrophic growth rather than a stable opening-closing process (Sammis & Julian, 1987).

Chouet (1986; 1988) considered the displacement of the walls of a fluid-filled crack caused by a pressure disturbance in the fluid as a possible model for the generation of low-frequency earthquakes, as well as tremor, if the disturbance is sustained. This model is qualitatively different to that proposed by Aki *et al.* (1977), since it assumes the vibration of only one crack with no inflow or outflow of fluid taking place. The characteristics of the far-field wavefield radiated by a rectangular shaped vibrating crack, filled with an inviscid fluid and assuming that the surrounding bedrock behaves as a Poisson solid, were found to depend on the following parameters: (a) the crack geometry; (b) the position and the area over which the pressure disturbance occurs; (c) boundary conditions for the stress on the crack's surface and the fluid flow at the crack perimeter; and (d) a dimensionless quantity called the crack stiffness $C$ and the fluid-solid impedance contrast $Z$, defined as

$$C = \frac{bL}{\mu d}, \quad Z = \frac{\rho_s \alpha}{\rho_f a} \tag{3.17}$$

where $b$ is the bulk modulus of the fluid, $\mu$ is the rigidity of the solid, $L$ is the crack length, $d$ is the crack thickness, $\rho_s$ is the density of the solid with $\alpha$ its P wave velocity and $\rho_f$ the density of the fluid with P wave velocity equal to $a$.

For many different combinations of the parameters (a)-(d) the fluid-filled crack model was found to have longitudinal and lateral modes of oscillation that are given by $2L/n$ and $2W/n$, where $n = 2, 3, 4...$ with $L, W$ the length and width of the rectangular crack. The spectrum of the far-field radiated waves is dominated by sharp peaks representing the mixing of the longitudinal and lateral modes of the

resonating crack. However, the fundamental period of resonance for the crack was found by Chouet (1988) to be much longer than the expected one due to the existence of a slow wave propagating along the fluid-solid boundary, which he called 'crack wave'. This kind of wave exhibits inverse dispersive properties in the sense that both group and phase velocities tend to zero with increasing wavelengths and/or increasing crack stiffness. After numerical calculations Ferrazzini & Aki (1987) found that a fluid-filled crack with 1 km length, 0.5 m thickness, density ratio of $\rho_s/\rho_f = 2.5$ and velocity ratio of $\alpha/a = 1.5$ will have a resonance period of 10 s. Ferrazzini & Aki (1987) further suggest that this model provides a geologically more reasonable explanation for the observation of 10 s-period tremor at Mt. Aso first made by Sassa (1936), than the oscillations of a magma chamber with a diameter of 4-8 km.

The calculated quality factor Q of the vibrating fluid-filled crack, which reached a maximum value of 20 for an impedance constrast equal to 40, showed a substantial difference to the values of $Q = 40$ reported by Ferrazzini & Aki (1992) for Hawaiian tremor. Chouet (1992) attributed this difference to two reasons: first, the model considers a fluid consisting of one phase only, while in reality some percentage of gas bubbles should be present (even though this factor restricts the applicability of the model only to shallow tremor). Second, it is highly unlikely that the recorded tremor is the result of only one fluid-filled crack and the mixing of waves radiated by many resonating cracks may have created the observed difference.

### *3.5.3 Hydrothermal boiling*

The fact that the formation of bubbles in a liquid is an efficient way of seismic energy generation has long been recognised and utilised in exploration geophysics (e.g. Dobrin & Savit, 1986). Geysers and geothermal reservoirs are natural sources of such seismic energy and seismological studies of the Old Faithful geyser revealed the existence of tremor-like signals related to boiling of groundwater (Kieffer, 1984; Kedar *et al.*, 1996). Leet (1988) suggested that processes similar to the ones observed

at Old Faithful could be used to explain the generation of volcanic tremor recorded during quiet periods at certain volcanoes, which he called 'noneruption tremor'. Two restrictions regarding this model are: (a) the magma chamber underneath the volcano acting as the source of heat, should not reside at a higher elevation level than the groundwater table; and (b) the process should operate at shallow depths, so that steam can be separated from the liquid. Obviously, hydrothermal boiling cannot explain tremor processes operating at depths greater than a few kilometers below the earth's surface.

Boiling of groundwater causes the formation and growth of bubbles in the liquid that may collapse if they encounter a liquid region of lower temperature. Either of these two mechanisms can generate seismic energy, but Leet (1988) found that bubble collapse is $10^2$-$10^4$ times more efficient in converting thermal energy to seismic energy. The boiling heat transfer rates in order for bubble collapse to generate 1 Hz tremor should be about 1000 MW, which Leet (1988) notes is the upper limit of observed heat flow in volcanic crater lakes and geothermal areas. The resulting signal is expected to be resembling white noise, with equal energy in all frequency bands, which is in contrast to the sharply peaked tremor spectra. However, assuming that the groundwater is contained in a channel the boiling process may set it into resonance, so that the frequency response of the channel will be convolved with the broadband noise. The length of the channel required to generate a signal with frequencies in the range 0.5-5 Hz is given by $L = \alpha/2f$, where $\alpha$ is the sound velocity of the liquid taking values of 50-1500 m $s^{-1}$ for groundwater and thus $L$ is in the range 1-1000 m.

### *3.5.4 Resonance of large magma bodies*

Among the first models used to explain the occurrence of volcanic tremor is that of the free oscillations of magma bodies of various shapes. For example Sassa (1936) and later Shima (1958) and Kubotera (1974) suggested that the observed 10 s period tremor at Mt. Aso was caused by the oscillation of a spherical magma

chamber beneath the volcano. However, a simple calculation of the radius $r$ of the chamber using the equation $f = 4.4\alpha/2\pi r$, where $\alpha$ is the sound velocity in the melt taking a value of 1-2 km $s^{-1}$ and $f$ the frequency of oscillation, yields a radius value of 7-14 km. Furthermore, no exact physical mechanism which could set the whole chamber into oscillation was identified.

Assuming that the low-frequency earthquakes may be a kind of impulse response of the tremor generating system Chouet (1985) proposed a model to explain such earthquakes by studying the oscillations of a buried magmatic pipe. The pipe consisted of three parts: at the top a hemispherical cavity filled with gas was considered to be triggering the oscillations due to excess gas-pressure, in the middle the resonating pipe had a cylindrical shape and was filled with magma, and at the bottom the pipe was shut by a horizontal disk. The calculated free surface response of this system showed an impulsive signature in the vicinity of the pipe, but evolved to a harmonic wavetrain at larger distances. In the frequency domain the system exhibited sharp peaks corresponding to the well known organ-pipe modes, with amplitudes that depend on the amount of energy lost due to viscous damping in the fluid and radiation of seismic energy in the solid.

Based on similar ideas about the relationship of tremor and low-frequency earthquakes, Crosson & Bame (1985) studied the resonance of a magma filled spherical cavity encased in country rock which contained a smaller cavity filled with gas. The motivation for such a model also came from observations at Stromboli, where low-frequency earthquakes were found to originate a few seconds prior to explosions. Thus expansion of the gas-filled cavity could set the magma-filled one into resonance ('breathing mode'). The signal generated by such an oscillation had a frequency content of 1-5 Hz, consistent with the observations and an impulsive signature in the time domain. Again it was assumed that sustained expansions of the gas-filled pocket (probably due to pressure variations) would give rise to continuous tremor.

## 3.6 Summary

Volcanic tremor has attracted considerable attention by seismologists because of its potential value as a tool for forecasting eruptions and better understanding the physical processes that occur inside active volcanoes. However, unlike tectonic earthquakes where the dominant source process is brittle failure of rock, the driving mechanism of tremor seems to involve complex interactions of magmatic fluids with the surrounding bedrock. These interactions are responsible for the following distinct characteristics found in volcanic tremor recorded at many volcanoes worldwide: (a) the onset of tremor may be emergent or impulsive, with its amplitude showing in many cases a direct relationship to the volcanic activity; (b) in the frequency domain the spectra consist of a series of sharp peaks in the band 0.1-7 Hz, representing either a fundamental frequency and its harmonics, or a random distribution while quite often they exhibit temporal variations in their content; (c) the depth of the source can vary considerably from one volcano to another in the range of a few hundred meters to 40 km; (d) tremor may occur prior to and/or after eruptions with a duration that ranges from several minutes to several days or months. The methods used to study tremor include spectral analysis using both the Fourier Transform and the Maximum Entropy Method, polarisation analysis of the wavefield and methods that make use of array data to deduce the backazimuth and type of the seismic waves as well as the location of the source. Visual and/or recorded acoustic observations of the on-going volcanic activity have assisted in many cases to further constrain proposed physical mechanisms for the generation of tremor. The models suggested as possible sources of tremor can be grouped as follows: (a) fluid-flow induced oscillations of conduits transporting magmatic fluids; (b) excitation and resonance of fluid-filled cracks; (c) bubble growth or collapse due to hydrothermal boiling of groundwater; (d) a variety of models involving the oscillations of magma bodies with different geometries. It has been proposed by many authors that the source of tremor is not unique and may differ from one volcano to another, a fact that adds more difficulty to the source modelling efforts.

# Chapter 4
# Volcanic tremor: analysis and results

## 4.1 Introduction

This chapter contains a description of the main features of volcanic tremor signals recorded before and during the 1996 Vatnajökull eruption. The analysis presented covers the tremor appearance in the time and frequency domain and also uses tools from the discipline of nonlinear dynamics in order to recover information about its source processes.

## 4.2 Evolution of tremor behaviour in the time domain

During September 28th-29th the seismograms recorded at the closest station to the eruption site (HOT23) were severely contaminated by oceanic microseismic noise and no other seismic signals were visible. However, after highpass filtering at 0.5 Hz a low-amplitude signal can be clearly seen (Fig. 4.1). Tremor activity became visible on the seismograms at the onset of the eruption, as a relatively low-amplitude, continuous signal just above the level of oceanic microseismic noise (Fig. 4.2). During the night of October 1st the amplitude of the signal progressively increased, being visible at HOT23 without having to perform any filtering. Similar activity continued until midday when high-amplitude, cigar-shaped bursts started being superposed on the lower amplitude background tremor (Fig. 4.3). The number of bursts steadily declined as the eruption progressed (Fig. 4.4a), while their average duration (measured using *pql*) was of the order of 250 s having a standard deviation that varied considerably from day to day (Fig. 4.4b). After the eruption became subaerial there were episodic cycles of high-amplitude tremor mixed with periods when only microseismic noise could be seen. The next closest ($< 80$ km) station to

the eruption site, HOT25, recorded only a number of high-amplitude bursts during the first day of the eruption.

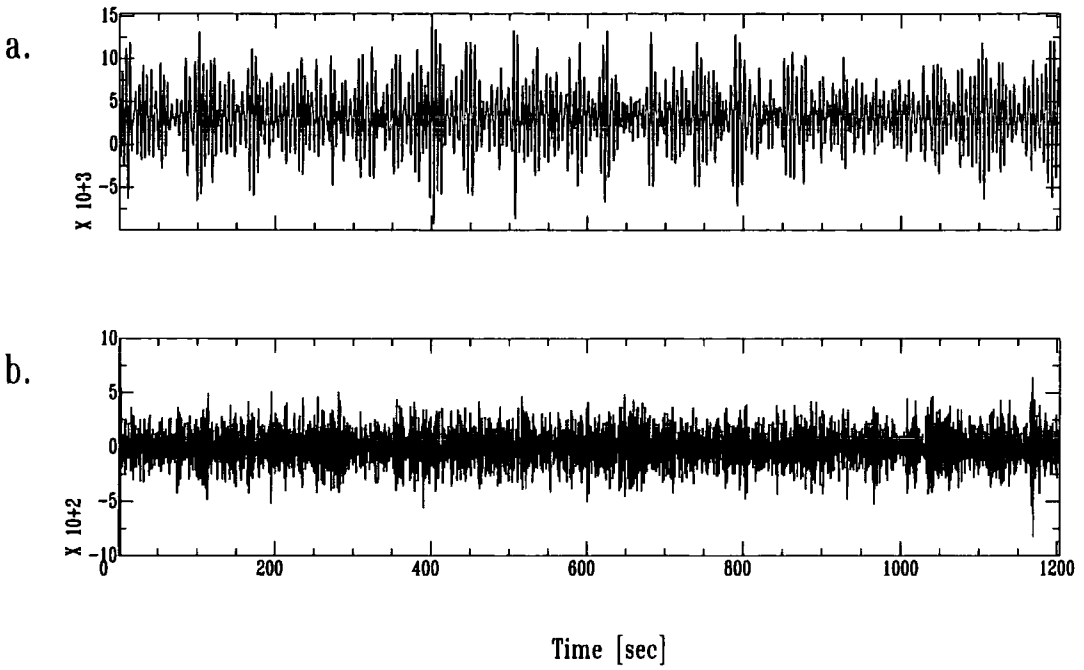


Figure 4.1: (a) Vertical component velocity waveform recorded at HOT23 two days before the onset of the eruption showing contamination with microseismic noise. (b) The same trace after highpass filtering at 0.5 Hz, revealing a low-amplitude, high-frequency signal.

## 4.3 Spectral analysis

In the case of the Vatnajökull eruption, it is not possible to draw a definite conclusion about the occurrence of pre-eruptive tremor due to the presence of oceanic microseismic noise. Thus, the spectral analysis is aimed at investigating this possibility, as well as indicating the periods when the frequency content of the tremor signal changed substantially. To better observe these temporal frequency variations, a two-dimensional representation of the variations of spectral energy and frequency of the observed signal as time elapses (spectrogram) is used.

Spectrograms were created for each of the three-component seismograms recorded by station HOT23 over successive time intervals of twelve hours, for the period

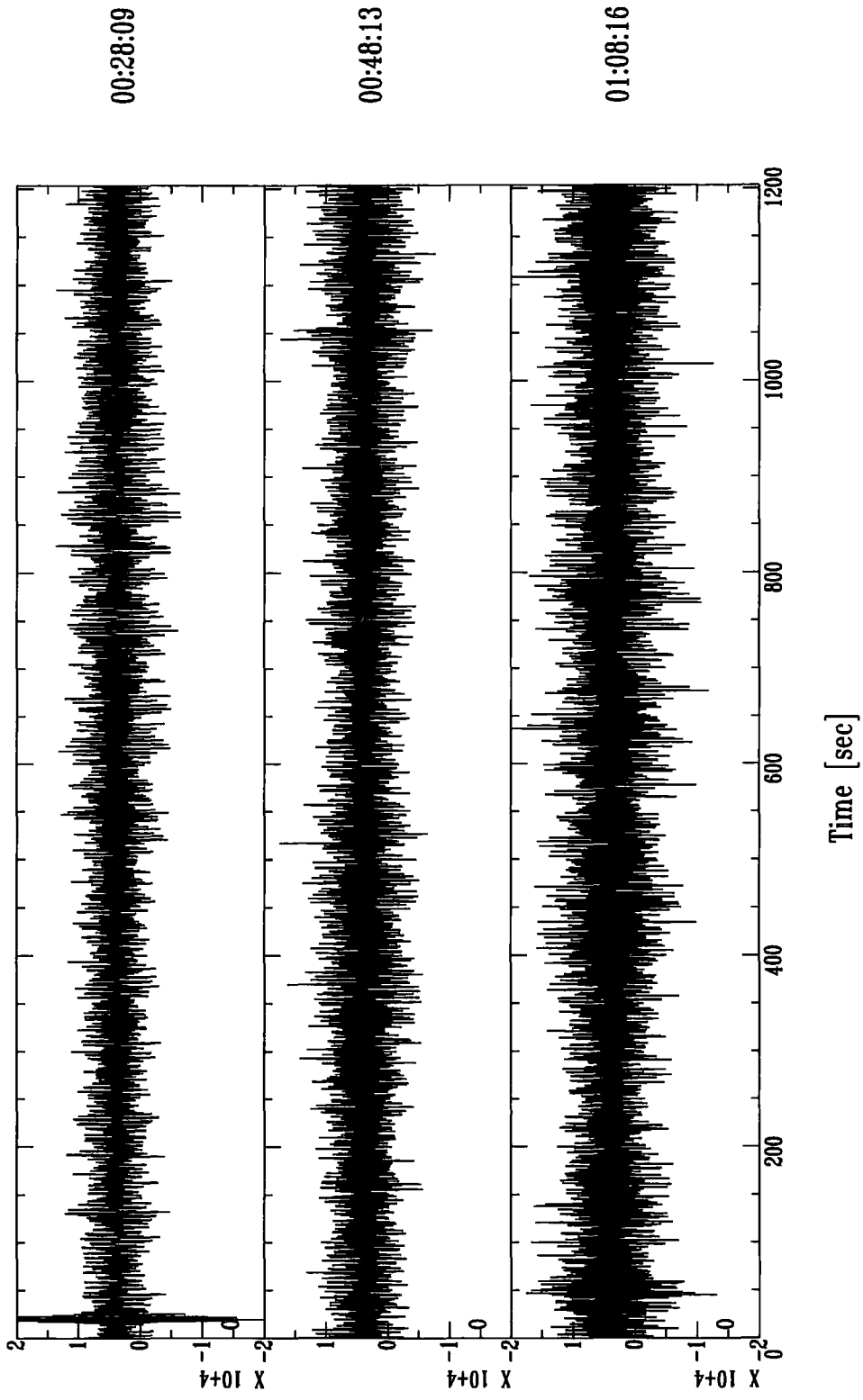


Figure 4.2: One hour of continuous volcanic tremor recorded during the onset of the subglacial eruption at HOT23. The times, in GMT, given on the right are the start times for each trace. The amplitude scale is normalised to the largest value of the three traces (last trace). The large amplitude signal at the beginning of the first trace is an earthquake.

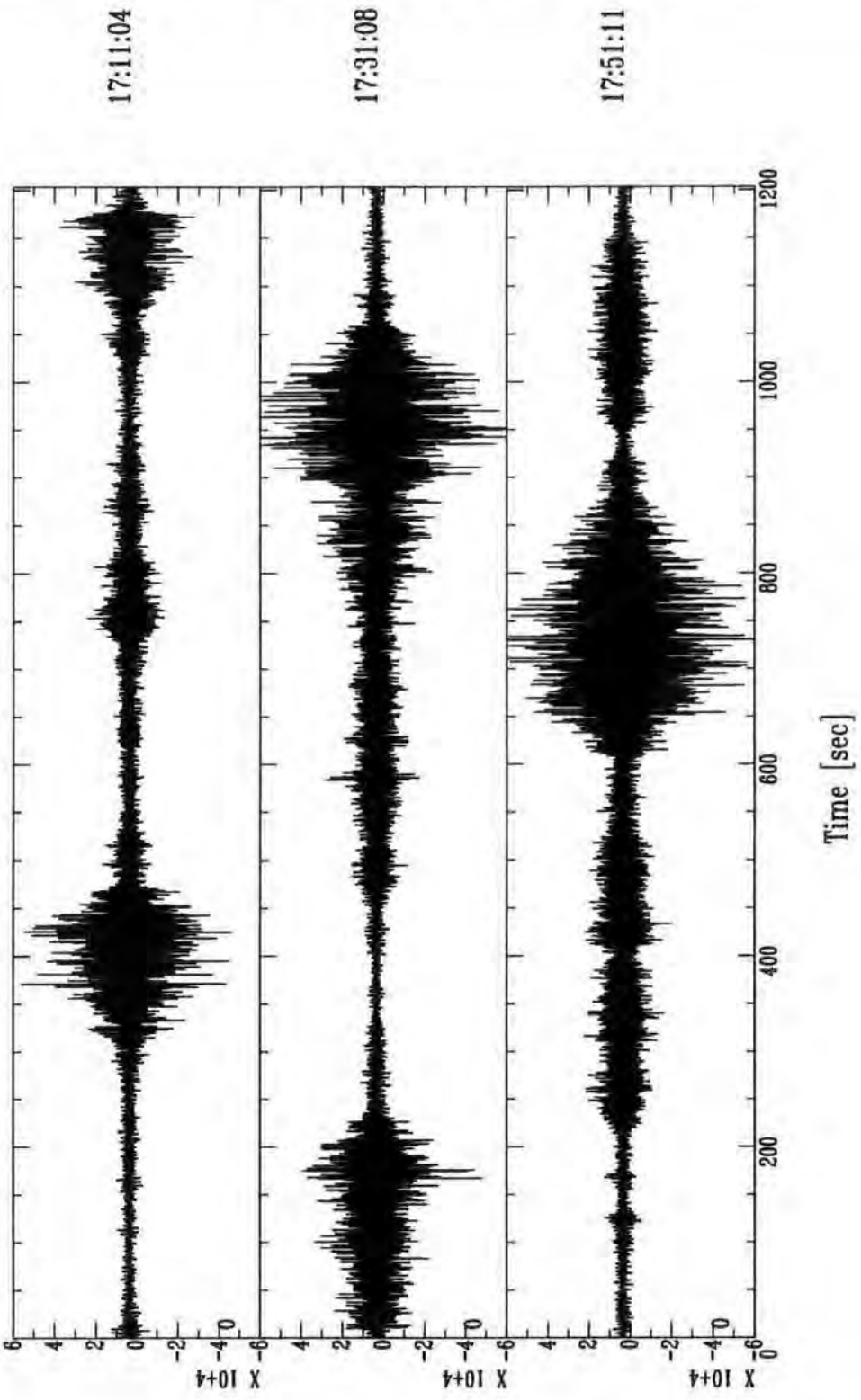


Figure 4.3: Same as in Fig. 4.2 for tremor exhibiting high-amplitude, cigar-shaped bursts that are superposed on low-amplitude background tremor. Note how the amplitude of some of the bursts decays exponentially while in others it reaches a maximum and decays abruptly immediately afterwards.

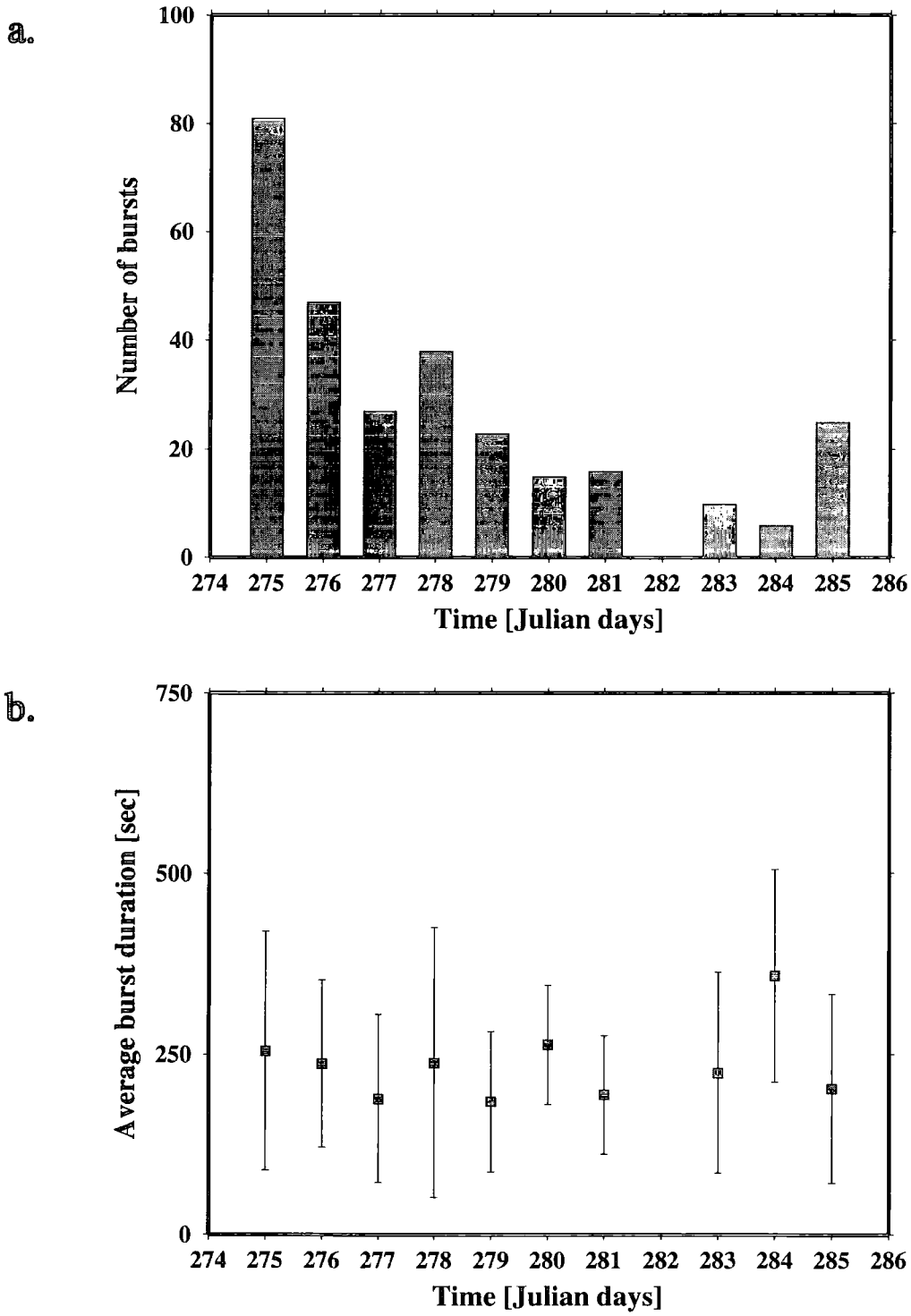


Figure 4.4: (a) Distribution of the number of bursts during the whole period of the eruption (October 1st-11th). (b) Average duration and standard deviation of the bursts for each day.

September 28th-October 13th. The 20 min long Miniseed files were first converted to AH format and then pasted together into files of 12 hours duration each, using the program *ahmerge* provided by the IRIS-PASSCAL software library. The program *ahspectgm* (B. R. Julian, pers. comm. 1999) was used to calculate the power spectrum for each of the data files using a 100 s long sliding window, with 50% overlap. *ahspectgm* normalises its output by dividing each spectral value by the average power density for each window and then writes this output by default to a GMT (Wessel & Smith, 1995) gridfile where each grid point has as coordinates the triplet frequency, time, amplitude. The base 10 logarithm of the amplitude was then obtained by using the program *grdmath* which is part of the GMT package. The procedure described above was automated by means of the C-shell script *mkgrd* and results were plotted for each day using the GMT script *plotspectgm.*

The spectrograms for September 28th and 29th (before the onset of the earthquake swarm) revealed the existence of a seismic signal around five narrow frequency bands of 0.5-0.7, 1.6, 2.2, 2.8 and 3.2 Hz. The northsouth and vertical components exhibited larger spectral amplitudes than the eastwest component (Fig. 4.5). However, after more detailed examination of individual spectra it was found that this is due to the fact that the ocean microseismic noise is stronger on the eastwest component, creating the observed amplitude difference. After the episodic swarm at Bárdarbunga the tremor signal gradually became broadband, even though isolated peaks at the same frequency bands could still be identified in the spectrograms (Fig. 4.6). The continuous tremor and the high-amplitude bursts exhibited a high frequency content and a sharp spectral amplitude decay in the higher frequencies when compared to the low-amplitude background tremor (Fig. 4.7a and b). Spectrograms of the data recorded on October 13th do not not show the presence of any higher frequency signal, thus marking the end of the tremor activity.

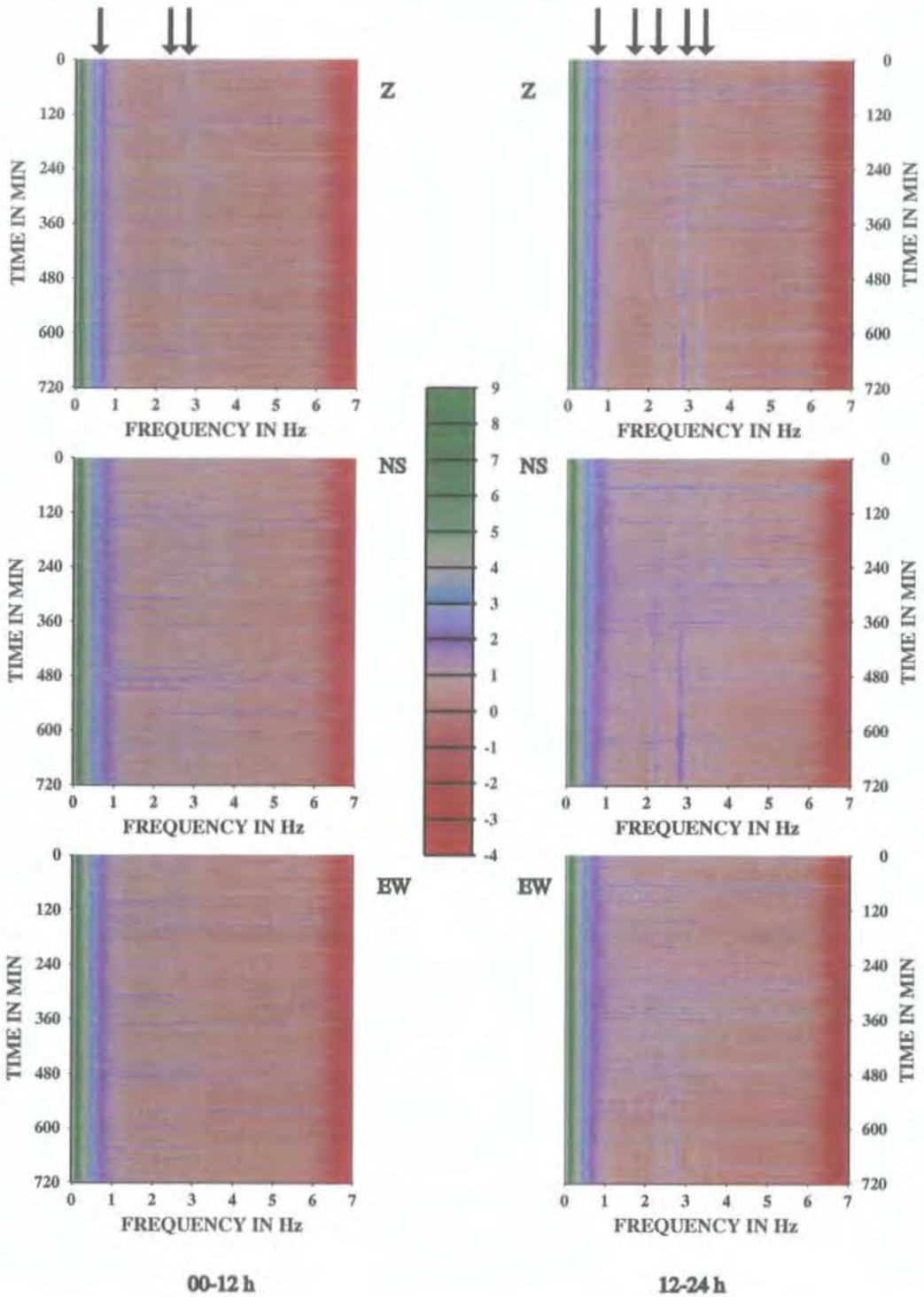


Figure 4.5: Tremor spectrograms for September 28. Each plot represents twelve hours of data for the three-component seismograms recorded by station HOT23. The amplitude colour scale is logarithmic. Vertical arrows show the frequency bands observed. The high-amplitude signal below 0.3 Hz represents ocean microseismic noise. Horizontal transient events represent icequakes.

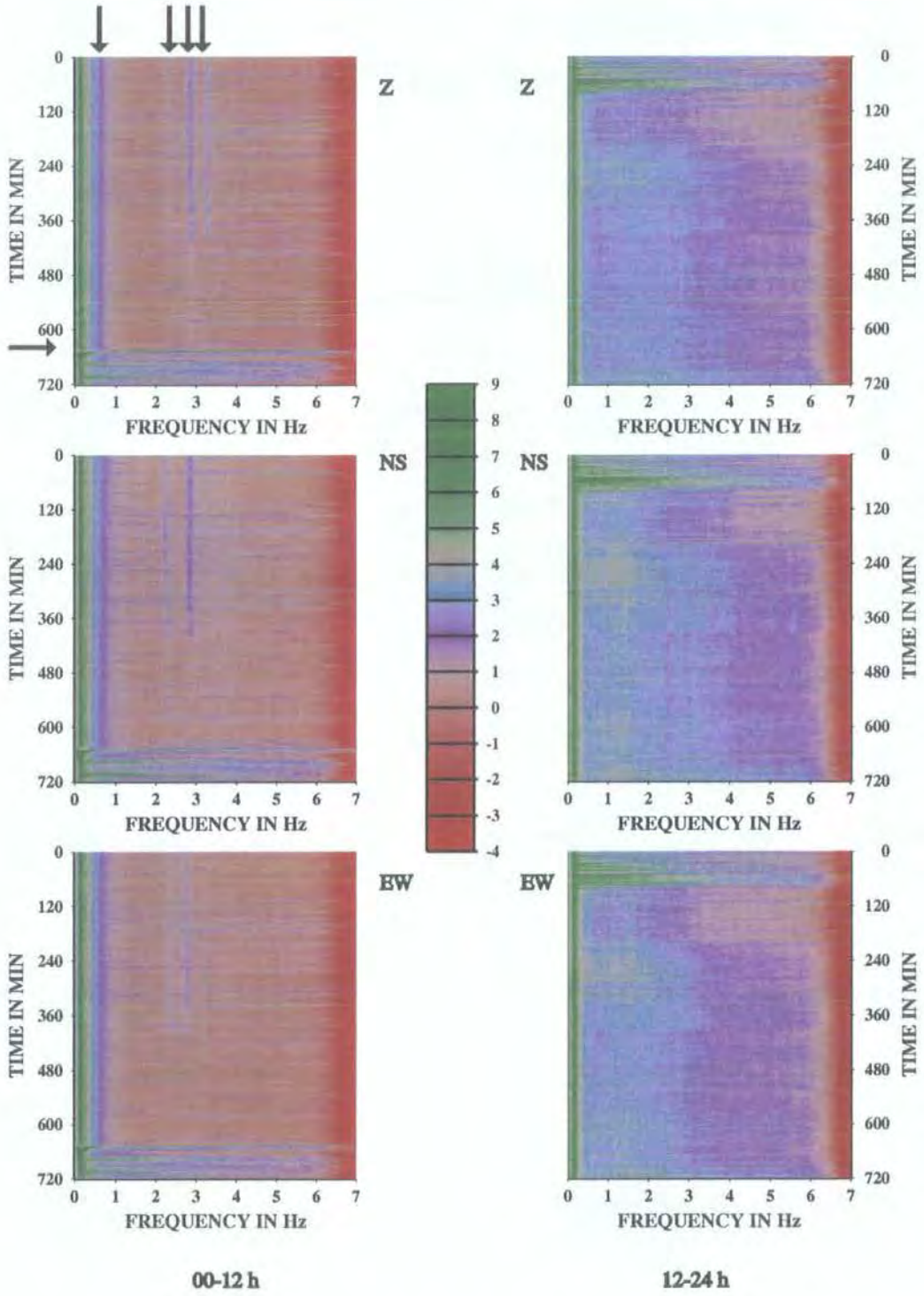


Figure 4.6: Same as in Fig. 4.5 for September 29. The horizontal arrow shows the onset of the large event at Bárdarbunga and the swarm that followed it. Note the appearance of the broadband signal after the occurrence of the swarm.

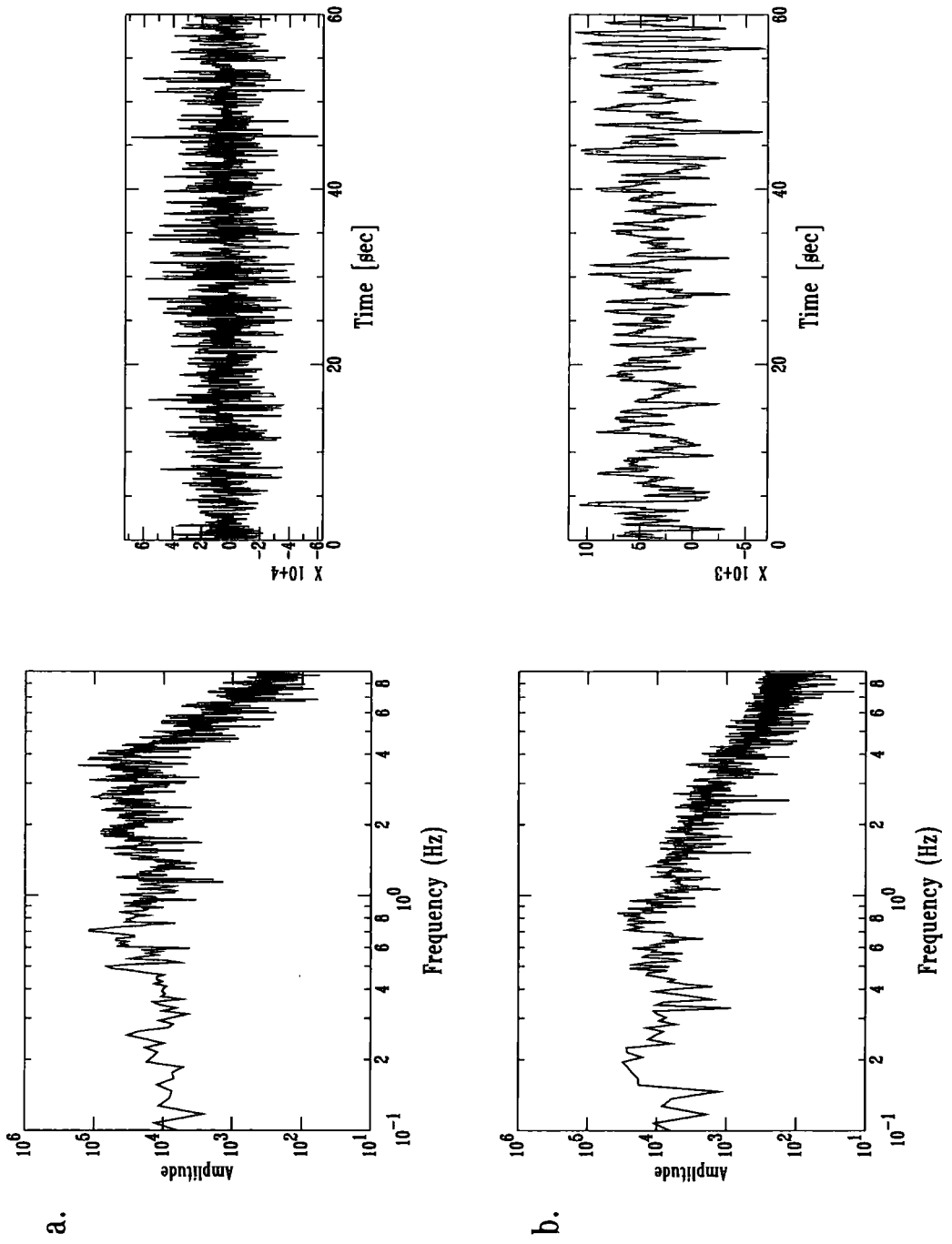


Figure 4.7: $Log_{10}$-$Log_{10}$ graphs of the amplitude spectrum and corresponding vertical component velocity waveforms for one minute of (a) a high-amplitude burst, and (b) low-amplitude background tremor exhibiting different rates of decay at high frequencies, as well as different frequency contents.

## 4.4 Volcanic tremor and nonlinear dynamics

Most tremor source models that have been previously proposed (cf. section 3.5) assume either explicitly or implicitly that the oscillating body (conduit, crack or pipe) behaves as a linear oscillator that may be set into resonance as a result of a sustained disturbance. Observations suggest, however, that tremor source processes exhibit more complexity than any linear model can account for. Fukao *et al.* (1998) reported the occurrence of damped oscillations in volumetric strain records shortly before and after the 1986 Izu-Oshima volcano eruption, Japan, which were followed by volcanic tremor episodes. These oscillations had some unusual characteristics, such as a low frequency content of either 20 or 40 mHz, and dramatic changes in the polarity of the initial motion. Fukao *et al.* (1998) attributed this behaviour to an episodic supply of magma to the conduit and its subsequent drainage back into the reservoir. Fukao *et al.* (1998) also noted that if this disturbance is causing the excitation of tremor, then the input forcing frequency they observed is abnormally low in comparison to the resulting high frequency (1-10 Hz) tremor signal. These observations are in agreement with theoretical principles stating that the frequency output of a linear oscillator cannot contain frequencies that were not present in its input; thus a nonlinear process of some kind is essential to the ability of a system to generate tremor (Julian, 1994).

Nonlinear oscillations are usually described by ordinary or partial differential equations, which are much more difficult to analyse mathematically than their linear counterparts. One difficulty is that it is impossible to solve such equations analytically so one must rely heavily on numerical integration and graphical methods of solution representation in order to have a qualitative view of their behaviour. One such graphical method uses as coordinates the solution $x$ and its time derivatives that appear in the equation ($\dot{x}$, $\ddot{x}$...$x^{(n)}$) forming an $n+1$ dimensional space that is called the phase or state space (Jordan & Smith, 1987). The behaviour of the solutions will depend on the initial conditions chosen and on the values of the free parameters present in the equations. Possible drifting in the values of these param-

eters will cause a change in the qualitative character of the solutions, a phenomenon which is defined as bifurcation (Drazin, 1994). After some parameter has reached a critical value, due to a series of repeated bifurcations, the solution will move to an aperiodic and almost random-looking regime, which Li & York (1975) called chaos.

Lorenz (1963) first demonstrated the existence of chaotic solutions by solving numerically a set of three coupled nonlinear differential equations, that represented a simplified version of the Navier-Stokes equations in fluid dynamics. Lorenz (1963) also showed, by plotting the solutions in the phase space, that the orbits were attracted to a specific region and were unable to escape from it. The geometrical object that was formed in the phase space, had a fractal structure and a non-integer dimension, therefore, it was later called a 'strange' attractor (Ruelle & Takens, 1971). Since Lorenz's discovery, systems governed by nonlinear differential equations that may have chaotic solutions, were found to exist in almost every scientific discipline. Geophysical examples of such systems include the vertical ground movements in the Campi Flegrei caldera (Cortini *et al.*, 1991), rays that propagate through strongly laterally varying media (Keers *et al.*, 1997) and variations in the period of rotation of the earth (Frede & Mazzega, 1999).

Time series generated by nonlinear processes usually have two distinct spectral characteristics: (a) they are broadband as a result of the repeated bifurcations that have taken place (thus looking similar to white noise); and (b) their spectrum exhibits exponential decay at high frequencies, which is being used as a criterion for distinguishing low-dimensional chaos from stochastic processes (Sigeti & Horsthemke, 1987). However, when dealing with nonlinear time series spectral analysis can provide little information about the underlying physics. A much more fruitful approach for studying such signals is to reconstruct the phase space from the time series and extract useful information from the evolution of the orbits that describe the states of the system. This idea forms the basis of the disciplines of nonlinear dynamics and nonlinear time series analysis, both of which have experienced a tremendous growth over the last decade. Having observed the two spectral charac-

teristics (a)-(b) of chaotic behaviour in the Vatnajökull tremor data, the rest of this chapter describes an attempt to investigate further their phase space properties.

## 4.5 The TISEAN software package

The nonlinear time series analysis of the tremor data was conducted using the Time SEries ANalysis (TISEAN) software package (Hegger *et al.*, 1999) which is freely available on the internet from the Max Planck Institute for Physics of Complicated Systems, at http://www.mpipks-dresden.mpg.de/. TISEAN consists of a collection of 76 programs covering a wide range of applications such as spectral analysis, phase space reconstruction, nonlinear prediction, nonlinear noise reduction etc. A detailed description of the methods implemented by TISEAN can be found in Kantz & Schreiber (1996) and Abarbanel (1996).

TISEAN has no graphical interface, however, all of its programs behave by default as UNIX standard filters (i.e. taking data from standard input and writing the results to standard output), so that results may be piped to another program for further processing or to GMT programs for display purposes. One problem that has to be considered when using TISEAN programs is that they require the data to be in ASCII format. In order to avoid disk space problems the 20 min Miniseed data were converted to AH format, then to ASCII using the program *ah2asc* (provided by the IRIS-PASSCAL software library) and then piped directly to any TISEAN program, in the sequence

```
ms2ah (datafile) | ah2asc | sed 1,79d | (TISEAN routine)
```

with the `sed` line editor being called to remove the trace header from the beginning of the file.

## 4.6 Reconstruction of the phase space

The problem of reconstruction of the phase space from a scalar time series (such as a seismogram) is of great practical importance, since it is the starting point of all nonlinear time series analysis methods. Any time series resulting from a nonlinear process can be considered as the projection on the real axis of a higher dimensional geometrical object, which describes the behaviour of the system under study (Kantz & Schreiber, 1996). Takens (1981), and later Sauer *et al.* (1991), showed that it is possible to recover this object from a series of scalar measurements $s(t)$ in an $m$-dimensional Euclidean space by using points $\mathbf{y}$ with coordinates

$$\mathbf{y} = s(t), s(t+\tau), ..., s(t+(m-1)\tau) \tag{4.1}$$

where $\tau$ is called the delay time and for a digitised time series is a multiple of the sampling interval used. The dimension $m$ of the reconstructed space is considered as the sufficient dimension for recovering the object without distorting any of its topological properties, thus it may be smaller than the true dimension of the space where this object lies. This procedure of phase space reconstruction is termed as embedding and Takens' formulation is called the delay embedding theorem, with $m$ being the embedding dimension. In practical applications both the delay time and the embedding dimension have to be determined from the time series itself.

In the case of the tremor signals that were recorded during the 1996 Vatnajökull eruption, a selection of suitable data for the reconstruction of the phase space had to be made. The main criterion for suitability concerns the amount of contamination of the data with oceanic microseismic (or possibly other) noise. Earlier studies have revealed that filtering the data in order to remove the noisy part of the signal may result in a change in the original number of degrees of freedom (therefore of the embedding dimension) of the system (Brandstätter & Swinney, 1987; Abarbanel *et al.*, 1993). In this study only vertical component data, recorded during the first two days of the eruption (October 1st-2nd) are considered, where tremor could be

clearly seen with a high signal-to-noise ratio.

### *4.6.1 Selection of the delay time*

One proposed way of choosing the delay time $\tau$ for phase space reconstruction is by calculating the autocorrelation function of the data and choosing $\tau$ as the time of the first zero crossing (e.g. Kantz & Schreiber, 1996). A characteristic of chaotic time series is that their autocorrelation functions drop to zero very quickly, reflecting the fact that the past states of the system decorrelate exponentially from the future ones. By calculating the autocorrelation function of the tremor data for a timelag spanning 0-100 it was found that in most cases the first zero crossing was reached very quickly at a delay time of 3-4 (Fig. 4.8a and b).

An objection to the selection of the delay time in this way is that the autocorrelation function only takes into account linear correlations of the data (Abarbanel, 1996). Fraser & Swinney (1986) proposed a kind of nonlinear autocorrelation function for time delay selection, which they called Average Mutual Information (AMI) defined as

$$I(\tau) = \sum_{ij} p_{ij}(\tau) \ln p_{ij}(\tau) - 2 \sum_{i} p_i(\tau) \tag{4.2}$$

where $p_i$ is the probability that the signal $s(t)$ assumes a value inside the $i$th bin of a histogram, while $p_{ij}$ is the probability that $s(t)$ is in bin $i$ and $s(t+\tau)$ is in bin $j$. When $\tau$ becomes large, then $s(t+\tau)$ conveys no information about $s(t)$ and $p_{ij}$ factorises to $p_i p_j$ yielding $\mathrm{I}(\tau) = 0$. Based on the fact that the first minimum of AMI marks the delay time where $s(t+\tau)$ adds maximum information to the knowledge we have from $s(t)$ (or where the redundancy is the least), this time is considered as the best choice of $\tau$.

The TISEAN program *mutual* calculates the AMI for the data for a range of delay times specified by the user, and its output consists of a two column ASCII list, with

the first column being $\tau$ and the second the value of the AMI. AMI was calculated for the data for timelags 0-100 and for time windows of 5, 10, 20 min having very small variation and showing no minimum in each case (Fig. 4.8c and d). An absence of a minimum from the AMI graph usually indicates that the data have not been sufficiently sampled (Abarbanel, 1996). Two-dimensional phase portraits of the tremor attractor reconstructed for different delay times (Fig. 4.9) seem to support this possibility, since the attractor assumes a fuzzy appearance at delay times larger than 2. Combining the results from the two methods of delay time selection, it is concluded that the best choice is $\tau = 1$. A consequence of undersampling is that it precludes application to the data of any method for the calculation of fractal dimensions, which require well resolved phase space orbits in order to give reliable results.

### *4.6.2 Selection of the embedding dimension*

#### *4.6.2.1 The false nearest neighbours method*

The selection of the sufficient dimension that should be used for the embedding relies on the principle that orbits of attractors describing non-periodic signals should not intersect. Any intersection means that the orbit is revisiting exactly the same parts of the phase space, which implies periodic rather than chaotic behaviour. This kind of intersection or overlap between orbits results when the attractor is embedded in a dimension lower than the sufficient one stated by the embedding theorem. If two points $\mathbf{y}^a$ and $\mathbf{y}^b$ are close in the same neighbourhood in the phase space, this is so either because the dynamic evolution of the orbits brought them close or because of an overlap resulting from the projection of the attractor to a lower dimension. In order to decide which of the two possibilities is true, a comparison should be made of the Euclidean distance of the two points $|\mathbf{y}^a - \mathbf{y}^b|$ in two consecutive embedding dimensions $d$ and $d+1$. For an embedding dimension $m$ and delay time $\tau$ these distances are given by (Kennel *et al.*, 1992)

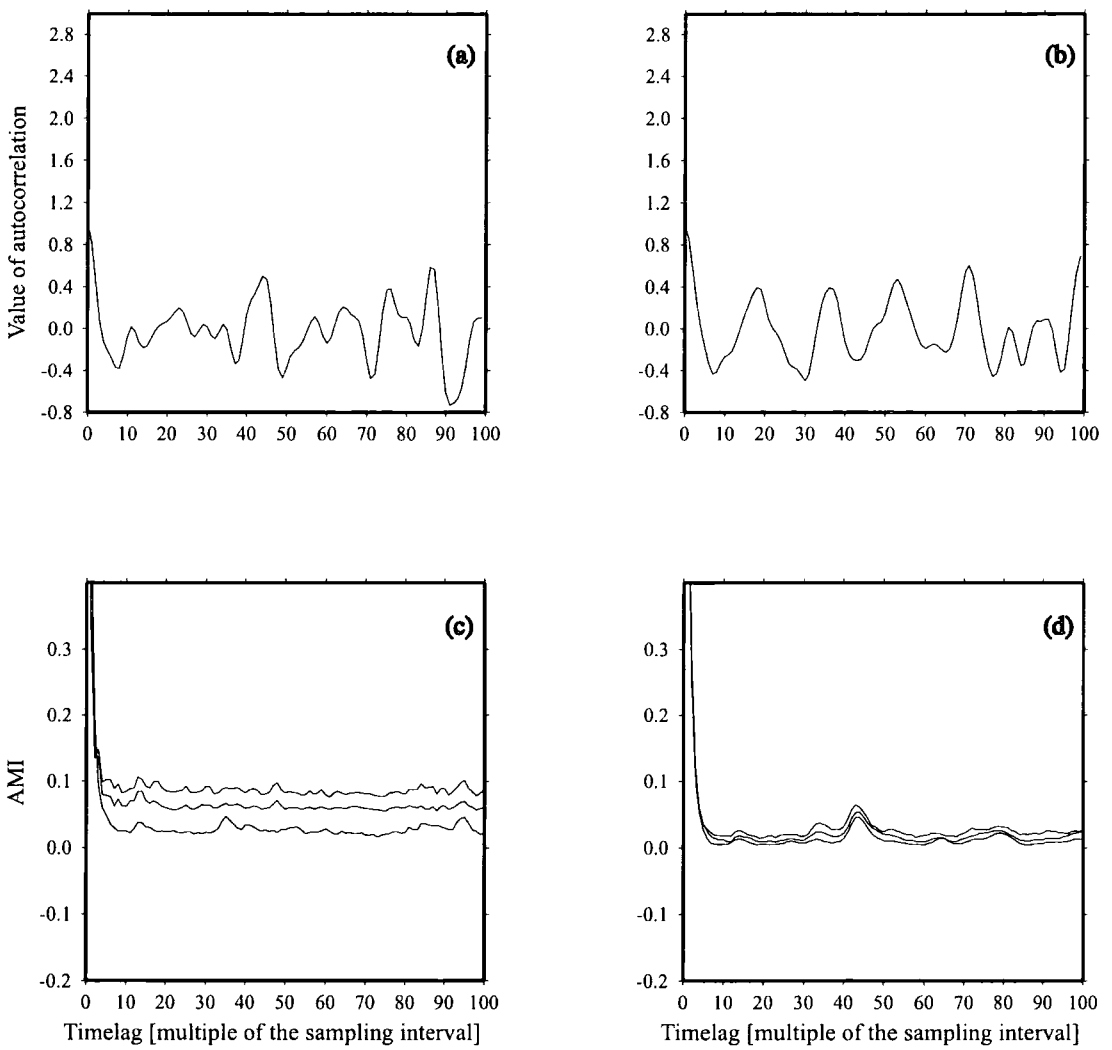


Figure 4.8: Top panel: Autocorrelation function calculated for a 5 s window of (a) high-amplitude burst and (b) continuous tremor. Lower panel: Average mutual information calculated for delay times 1-100 using 5, 10 and 20 min of data for (c) a data segment that contains a high-amplitude burst and (d) continuous tremor.

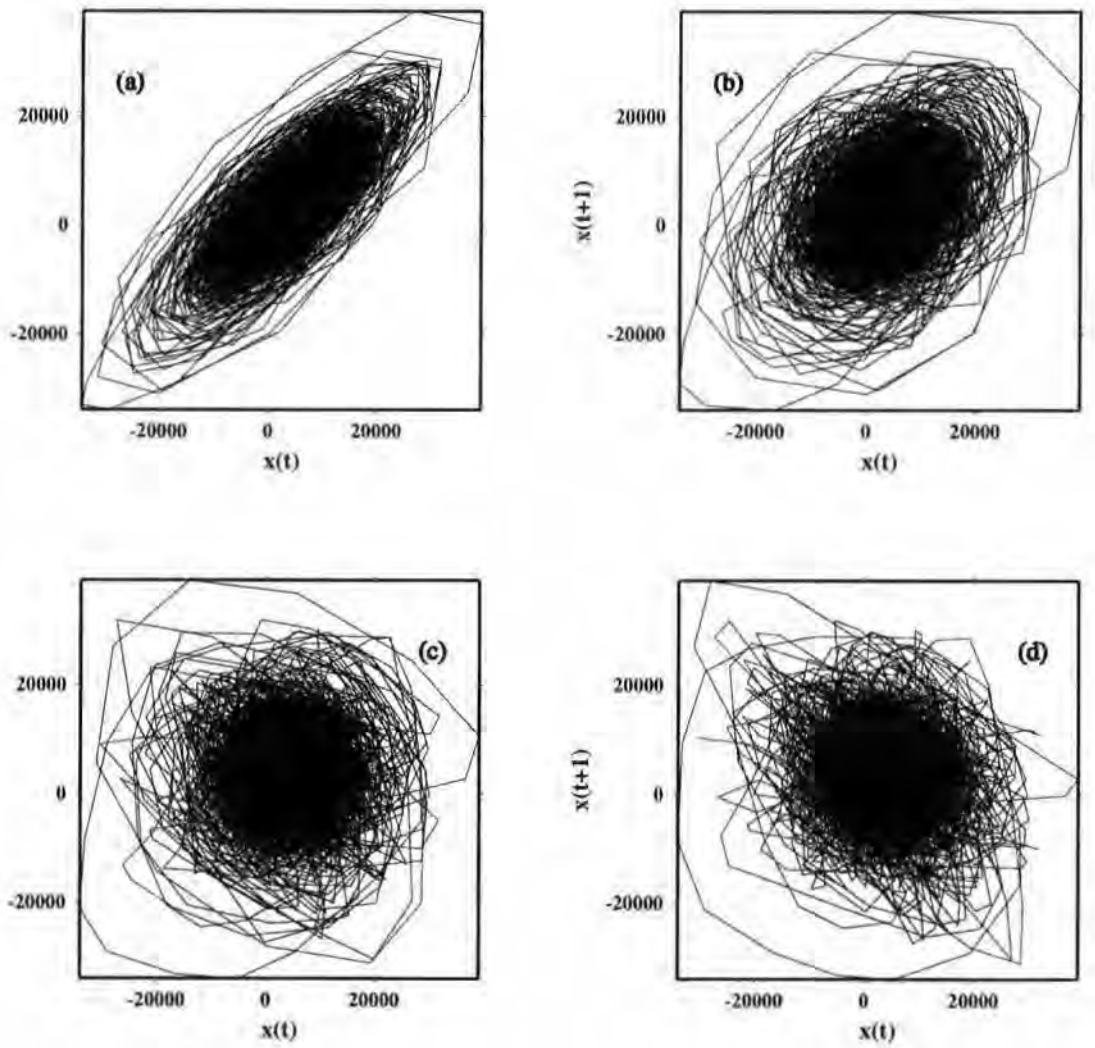


Figure 4.9: Two-dimensional phase portraits of the tremor attractor, reconstructed using 20 min of data (24,000 samples) and delay time (a) $\tau = 1$, (b) $\tau = 2$, (c) $\tau = 3$ and (d) $\tau = 4$.

$$R_d^2 = \sum_{m=0}^{d-1} [s^a(t + m\tau) - s^b(t + m\tau)]^2 \tag{4.3}$$

Moving from dimension $d$ to $d + 1$ means that a new coordinate is being added in each delay vector, which is equal to $s(t + d\tau)$. The Euclidean distance of the two points in dimension $d + 1$ will thus be

$$R_{d+1}^2 = R_d^2(t) + |s^a(t + d\tau) - s^b(t + d\tau)|^2 \tag{4.4}$$

The relative distance between the two points in dimensions $d$ and $d + 1$ will then be the ratio

$$\sqrt{\frac{R_{d+1}^2 - R_d^2}{R_d^2}} = \frac{|s^a(t + d\tau) - s^b(t + d\tau)|}{R_d} \tag{4.5}$$

If this distance ratio is larger than a predefined value, say $v$, then the points $\mathbf{y}^a$ and $\mathbf{y}^b$ are characterised as 'false' neighbours, being in the same neighbourhood because of the projection and not because of the dynamics. The procedure is repeated for all pairs of points at higher dimensions until the percentage of the false neighbours becomes zero and then the attractor is said to be unfolded. For limited datasets, Kennel *et al.* (1992) found it necessary to add a second criterion for characterising two points as false neighbours, which is

$$R_{d+1} > \frac{rms}{v} \tag{4.6}$$

where $rms$ is the standard deviation of the data around its mean. Taking $rms$ as a representative measure of size of the attractor, this criterion reflects the fact that if two points are false neighbours, they will be stretched to the extremities of the attractor when they get unfolded from each other at dimension $d + 1$. The authors also noted that a false nearest neighbours algorithm that does not implement this criterion will give an erroneously low embedding dimension even for high-dimensional

stochastic processses.

### *4.6.2.2 Application to the tremor data*

Naturally, two important issues that have to be addressed concern the length of the analysis window that should be used and the selection of a suitable value for $v$. The analysis window length is usually chosen in such a way that the points resulting from the embedding, populate the attractor as densely as possible. However, the long duration of the tremor data poses a trade-off between large windows, that would also include more noise (and need extra computer time for each analysis) and smaller windows that may give biased false neighbours statistics. Since the time series length used in similar studies was usually in the range of 10,000-32,000 samples (e.g. Brandstätter & Swinney, 1987; Frede & Mazzega, 1999) the analysis of the tremor data was conducted using segments with a duration of 20 min (24,000 samples).

The program *false_nearest* uses the two criteria suggested by Kennel *et al.* (1992) in order to calculate the percentage of false neighbours in a range of dimensions specified by the user. The output of the program is a two column ASCII file, where the first column represents the embedding dimension and the second the corresponding fraction of false neighbours found. Using the C-shell script *calc_distrat_dis* it was possible to calculate the fraction of false neighbours in dimensions 1-10, changing the value of $v$ in the range of 1-20 in every run. The output represents the triplet of values (embedding dimension, $v$, fraction of false neighbours) and was converted to a GMT gridfile using the program *xyz2grd*. Most of the data show a zero percent of false neighbours at either dimension 7 or 8 for $v$ = 9-17 (Fig. 4.10) which agrees with the results of Abarbanel (1996) who found that a suitable value for $v$ (for most nonlinear systems) is around 15. Knowing the exact embedding dimension $m$ of the tremor attractor makes it possible to estimate the upper bounds of its fractal dimension $D_F$, since according to the embedding theorem $m > 2D_F$, thus in this case the upper values of $D_F$ are between 3.5-4.0.

The percentage of false neighbours did not drop to zero for a number of time segments that were recorded in the early hours of October 1st (01:48-07:10 GMT) implying the presence of random noise in the data (Fig. 4.11). As a stochastic process, noise should have infinite degrees of freedom, showing no tendency to unfold at any specific dimension. Nonlinear deterministic signals that are contaminated by noise usually show a non-zero percentage of false neighbours even at high dimensions. This effect can be easily demonstrated by adding different amounts of random noise to a data segment that otherwise has a zero percent of false neighbours at dimension 8 (Fig. 4.12). A possible explanation for the presence of a random noise source in that time interval is the interaction of rising magma with ice and the subsequent flash boiling that took place. The fact that this noise source disappears later may be attributed to two factors: first, the ice melting and boiling process has moved from the rock-ice interface upwards entirely into the ice cap and second, the flanks of magma-ice interface should have cooled rapidly and solidified as pyroclastic glass having a temperature of 0° C (Gudmundsson *et al.*, 1997) precluding any further boiling. Taking into account that the sensor at station HOT23 was installed on a rock outcrop and not on ice makes this explanation quite plausible.

## 4.7 Temporal variations of phase space dynamics

### *4.7.1 The cross-prediction method*

Changes in the dynamics of the orbits in the phase space usually represent variations of the physical parameters that control a nonlinear system and consequently are of great importance for any modelling effort. Since in most cases the only available data is a time series, monitoring the temporal changes in the dynamics is the most appropriate way of detecting different dynamical regimes in a signal. One method to do this is to divide the time series into segments and calculate for each segment a quantity (e.g. the fractal dimension) relevant to the dynamics, mapping in effect its variation as time elapses. Two problems regarding this approach are: (a) the choice of an appropriate quantity, bearing in mind that a reliable estimation

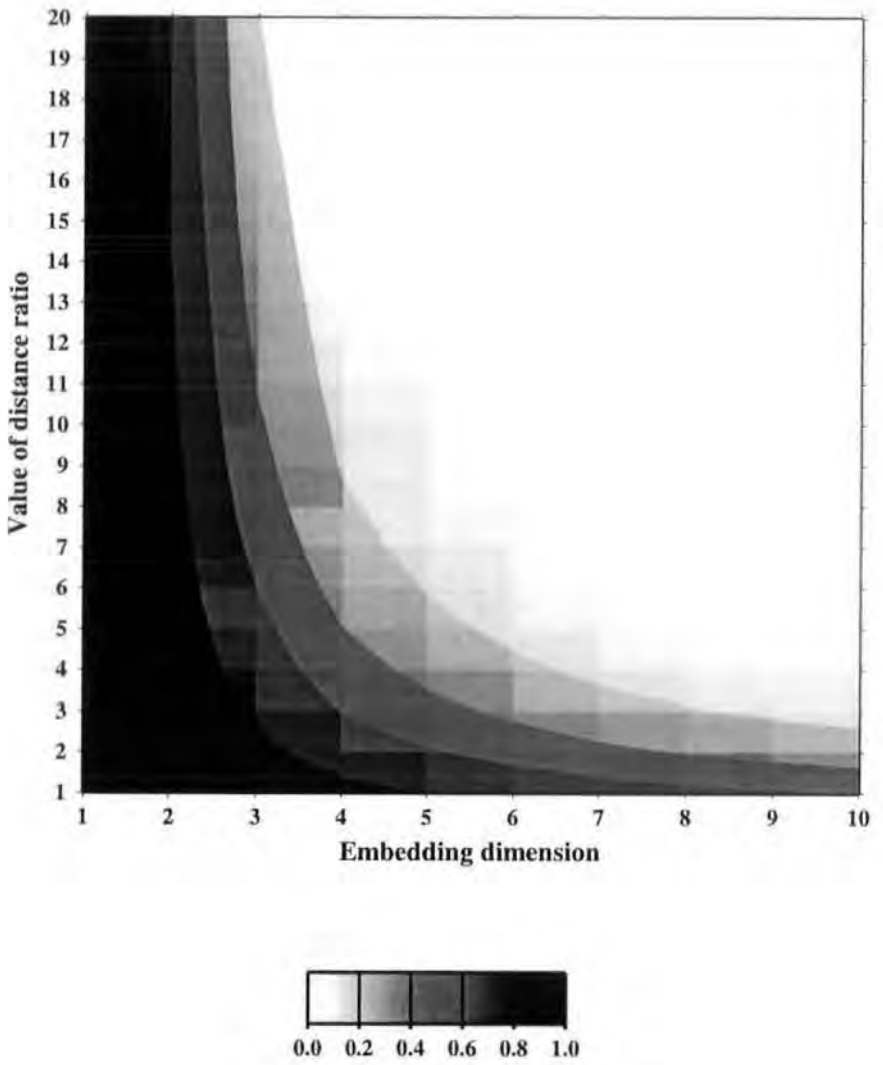


Figure 4.10: Diagram showing the variation of the fraction of false neighbours (grey scale) as a function of the value of distance ratio $v$ and the embedding dimension (see text for details).

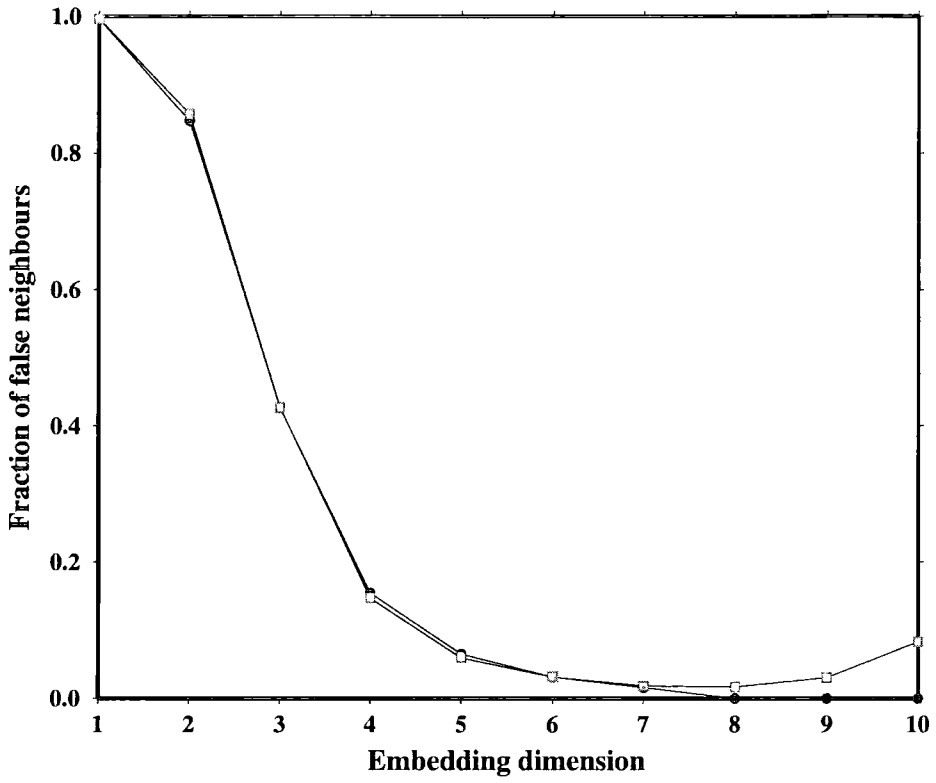


Figure 4.11: Distribution of the fraction of false nearest neighbours calculated for a data segment recorded on October 1st at 00:28 GMT (black circles) and at 05:08 GMT on the same day (grey squares) for $v = 10$, showing a non-zero percentage of false neighbours in dimensions 1-10.

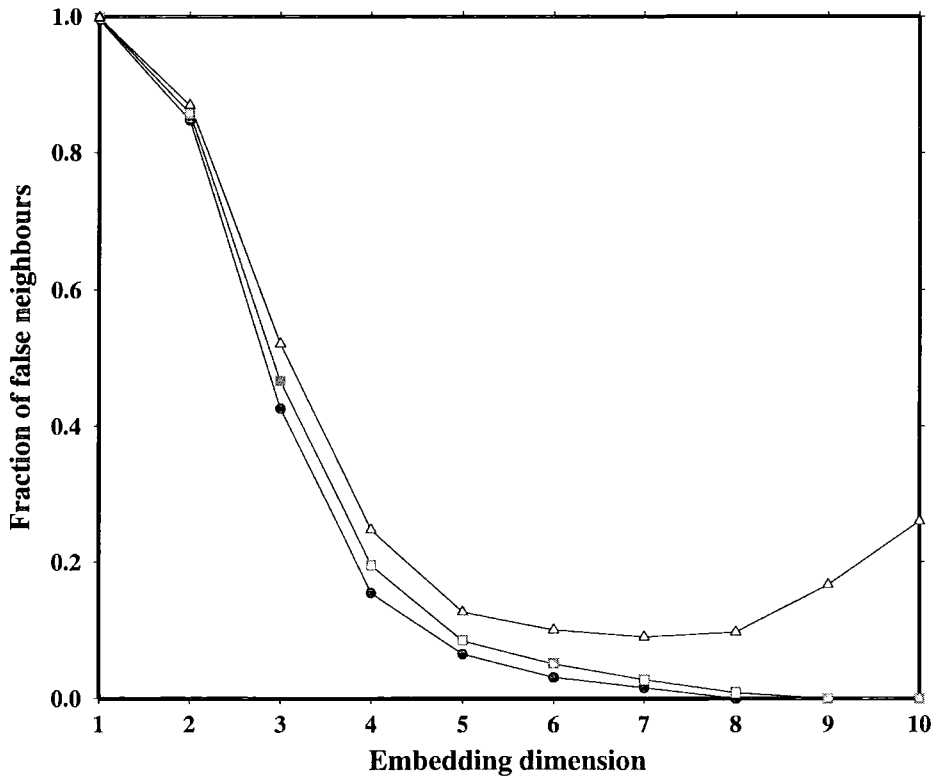


Figure 4.12: The effect of different amounts of random noise on the false nearest neighbours statistics for $v = 10$. Black circles indicate the original data, grey squares and white triangles indicate the same data with the addition of 5% and 10% of random noise respectively.

of fractal dimensions needs very well resolved orbits and noise levels lower than 2% (Kantz & Schreiber, 1996); and (b) how measurements from different segments can be directly compared instead of just estimating their statistical properties.

Schreiber (1997) proposed a method that utilises the direct comparison of prediction errors between different parts of a given time series. Based on the assumption that the signal is a deterministic one, then after reconstructing the phase space using delay vectors $\mathbf{y}_1, \mathbf{y}_2, ..., \mathbf{y}_N$ the dynamics may be approximated by the difference equation $\mathbf{y}_{n+1} = \mathbf{F}(\mathbf{y}_n)$. Knowing the present state of the system $\mathbf{y}_n$ it is possible to predict one step into the future $\mathbf{y}_{n+1}$ in the following way: since the function $\mathbf{F}$ describing the evolution of the dynamics is continuous, a past state $\mathbf{y}_{n'}$ very close to the present one is taken and its image $\mathbf{y}_{n'+1}$ is used as the predicted future value. However, when using such a prediction scheme two issues should be taken into account: (a) predictions will become exponentially inaccurate as one tries to predict more than one step into the future; and (b) since all interpoint distances are contaminated with an uncertainty due to the finite resolution of the data, all points closer than a distance $\epsilon$ are equally good for predicting $\mathbf{y}_{n+1}$. By forming a neighbourhood $\mathcal{U}_{(y_{n'})}$ of radius $\epsilon$ around $\mathbf{y}_n$, the final predicted value $\hat{\mathbf{y}}_{n+1}$ will be the arithmetic mean of all the images $\mathbf{y}_{n'+1}$

$$\hat{\mathbf{y}}_{n+1} = \frac{1}{|\mathcal{U}_{(y_{n'})}|} \sum \mathbf{y}_{n'+1} \tag{4.7}$$

where $|\mathcal{U}_{(y_{n'})}|$ is the number of points in neighbourhood $\mathcal{U}_{(y_{n'})}$. This method of prediction was first suggested by Lorenz (1969) and was later used by Kennel & Isabelle (1992) for detecting deterministic structure in real datasets.

In order to compare the prediction errors of different parts of a time series, it is split into a number of non-overlapping segments of equal length. If the prediction is performed inside the segment $i$, then the resulting predicted value will be $\hat{\mathbf{y}}^i_{n+1}$. Instead of comparing it with the actual value $\mathbf{y}_{n+1}$ in that segment, it is compared with its equivalent in segment $j$, and define the root mean squared prediction error

$\gamma(i,j)$ as (Schreiber, 1997)

$$\gamma(i,j) = \sqrt{\frac{1}{N}\sum_{n=0}^{N-1}(\hat{\mathbf{y}}_{n+1}^{i} - \mathbf{y}_{n+1}^{j})^2} \tag{4.8}$$

where $N$ is the total number of points in each segment. The distribution of the rms prediction error in the $i,j$ plane will then indicate which segments have similar dynamics and thus predict each other well by yielding a minimum error.

### *4.7.2 Application to the tremor data*

The cross-prediction method described above was applied to the tremor data in order to investigate the possibility of temporal variations of phase space dynamics. An analysis window of 20 min was again chosen, with a length for each segment of 1 min (1,200 samples). In practice the selection of the segment length should be determined in such a way so that enough points will be available for a reliable estimate of $\gamma(i,j)$ without making the segments unnecessarily long, which may result in degrading the time resolution of the prediction error distribution. The initial neighbourhood size $\epsilon$ was taken as the variance of the samples in the analysis window divided by 1000 and a minimum number of 30 neighbours was required in order to make each prediction. If the neighbours found were less than 30, the neighbourhood size increased by a factor of 1.2 until the minimum number was reached. The embedding parameters are as determined earlier, i.e. $\tau = 1$ and $m$ = 7-8. The program *nstat_z* takes all these parameters as command-line arguments and applies the cross-prediction method to the data. Its output is a three column ASCII list, with the first column being the index number of the segment used to do the prediction, the second the index number of the predicted segment and the third column being the corresponding rms prediction error. The output was subsequently piped to *xyz2grd* in order to create a GMT gridfile.

The analysis revealed two different patterns of the distribution of the rms pre-

diction error, each being correlated to the tremor activity seen on the seismograms. For continuous tremor recorded during the early hours of October 1st the prediction error shows an almost flat surface in the $(i, j)$ plane (Fig. 4.13a), indicating similar dynamics throughout the 20 min of the analysis window. This changes dramatically when the cigar-shaped bursts start appearing superposed on the background tremor. The prediction error surface becomes distorted and the segments that correspond to the bursts can only predict well themselves forming a minimum, giving a maximum error when they are used to predict the segments of the background tremor (Fig. 4.13b). In cases when there was more than one burst in the analysis window, it was found that the segments corresponding to the one could predict equally well the segments of the other, indicating again similarity of phase space dynamics. This result complements the observations made in the spectral analysis section (section 4.3), where the bursts exhibited a much faster decay at higher frequencies than the background tremor.

## 4.8 Comparison of results with a previous study

The only previous study that attempted to analyse volcanic tremor from Puu Oo crater, Hawaii, using nonlinear dynamics methods was published by Chouet & Shaw (1991). Having recorded the tremor activity at a rate of 200 samples $s^{-1}$ they were able to construct phase space portraits of the tremor attractor (Fig. 4.14) that have many similarities with the phase space portraits of the Vatnajökull tremor shown in Fig. 4.9. The calculation of the fractal dimension of the attractor at different stations, for sliding windows of 10 s showed that it was fluctuating in the range of 3.1-4.1 with a mean of 3.75. Due to the presence of noise superposed on the tremor signal, Chouet & Shaw (1991) considered these values to be representing the upper bounds of the attractor dimension. The fact that these values were low ($< 10$) was interpreted as an indication that the tremor dynamics 'oscillate' between a stable, quasi-periodic and a chaotic regime.

The similarities between the properties of the Vatnajökull and Hawaiian tremor

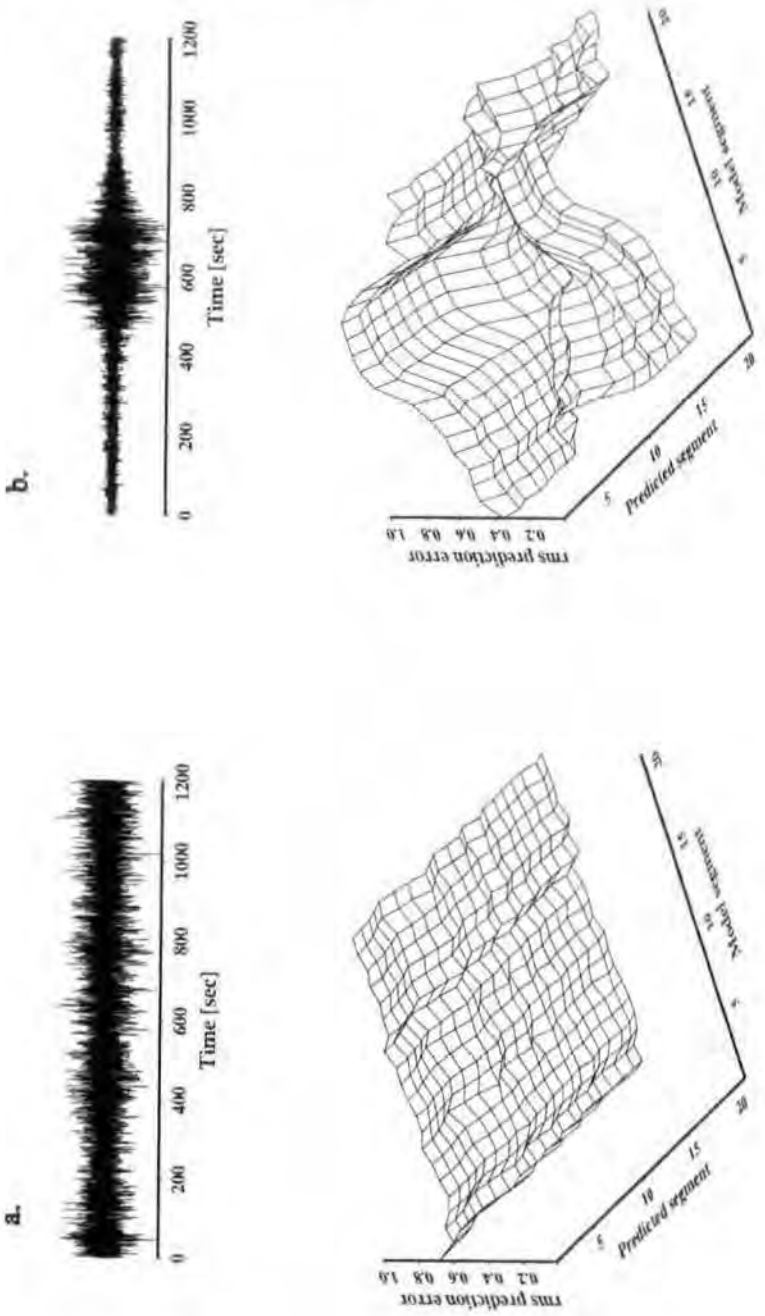


Figure 4.13: Distribution of the rms prediction error versus model and predicted data segments for (a) continuous tremor, (b) cigar-shaped bursts and low-amplitude background tremor.

as demonstrated by the attractors appearance and the upper bounds of their fractal dimensions, point to the possibility of a universal behaviour of tremor source processes. Furthermore, the conclusion of Chouet & Shaw (1991) of a tremor process that operates between two different regimes, agrees well with the results obtained by the cross-prediction method. Tremor starts in a continuous manner at the beginning of the eruption exhibiting chaotic behaviour and later evolves to a stable, quasi-periodic signal interrupted by large amplitude, chaotic bursts. A detailed discussion about the physical mechanism that might be responsible for the excitation of the Vatnajökull tremor will be presented in Chapter 6.

## 4.9 Summary

Volcanic tremor during the 1996 Vatnajökull eruption started as a continuous signal, with increasing amplitude as time elapsed, and evolved to low-amplitude background tremor interrupted by high-amplitude, cigar-shaped bursts that had an average duration of 250 s. Spectral analysis conducted for the period September 28th-October 13th shows the existence of pre-eruptive tremor (that was not visible because of the oceanic microseismic noise) during September 28th-30th, around five narrow frequency bands at 0.5-0.7, 1.6, 2.2, 2.8 and 3.2 Hz. After the earthquake swarm at Bárdarbunga tremor became broadband, but isolated peaks at the same bands were still visible in the spectrograms. The amplitude spectrum of a burst or continuous tremor was found to have a much sharper decay at high frequencies than that of the background tremor. In order to investigate the possibility that the tremor signals originated from a nonlinear source mechanism, tremor data with a high signal-to-noise ratio have been analysed using methods from the discipline of nonlinear dynamics. The phase space was reconstructed from the vertical component seismograms using the delay embedding theorem suggested by Takens (1981). A delay time of 1 was selected after examining both the autocorrelation function and the Average Mutual Information of the data. The sufficient embedding dimension for phase space reconstruction was selected by applying the false nearest neighbours

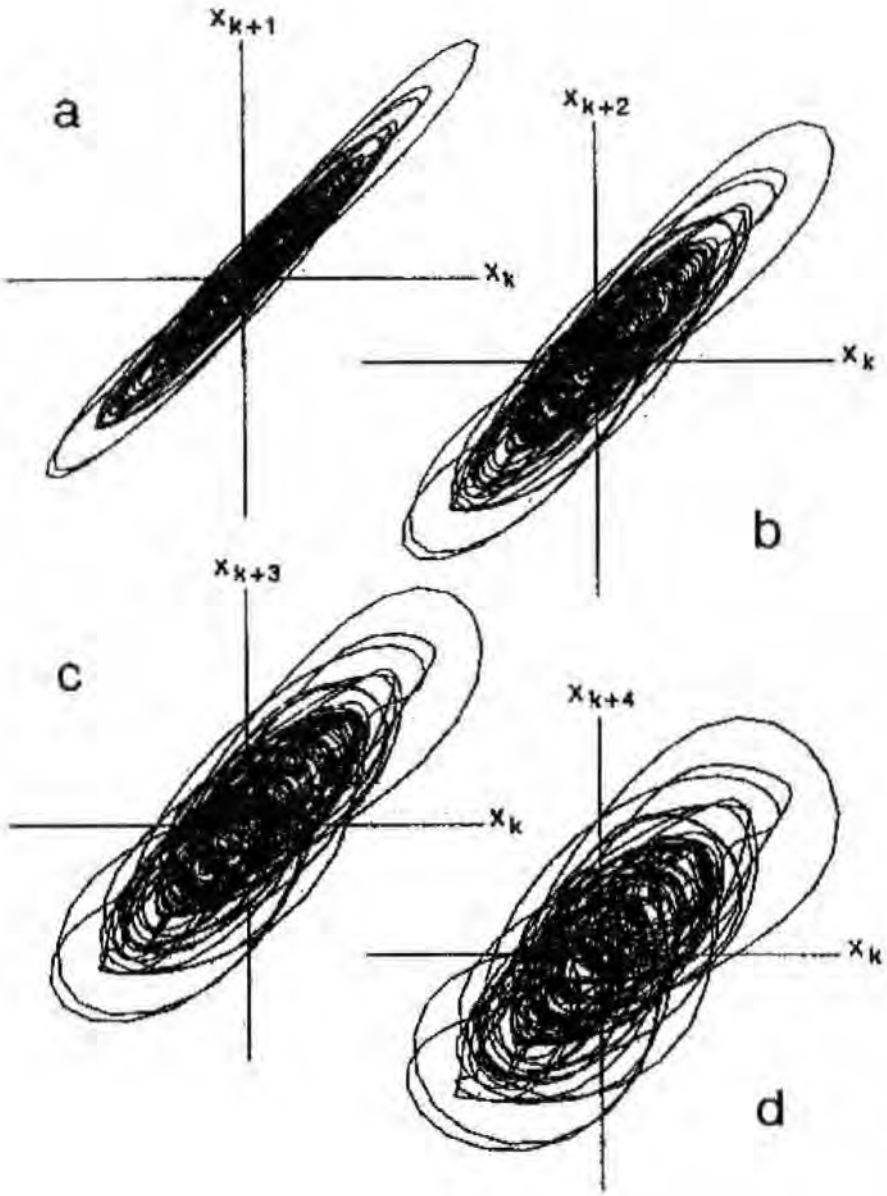


Figure 4.14: Two-dimensional phase portraits of the attractor reconstructed from tremor data recorded at Puu Oo crater, using a delay time (a) $\tau = 1$, (b) $\tau = 2$, (c) $\tau = 3$, (d) $\tau = 4$. Note how the orbits are much smoother, when compared with the orbits obtained from the Vatnajökull tremor shown in Fig. 4.8, since the data recording has been done at a 10 times faster rate (from Chouet & Shaw, 1991).

method, which revealed complete unfolding of the tremor attractor at dimensions 7-8, implying upper bounds of its fractal dimension in the range of 3.5-4.0. The prediction errors of different segments of the tremor time series were compared in order to check whether the attractor dynamics change substantially with time. It was found that, for continuous tremor, there was no dynamical variation, in contrast to the background tremor and the superposed bursts that gave a maximum prediction error when the former was used to predict the latter. These results are similar to the ones published, after analysing the phase space properties of Hawaiian tremor, by Chouet & Shaw (1991).

# Chapter 5

# Seismic imaging of the magmatic system of a slow spreading mid-ocean ridge

## 5.1 Introduction

In the summer of 1998 the research cruise RRS Discovery 235c, funded by the UK's Natural Environment Research Council (NERC), implemented the second phase of the RAMESSES (Reykjanes Axial Melt Experiment: Structural Synthesis from Electromagnetics and Seismics) experiment by shooting 34 across-axis and 5 along-axis multichannel seismic reflection profiles over the 57°45'N axial volcanic ridge (Fig. 5.1). The aim of this experiment was to obtain high-quality seismic reflection data in order to determine the shape and lateral extent of the magma body beneath this AVR. So far Lines 3 and 32 have been processed by two MSc students at the University of Durham (Farouk, 1999; Wareham, 1999), while Line 31 was processed by an undergraduate student at the University of Cambridge (Hall, 1999) as part of dissertation projects. All three lines revealed some weak reflection events that were interpreted as originating from the upper part of a thin melt lens. This chapter deals with the processing of data from Line 37 located along the AVR axis, in an attempt to image the axial magmatic system and map its extent and lateral variability.

## 5.2 Experimental configuration and cruise details

The configuration employed for the RAMESSES reflection survey consisted of a 2.4 km long multichannel streamer, with an array of 96 hydrophone groups located at 25 m intervals along the length of the streamer (Fig. 5.2). An airgun array comprising twelve airguns of varying volumes, firing every 15 seconds, was used as

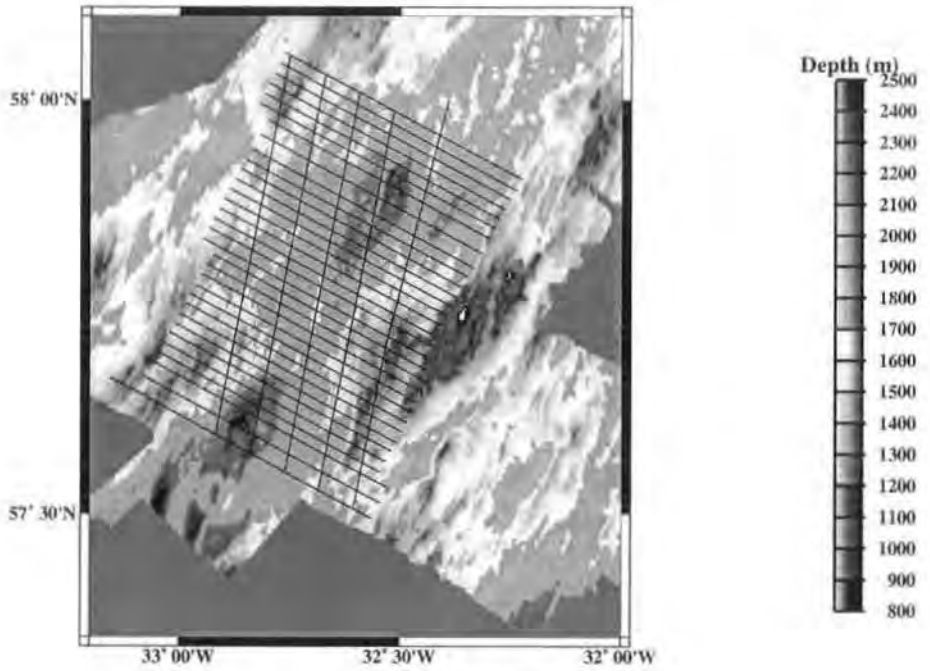


Figure 5.1: Seismic lines shot during the RAMESSES phase two experiment.

the seismic source. Optimum towing depths for the airgun array and the streamer were 8 m and 12 m respectively. An on-board GPS (Global Positioning System) receiver provided the precise location of the vessel for every shot fired.

The cruise had a total duration of 19 days and 9 hours, sailing from Southampton on Wednesday July 15th (day 196) and returning on Monday 3rd August (day 215). Of this time, 9 days and 14 hours were spent on passage to and from Southampton to the work area, while 8 days and 3 hours were spent shooting and 1 day and 16 hours were spent on instrument deployment and recovery. In addition to the multichannel reflection data, gravity, magnetic and bathymetry datasets were simultaneously acquired. Line 37 (Fig. 5.3) was shot in a southsoutheasterly direction, on Saturday

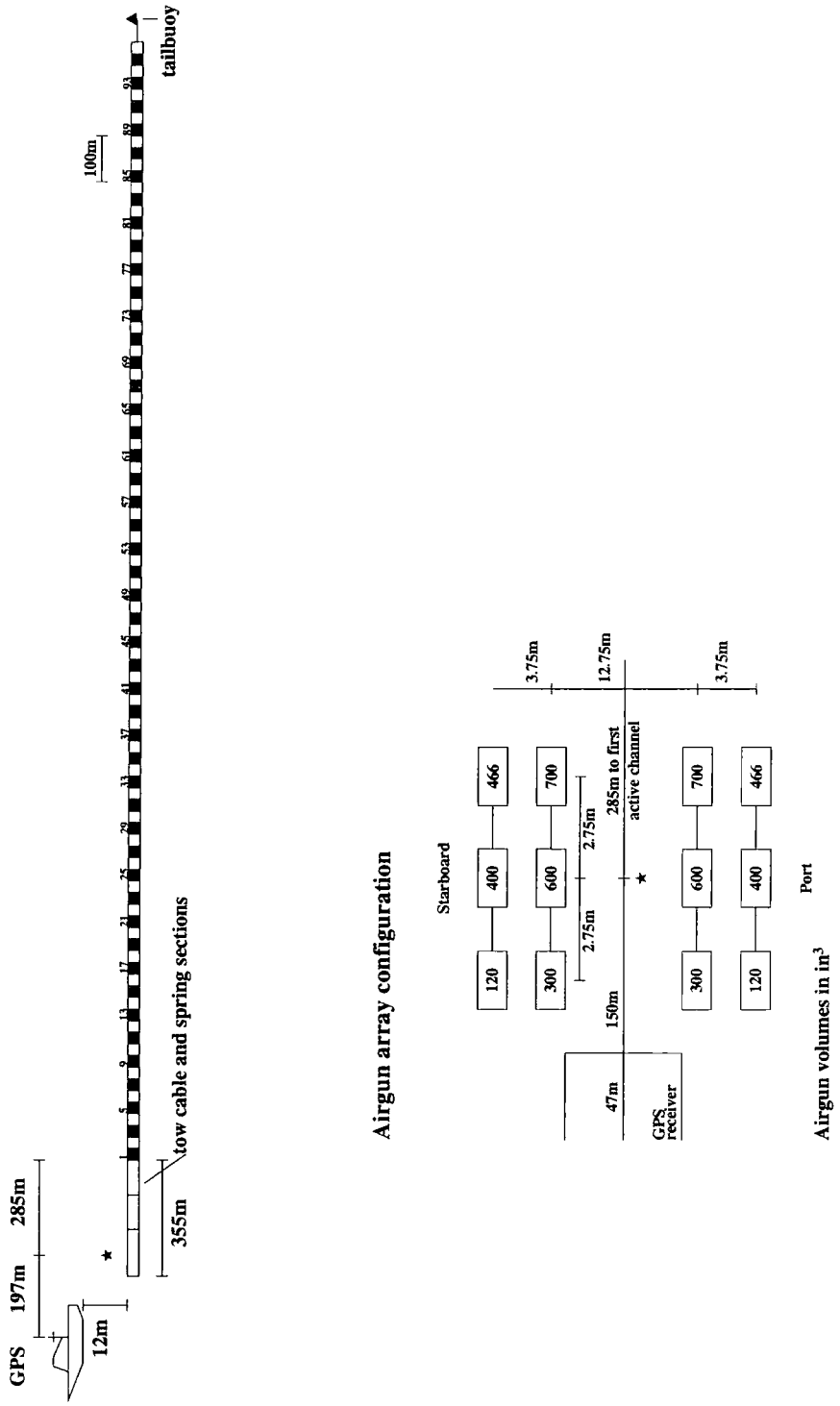


Figure 5.2: Multichannel streamer and array configuration, used during the cruise RRS Discovery 235c (from Peirce & Sinha, 1999).

July 26th (day 206) between 00:00 and 04:34 (GMT), resulting in 1277 shots being fired. The line was located between 58°01'N, 32°36'W and 57°33'N, 32°46'N. Further information and cruise details are contained in the RRS Discovery 235c cruise report (Peirce & Sinha, 1999).

## 5.3 Data processing

### *5.3.1 The ProMAX software package*

The Landmark 2-D geophysical processing software ProMAX version 1998.1, was used for processing the reflection data from Line 37. ProMAX runs in the X-windows and consists of a variety of tools that allow the user to apply a wide range of filtering, noise reduction, deconvolution and migration techniques. Each stage is performed by a set of consecutive commands that comprise a 'flow': first the raw data are input, some task(s) is(are) performed on them and the final result is output. In this way the result of one flow can be used as input to another flow for further processing. ProMAX also enables the user to compare different processing parameters on screen, as well as to make a hardcopy of the result of each flow, e.g. Versatec plots of stacked sections. A detailed description of the methods implemented by ProMAX and referred to hereafter in this chapter can be found in Hatton *et al.* (1986) and Sheriff & Geldart (1995).

### *5.3.2 Raw data input and editing*

Raw data from Line 37, in the form of shot gathers, were read from a field magnetic tape where they were stored in SEG-D format. The data were read from tape using the ProMAX tool *SEG-D input* and written to the ProMAX hard drive in demultiplexed form. A typical example of a shot gather is shown in Fig. 5.4. In total the raw data tape contained 1277 shot gathers, however, shot gathers 1-172 were excluded from any processing as they were obtained at the time when the ship

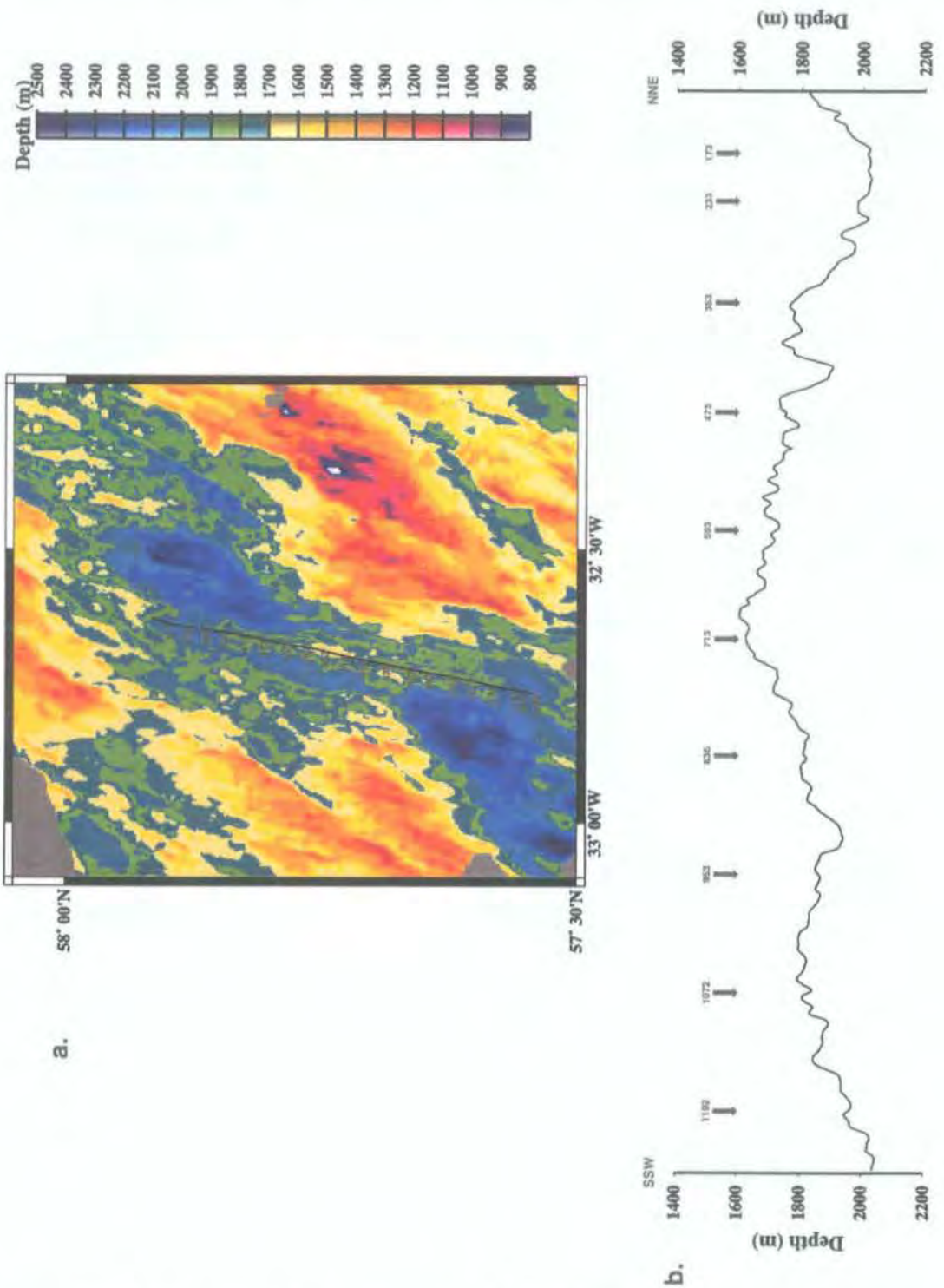


Figure 5.3: (a) Location of Line 37 within the RAMESSES study area. Every 60th shot is annotated. The colour scale indicates the seabed topography. (b) Seabed topography along Line 37. The numbers and vertical arrows indicate the positions of annotated shots fired in (a).

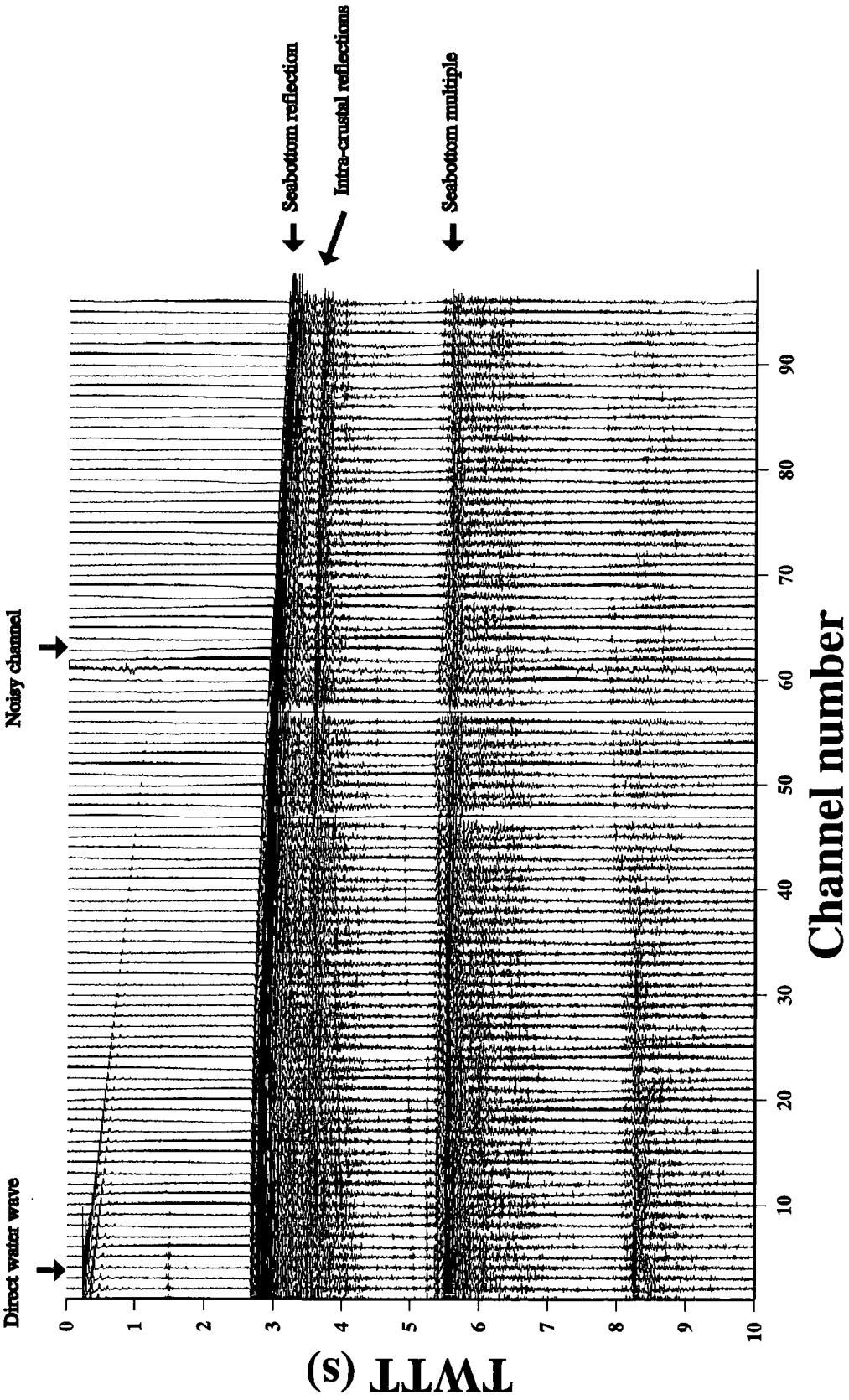


Figure 5.4: Example raw shot gather with the main arrivals annotated and highlighted by arrows.

was turning onto the line and the streamer was not linearly following the vessel.

Raw data editing consisted of the following three stages:

**Trace killing.** Shot gathers were viewed on screen, one at a time, using the *Trace Display* tool so that excessively noisy channels could be identified. Each noisy channel was specified using the picking tools of the *Trace Kill/Reverse* editor and an entry was made in a corresponding ProMAX database file. In a separate flow *Trace Kill/Reverse* takes as input the raw data and zeroes the noisy traces that are specified in the database file.

**Trace muting.** A top mute was set by interactively picking cut-off times whilst in *Trace Display* in order to zero the top part of each trace containing the direct water wave. In a similar manner a bottom mute was set in order to zero the last 3 s TWTT from each trace, since they contained only higher order sea bottom multiples. The mute time windows were written in separate database files and the tool *Trace Muting* was used in order to set traces to zero above and below the specified times.

**True Amplitude Recovery.** Spherical divergence, absorption by anelastic propagation, scattering and other transmission losses gradually reduce the amplitude of the seismic wavelet during its path in the earth. The *True Amplitude Recovery* tool was used to apply amplitude corrections for: (a) geometrical spreading, based on travel time and velocity considering that the amplitude decays inversely with distance from the shot point. The velocity function used was derived from the wide-angle model published by Navin *et al.* (1998); (b) absorption of source energy due to its conversion to heat by the anelastic movement of rock particles. An anelastic attenuation constant value of $\alpha$=5×10$^{-6}$ m$^{-1}$ was input into the *True Amplitude Recovery* editor which used the equation exp($\alpha x$), where $x$ is distance from the source; and (c) A gain of 2 dBs$^{-1}$ was chosen to account for transmission losses due to partial reflections at interfaces and scattering from small irregularities and inhomo-

geneities. All corrections were applied up to a maximum time of 5 s TWTT to avoid enhancing any noise below the area of interest. Fig. 5.5 compares a shot gather before and after the application of amplitude recovery corrections.

### *5.3.3 Geometry*

The GPS navigation system on board the RRS Discovery recorded the latitude and longitude of the ship at 10 second intervals. Also, the exact times of a number of shots were noted at regular intervals on an acquisition log. Using this information, and by interpolation, the exact location of each shot was calculated and then projected along a linear representation of the north-south profile (190° azimuth) using the GMT script *do_geom*, which converts latitude and longitude into metres offset from a specified location, e.g. the start of the line. These locations were then imported into the *SIN Ordered Parameter File* of the *2D Marine Geometry Spreadsheet.* Other parameters loaded into the spreadsheet are shown in Table 5.1. The data were then binned using the *2D Marine Geometry Spreadsheet* tool and the resulting geometry information loaded into the trace headers using the *Inline Geometry Header Load.*

**Table 5.1** Parameters used in geometry spreadsheet (see also Fig. 5.2).

| Parameter type | Value |
|---|---|
| Group interval | 25 m |
| Streamer depth | 12.5 m |
| Channel numbers | 1-96 |
| Minimum offset | 285 m |
| Number of shots | 1092 |
| X coordinate of first shot | 2660 m |

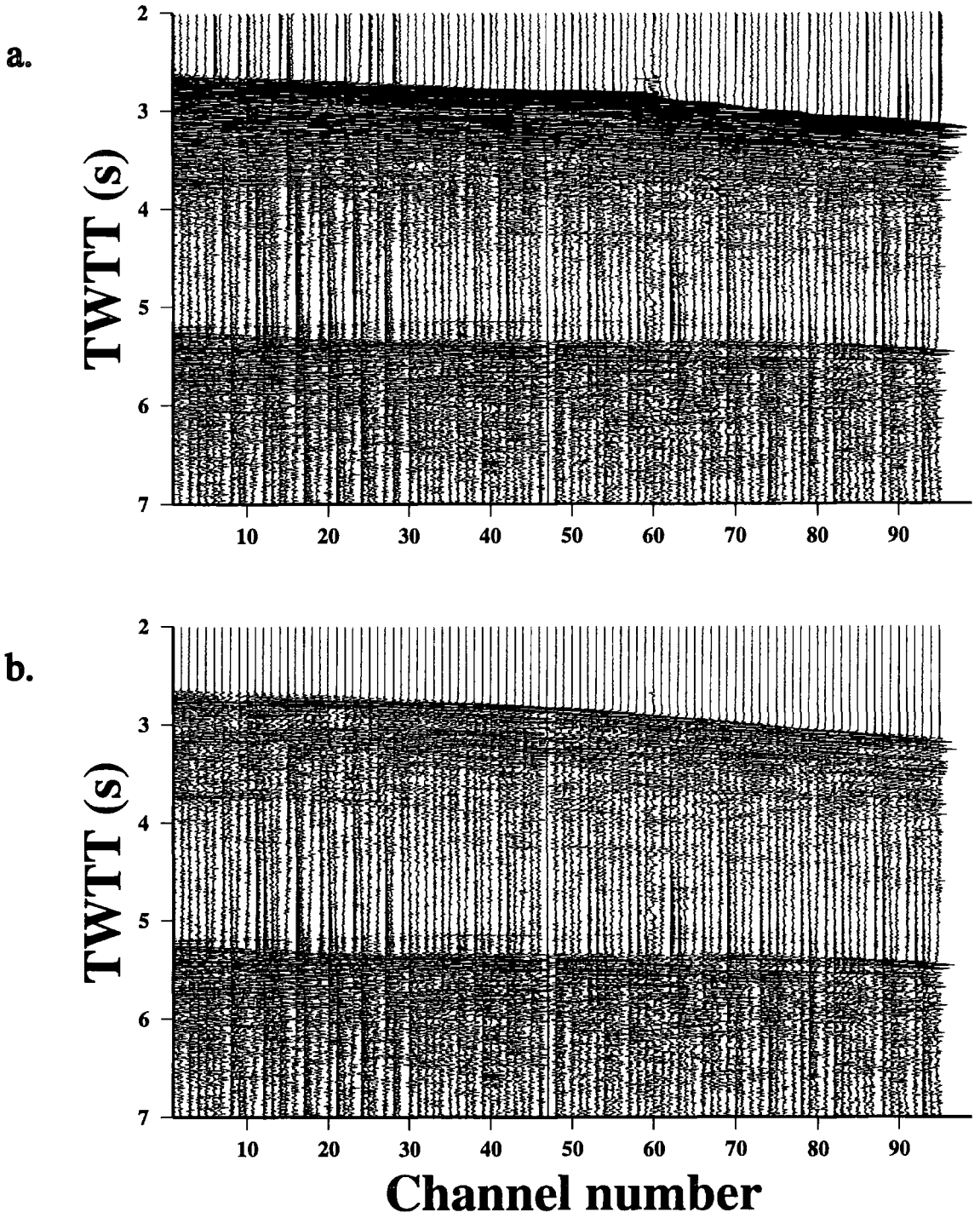


Figure 5.5: (a) Example raw shot gather with no amplitude corrections applied. (b) The same shot gather after the application of the amplitude corrections discussed in section 5.3.1.

### *5.3.4 Common mid-point (CMP) sorting*

The *Inline Sort* tool was used to change the sort order of the edited and amplitude corrected data file such that the data were transformed from common shot gathers into gathers of traces sharing common mid-points, based on their spatial locations. The maximum fold of coverage, i.e. the maximum number of traces per CMP gather is, theoretically, 32 for the acquisition geometry shown in Fig. 5.2. However, due to the fact that the ship was not moving across the ground at a constant velocity the distance between the shots was not exactly equal, resulting in a maximum number of traces per CMP gather in the range of 32-39. It should be noted that ProMAX tools use the term CDP (Common Depth Point) for such sorted gathers, which rather implies that all interfaces are expected to be planar and horizontal.

### *5.3.5 Brute stack and static corrections*

Once the data were sorted, the *Normal Moveout* tool was used to apply NMO corrections which are intended to flatten the approximately hyperbolic loci of the primary reflection events within the gathers. When the gather is summed (stacked) the primary reflections interfere constructively and multiples with residual move-out destructively. Although the signal-to-noise ratio is increased by stacking, the cancellation effect of incoherent/random noise is a maximum of $\sqrt{N}$, where N is the number of traces. Fig. 5.6 shows part of the brute stack obtained by summing over the CMP gathers using the *CDP Ensemble Stack* tool, which applied an NMO correction with a constant velocity of 1500 m $s^{-1}$. This brute stack illustrates the problems of coherent noise (dipping events, diffraction hyperbolae etc.) that are encountered in most marine, multichannel reflection datasets collected in unsedimented areas with a ragged seabed topography.

Another function of the brute stack is its use for determining static corrections, in order to account for any changes in the source and streamer depth, such that events in the CMP gathers line up in a horizontal manner. The seabed reflection is chosen

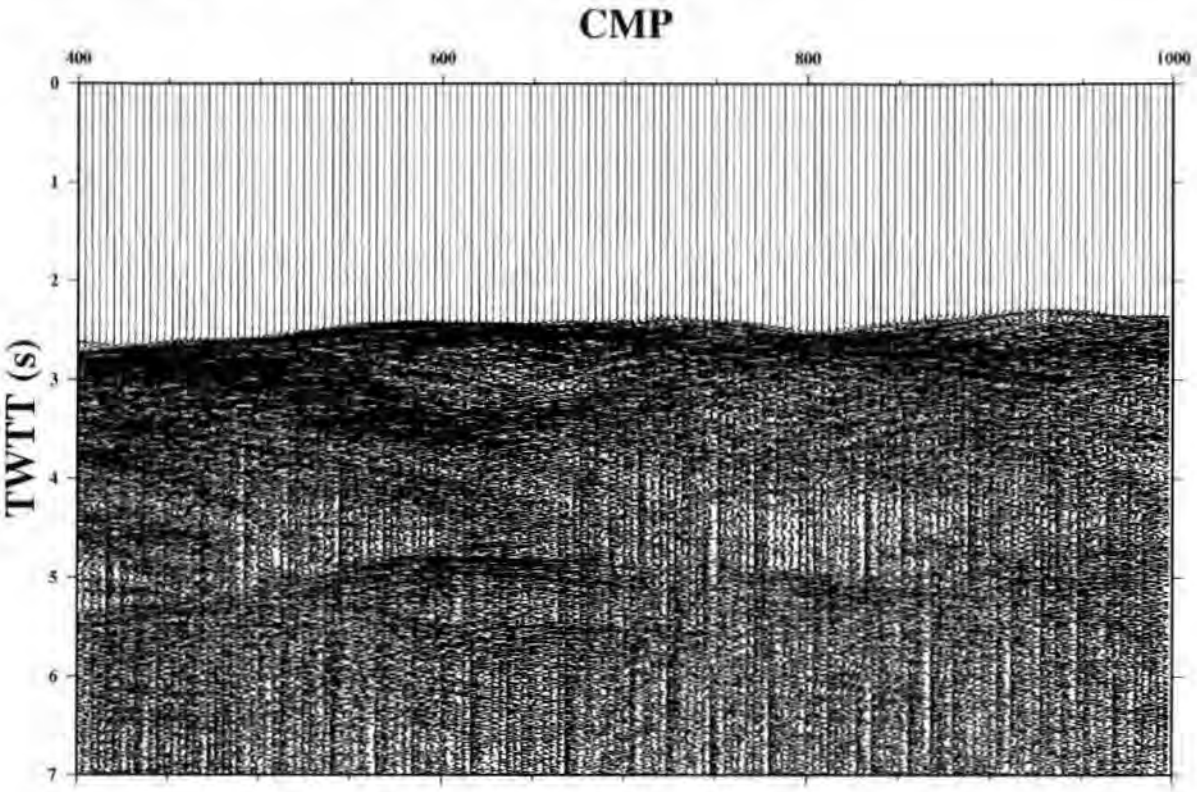


Figure 5.6: Part of the brute stack of Line 37. Note the coherent noise events throughout the section and that the sea bottom reflections do not stack well, while there is evidence of out-of-plane seabed imaging in places.

as the event to base the corrections on, because the approximately constant velocity of sea water means that the correct NMO could be applied without detailed velocity analysis. This horizon was picked interactively whilst displaying the brute stacked section and the picks were written to the ProMAX database. In all subsequent stacks (where different velocity functions were used) these seabed picks were specified as the autostatics horizon and the *Horizon Trim Statics* tool was run on the data after they had been NMO corrected. This process removed any residual moveout by lining up all the seabed reflection events within the gathers with respect to the same reflection event on the first trace of each gather.

### *5.3.6 Pre-stack deconvolution*

The earth essentially acts as a low-pass filter, absorbing the higher frequencies from the seismic signal as it passes through it. In addition, the source wavelet is altered by noise from multiples, in particular from seabed reverberations and ghost arrivals. Reflection events are, thus, less easy to identify. Therefore, deconvolution is an inverse filter designed to sharpen the recorded wavelet by removing the undesirable effects of the earth's response to the propagating seismic wave.

Statistical deconvolution methods attempt to design an inverse filter without any previous knowledge either of the source signature or the reflectivity function. These methods assume that geology (the reflectivity function) is random and multiples can be identified by their cyclicity. Spiking deconvolution is a widely used method of statistical deconvolution that attempts to minimise, in a least squares sense, the difference between the observed wavelet and the theoretical conception of a reflection event, i.e. a spike. ProMAX features two types of spiking deconvolution: the minimum phase option corrects both the amplitude and phase of the wavelet (assuming that the wavelet is minimum delay and that the convolutional model holds), while the zero phase option flattens the amplitude spectrum of the data. The length of the inverse filter to be applied to the data is an input parameter whose value is chosen subjectively from tests with different values. After testing length values in the range 180-250 ms in increments of 10 ms, using both spiking deconvolution types, the minimum phase option with a filter length of 250 ms showed the best signs of compressing the effective in the data into a spike (Fig. 5.7).

Deterministic deconvolution on the other hand, attempts to design an inverse filter based on some knowledge (even if this is only approximate) about the source wavelet. In the case of the RAMESSES experiment there was no direct recording of the airgun array signature available. Therefore, an attempt to approximate the source wavelet was made in two different ways: (a) by stacking the direct water wave recorded by the near-offset channel for all shots; and (b) by stacking the seabed reflections from Line 28 at a point where the seabed was covered with sediments,

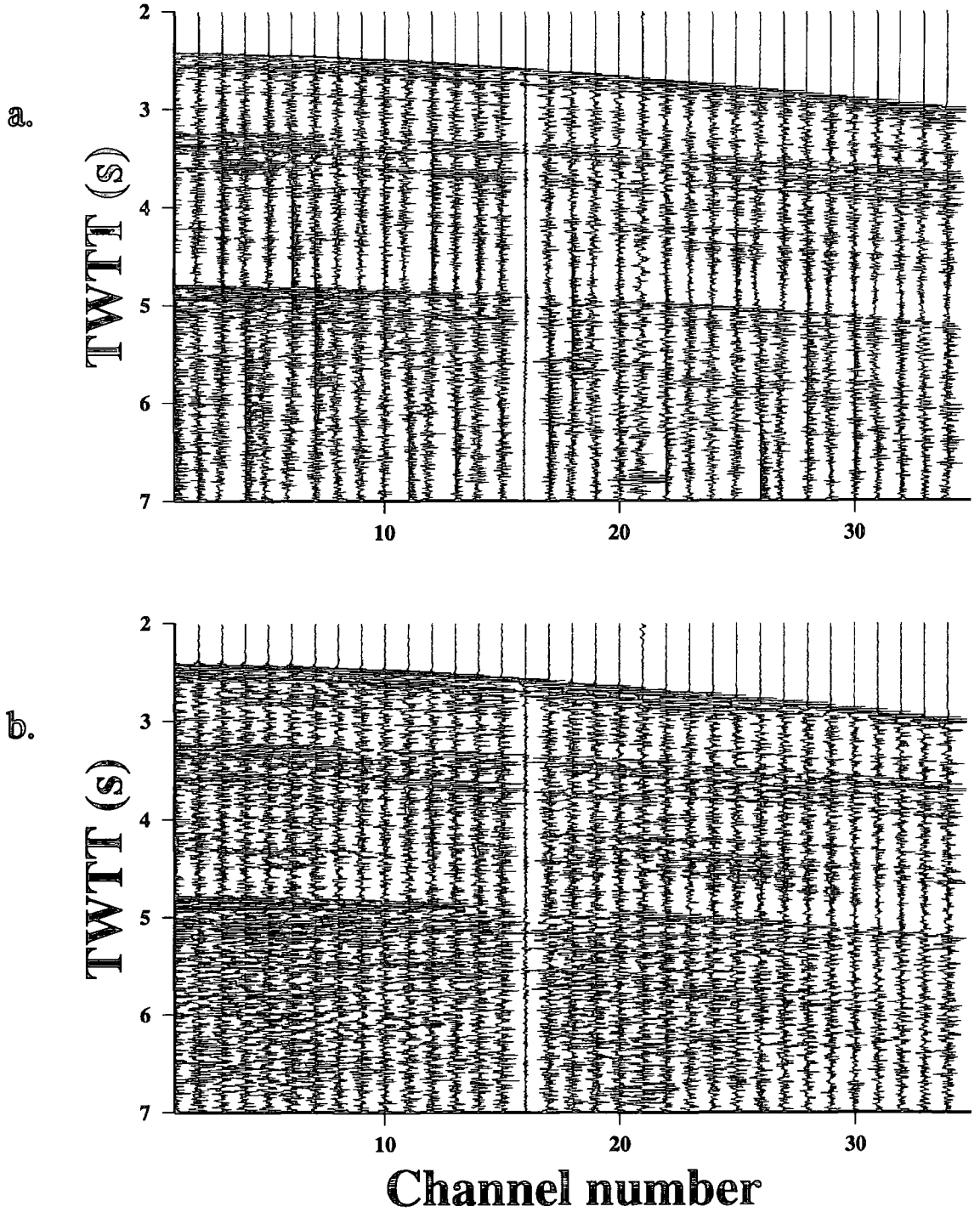


Figure 5.7: Spiking deconvolution. (a) Example of raw CMP gather. (b) The same CMP gather after the application of minimum phase spiking deconvolution and bandpass filtering. Note the enhancement of noise below 4 s in the deconvolved CMP gather.

such that the resulting wavelet will have suffered minimum distortion. Using the ProMAX tool *Filter Generation* an inverse filter was designed for each wavelet and then tested on the data using the *Filter Application* tool. The two filters seemed to yield similar results, with the seabed-derived filter performing marginally better than that for the first breaks, and much better when compared with the results of the statistical deconvolution (Fig. 5.8). Thus, it was decided to deconvolve the data with the seabed-derived filter pre-stack. The act of deconvolution causes spectral whitening, thus once deconvolved the data were bandpass filtered using 1-2 Hz lower and 50-75 Hz upper cut-off frequencies.

### *5.3.7 Data enhancement: coherency filtering*

The coherency filtering technique was applied to the data in an attempt to enhance them pre-stack. The *Coherency Filtering* tool applies a frequency domain coherency weighting to each trace in a CMP gather. The coherency weighting is the ratio of signal power to signal-plus-noise power for every frequency of interest. The signal power is the magnitude of a complex sum of consecutive cross-power estimates, over a range of traces about the weighted trace. The signal-plus-noise power is the magnitude of the complex sum of power estimates of traces over the range about the weighted trace. These power estimates are derived for given lengths of the auto- and cross-correlations. After testing different input parameters it was found that a panel size of 200 traces, with a power estimation window of 41 traces and length of auto- and cross-correlations of 200 ms in the frequency range of 1-90 Hz, produced optimum results (Fig. 5.9).

### *5.3.8 Velocity analysis and stacking*

The Line 37 data were first stacked using as a velocity function the along-axis wide-angle model published by Navin *et al.* (1998). This model was converted from depth into two-way travel time using the thicknesses and interval velocities of

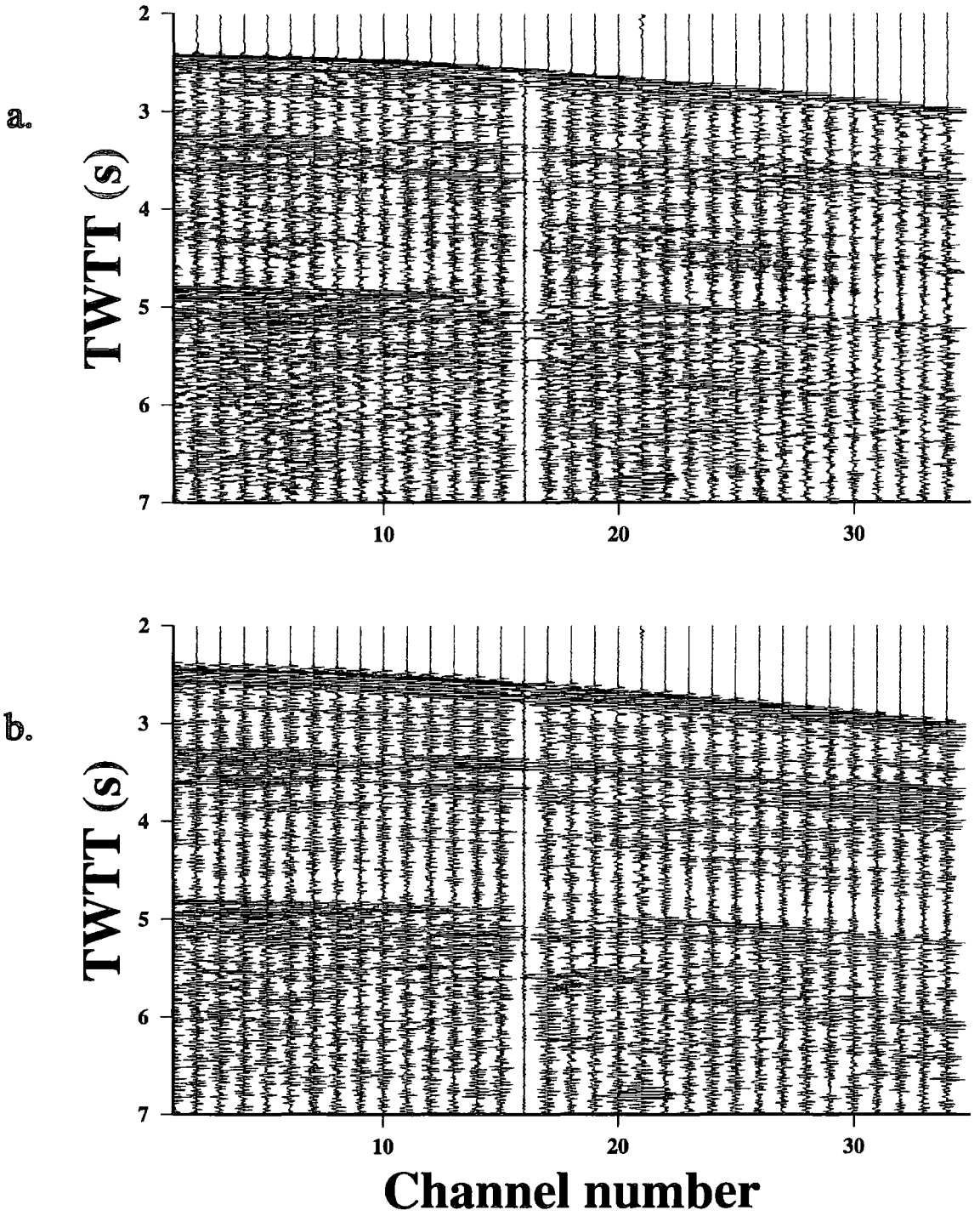


Figure 5.8: Deterministic deconvolution. The same CMP gather shown in Fig. 5.7a and b (a) deconvolved using the minimum phase spiking deconvolution compared with (b) where it is deconvolved using the inverse filter designed from the seabed reflections from Line 28. Both CMP gathers are bandpass filtered 1-2-50-75 Hz.

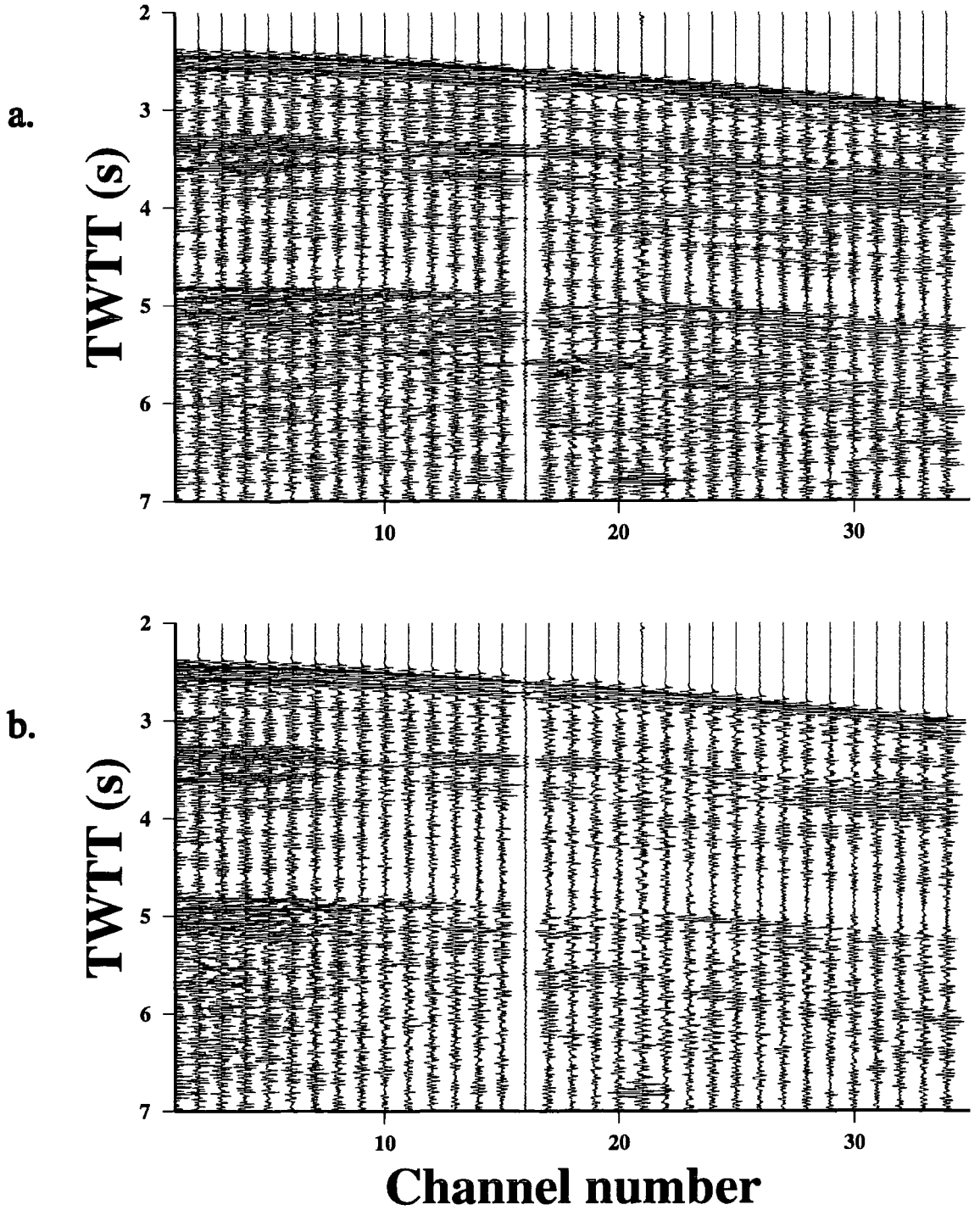


Figure 5.9: Coherency filtering. (a) CMP gather after deconvolution, (see Fig. 5.8) compared with (b) which is the same CMP gather after the application of the coherency filtering. Note how much easier individual reflection events can now be identified.

each layer. The interval velocities were then converted to root mean square (rms) velocities as they closely approximate the optimum CMP stacking velocities, using the equation

$$V_{rms} = \sqrt{\frac{\sum V_i^2 t_i}{\sum t_i}} \tag{5.1}$$

where $V_{rms}$ is the RMS velocity, $V_i$ is the interval velocity and $t_i$ is the time in each layer. Table 5.2 shows the stacking velocities obtained after conversion of the wide-angle model.

**Table 5.2** Stacking velocities derived from the wide-angle model.

| **TWTT (ms)** | **Velocity (m s$^{-1}$)** |
|---|---|
| 0 | 1500 |
| 2890 | 2040 |
| 3330 | 2570 |
| 3540 | 2820 |
| 3600 | 2900 |
| 3790 | 3070 |
| 4430 | 3730 |
| 4760 | 3920 |
| 5070 | 4150 |
| 5291 | 4300 |

The next step was to create a more detailed velocity function that would produce a better quality stacked section. In order to improve the signal-to-noise ratio, the CMP gathers were grouped together in ensembles of 25 specified using the ProMAX macro *Supergather Formation.* Once formed into supergathers, the header value SG_CDP was set to the central CMP number in each set of supergathers for each CMP. This header value was then defined as a primary header sort term in the *Disk Data Input* tool.

The *Velocity Analysis Precompute* tool was then used to precompute the velocity analysis panels. These precomputed supergathers were input to the *Interactive Velocity Analysis* tool where it was possible to pick velocities after inspecting a semblance plot, constant velocity stack panels and a single CMP gather with NMO applied interactively. Fig. 5.10 shows the display panels with some chosen velocity picks that were based on maximum coherency peaks ('bright bull's eyes') on the semblance plot. The velocity picks made in this way were then written to a file and stored in the ProMAX database so that it could be used by the *Normal Moveout Correction* tool.

Large scale Versatec plots of the seismic sections stacked with the two different velocity functions were produced and directly compared. This comparison showed that, even though the same reflection events appeared on both sections, the section stacked with the velocity analysis picks proved to have sharper events. Therefore, despite the fact that these picks possess an amount of uncertainty, it was decided that this section should be used hereafter during the post-stack processing stages. Fig. 5.11 shows a part of the section stacked with the two velocity functions.

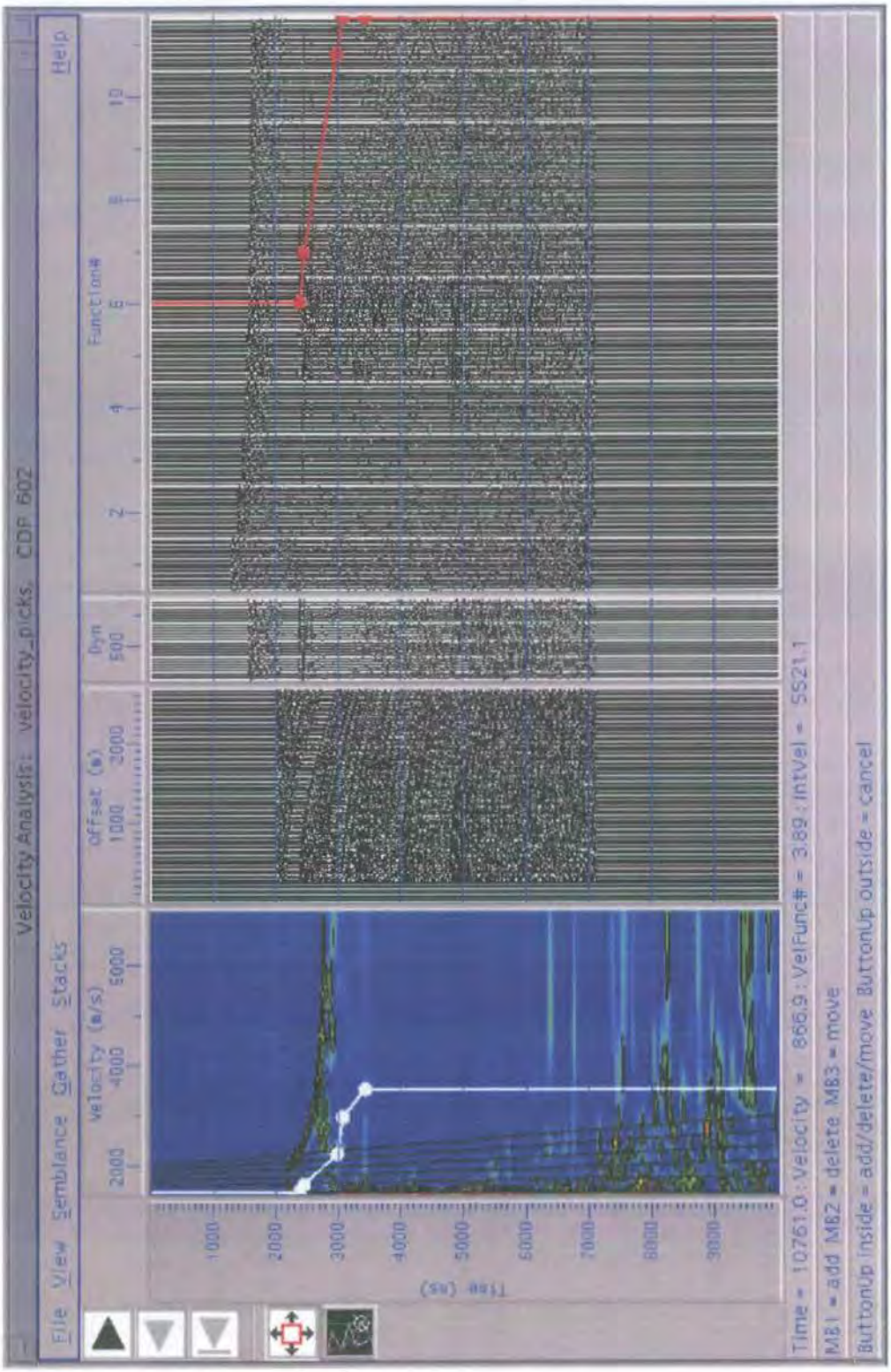


Figure 5.10: The ProMAX velocity analysis window. Velocities were picked using 'bulls eye's' on the semblance plot. The noisy nature of the velocity stacks illustrates the smearing on the semblance plot and how difficult it is to pick the correct velocities.

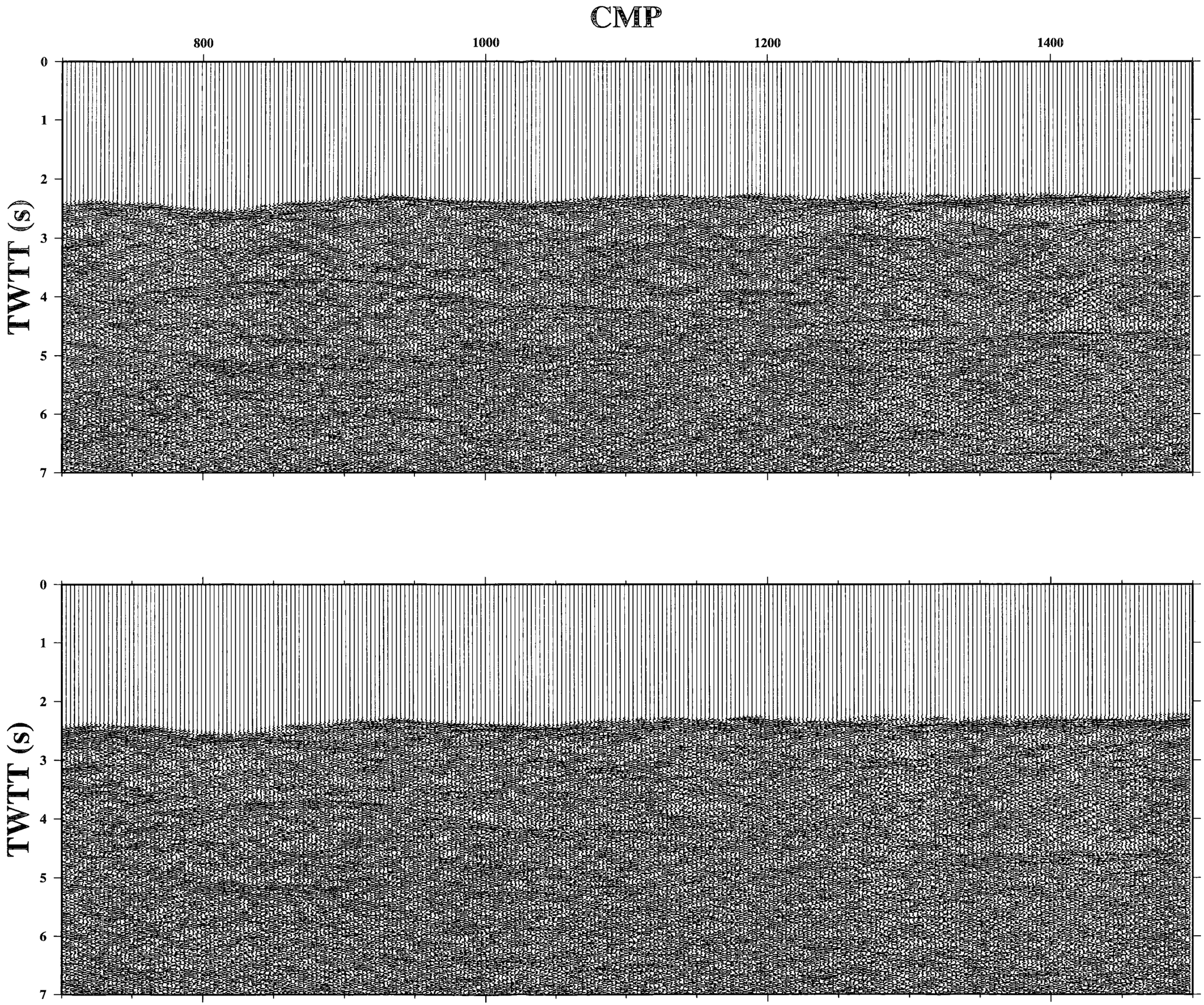


Figure 5.11

Figure 5.11: Part of the Line 37 seismic section stacked using the wide-angle velocity model (bottom) and the velocity picks made via semblance analysis (top). Note that all reflection events look sharper in the top section when compared to the bottom one. Both sections have been bandpass filtered using cut-off frequencies 1-2-50-75 Hz and are displayed after the application of automatic gain control (AGC) with an operator length of 500 ms.

### *5.3.9 Post-stack deconvolution*

Post-stack deconvolution was carried out in a similar manner to the pre-stack deconvolution described earlier. This time the stacked data were predictively deconvolved using the minimum phase predictive deconvolution option that exists in the *Spiking/Predictive Deconvolution* tool. The operator length was again chosen to be 250 ms and several values in the range of 20-40 ms were tested as prediction distances. The second zero crossing of the autocorrelation function of the data is considered as a good choice for the prediction distance, however this was found to flunctuate between 25-45 ms. After deconvolving the data using prediction lags values in the range 25-45 ms, it was found that the prediction distance that gave optimum results was 30 ms. The predictively deconvolved section showed some improvement in certain parts where ringing was more severe, while in other parts no improvement could be observed (Fig. 5.12).

Figure 5.12: Part of the seismic section without post-stack deconvolution (bottom) and the same part predictively deconvolved (top). The display parameters are the same as in the previous figure.

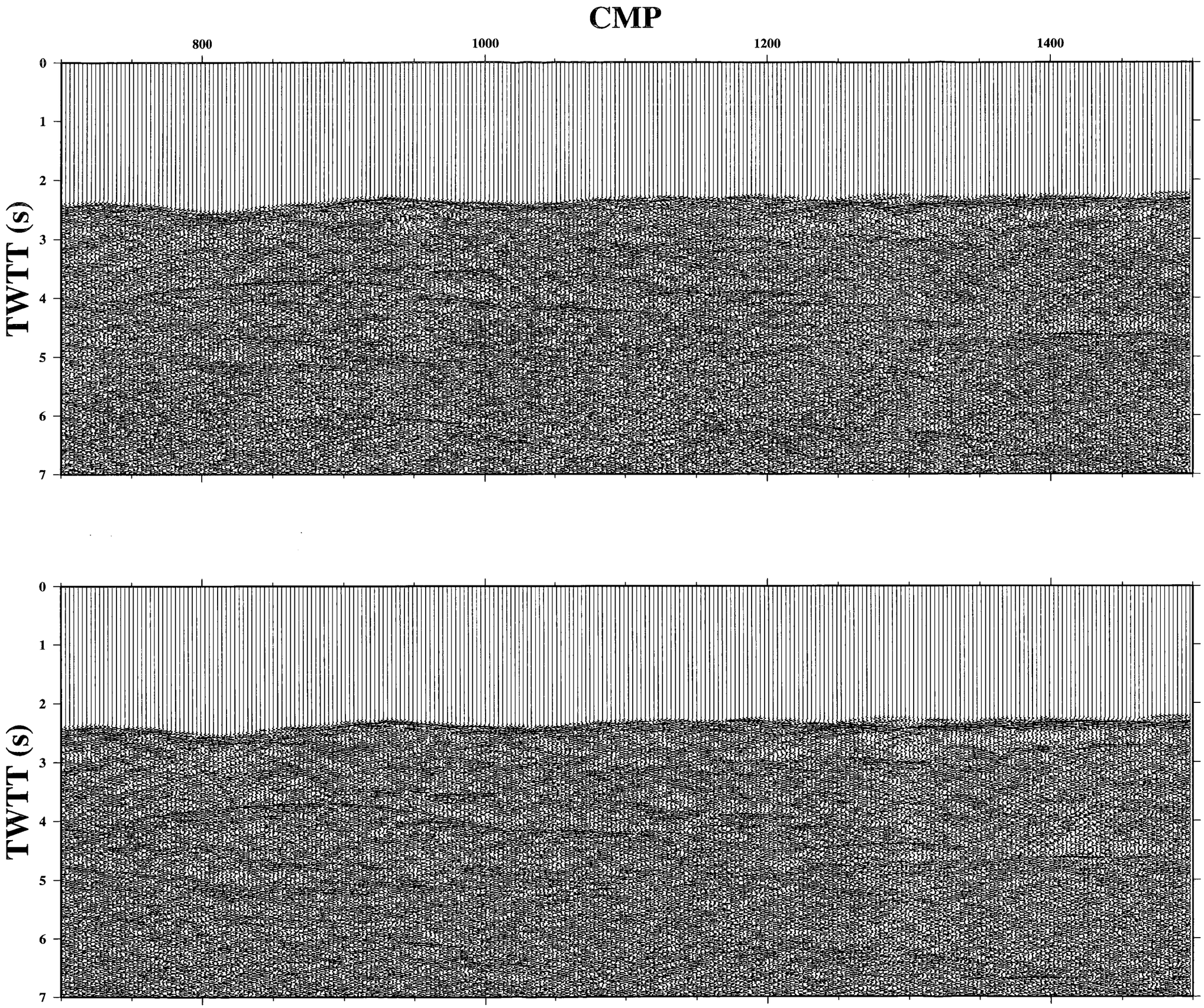


Figure 5.12

### *5.3.10 Dynamic S/N filtering*

Dynamic S/N filtering can be applied to both pre- and post-stacked data to enhance the lateral coherency. The method works using two main assumptions: (a) the noise contribution to each sample is assumed random; and (b) a window has been chosen over a linear dip. The *Dynamic S/N Filtering* tool examines every trace $x$ individually and considers it as being composed of a signal $s$ and a noise component $n$

$$x_1(t) = s_1(t) + n_1(t) \tag{5.2}$$

The data are Fourier transformed to the frequency domain where the complex components can be represented by

$$X_1(f) = S_1(f) + N_1(f) \tag{5.3}$$

Following that each trace is multiplied by its complex conjugate considering each frequency separately

$$X_1(f)X_1^*(f) = |X_1(f)|^2 = |S_1(f)|^2 + |N_1(f)|^2 + S_1(f)N_1^*(f) + S_1^*(f)N_1(f) \tag{5.4}$$

The first two terms are real and positive and have zero phase, while the last two cross-product terms have random phases. Summing over $m$ traces in the window and dividing by the number of traces, yields the average power of the signal and the noise

$$\frac{1}{m}\sum_{i=1}^{m} X_i(f)X_i^*(f) \tag{5.5}$$

If the signal and noise are uncorrelated, the random phase cross-products sum approximately to zero. However, this approximation can only be made if the number of traces is large enough. The previous equation then can be written as

$$\frac{1}{m}\sum_{i=1}^{m}[|S_i(f)|^2 + |N_i(f)|^2] \tag{5.6}$$

The product of each trace sample and the complex conjugate of the neighbouring trace can be computed

$$\begin{aligned} X_1(f)X_2^*(f) &= (S_1(f) + N_1(f))(S_2^*(f) + N_2^*(f)) \\ &= S_1(f)S_2^*(f) + N_1(f)N_2^*(f) + S_1(f)N_2^*(f) + N_1(f)S_2^*(f) \end{aligned} \tag{5.7}$$

Assuming that the signal has the same amplitude on all traces, the first term has a magnitude equal to the signal power. The phase is determined by the dip, or time moveout between traces 1 and 2. This time moveout will be the same between any pair of adjacent traces if the signal event is linear. The remaining three terms all have random phases. The average power of the signal is found by summing over adjacent trace products between 1 and $m$

$$\frac{1}{m-1}\sum_{i=1}^{m-1} X_i(f)X_{i+1}^*(f) \tag{5.8}$$

As before, if the noise and the signal are uncorrelated, this can be approximated to

$$\frac{1}{m-1}\sum_{i=1}^{m-1} S_i(f)S_{i+1}^*(f) \tag{5.9}$$

The magnitude of the sum is the signal power. The weight applied at a given frequency to the central trace in the sample will be

$$\frac{S^2(f)}{S^2(f) + N^2(f)} \tag{5.10}$$

where S(f) is signal power and N(f) is noise power. The input parameters found to produce optimum results were a horizontal length of 200 traces, a time window

length of 500 ms and a time window overlap of 100 ms in order to minimise edge effects. The cut-off frequencies were again 1-90 Hz. Fig. 5.13 shows part of the section where the reflection events are much more enhanced after the application of dynamic S/N filtering.

Figure 5.13: Part of the predictively deconvolved section without dynamic S/N filtering applied (bottom) compared with the same part after the application of dynamic S/N filtering. Note how the lateral coherency of the reflection events has improved. The improvement is much more obvious in large scale plots. The display parameters are the same as in the previous figure.

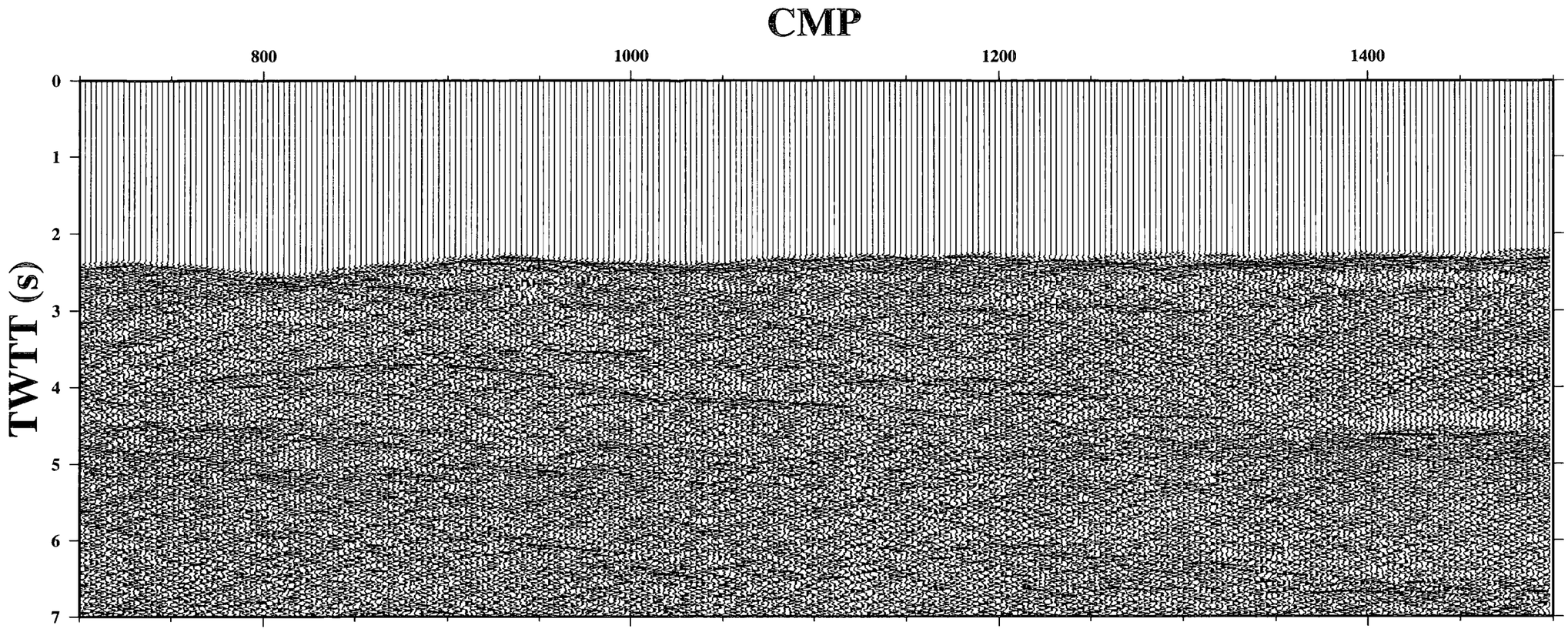


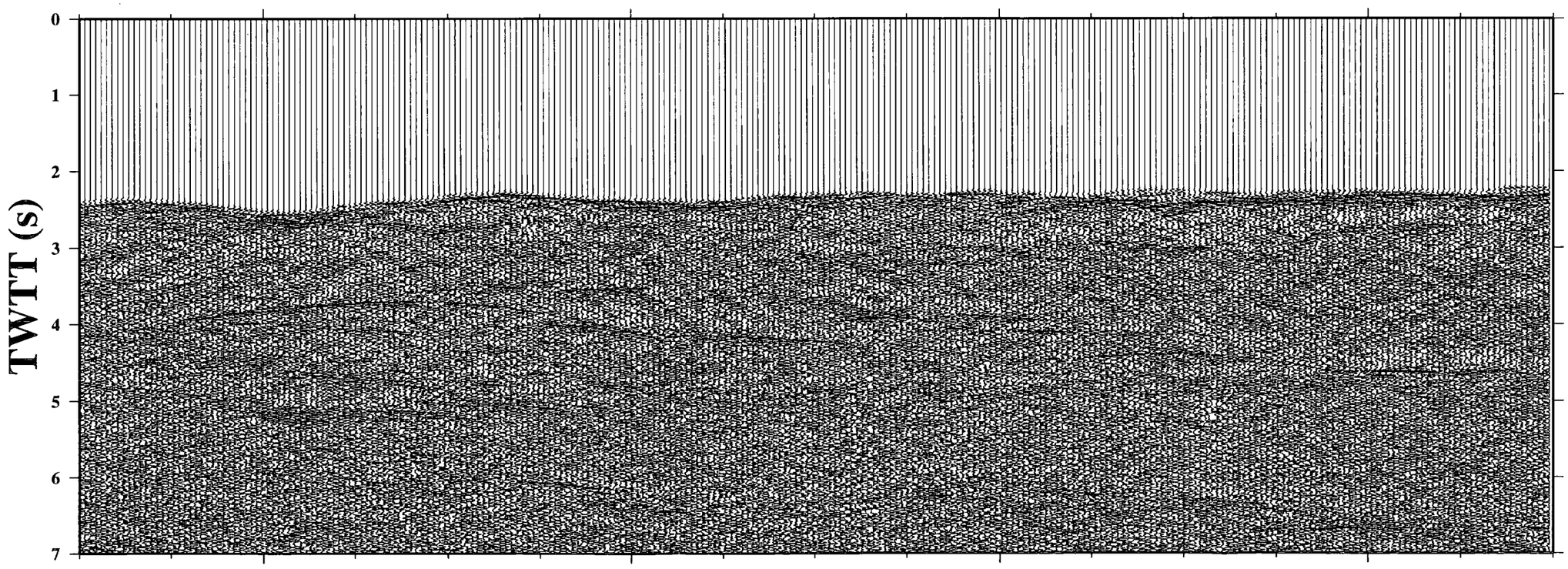


Figure 5.13

### *5.3.11 Migration*

Migration acts to reconstruct the stacked section so that reflection events are repositioned at their correct locations and two-way travel times, and is usually the last stage in seismic reflection data processing (except perhaps for cosmetic processes related to plotting). After migration the resolution of a section is increased by removing the distorting effect of dipping layers and collapsing diffraction patterns back to their point sources. Two-dimensional time migration uses rms velocities analytically and leaves the vertical coordinate as two-way travel time, however, it is constrained to the plane of the section. Two time migration techniques were tested on the data, namely *Memory Stolt F-K* and *Kirchhoff Time Migration*, both of them being able to handle dips of up to 90°.

*Memory Stolt F-K Migration* is a three step process that involves (a) stretching the input wavefield to simulate the response of a constant velocity earth model; (b) migrating by Fourier transforming the wavefield from the T-X to the F-K domain, mapping onto the $k_z$-$k_x$ domain and then transforming back the result to the T-X domain; and (c) reversing the original wavefield stretching. At first the velocity function derived from the velocity analysis procedure was used to migrate the section, using as the Stolt stretch factor a value of 0.6 (recommended by the ProMAX manual for velocity functions that increase with depth), maximum frequency to be migrated 50 Hz and a velocity scale factor of 90. Unfortunately this led to an over-migrated section, where most of the reflection events could no longer be identified. The use of the wide-angle velocity model with the same migration parameters produced almost the same results. It was decided, therefore, to migrate the section using a constant (water) velocity of 1500 m $s^{-1}$ and a Stolt stretch factor of 1.0, producing an improved seismic section (Fig. 5.14 top). Since most of the distortion effects originate by the scattering of energy from the rough seafloor, the choice of water velocity can be considered adaquate in collapsing the diffraction hyperbolae associated with the seabed.

*Kirchhoff Time Migration* involves the summing of amplitudes over diffraction

hyperbolae, the curvature of which is determined using the velocity field. The extent over which the summation spans is known as the migration aperture. This parameter is important in preventing the removal of steeply dipping reflectors and was, therefore, set to the default parameter which automatically calculated the optimum aperture. The maximum frequency to be migrated was set again to 50 Hz and the maximum dip to migrate was set to 70°. The same problems with the velocity field when the F-K migration was applied, were encountered with the Kirchhoff migration as well. The section was again migrated using the same constant velocity as before, producing similar results with that of the Stolt F-K (Fig. 5.14 bottom). Since there is no substantial difference between the results produced by the two methods, *Memory Stolt F-K Migration* was preferred as the final migration method because it is much cheaper in computer time than *Kirchhoff Time Migration.* The final migrated section is included as an enclosure at the end of this thesis.

---

Figure 5.14: Top plot shows part of the seismic section migrated using the *Memory Stolt F-K Migration* algorithm, while the bottom plot shows the same part migrated using the *Kirchhoff Time Migration* algorithm. Even though both sections look considerably improved compared with the unmigrated sections, they look similar compared to each other. The display parameters are the same as in Fig. 5.13.

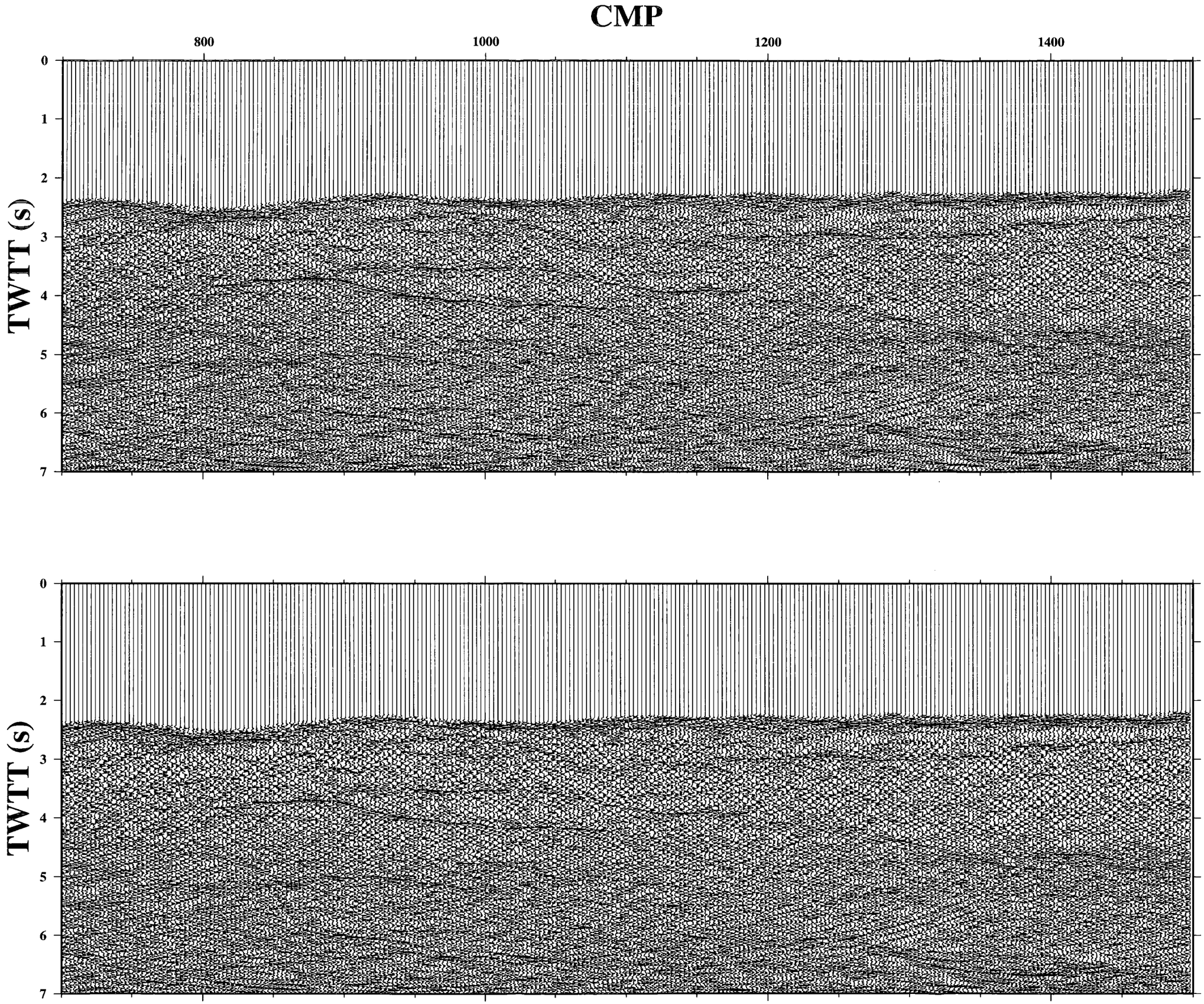


Figure 5.14

## 5.4 Concluding remarks on the processing scheme

An overview of the processing scheme described in this chapter and applied to Line 37 of the RAMESSES dataset is shown in Fig. 5.15. A comparison of this scheme with the ones used to process reflection data from the same AVR, either from other RAMESSES lines (Wareham, 1999; Farouk, 1999; Hall, 1999) or the RAMESSES 4-fold data (Inglis, 1995) can be summarised in the following points:

**Deconvolution.** The processing done by Inglis (1995) is the only one that attempted to deconvolve the data pre-stack using inverse filters designed from the direct water wave or the seabed reflections. It was found that both of them deteriorated the quality of the stacked section. However the very low signal-to-noise ratio of the 4-fold data and the rough seabed topography probably played a major role as well. The operator lengths used by Wareham (1999) and Farouk (1999) during pre-stack deconvolution were shorter (180 and 190 ms respectively) than the optimum value of 250 ms found in this study, or the operator length of 200 ms used by Hall (1999). The conclusion is more unanimous for the post-stack predictive deconvolution, where it was found that the resulting sections were slightly or not improved at all (Inglis, 1995; Wareham, 1999; Farouk, 1999).

**F-K filtering.** In theory F-K filtering is the preferred option in many processing schemes when it comes to a decision of how to attenuate coherent noise present in the data. F-K filtering was also applied to Line 37 at the early processing stages pre-stack. However, no significant improvement could be observed in the stacked sections. Similar observations of slight, or no improvement after F-K filtering, were also reported by Inglis (1995), Wareham (1999) and Farouk (1999) attributing this failure to the inability of the filter to distinguish real reflection events from coherent noise due to their partial overlap in the F-K domain. In contrast, Hall (1999) found that F-K filtering did improve the data substantially when applied pre-stack.

**Migration.** None of the previous studies reported any problem of overmigrated sections, of the kind encountered during the processing of Line 37. It should be noted, however, that three of them (Inglis, 1995; Wareham, 1999; Farouk, 1999) were using older versions of the ProMAX processing software, which seemed to be more tolerant to abrupt velocity changes than the newest version currently in use. Hall (1999) migrated the section with water velocity without trying any other velocity function.

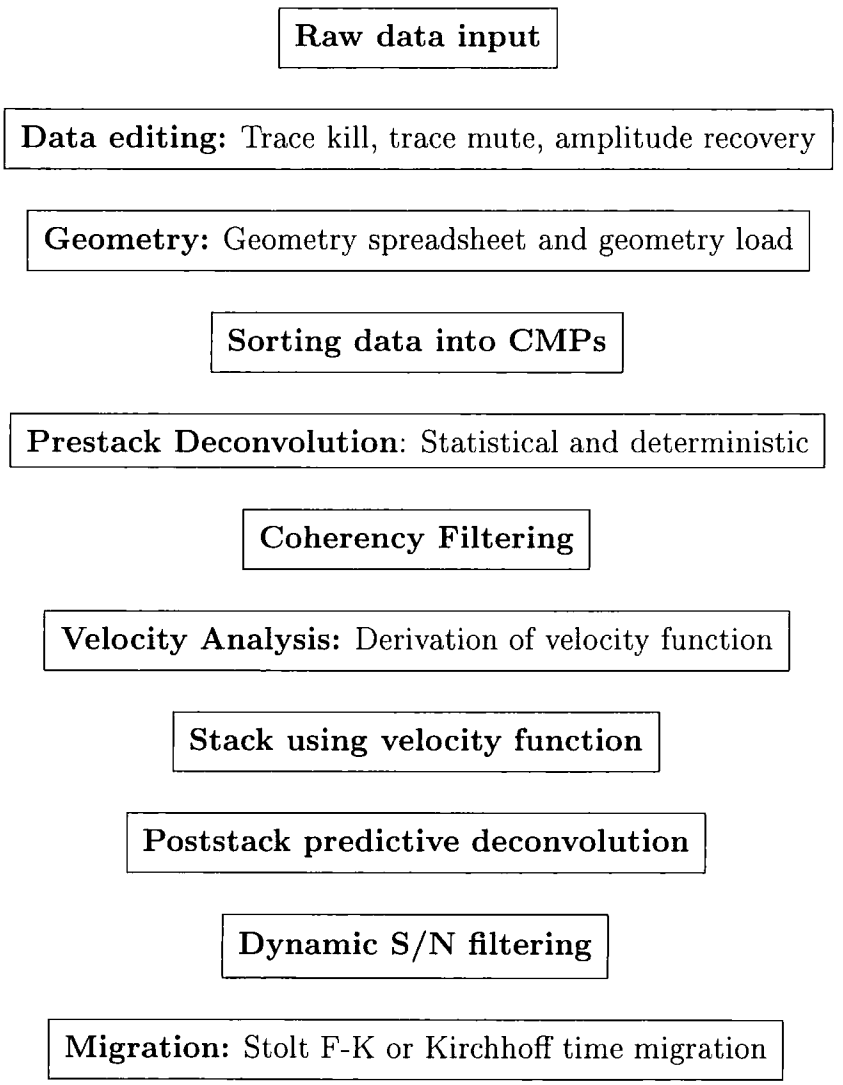


Figure 5.15: Diagram of the final processing scheme applied to Line 37 in a top-down order, showing the ProMAX tasks used to accomplish each stage.

## 5.5 Summary

The second phase of the RAMESSES (Reykjanes Ridge Axial Melt Experiment: Structural Synthesis from Electromagnetic and Seismics) project took place in the summer of 1998 and involved the acquisition of multichannel seismic reflection data by shooting 34 across-axis and 5 along-axis profiles over the magmatically active 57°45'N axial volcanic ridge. The aim of this survey was to improve the resolution of the results obtained during the first phase of the project, thus allowing a better understanding of the processes of crustal accretion at slow spreading ridges. The data from the along-axis Line 37 were initially edited and then sorted into common mid-point gathers (CMP) based on the geometry inferred from the navigation information. Both statistical and deterministic deconvolution schemes were applied pre-stack, with the latter performing much better than the former. In order to lower the contribution of random noise, the coherency filtering technique was applied pre-stack and afterwards the CMP gathers were stacked using the velocity function derived from semblance plot picks. In the post-stack processing the data were predictively deconvolved to remove any ringing and run through the dynamic signal-to-noise filter applied in order to improve the lateral coherency of the reflection events. Stolt F-K and Kirchhoff time migration were performed using a constant, sea water velocity (1500 m $s^{-1}$) because both algorithms seemed to be less tolerant to abrupt lateral changes of the velocity function, producing overmigrated seismic sections. Interpretation of the final processed section will be presented in the next chapter.

# Chapter 6
# Interpretation, discussion and conclusions

## 6.1 Introduction

In this chapter the main features of the 1996 Vatnajökull eruption are summarised, possible eruption mechanisms based on geophysical and geochemical evidence are discussed and a physical model for the co-eruptive tremor source is presented. The reflection events present in the processed seismic section of Line 37 of the RAMESSES experiment are identified and an interpretation of the magma injection processes and magma chamber formation for the 57°45'N axial volcanic ridge is given. Suggestions for further work on the Vatnajökull eruption and RAMESSES datasets are also included.

## 6.2 The 1996 Vatnajökull eruption

### *6.2.1 Salient characteristics of the eruption*

The 1996 eruption at the Vatnajökull glacier was preceded and accompanied by a variety of phenomena, that may be summarised as follows:

- The eruption appeared to affect a much larger area than just the fissure area between Bárdarbunga and Grimsvötn, and the seismic activity was distributed over three volcanic systems (Tungafellsjökull, Bárdarbunga, Grimsvötn). Furthermore, examination of the seismicity of this area for a period of four and a half years before the eruption revealed a considerable increase in seismic activity during the first half of 1996 at the nearby Hamarinn volcano (Fig. 6.1).

- The earthquake at Bárdarbunga (with a moment magnitude of 5.6) that pre-

ceded the eruption was unusual because (a) its focal mechanism appeared not to be consistent with a double-couple source (Nettles & Ekström, 1998), (b) volcanic earthquakes of this magnitude are generally rare, with the possible exceptions of the $M_s = 5.1$ earthquake that initiated the eruption at Mt. St Helens and the $M_s = 5.5$ earthquake that preceded the Ito-Oki submarine eruption. Most major eruptions that had been seismically monitored in the last century involved events with magnitudes no larger than 4 (McNutt, 1996).

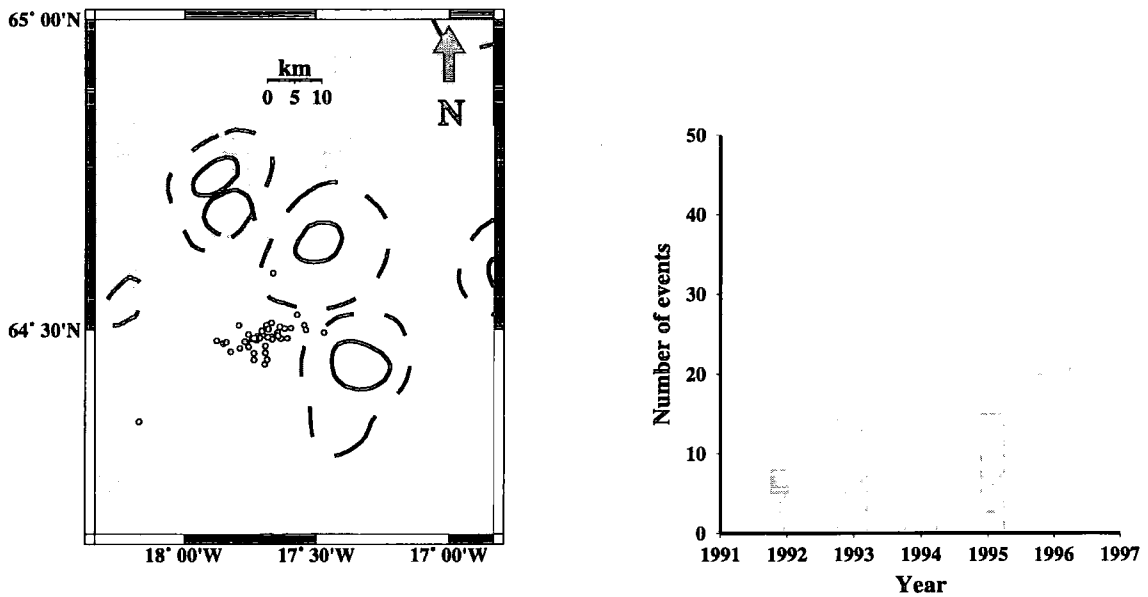


Figure 6.1: Epicentre locations of the swarm that occurred in Hamarinn volcano (see also Fig. 1.11) and annual distribution of seismicity for the period 1992-1996 before the Vatnajökull eruption. Numbers were obtained from the SIL database.

- No events with clear P and S phases were identified (at least during the main phase of the eruption September 29th - October 6th) that could be classified as high-frequency events according to the classification scheme used in Chapter 2 and be attributed to shear failure of rock. Such events are very common before and after major eruptions and are thought to be the result of concentrated stresses in the crust beneath the volcano, because of the upward movement of magma (McNutt, 1996). The lack of such events may also imply that the

crust beneath Vatnajökull is more ductile than brittle.

- Volcanic tremor started pre-eruptively as a harmonic signal but changed to broadband co-eruptively, exhibiting many similarities with volcanic tremor recorded during eruptions at other volcanoes in Iceland (R. Stefánsson, pers. comm. 1999).

### *6.2.2 Possible physical mechanisms*

#### *6.2.2.1 Geophysical evidence and arguments*

The large earthquake that occurred approximately two days before the eruption attracted a great deal of attention from seismologists, firstly because of its anomalous nature and secondly because it could provide clues as to the mechanism of the eruption itself. The corresponding teleseismic data were inverted in order to recover its focal mechanism, depth and rupture history using two different methods: (a) Nettles & Ekström (1998) used a modified version of the CMT algorithm (Arvidsson & Ekström, 1998), which fits first arriving surface waves at periods of 40-150 s, calculates the synthetic seismograms using ray theory and includes reflections and conversions near the source by using a layer matrix method for a flat-layer local crustal model; (b) Zobin (1999) used a finite fault parametrization method (Hartzel & Heaton, 1983) by choosing a fault plane of fixed dimensions and orientation, embedded at an appropriate depth in the crustal structure of the source region. The fault plane was chosen to be a $10\times10$ km$^2$ rectangle divided into 100 subfaults of $1\times1$ km$^2$ surface area.

The results obtained by the first method (Fig. 6.2) indicated a large CLVD (Compensated Linear Vector Dipole) component with a seismic moment of $2.8\times10^{17}$ N m. The deviation from the douple-couple mechanism was estimated using the dimensionless parameter $\epsilon$

$$\epsilon = \frac{-\lambda_2}{max(|\lambda_1|, |\lambda_3|)} \tag{6.1}$$

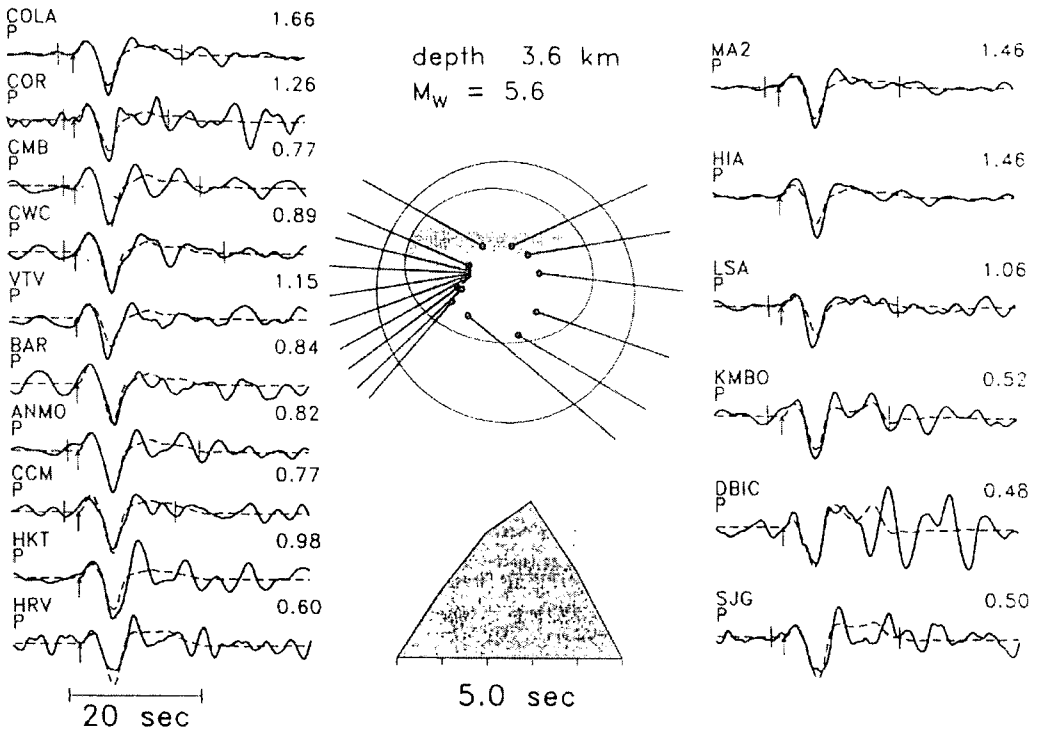


Figure 6.2: Focal mechanism corresponding to the full moment tensor solution and source time function for the Bárdarbunga earthquake, determined using the modified CMT algorithm. Solid lines represent broadband teleseismic P waveforms and dashed lines represent calculated synthetic seismograms. Maximum amplitudes in microns are shown at right of seismograms; arrows show picked first arrivals and thin vertical bars show time window included in the inversion. No time window is shown for those traces not included in the inversion due to high background noise level (from Nettles & Ekström, 1998).

where $\lambda_1, \lambda_2, \lambda_3$ are the diagonal elements of the moment tensor in the principal axis coordinate system, ordered such that $\lambda_1 \geq \lambda_2 \geq \lambda_3$. For the Bárdarbunga event $\epsilon = 0.3$, whereas an $\epsilon$ value of zero corresponds to a pure douple-couple and a value of $\pm$ 0.5 to a pure CLVD. The optimum depth for a point source was found in the range 3-7 km, with a value of 3.6 km yielding the best fit of observed and synthetic waveforms, while the duration of the source time function was found to

be 5 s. Nettles & Ekström (1998) interpreted this focal mechanism as the result of thrust motion on planes of varying strike that form an outward dipping cone-shaped, ring-fault beneath the Bárdarbunga caldera.

The second method also indicated a complicated rupture history which was interpreted as the breaking of an asperity beneath Bárdarbunga due to an inflating magma chamber. The optimum hypocentral depth was found to be 4 km and the final slip on the fault was represented by an ellipse-shaped rupture having a maximum displacement of 45 cm (Fig. 6.3), while the broken asperity was thought to be situated between 3 and 6 km depth. The estimated seismic moment was of the order of $3.2 \times 10^{17}$ N m and the source time function duration was found to be 3 s, in good agreement with the Harvard CMT solution.

Even though the two interpretations regarding the nature of the Bárdarbunga event differ, the physical mechanism for the eruption suggested by the two studies is quite similar. It is assumed that a shallow magma chamber exists beneath the Bárdarbunga caldera, fed by a deeper source through a narrow conduit (Fig. 6.4). Inflow of magma in the chamber is likely to cause its inflation and the accumulation of compressive stresses, which will result either in rupturing on pre-established zones of weakness, such as a cone fault under the caldera, or the breaking of an asperity. Another possible result of such a process is the emplacement of lateral dykes at the depth of neutral buoyancy which may lead to a lateral eruption.

This interpretation is consistent with the results obtained from the analysis of the HOTSPOT data (Chapters 2 and 4), that indicate:

- Pre-eruptive tremor signals occurred at least two days before the main eruption and just before the onset of the episodic earthquake swarm that preceded it, and they may be interpreted as an indication of flow of magma from a deeper source to a shallow chamber beneath Bárdarbunga.

- The fact that the epicentres of the earthquakes that followed the large event at Bárdarbunga form a curved line along the western caldera rim gives an

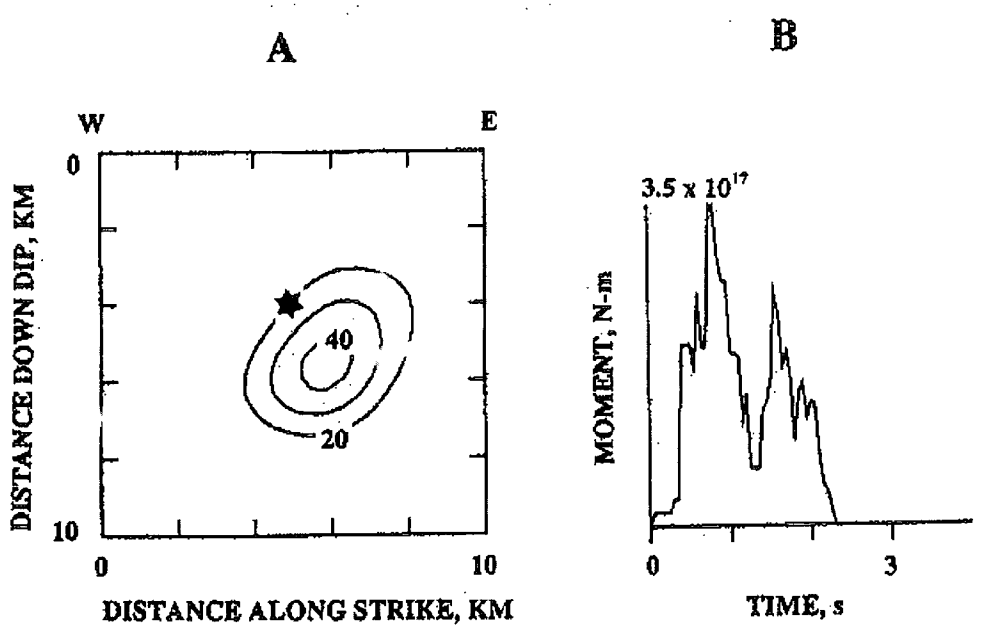


Figure 6.3: (A) Contours of final slip in centimetres on the fault plane. Cumulative slip is contoured at 10 cm intervals beginning at 20 cm. The black star indicates the position of the hypocentre. (B) Moment release as a function of time. The maximum moment value is marked on the vertical axis (from Zobin, 1999).

element of support for the ring-fault rupture mechanism proposed by Nettles & Ekström (1998). Furthermore, numerical studies of the stress field around shallow magma chambers indicate that the initiation of ring-faults is possible for sill-like magma chambers affected by doming of an area much larger than that of their caldera (Gudmundsson *et al.*, 1997). These considerations are consistent with the observations of early activity in Hamarinn volcano and the shifting of seismicity towards Tungafellsjökull during October 3rd-6th.

- The shift in the location of the epicentres during September 29th-30th towards Grimsvötn and the change of the event character from low-frequency to mixed-frequency may suggest a lateral migration of magma from a shallow chamber beneath Bárdarbunga, and fluid-injection crack-widening processes that finally resulted in the formation of an eruption fissure. Similar shifting of epicentres,

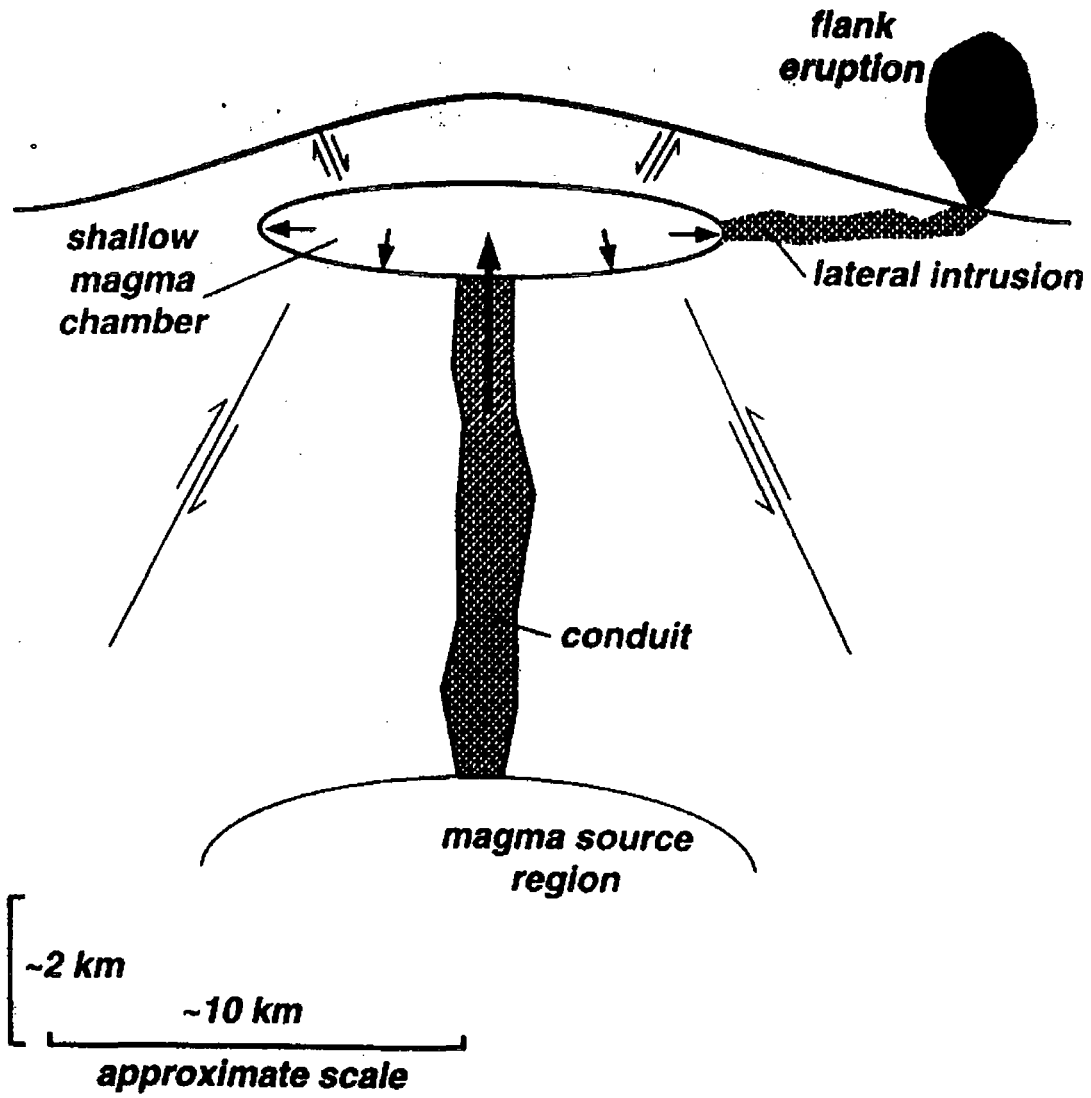


Figure 6.4: Schematic diagram illustrating the possible physical mechanism of the 1996 Vatnajökull eruption. Inflation of a shallow magma chamber fed from a deeper source leads to an increase of the pressure inside the magma chamber, increasing the stresses on rocks around it. Such stress increases may lead to rupture on cone faults beneath the caldera or breaking of asperities (from Nettles & Ekström, 1998).

indicating lateral movement of magma, has been also documented during the September 1977 and July 1978 rifting episodes at Krafla volcano (Brandsdóttir & Einarsson, 1979; Einarsson & Brandsdóttir, 1980).

Based solely on geophysical observations, the mechanism described above is an adequate explanation for the seismicity and course of events that occurred during the eruption. However, the incorporation with these observations of the results obtained by analysis of erupted tephra samples, described in the next section, alters this interpretation substantially.

### *6.2.2.2 Geochemical evidence and arguments*

Samples from the tephra deposited on the glacier between October 2nd-12th were collected and analysed by two groups independently (Sigmarsson *et al.*, 2000; Steinthorsson *et al.*, 2000). Their results can be summarised in the following points:

- The erupted magma was found to be basaltic icelandite, with an abnormally high abundance of phosphorus ($P_2O_5$ up to 1.28 wt.%). This magma composition may be produced after 50% fractional crystallisation of a tholeiitic basalt and the accumulation of phosphorus-rich minerals (such as apatite) shortly before the eruption.

- Measurements of $^{87}Sr/^{86}Sr$ and $\delta^{18}O$ isotope ratios for some of the samples indicate that this basaltic icelandite has an isotope composition indistinguishable from the basalts found in the Grimsvötn volcanic system and clearly different from those found in Bárdarbunga (Fig. 6.5) (Sigmarsson *et al.*, 2000). Results from other samples however, indicate an intermediate composition between the two systems (Fig. 6.6) that can be explained in terms of magma mixing (Steinthorsson *et al.*, 2000).

- More detailed examination of the oxygen isotope chemistry showed substantial contamination of the erupted magma, as a result of assimilation of hydrated

melts formed by anatexis of crustal rocks (Steinthorsson *et al.*, 2000).

Based on the geochemical results, a different eruption mechanism to the one suggested by the geophysical observations has been put forward. Sigmarsson *et al.* (2000) noted that even though the erupted magma originated from the Grimsvötn volcanic system, it cannot have migrated from a shallow magma chamber beneath Grimsvötn, because the crust there is too hot for a basaltic magma to have cooled and evolved to a basaltic icelandite. Therefore it is considered more likely that magma moved vertically, rather than horizontally, from a chamber located in the area between Bárdarbunga and Grimsvötn, forming the observed fissure. Sigmarsson *et al.* (2000) also proposed that this magma body is probably the non-erupted magma left in the crust after the 1938 eruption (cf. Fig. 1.11) which cooled and crystallised over a period of 60 years, forming basaltic icelandite melt. Since the volume of the erupted magma is estimated to be about 0.4 $km^3$ (taking into account the 50% fractional crystallisation that took place), then the minimum volume of the parental magma body should be 0.8 $km^3$.

The above scenario, however, leaves unexplained the occurrence of precursory seismic activity at Bárdarbunga, the observed migration of epicentres towards Grimsvötn, and the magma contamination mechanism. Steinthorsson *et al.* (2000) suggested a more plausible model that explains most of the geochemical and geophysical observations related to the eruption. According to their model, the 1996 eruption was triggered by a fissure opening up by magma surging southward from the Bárdarbunga volcanic system (cf. Fig. 6.4). This enabled magma at the crust-mantle boundary, or stored in a magma chamber, to ascend and incorporate on its way anatectic melts formed in the partially hydrated crust. During ascent through the cool and hydrous uppermost crust, homogenisation and rapid crystallisation took place, resulting in the observed products. This model may also explain the large CLVD component of the Bárdarbunga earthquake as a result of concentrated tensile stress in the area where magma was forcing its way to the upper parts of the crust. Events with similar large CLVD components, attributed to compressive stresses caused by

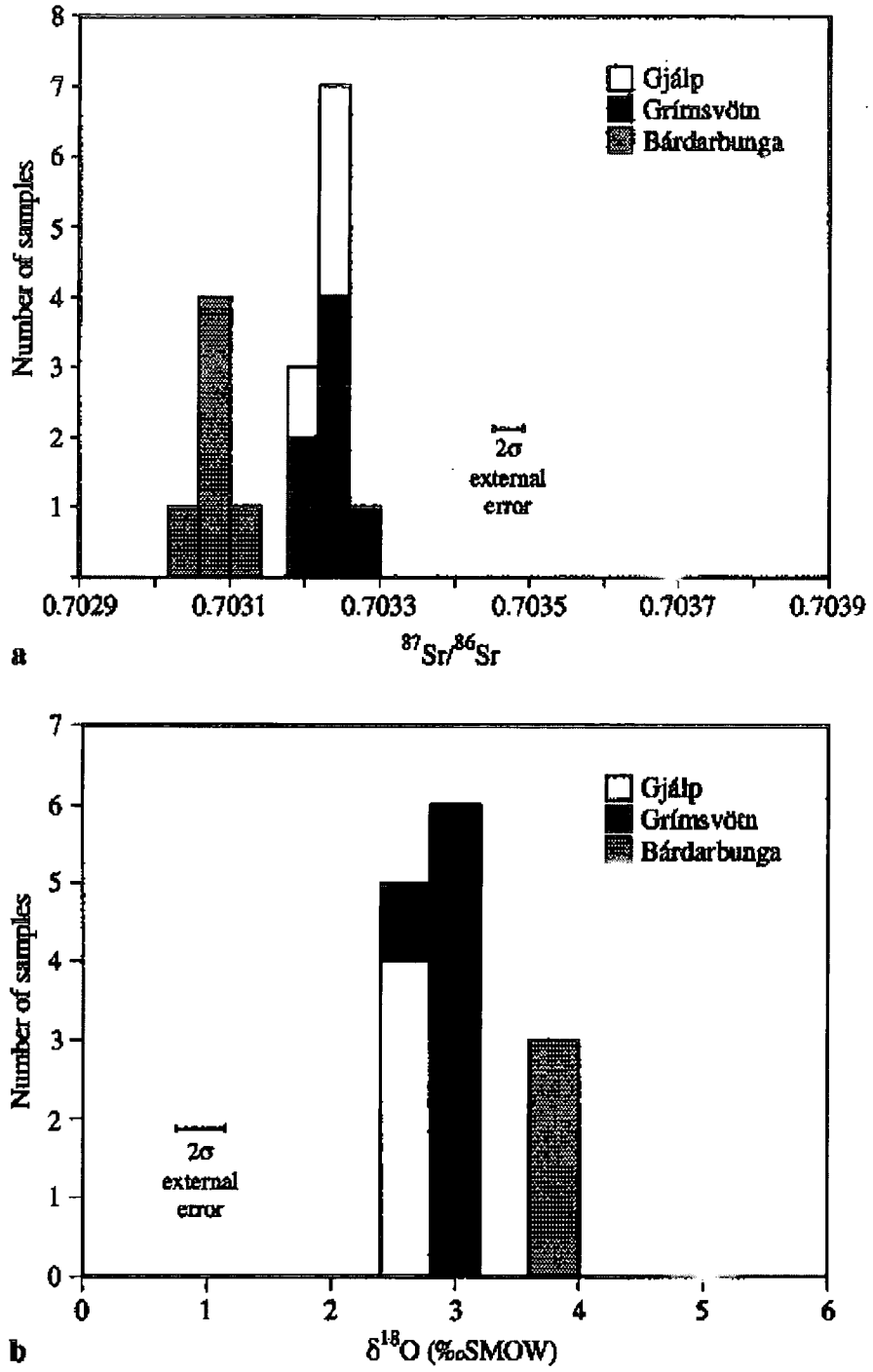


Figure 6.5: Histograms displaying (**a**) $^{87}Sr/^{86}Sr$ and (**b**) $\delta^{18}O$ in tephra and lava samples from two volcanic systems and tephra samples erupted during the 1996 Vatnajökull eruption (Gjálp). Both volcanic systems have discrete isotope compositions. The products associated with the 1996 eruption appear to be related to magma originating from the Grimsvötn system (after Sigmarsson *et al.*, 2000).

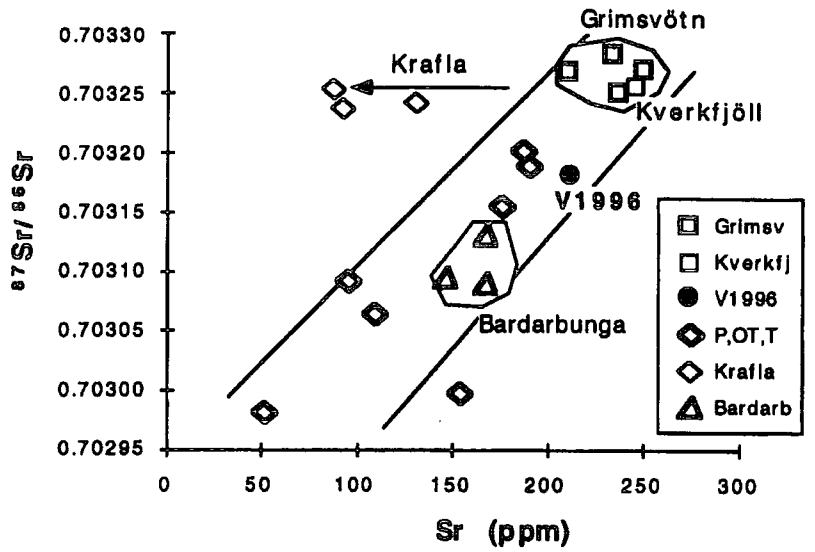


Figure 6.6: Graph showing Sr-isotopic ratios vs. Sr concentration for different volcanic systems in Iceland. The sample corresponding to the 1996 eruption (V1996) falls between the Grimsvötn and Bárdarbunga volcanic systems in terms of isotopic ratios (after Steinthorsson *et al.*, 2000).

dyke injection, include the Long Valley (Julian, 1983) and Tori Shima earthquakes (Kanamori *et al.*, 1993).

### *6.2.3 A physical tremor source model: turbulent slug flow*

The analysis of the co-eruptive tremor data recorded during October 1st-2nd (Chapter 4) indicates that the tremor process 'oscillates' between two different states, namely a quasi-periodic and a superposed aperiodic, chaotic one. Even though none of the source models that have been proposed thus far (section 3.5) may be used to explain these observations, it is very likely that these two regimes represent fluid-flow variations. Such a fluid-flow model should be able to explain the following characteristics:

- Co-eruptive tremor had a long duration of approximately two days, which coincided with the onset of the eruption, and its amplitude fell below the ambient noise level after the fissure was formed.

- The observations presented in Chapter 4, as well as theoretical considerations (e.g. Julian, 1994), indicate that a nonlinear rather than a stochastic source generated the tremor signals. Furthermore, the low value determined for the embedding dimension means that only a few degrees of freedom may be needed to describe the source, using ordinary and not partial differential equations (Procaccia, 1988).

- Continuous tremor has the same characteristics in the frequency domain and in phase space with the high-amplitude, cigar-shaped bursts which in most cases show a slow amplitude build-up reaching a maximum and then followed by rapid decay (cf. Fig. 4.3).

The geophysical evidence presented earlier and knowledge of the structure of volcanoes in Iceland point to the possibility of a simple magma plumbing system beneath the fissure area, consisting of a magma reservoir and a pipe-like conduit. On the other hand, the geochemical evidence showing contamination of the ascending magma by assimilation of crustal rocks requires a flow regime other than laminar, so that the fluid will be able to extract material from the conduit walls. An important physical quantity used to characterise a flow is the Reynolds number, defined as

$$Re = \frac{ud}{v} \tag{6.2}$$

where $u$ is flow velocity, $d$ a measure of the characteristic dimension of the flow and $v = \eta/\rho$ is the kinematic viscocity of the fluid (its shear or dynamic viscosity divided by its density). When the Reynolds number increases above a value of 2300, usually due to an increase in the flow velocity, intermittent turbulence or turbulent slugs are observed in the transition from purely laminar pipe flow to completely

turbulent flow (e.g. Faber, 1995). The slug is a region of turbulence in the pipe that is separated from other turbulent segments by regions of laminar flow (Fig. 6.7). A necessary condition in order to have turbulent slug flow is that the ratio of the length of the pipe $l$ to its diameter $d$ must be greater than 50. This means that taking the length of the pipe to be 1-3 km (usually assumed depth for magma reservoirs in Iceland) its diameter will be 20-70 m, which is in the range estimated for other volcanoes around the world (Ida, 1996).

Turbulence moves through the pipe at a lower velocity than that of the laminar flow, slowing the incoming fluid down. This has the consequence that in a region of turbulence the pressure gradient will be steeper than where the flow is laminar, so that these pressure variations may act as a variable force on the conduit walls (Wallis, 1969). Laboratory measurements of the shear stress applied to the conduit walls during the passage of a turbulent slug (using water as fluid) have revealed that the stress signature starts with an initial sharp peak followed by a more gradual increase to a maximum at the trailing edge of the slug (Van Atta & Mautner, 1984) (Fig. 6.8). Taking into account the lack of high-frequency events, the crust beneath Vatnajökull is more likely to behave in a ductile manner, thus the conduit walls should be expected to be deformable and the radius of the pipe should change in space as well as in time as the slug moves upwards. However, the mathematical formulation and exact parameters of such an oscillation, capable of generating low-dimensional chaotic tremor signals, still remain uncertain and constitute a field for future studies.

This fluid-flow model, therefore, is a good candidate for explaining the excitation of observed tremor during the Vatnajökull eruption, and the following scenario may be put forward: assuming that the magma reservoir is connected to the surface by a narrow cylindrical conduit, then as the Reynolds number increases shortly before the eruption, turbulent slugs may develop and ascend through it. The slugs will be separated from each other by intervals of laminar flow and will exert a variable force on the conduit walls. Continuous tremor, therefore, may be the result

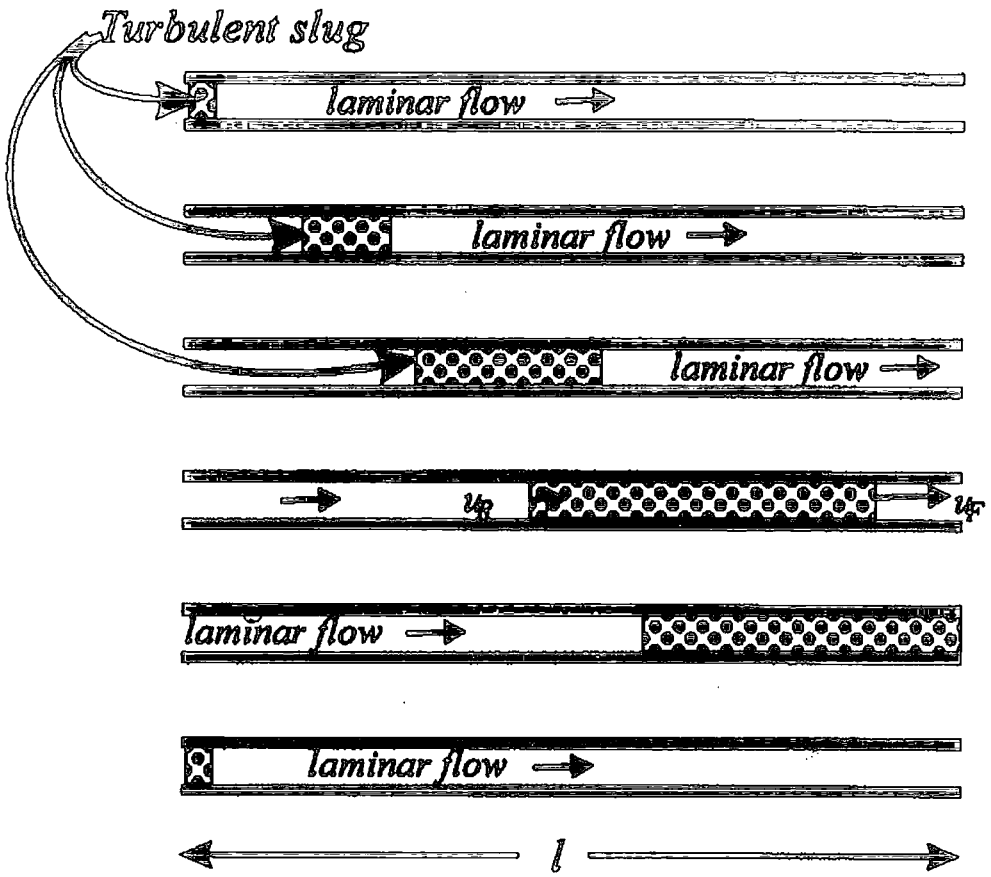


Figure 6.7: The cycle of generation of turbulence slugs. Time increases from top to bottom. Initially, laminar flow in the conduit has reached a Reynolds number at which turbulence is generated at the intake. The turbulence slows the flow and $Re$, therefore, decreases so that the fluid behind the turbulent section or slug again flows laminarly. As the turbulent slug progresses through the conduit, it lengthens because its forward end progresses more rapidly than the average flow velocity while the rear end is slower. Eventually the slug leaves the end of the conduit and the flow velocity increases until a new slug is generated. $u_R$ indicates the fluid velocity at the rear of the slug and $u_F$ at the front (from Hellweg, 2000).

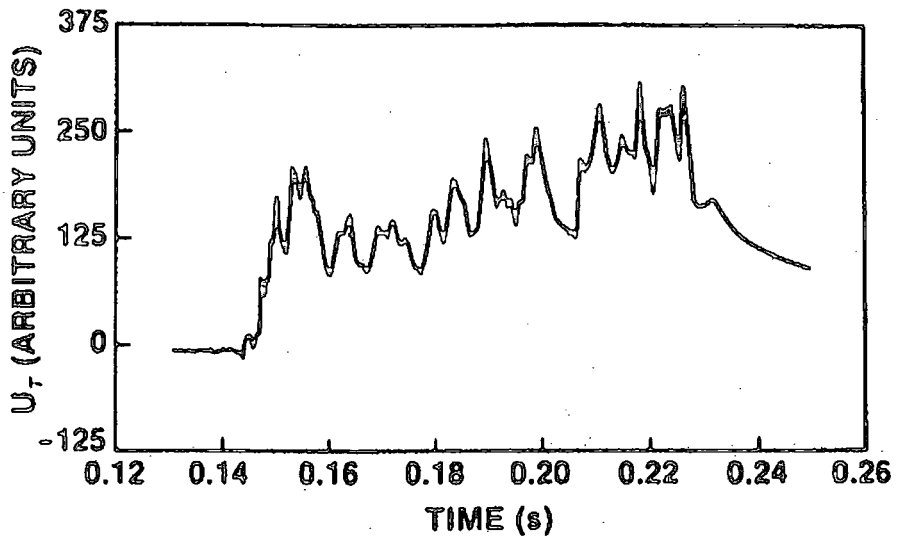


Figure 6.8: Graph showing a typical wall shear stress ($U_\tau$) signature measured during the passage of a turbulent slug. The series of well defined peaks and troughs reflect the fact that the slug is an unsteady, growing patch of turbulence with a highly variable (in time and space) pressure gradient (from Van Atta & Mautner, 1984).

of ascending turbulent slugs separated by small intervals of laminar flow, when the Reynolds number is high. As the eruption evolves and the Reynolds number decreases, these intervals become larger giving rise to background tremor, while sporadic slugs generate the observed bursts.

### *6.2.4 Conclusions*

Combining the geophysical and geochemical results published and presented in this thesis, the course of events during the 1996 Vatnajökull eruption can be divided into three stages and can be interpreted as follows:

**Stage 1 (September 28th-September 29th):** The pre-eruptive tremor signal detected by the spectral analysis of the HOT23 data probably reflects inflow of

magma from a deeper source to a shallow chamber beneath Bárdarbunga. Accumulation of magma inside the chamber caused its roof to inflate, creating all the necessary conditions for complicated rupture patterns along pre-established zones of weakness (such as ring-faults), that may have generated the large Bárdarbunga event and the low-frequency earthquakes that followed it.

**Stage 2 (September 29th-September 30th):** Lateral movement of magma from Bárdarbunga towards Grimsvötn, is supported by locations of events, using HOTSPOT and HOTSPOT and SIL arrival times, that show a gradual migration of epicentres along the eruption fissure. The classification of the volcanic earthquakes also revealed that the events occurring in the fissure were mixed-frequency events with clear onsets, indicating that fluid-injection and crack-widening processes may have taken place.

**Stage 3 (September 30th-October 2nd):** Magma surging laterally from the Bárdarbunga volcanic system facilitated the rupturing of the roof of the chamber of another magma body, remnant of the 1938 eruption, situated beneath the area where the eruption fissure was formed. Since this body had been cooled and crystallised for about 60 years, it is reasonable to assume that volatile exsolution was causing pressure build-up on its chamber roof, favouring an upward movement (Parfitt *et al.*, 1993). Thus, the mixed magma started moving along a vertical conduit, initially in a laminar fashion but later forming turbulent slugs, assimilating on its way crustal rocks, heating the ice and finally reaching the surface and erupting as volcanic tephra on the glacier.

### *6.2.5 Suggestions for future work*

Some suggestions for future work on the 1996 Vatnajökull eruption dataset are:

- Spectral analysis (by means of spectrograms) of data for the period starting

in August 1996, when station HOT23 was installed, up until the time of the eruption so as to determine the onset of the pre-eruptive tremor and detect possible temporal changes in the frequency content of the signal. This could help identify a specific source mechanism for pre-eruptive tremor and make estimations of the quantity of magma that flowed into the chamber beneath Bárdarbunga.

- Relocation of all the picked earthquakes using an improved one-dimensional, or possibly a three-dimensional, velocity model based on analysis of receiver functions and surface waves over Iceland (G. Nolet, pers. comm. 1999; V. Schlindwein, pers. comm. 2000). This would allow a reliable estimation of hypocentral depths that may possibly reveal special distribution patterns, e.g. hypocentres delineating an outward dipping ring-fault structure, as found at Rabaul caldera, Papua New Guinea (Mori & McKee, 1987).

- Obtain focal mechanisms of the events that followed the large Bárdarbunga earthquake to further constrain the scenarios regarding the physical mechanism of the eruption. The nature of these earthquakes (emergent onsets, lack of S phases) precludes the use of P or S waves polarities and amplitudes for moment tensor determination (e.g. Julian & Foulger, 1996). A waveform inversion method designed for regional data that would also allow non douple-couple mechanisms (e.g. Randall *et al.,* 1995), may prove much more suitable.

Further suggestions regarding future volcano monitoring of the Vatnajökull area could include:

- The large interstation spacing of the HOTSPOT stations ($>$ 50 km) points to the necessity of the installation of a number of broadband seismometers distributed over the three volcanic systems (Bárdarbunga, Grimsvötn, Tungafellsjökull) with a reduced spacing ($<$ 10 km). Even though the servicing of the network in an area such as northwest Vatnajökull may prove extremely difficult, such a configuration would help the classification of volcanic signals

by limiting the possibility of distorted waveforms due to propagation effects. Additionally, it would be possible to directly compare waveforms recorded at stations close to each other and use only a local velocity model when locating the events rather than a large scale one-dimensional model. It may also be possible to use the multi-station data to delineate the source area of tremor, e.g. by using the semblance method (section 3.3.3.2).

- Some of the instruments should record at a higher sampling rate of 200-400 samples $s^{-1}$, so that the tremor process will be sufficiently sampled. By modifying the code in the *nstat_z* TISEAN program (sections 4.7.1 and 4.7.2) it will be possible to use the method of cross-prediction (Schreiber, 1997) to directly compare the fractal dimension, instead of the prediction error, for pairs of segments. This would allow a detailed examination of the properties of the tremor attractor, since a knowledge of the temporal variation of the fractal dimension will give a measure of the self-orginisation (degrees of freedom present) that can be used subsequently for source modelling purposes.

- The installation of sensitive microphones that record air pressure variations could provide data that may be used for the application of methods for the determination of the physical properties of magma columns (section 3.4).

## 6.3 Seismic imaging of the 57°45'N AVR

### *6.3.1 Interpretation of reflection events*

The final seismic section for Line 37 is given in an enclosure at the end of this thesis, with the reflection events that could correspond to geological boundaries clearly marked. After comparison with the synthetic seismic section (Fig. 6.9) generated by forward modelling of the wide-angle model (Navin *et al.*, 1996), the following observations may be deduced (all times given correspond to two-way travel times annotated every 1000 ms on the vertical axis of the section):

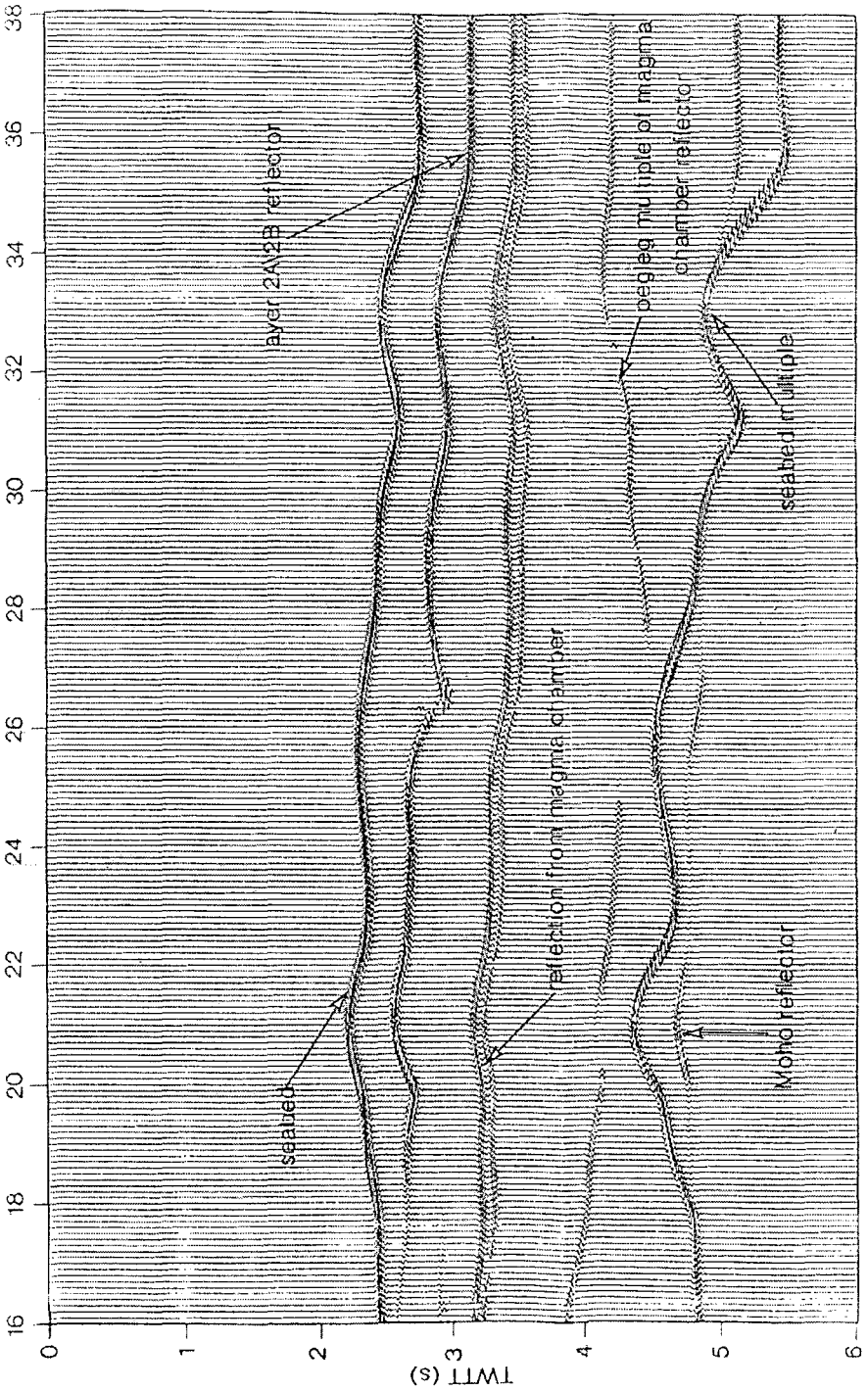


Figure 6.9: Along-axis synthetic seismic section generated using the wide-angle model of Navin (1996). The main reflectors are labelled and the horizontal axis represents offset distance in km. The position of this synthetic section relative to the observed seismic section is noted on the Versatec plot provided at the end of the thesis.(from Navin, 1996).

- The discontinuous reflection events that start at 3 s and progressively get shallower reaching 2.65 s may correspond to the boundary between layers 2A and 2B. The 2A/2B boundary is either caused by a transition from the pillow lavas of layer 2A into the sheeted dykes of layer 2B or it may be a porosity boundary due to increased confining pressure closing the pore space and fractures at depth.

- The faint reflection events at 3.35 s may correspond to reflections from the upper part of a melt lens, while the events appearing underneath at 3.9-4.1 s may be the peg-leg multiples from it. A similar pattern to this, was found by Inglis (1995) and Navin (1996) after processing the along-axis 4-fold normal incidence data. However, it was not possible (due to noise) to observe any polarity reversals on these reflection events, that would further support this interpretation.

- The two areas marked by arrows correspond to calderas and areas where lava flows were found, based on the seafloor imaging conducted only in the northern part of the study area (Parson *et al.,* 1993). However, no noticeable reflection events that could be attributed to the presence of melt, are observed underneath. This can be explained either by the assumption that non-erupted magma has crystallised, or that the remaining magma bodies are too small ($< 1$ km) to be sufficiently resolved. Unfortunately the age of the lava flows, which could help distinguish between the two possibilities, is not known.

- The three dipping reflection events marked by question marks are not predicted by the synthetic section and no similar features have been imaged in other mid-ocean ridges around the world. They could be either intra-crustal reflections representing possibly fault surfaces, or artefacts created during the stage of data acquisition, e.g. side-swipe events. If the former interpretation is true, then reflection events from these structures should be also present in the adjacent along-axis lines and it will be possible to image their extent in three dimensions.

### *6.3.2 Conclusions*

The main conclusions stemming from the processing and interpretation of Line 37 data concern the following areas:

**Nature of the data and processing:** In general, seismic reflection data shot over slow spreading ridges contain large amounts of coherent noise that significantly lower the signal-to-noise ratio. Even though the RAMESSES dataset was substantially improved compared to the reflection data shot in the first survey (32-fold versus 4-fold), the amount of coherent noise was still high and careful processing was needed in order to recover the reflection events. Stacking the data with velocity functions either derived from semblance plot picks or from the wide-angle model proved to be a more robust approach to increase the signal-to-noise ratio than traditional noise attenuation methods like F-K filtering. Also an important processing step was the application of pre-stack deterministic deconvolution, which substantially improved the quality of the data and performed a lot better than the statistical deconvolution techniques.

**The magmatic processes at the 57°45'N AVR:** The reflection events found in the along-axis Line 37 provide some further evidence for the existence of a melt lens at the 57°45'N axial volcanic ridge, even though no reflector was imaged below the area where lava flows were observed on the seafloor. These observations can probably be explained in terms of a tectono-magmatic cycle, when there are short periods of episodic magma supply from the mantle and volcanic construction of the AVR, followed by longer periods of amagmatic crustal extension. In particular for the 57°45'N AVR, the constraints put by the modelling of the seismic and electromagnetic data collected during the first survey, indicate that the melt currently residing within the crust probably represents 20,000 years of crustal growth (Sinha *et al.*, 1998). Sinha *et al.* (1998) further suggest based on thermal arguments, that if magma is being injected episodically in the crust in cycles of 20,000 years (assuming that the magma supply rate is not changed), it takes less than 2,000 years to

get completely crystallised. This suggestion puts forward the idea that the resulting magma bodies along the AVR are transient rather than steady-state features. However, more observations from the remaining RAMESSES lines should be included in order to draw definite conclusions about the time/space frame that magma bodies may reside at crustal levels in this particular AVR.

### *6.3.3 Suggestions for future work*

The ProMAX processing software offers a wide variety of tools that could be used to further enhance the data (the rest of the RAMESSES lines are already being processed by C. Gill at the University of Durham). The following suggestions may be applied not only for further processing of Line 37, but also for processing the remaining RAMESSES lines:

- Investigation of other techniques of deterministic deconvolution by designing the inverse filter using either sonobuoy data recorded during the RRS Discovery 235c cruise, or by numerically simulating the airgun array source signature. This would further improve the quality of the data pre-stack.
- Improve the static corrections by applying hand statics. The exact static correction for every channel position for each shot could be calculated using the source and streamer depth information collected during the cruise. This would further decrease the time uncertainty where reflection events appear.
- Apply dip moveout (DMO) corrections in order to reduce smearing effects from dipping reflectors in CMP gathers, which will help producing a better quality stack.
- Repeat the velocity analysis decreasing the number of CMP gathers (e.g. from 25 used in this study to 15) in the supergather formation when calculating the semblance. This would result in smaller amounts of coherent noise being included, making easier the picking of velocities on the semblance plot.

# References


Abarbanel, H. D. I., 1996. Analysis of observed chaotic data, Springer, New York.

Abarbanel, H. D. I., Brown, R., Sidorowich, J. J., Tsimring, L. S., 1993. The analysis of observed chaotic data in physical systems, Rev. Mod. Phys., 65, 1331-1392.

Aki, K., 1957. Space and time spectra of stationary stochastic waves, with special reference to microtremors, Bull. Earthq. Res. Inst. Tokyo Univ., 25, 415-457.

Aki, K., 1959. Correlational study of near earthquakes waves, Bull. Earthq. Res. Inst. Tokyo Univ., 37, 207-232.

Aki K., Fehler, M., Das, S., 1977. Source mechanism of volcanic tremor: fluid-driven crack models and their application to the 1963 Kilauea eruption, J. Volcanol. Geoth. Res., 2, 259-287.

Aki, K., 1992. State of the art in Volcanic Seismology, In: P. Gasparini, R. Scarpa, K. Aki (Eds), Volcanic Seismology, IAVCEI Proceedings in Volcanology, 3, 3-10.

Aki, K., Koyanagi, R. Y., 1981. Deep volcanic tremor and magma ascent mechanism under Kilauea, Hawaii, J. geophys. Res., 86, 7095-7110.

Allen, R. M., Nolet, G., Morgan, W. J., Vogfjörd, K., Bergsson, B. H., Erlendsson, P., Foulger, G. R., Jakobsdóttir, S., Julian B. R., Pritchard, M. J., Ragnarsson, S., Stefánsson, R., 1999. The thin hot plume beneath Iceland, Geophys. J. Int., 137-51-63.

Almendros, J., Ibanez, J. M., Alguacil, G., Del Pezzo, E., Ortiz, R., 1997. Array tracking of the volcanic tremor source at Deception island, Antarctica, Geophys. Res. Lett., 24, 3069-3072.

Angeheister, G., Gebrande, H., Müller, H., Goldflam, P., Weigel, W., Jacoby, W. R., Pálmason, G., Björnsson, S., Einarsson, P., Pavlenkova, N. I., Zverev, S. M., Litvinenko, I. V., Loncarevic, B., Solomon, S. C., 1980. Reykjanes Ridge Iceland Seismic Experiment (RRISP 77), J. Geophys., 47, 228-238.

Anstey, N. A., 1981. Seismic prospecting instruments volume 1: Signal characteristics and instrument specifications, Gebruder Bornträger, Berlin.

Arvidsson, R., Ekström, G., 1998. Teleseismic CMT solutions for small earthquakes, $M_w \geq 4.5$ - A new global approach, Bull. Seism. Soc. Am., 88, 1003-1013.

Bame, D., Fehler, M., 1986. Observations of long-period earthquakes accompanying hydraulic fracturing, Geophys. Res. Lett., 13, 149-152.

Beblo, M., Björnsson, A., 1980. A model of electrical resistivity beneath northeast Iceland, correlation with temperature, J. Geophys., 47, 184-190.

Beblo, M., Björnsson, A., Arnason, K., Stein, B., Wolfgram, B., 1983. Electrical conductivity beneath Iceland- constraints imposed by magnetotelluric results on temperature, partial melt, crust-structure and mantle-structure, J. Geophys., 53, 16-23.

Benoit J., McNutt, S. R., 1997. New constraints on the source processes of volcanic tremor at Arenal volcano, Costa Rica, using broadband seismic data, Geophys. Res. Lett., 24, 449-452.

Bergé, P., Pomeau, Y., Vidal, C., 1986. Order within Chaos: Towards a deterministic approach to turbulence, John Wiley, New York.

Bjarnasson, I. T., Menke, M., Flóvenz, O. G., Caress, D., 1993. Tomographic image of the Mid-Atlantic plate boundary in southwestern Iceland. J. Geophys. Res. 98, 6607-6622.

Björnsson, H., 1988. Hydrology of ice caps in volcanic regions. Soc. Sci. Isl. Reykjavik 45, 139.

Björnsson, H., Einarsson, P., 1990. Volcanoes beneath Vatnajökull, Iceland: Evidence from radio echo-sounding, earthquakes and jökulhlaups. Jökull 40, 147-167.

Bond, T., 2000. A study of very long period seismicity at Kilauea volcano, Hawaii, MSc thesis, University of Durham.

Bott, M. H. P., 1985. Plate tectonic evolution of the icelandic transverse ridge and adjacent regions, J. Geophys. Res., 90, 9953-9960.

Bratt, S. R., Purdy, J. M., 1984. Structure and variability of oceanic crust on the flanks of the East Pacific Rise between 11° and 13° N, J. Geophys. Res., 89, 6111-6125.

Brandsdóttir, B., Einarsson, P., 1979. Seismic activity associated with the September 1977 deflation of the Krafla central volcano in NE Iceland, J. Volcanol. Geotherm. Res., 6, 197-212.

Brandsdóttir, B., Einarsson, P., 1992. Volcanic tremor and low-frequency earthquakes in Iceland, In: P. Gasparini, R. Scarpa, K. Aki (Eds), Volcanic Seismology, IAVCEI Proceedings in Volcanology, 3, 212-222.

Brandstätter, A., Swinney, H. L., 1987. Strange attractors in weakly turbulent Couette-Taylor flow, Phys. Rev. A, 35, 2207-2220.

Brown, G. C., Mussett, A. E., 1981. The inaccessible earth, George Allen and Unwin.

Båth, M., 1960. Crustal structure of Iceland, J. Geophys. Res., 65, 1793-1807.

Båth, M., 1974. Spectral analysis in Geophysics, Elsevier Science, Amsterdam.

Burg, J. P., 1967. Maximum Entropy spectral analysis, In: Childers (Ed), Modern spectral analysis, IEEE press, 34-41.

Calvert, A. J., 1995. Seismic evidence for a magma chamber beneath the slow-spreading Mid-Atlantic Ridge, Nature, 377, 410-413.

Cann, J. R., 1974. A model for oceanic crustal structure developed, Geophys. J. R. Astr. Soc, 39, 169-187.

Chouet, B., 1985. Excitation of a buried magmatic pipe: A seismic source model for volcanic tremor, J. Geophys. Res., 90, 1881-1893.

Chouet, B., 1986. Dynamics of a fluid-driven crack in three dimensions by the finite difference method, J. Geophys. Res., 91, 967-992.

Chouet, B., 1988. Resonance of a fluid-driven crack: radiation properties and implications for the source of long-period events and harmonic tremor, J. Geophys. Res., 93, 4375-4400.

Chouet, B., Shaw, H. R., 1991. Fractal properties of tremor and gas piston events observed at Kilauea volcano, J. Geophys. Res., 96, 10,177-10,189.

Chouet, B., 1992. A seismic model for the source of long-period events and harmonic tremor, In: P. Gasparini, R. Scarpa, K. Aki (Eds), Volcanic Seismology, IAVCEI Proceedings in Volcanology, 3, 133-156.

Chouet, B., De Luca, G., Milana, G., Dawson, P., Martini, M., Scarpa, R., 1998. Shallow velocity structure of Stromboli volcano, Italy, derived from small aperture array measurements of Strombolian tremor, Bull. Seis. Soc. Am., 88, 653-666.

Chouet, B., Saccaroti, G., Dawson, P., Martini, M., Scarpa, R., DeLuca, G., Milana, G., Cattaneo, M., 1999. Broadband measurements of the sources of explosions at Stromboli volcano, Italy, Geophys. Res. Lett., 26, 1937-1940.

Christenson, G. L., Purdy, G. M., Rohr, K. M. M., 1993. Structure of the northern symmetrical segment of the Juan de Fuca ridge, Marine Geophys. Res., 15, 219-240.

Christenson, G. L., Purdy, G. M., Fryer, G. J., 1994. Seismic constraints on shallow crustal emplacement processes at the fast spreading East Pacific Rise, J. Geophys. Res., 99, 17957-19973.

Collier, J. S., Sinha, M. C., 1990. Seismic images of a magma chamber beneath the Lau Basin back-arc spreading centre, Nature, 346, 646-648.

Collier, J. S., Singh, S. C., 1997. Detailed structure of the top of the melt body beneath the East Pacific Rise at 9o40'N from waveform inversion of seismic reflection data, J. Geophys. Res., 102, 20,287-20,304.

Cortini, M., Cilento, L., Rullo, A., 1991. Vertical ground movements in the Campi Flegrei caldera as a chaotic dynamic phenomenon, J. Volcanol. Geotherm. Res., 48, 103-113.

Crosson, R. S., Bame, D. A., 1985. A spherical source model for low frequency volcanic earthquakes, J. Geophys. Res., 90, 10,237-10,247.

Cudrak, C. F., Clowes, R. M., 1993. Crustal structure of Endeavour ridge, Juan de Fuca ridge, from a detailed seismic refraction survey, J. Geophys. Res., 98, 6329-6349.

Darbyshire, F. A., Bjarnason, I. T., White, R. S., Flóvenz, O. G., 1998. Crustal structure above the Iceland mantle plume imaged by the ICEMELT refraction profile, Geophys. J. Int. 135, 1131-1149.

DeMets, C., Gordon, R. G., Argus, D. F., Stein, S., 1994. Current plate motions, Geophys. J. Int., 101, 425-478.

Detrick, R. S., Buhl, P., Vera, E. E., Mutter, J. A., Orcutt, J. A., Madsen, J., Brocher, T., 1987. Multichannel seismic imaging of a crustal magma chamber along the East Pacific Rise, Nature, 326, 35-41.

Detrick, R. S., Mutter, J. C., Buhl, P., Kim, I. I., 1990. No evidence from multichannel reflection data for a crustal magma chamber in the MARK area on the Mid-Atlantic Ridge, Nature, 347, 61-63.

Dobrin, M., Savit, C., 1986. Introduction to geophysical prospecting, John Wiley, New York.

Drazin, P. G., 1994. Nonlinear systems, Cambridge University Press, New York.

Du, Z. J., Foulger, G. R., 1999. The crustal structure beneath the northwest fjords, Iceland, from receiver functions and surface waves, Geophys. J. Int., 139, 419-432.

Dvorak, J. J., Okamura, A. T., 1985. Variations in tilt rate and harmonic tremor amplitude during the January-August 1983 East Rift eruptions of Kilauea volcano, Hawaii, J. Volcanol. Geoth. Res., 25, 249-258.

Einarsson, T., 1954. A survey of gravity in Iceland, Visindafelag Isl. Rit., 30, 22.

Einarsson, P., 1978. S-wave shadows in the Krafla caldera in NE-Iceland: Evidence for a magma chamber in the crust. Bull. Volcanol. 41, 1-9.

Einarsson, P., Brandsdóttir, B., 1980. Seismological evidence for a lateral magma intrusion during the July 1978 deflation of the Krafla volcano in NE Iceland, J. Geophys., 47, 160-165.

Einarsson, P., 1991. Earthquakes and present-day tectonism in Iceland. Tectonophysics 189, 261-279.

Einarsson, P., Brandsdóttir, B., 1984. Seismic activity preceding and during the 1983 volcanic eruption Grimsvötn, Iceland. Jökull 34, 13-23.

Einarsson, P., Brandsdóttir, B., Gudmundsson, M. T., Björnsson, H., 1997. Center of the Iceland hotspot experiences volcanic unrest, EOS, 78, 374-375.

Ereditato D., Luongo, G., 1994. Volcanic tremor wavefield during quiescent and eruptive activity at Mt. Etna (Sicily), J. Volcanol. Geoth. Res., 61, 239-251.

Eysteinsson, H., Hermance, J. F., 1985. Magnetotelluric measurements across the eastern neovolcanic zone in south Iceland, J. Geophys. Res., 90, 10093-10103.

Faber, T. E., 1995. Fluid dynamics for physicists. Cambridge University Press, Cambridge.

Farouk, H., 1999. Processing and interpretation of a multichannel streamer seismic reflection profile collected over the Reykjanes ridge, MSc thesis, University of Durham.

Fedotov, S. A., 1981. Magma rates in feeding conduits of different volcanic centres, J. Volcanol. Geoth. Res., 9, 379-394.

Fehler, M. C., 1983. Observations of volcanic tremor at Mt. St Helens volcano, J. Geophys. Res., 88, 3476-3484.

Ferrazzini, V., Aki, K., 1987. Slow waves trapped in a fluid-filled infinite crack: implication for volcanic tremor, J. Geophys. Res., 92, 9215-9223.

Ferrazzini, V., Aki, K., Chouet, B., 1991. Characteristics of seismic waves composing Hawaiian volcanic tremor and gas-piston events observed by a near source array, J. Geophys. Res., 96, 6199-6209.

Ferrazzini, V., Aki, K., 1992. Preliminary results from a field experiment on volcanic events at Kilauea using an array of digital seismographs, In: P. Gasparini, R. Scarpa, K. Aki (Eds), Volcanic Seismology, IAVCEI Proceedings in Volcanology, 3, 168-189.

Ferrick, M. G., Qamar, A., St. Lawrence, W. F., 1982. Source mechanism of volcanic tremor, J. Geophys. Res., 87, 8675-8683.

Ferrick, M. G., St. Lawrence, W. F., 1984. Comment on 'Observations of volcanic tremor at Mt. St Helens volcano' by Michael Fehler, J. Geophys. Res., 89, 6349-6350.

Ferrucci, F., Godano, C., Pino, N. A., 1990. Approach to the volcanic tremor by covariance analysis: Application to the 1989 eruption of Mt Etna (Sicily), Geophys. Res. Lett., 17, 2425-2428.

Fowler, C. M. R., 1976. Crustal structure of the Mid-Atlantic ridge crest at 37°N, Geophys. J. R. astr. Soc., 47, 459-491.

Fowler, C. M. R., 1978. The Mid-Atlantic ridge: Structure at 45°N, Geophys. J. R. astr. Soc., 54, 167-186.

Fowler, C. M. R., 1990. The solid earth: An introduction to solid earth geophysics, Cambridge University Press, Cambridge.

Fraser, A. M., Swinney, H. L., 1986. Independent coordinates for strange attractors from mutual information, Phys. Rev. A, 33, 1134-1140.

Frede, V., Mazzega, P., 1999. Detectability of deterministic nonlinear processes in earth rotation time series- I. Embedding, Geophys. J. Int., 137, 551-564.

Fukao, Y., Fujita, E., Hori, S., Kanjo, K., 1998. Response of a volcanic conduit to step-like change in magma pressure, Geophys. Res. Lett., 25, 105-108.

Furumoto, M., Kunimoto, T., Inoue, H., Yamada, I., Yamaoka, K., Akami, A., Fukao, Y., 1990. Twin sources of high-frequency volcanic tremor of Izu-Oshima volcano, Japan, Geophys. Res. Lett., 17, 25-27.

Furumoto, M., Kunimoto, T., Inoue, H., Yamaoka, K., 1992. Seismic image of the volcanic tremor source at Izu-Oshima volcano, Japan, In: P. Gasparini, R. Scarpa, K. Aki (Eds), Volcanic Seismology, IAVCEI Proceedings in Volcanology, 3, 201-211.

Garcés, M. A., 1997. On the volcanic waveguide, J. Geophys. Res., 102, 22,547-22564.

Garcés, M. A., McNutt, S. R., 1997. Theory of the airborne sound field generated in a resonant magma conduit, J. Volcanol. Geoth. Res., 78, 155-178.

Garcés, M. A., Hansen, R. A., 1998. Waveform analysis of seismoacoustic signals radiated during the Fall 1996 eruption at Pavlof volcano, Alaska, Geophys. Res. Lett., 25, 1051-1054.

Garcés, M. A., Hagerty, M. T., Schwartz, S. Y., 1998. Magma acoustics and time-varying melt properties at Arenal volcano, Costa Rica, Geophys. Res. Lett., 25, 2293-2296.

Garcés, M. A., Iguchi, M., Ishihara, K., Morrisey, M., Sudo, Y., Tsutsui, T., 1999. Infrasonic precursors to a vulcanian eruption at Sakurajima volcano, Japan, Geophys. Res. Lett., 26, 2537-2540.

Garcés, M. A., McNutt, S. R., Hansen, R. A., Eichelberger, J. C., 2000. Application of wave-theoretical models to the interpretation of explosion and eruption tremor signals radiated by Pavlof volcano, Alaska, J. Geophys. Res., 105, 3039-3058.

Gebrande, H., Müller, H., Einarsson, P., 1980. Seismic structure of Iceland along RRISP profile I, J. Geophys. Res., 47, 239-249.

Goldstein, P., Chouet, B., 1994. Array measurements and modelling of sources of shallow volcanic tremor at Kilauea volcano, Hawaii, J. Geophys. Res., 99, 2,637-2,652.

Goldstein, P., Dodge, D., Firpo, M., Ruppert, S., 1998. What's new in SAC2000? Enhanced processing and database access. Seism. Res. Lett. 69, 202-205.

Gordeev, E. I., Saltykov, V. A., Synitsin, V. I., Chebrov, V. N., 1990. Temporal and spatial characteristics of volcanic tremor wavefields, J. Volcanol. Geoth. Res., 40, 89-101.

Gudmundsson, A., 1995. Infrastructure and mechanics of volcanic systems in Iceland. J. Volcanol. Geotherm. Res. 64, 1-22.

Gudmundsson, A., Marti, J., Turon, E., 1997. Stress fields generating ring faults in volcanoes. Geophys. Res. Lett. 24, 1559-1562.

Gudmundsson, O., Brandsdóttir, B., Menke, M., Sigvaldason, G. E., 1994. The crustal magma chamber of the Katla volcano in south Iceland revealed by 2-D seismic undershooting. Geophys. J. Int. 119, 277-296.

Gudmundsson, M. T., 1989. The Grimsvötn caldera, Vatnajökull: Subglacial topography and structure of caldera infill. Jökull 39, 1-20.

Gudmundsson, M. T., Björnsson, H., 1991. Eruptions in Grimsvötn, Vatnajökull, Iceland, 1934-1991. Jökull 41, 21-42.

Gudmundsson, M. T., Sigmundsson, F., Björnsson, H., 1997. Ice-volcano interaction of the 1996 Gjálp subglacial eruption. Vatnajökull, Iceland, Nature, 389, 954-957.

Gudmundsson, M. T., Milsom, J., 1997. Gravity and magnetic studies of the subglacial Grimsvötn volcano, Iceland: Implications for crustal and thermal structure, J. Geophys. Res., 102, 7691-7704.

Hall, L., 1999. The search for a magma chamber beneath the slow spreading Reykjanes ridge, BSc thesis, University of Cambridge.

Hagerty, M. T., Schwartz, S. Y., Garcés, M. A., Protti, M., 2000. Analysis of seismic and acoustic observations at Arenal volcano, Costa Rica, 1995-1997, J. Volcanol. Geoth. Res., 101, 27-65.

Hartzel, S. H., Heaton, T. H., 1983. Inversion of strong ground motion and teleseismic waveforms for the fault rupture history of the 1979 Imperial Valley, California earthquake, Bull. Seism. Soc. Am., 73, 1703-1724.

Hatton, L., Worthington, M. H., Makin, J., 1986. Seismic data processing, Blackwell Scientific Publications, London.

Hegger, R., Kantz, H., Schreiber, T., 1999. Practical implementation of nonlinear time series methods: The TISEAN package, CHAOS, 9, 413.

Hellweg, M., 2000. Physical models for the source of Lascar's harmonic tremor, J. Volcanol. Geotherm. Res., 101, 183-198.

Hersir, G. P., Björnsson, A., Pedersen, L., 1984. Magnetotelluric survey across the active spreading zone in southwest Iceland, J. Volcanol. Geoth. Res., 20, 253-265.

Hill, D. P., 1957. Recent geophysical exploration of the ocean floor, Phys. Chem. Earth, 2, 129-163.

Hofstetter, A. S., Malone, S. D., 1986. Observations of volcanic tremor at Mt. St Helens in April and May 1980, Bull. Seis. Soc. Am., 76, 923-938.

Houtz, R., Ewing, J., 1976. Upper crustal structure as a function of plate age, J. Geophys. Res., 81, 2490-2498.

Huang, P. Y., Solomon, S. C., 1988. Centroid depths of mid-ocean ridge earthquakes: Dependence on spreading rate, J. Geophys. Res., 93, 13445-13447.

Hurst, A. W., 1985. A volcanic tremor monitoring system, J. Volcanol. Geoth. Res., 26, 181-187.

Hurst, A. W., 1992. Stochastic simulation of volcanic tremor from Ruapehu, J. Volcanol. Geoth. Res., 51, 185-198.

Ida, Y., Kumazawa, M., 1986. Ascent of magma in a deformable vent, J. Geophys. Res., 91, 9297-9301.

Ida, Y., 1996. Cyclic fluid effusion accompanied by pressure change: implication for volcanic eruptions and tremor, Geophys. Res. Lett., 23, 1457-1460.

Inglis, M. A., 1995. Processing of problem marine seismic reflection data: The Reykjanes ridge, North Atlantic, MSc thesis, University of Durham.

Jakobsson, S., 1979. Petrology of recent basalts of the eastern volcanic zone, Iceland. Acta Nat. Isl. 26, 103.

Jakobsson, S., 1980. Outline of the petrology of Iceland. Jökull 29, 57-73.

Jordan, D. W., Smith, P., 1987. Nonlinear ordinary differential equations. Oxford University Press, Clarendon.

Joset, A., Holtzscherer, J. J., 1954. Expedition Franco-Islandaise au Vatnajökull Mars-Avril 1951, Resultats des sondages seismic. Jökull 4, 1-32.

Julian, B. R., 1983. Evidence for dyke intrusion earthquake mechanisms near Long Valley caldera, California. Nature 303, 323-325.

Julian, B. R., 1994. Volcanic tremor: Nonlinear excitation by fluid flow, J. Geophys. Res., 99, 11,859-11,877.

Julian, B. R., Foulger, G. R., 1996. Moment tensors from linear inversion of body-wave amplitude ratios: powerfull constraints on earthquake mechanisms, Bull. Seism. Soc. Am., 86, 972-980.

Jurkevics, A., 1988. Polarisation analysis of three-component array data, Bull. Seis. Soc. Am., 78, 1725-1743.

Kanamori, H., Ekström, G., Dzievonski, A., Barker, J. S., Sipkin, S. A., 1993. Seismic radiation by magma injection: An anomalous seismic event near Tori Shima, Japan, J. Geophys. Res., 98, 6511-6522.

Kantz, H., Schreiber, T., 1996. Nonlinear time series analysis. Cambridge University Press, Cambridge.

Kawakatsu, H., Ohminato, T., Ito, H., 1994. 10 s period volcanic tremors observed over a wide area in south-western Japan, Geophys. Res. Lett., 21, 1963-1966.

Kawakatsu, H., Kaneshima, S., Matsubayashi, H., Ohminato, T., Sudo, Y., Tsutsui, T., Uhira, K., Yamasato, H., Legrand, D., 2000. Aso94: Aso seismic observation with broadband instruments, J. Volcanol. Geoth. Res., 101, 129-154.

Keary, P., Vine, F., 1990. Global Tectonics, Blackwell Science, Oxford.

Kedar, S., Sturtevant, B., Kanamori, H., 1996. The origin of harmonic tremor at Old Faithful geyser, Nature, 379, 708-711.

Keers, H., Dahlen, F. A., Nolet, G., 1997. Chaotic ray behaviour in regional seismology, Geophys. J. Int., 131, 361-380.

Kennel, M. B., Brown, R., Abarbanel, H. D. I., 1992. Determining embedding dimension for phase-space reconstruction using a geometrical construction, Phys. Rev. A, 45, 3403-3411.

Kennel, M. B., Isabelle, S., 1992. Methods to distinguish possible chaos from coloured noise and to determine embedding parameters. *Phys. Rev. A*, **46**, 3111.

Kieffer, S. W., 1984. Seismicity at Old Faithful geyser: An isolated source of geothermal noise and possible analogue of volcanic seismicity, J. Volcanol. Geoth. Res., 22, 59-95.

Kubotera, A., 1974. Volcanic tremors at Aso volcano, In: L. Civetta, P. Gasparini, G. Luongo, A. Rapolla (Eds), Physical Volcanology, Elsevier, 29-48.

Larsen, G., 1984. Recent volcanic history of the Veidivötn fissure swarm, southern Iceland- an approach to volcanic risk assessment. J. Volcanol. Geotherm. Res. 22, 33-58.

Latter, J., 1979. Volcanological observations at Tongariro national park (2) Types and classification of volcanic earthquakes 1976-1978, Geophysics Division report, 150, Dept. Sci. and Ind. Res.

Lay, T., Wallace, T. C., 1995. Modern Global Seismology, Academic Press, New York.

Lawver, L. A., Müller, R. D., 1994. Iceland hotspot track, Geology, 22, 311-314.

Leet, R. C., 1988. Saturated and subcooled hydrothermal boiling in groundwater flow channels as a source of harmonic tremor, J. Geophys. Res., 93, 4835-4849.

Li, T. Y., York, J. A., 1975. Period three implies chaos, Amer. Math. Monthly, 82, 985-992.

Lorenz, E. N., 1963. Deterministic nonperiodic flow, J. Atmos. Sci., 20, 130-141. itemLorenz, E. N., 1969. Atmospheric predictability as revealed by naturally occuring analogues, J. Atmos. Sci., 26, 636.

Maeda, I., 2000. Nonlinear visco-elastic volcanic model and its application to the recent eruption of Mt Unzen, J. Volcanol. Geoth. Res., 95, 35-47.

Macdonald, K. C., 1982. Mid-ocean ridges: Fine scale tectonic, volcanic and hydrothermal processes within the plate boundary zone, Ann. Rev. Earth planet. Sci., 10, 155-190.

Macdonald, K. C., 1989. Anatomy of the magma reservoir, Nature, 339, 178-179.

MacGregor, L. M., Constable, S., Sinha, M. C., 1998. The RAMESSES experiment III: Controlled source electromagnetic sounding of the Reykjanes Ridge at 57°45'N, Geophys. J. Int., 135, 773-789.

McNutt, S. R., 1986. Observations and analysis of B-type earthquakes, explosions and volcanic tremor at Pavlof volcano, Alaska, Bull. Seis. Soc. Am., 76, 153-175.

McNutt, S. R., 1996. Seismic monitoring and eruption forecasting of volcanoes: A review of the state-of-the-art and case histories, In: Scarpa, Tilling (Eds), Monitoring and mitigation of volcanic hazards, 100-146.

MELT Seismic Team, 1998. Imaging the deep seismic structure beneath a mid-ocean ridge: The MELT experiment, Science, 280, 1215-1238.

Menke, W., Levin, V., Sethi, R., 1995. Seismic attenuation in the crust at the Mid-Atlantic boundary in south-west Iceland, Geophys. J. Int., 122, 175-182.

Menke, W., Brandsdóttir, Einarson, P., Bjarnasson, I. T., 1996. Reinterpretation of the RRISP-77 Iceland shear wave profiles, Geophys. J. Int., 126, 166-172.

Métaxian, J. P., Lesage, P., Dorel, J., 1997. Permanent tremor of Masaya volcano, Nicaragua: Wave field analysis and source location, J. Geophys. Res, 102, 22,529-22,545.

Minakami, T., 1960. Fundamental research for predicting volcanic eruptions (Part 1), Bull. Earthq. Res. Inst. Univ. Tokyo, 38, 497-544.

Montalbetti, J. F., Kanasewich, K. R., 1970. Enhancement of teleseismic body phases with a polarisation filter, Geophys. J. R. Astr. Soc., 21, 119-129.

Morton, J. L., Sleep, N. H., 1985. Seismic reflections from the Lau Basin magma chamber, In: D. W. scholl and T. L. Vallier (Eds), Geology and offshore resources of Pacific island arcs - Tonga region, Earth Sci. Ser., 2, Circum Pacific council for energy and mineral resources, Houston, Texas, 441-453.

Morton, J. L., Sleep, N. H., Normark, W. R., Tomkins, D. H., 1987. Sructure of the southern Juan de Fuca ridge from seismic refraction records, J. Geophys. Res, 92, 11315-11326.

Mori, J., McKee, C., 1987. Outward dipping ring fault structure at Rabaul caldera as shown by earthquake locations, Science, 235, 193-195.

Navin, D. A., 1996. Seismic investigation on crustal accretion at the slow-spreading Mid-Atlantic ridge- the Reykjanes ridge at 57°45'N, PhD thesis, University of Durham.

Navin, D. A., Peirce, C., Sinha, M. C., 1998. RAMESSES II- Evidence for accumulated melt beneath a slow spreading ridge from wide-angle refraction and multichannel reflection seismic profiles, Geoph. J. Int., 135, 746-772.

Neidel, N., Taner, M. T., 1971. Semblance and other coherency measure for multichannel data, Geophysics, 36, 483-497.

Nettles, M., Ekström, G., 1998. Faulting mechanism of anomalous earthquakes near Bárdarbunga volcano, Iceland. J. Geophys. Res. 103, 17973-17983.

Nishimura, T., Hamaguchi, H., Ueki, S., 1995. Source mechanisms of volcanic tremor and low-frequency earthquakes associated with the 1988-89 eruptive activity of Mt Tokachi, Hokaido, Japan, Geophys. J. Int., 121, 444-458.

Ohminato, T., Ereditato, D., 1998. Broadband seismic observations at Satsuma-Iwojima volcano, Japan, Geophys. Res. Lett., 24, 2845-2848.

Oikawa, J., Ida, Y., Yamaoka, K., Watanabe, H., Fukuyama, E., Sato, K., 1991. Ground deformation associated with volcanic tremor at Izu-Oshima volcano, Geophys. Res. Lett., 18, 443-446.

Pálmason, G., 1971. Crustal structure of Iceland from explosion seismology, Greinar Visindafelag Isl.

Parfitt, E. A., Wilson, L., Head, J. W., 1993. Basaltic magma reservoirs: Factors controlling their rupture characteristics and evolution, J. Volcanol. Geoth. Res., 55, 1-14.

Parson et al., 1993. En enchelon axial volcanic ridges at the Reykjanes Ridge: a life cycle of volcanism and tectonics, Earth Planet. Sci. Lett., 117, 73-87.

Peirce, C., Sinha, M. C., 1999. RAMESSES II - Reykjanes Axial Melt Experiment: Structural Synthesis of Electromagnetics and Seismics, RRS Discovery 235c cruise report.

Power, J. A., Lahr, J. C., Page, R. A., Chouet, B. A., Stephens, C. D., Harlow, D. H., Murray, T. L., Davies, J. N., 1994. Seismic evolution of the 1989-90 eruption sequence of Redoubt volcano, Alaska, J. Volcanol. Geoth. Res., 62, 69-94.

Pritchard, M. J., 2000. A seismological study of the mantle beneath Iceland, PhD thesis, University of Durham.

Procaccia, I., 1988. Universal properties of dynamically complex systems: the organisation of chaos, Nature, 333, 618-623.

Purdy, G. M., Detrick, R. S., 1986. Crustal structure of the Mid-Atlantic ridge at 23°N from seismic refraction studies, J. Geophys. Res., 91, 3739-3762.

Randall, G. R., Ammon, C. J., Owens, T. J., 1995. Moment tensor estimation using regional seimsograms from a Tibetan plateau portable network deployment, Geoph. Res. Lett., 22, 1665-1668.

Raitt, R. W., 1963. The crustal rocks, In: M. N. Hill (Ed), The Sea, 3, Wiley, New York.

Richards, A. F., 1963. Volcanic sounds: investigations and analysis, J. Geophys. Res, 68, 919-928.

Ripepe, M., 1996. Evidence for gas influence on volcanic signals recorded at Stromboli, J. Volcanol. Geoth. Res., 70, 221-233.

Ripepe, M., Poggi, P., Braun, T., Gordeev, E., 1996. Infrasonic waves and volcanic tremor at Stromboli, Geophys. Res. Lett., 23, 181-184.

Rohr, K., Mildreit, B., Yorath, C. J., 1988. Assymetric deep crustal structure across the Juan de Fuca ridge, Geology, 16, 533-537.

Ruelle, D., Takens, F., 1971. On the nature of turbulence, Commun. Math. Phys., 20, 167-192.

Sammis, C., Julian, B. R., 1987. Fracture instabilities accompanying dike intrusion, J. Geophys. Res, 92, 2597-2605.

Sassa, K., 1936. Volcanic microtremors and eruption earthquakes, Mem. Coll. Sci. Univ. Kyoto, Series A, 18, 255-293.

Sauer, T., York, J. A., Casdagli, M., 1991. Embedology, J. Stat. Phys., 65, 579.

Schick, R., Lombardo, G., Patané, G., 1982. Volcanic tremors and shocks associated with eruptions at Etna (Sicily), September 1980, J. Volcanol. Geoth. Res., 14, 261-279.

Schick, R., 1992. Volcanic tremor: Seismic signals of (almost) unknown origin, In: P. Gasparini, R. Scarpa, K. Aki (Eds), Volcanic Seismology, IAVCEI proceedings in Volcanology, 3, 157-167.

Schlindwein, V., 1994. Spektralanalyse harmonischer Tremorsignale am Vulkan Semeru, Indonesien, Diplomarbeit, Ludwig-Maximilians Universität München.

Schlindwein, V., Wasserman, J., Scherbaum, F., 1995. Spectral analysis of harmonic tremor signals from Mt. Semeru, Indonesia, Geophys. Res. Lett., 22, 1685-1688.

Schreiber, T., 1997. Detecting and analysing nonstationarity in a time series using nonlinear cross-predictions. Phys. Rev. Lett., 78, 843-846.

Scott, D. R., Stevenson, D. J., 1984. Magma solitons, Geophys. Res. Lett., 11, 1161-1164.

Scott, D. R., Stevenson, D. J., 1986. Magma ascent by porous flow, J. Geophys. Res., 91, 9283-9296.

Seidl, D., Schick, R., Riuscetti, M., 1981. Volcanic tremors at Etna: A model for hydraulic origin, J. Volcanol. Geoth. Res., 44, 43-56.

Seidl, D., Kirbani, S. B., Brüstle, W., 1990. Maximum entropy spectral analysis of volcanic tremor using data from Etna (Sicily) and Merapi (central Java), Bull. Volcanol., 52, 460-474.

Shaw, H. R., Chouet, B., 1991. Fractal hierarchies of magma transport in Hawaii and critical self-organisation of tremor, J. Geophys. Res., 96, 10,191-10,207.

Sheriff, R. E., Geldart, L. P., 1995. Exploration seismology, Cambridge University Press, Cambridge.

Sherburn, S., Scott, B. J., Nishi, Y., Suguhara, M., 1998. Seismicity at White island volcano, New Zealand: a revised classification and inferences about source mechanism, J. Volcanol. Geoth. Res., 83, 287-312.

Sherburn, S., Bryan, C. J., Hurst, A. W., Latter, J. H., Scott, B. J., 1999. Seismicity of Ruapehu volcano, New Zealand, 1971-1996: a review, J. Volcanol. Geoth. Res., 88, 255-278.

Shima, M., 1958. On the second volcanic micro-tremor at Aso volcano, Bull. Volcanol. Soc. J., 22, 1-6.

Sigeti, D., Horsthemke, W., 1987. High-frequency power spectra for systems subject to noise, Phys. Rev. A, 35, 2276.

Sigvaldasson, G. E., Steinthorsson, S., Oskarsson, N., Imsland, P., 1974. Compositional variation in recent Icelandic tholeiites and the Kverkfjöll hotspot. Nature 251, 579-582.

Sigmarsson, O., Karlsson, H. R., Larsen, G., 2000. The 1996 and 1998 subglacial eruptions beneath the Vatnajökull ice sheet in Iceland: contrasting geochemical and geophysical inferences on magma migration, Bull. Volcanol., 61, 468-476.

Sinha, M. C., Constable, S. C., Peirce, C., White, A., Heinson, G., MacGregor, L. M., Navin, D. A., 1998. Magmatic processes at slow spreading ridges: implications of the RAMESSES experiment at 57°45'N on the Mid-Atlantic Ridge, Geoph. J. Int., 135, 731-745.

Sinton, J. M., Detrick, R. S., 1992. Mid-ocean Ridge magma chambers, J. Geophys. Res., 97, 197-216.

Sleep, N. H., 1975. Formation of oceanic crust: some thermal constraints, J. Geophys. Res., 80, 4037-4042.

Smewing, J. D., 1981. Mixing characteristics and compositional differences in mantle derived melts beneath spreading axis: Evidence from cyclically layered rocks in the ophiolite of North Oman, J. Geophys. Res., 86, 2645-2659.

St Lawrence, W. F., Qamar, A., 1979. Hydraulic transients: A seismic source in volcanoes and glaciers, Science, 203, 654-656.

Stefánsson, R., Bödvarsson, R., Slunga, R., Einarsson, P., Jakobsdóttir, S., Bungum, H., Gregersen, G., Havskov, J., Hj elme, J., Korhonen, H., 1993. Earthquake prediction research in the south Iceland seismic zone and the SIL project. Bull. Seism. Soc. Am. 83, 696-716.

Steinthorsson, S., Hardarsson, B. S., Ellam, R. M., Larsen, G., 2000. Petrochemistry of the Gjálp 1996 subglacial eruption, Vatnajökull, SE Iceland, J. Volcanol. Geoth. Res., 98, 79-90.

Swanson, D. A., Duffield, W., Jackson, D., Peterson, D., 1979. Chronological narrative of the 1969-71 Mauna-Ulu eruption, Kilauea volcano, Hawaii, U. S. G. Surv. Prof. Pap., 1056, 1-55.

Sæmundsson, K., 1979. Fissure swarms and central volcanoes of the neovolcanic zones of Iceland. Geol. J. 19, 415-432.

Sæmundsson, K., 1980. Outline of the Geology of Iceland. Jökull 29, 7-28.

Takens, F., 1981. Detecting strange attractors in turbulence. Lecture notes in Math. Vol. 898, Springer, New York.

Trygvasson, E., 1962. Crustal structure of Iceland from dispersion of surface waves, Bull. Seis. Soc. Am., 52, 339-388.

Trygvasson, E., 1973. Seismicity, earthquake swarms and plate boundaries in the Iceland region, Bull. Seism. Soc. Am., 63, 1327-1348.

Trygvasson, K., Husebye, E. S., Stefánsson, R., 1983. Seismic image of the hypothesized Icelandic hotspot, Tectonophysics, 100, 97-118.

Tsuruga, K., Yomogida, K., Honda, S., Ito, H., Ohminato, T., Kawakatsu, H., 1997. Spatial and temporal variations of volcanic earthquakes at Sakurajima volcano, Japan, J. Volcanol. Geoth. Res., 75, 337-358.

Turner, I. M., 1998. Crustal accretionary processes at Mid-ocean ridges - Valu Fa ridge, Lau Basin, PhD thesis, University of Durham.

Ukawa, M., 1993. Excitation mechanism of large amplitude volcanic tremor associated with the 1989 Ito-Oki submarine volcano eruption, J. Volcanol. Geoth. Res., 55, 33-50.

Ulrych, T. J., Bishop, T. N., 1975. Maximum entropy spectral analysis and autoregressive decomposition, Rev. Geophys. Space Phys., 13, 183-200.

Van Atta, C. W., Mautner, T. S., 1984. The wall shear stress signature of a turbulent spot: direct measurements and momentum integral calculations, In: V. V. Kozlov (Ed) Laminar-turbulent transition, Springer, 607-616.

Vera, E. E., Mutter, J. C., Buhl, P., Orcutt, J. A., Harding, A. J., Kappus, M. E., Detrick, R. S., Brocher, T. M., 1990. The structure of 0 to 0.2 Ma old oceanic crust at 9° on the East Pacific Rise from expanded spread profiles, J. Geophys. Res., 95, 15529-15556.

Vila, J., Marti, J., Ortiz, R., Garcia, A., Correig, A. M., 1992. Volcanic tremors at Deception island (south Shetland islands, Antarctica), J. Volcanol. Geoth. Res., 53, 89-102.

Vine, F. J., 1966. Spreading of the ocean floor: New evidence, Scince, 154, 1405-1415.

Wallis, G. B., 1969. One-dimensional two-phase flow, McGraw Hill, New York.

Walker, G. P. L., 1974. The structure of eastern Iceland, In: L. Kristjansson (Ed) Geodynamics of Iceland and the North Atlantic area, D. reidel, Hingham, Mass., 177-188.

Wareham, M. A., 1999. A multichannel seismic reflection profile across the slow spreading Reykjanes ridge, MSc thesis, University of Durham.

Wegler, U., Seidl, D., 1997. Kinematic parameters of the tremor wavefield at Mt. Etna (Sicily), Geophys. Res. Lett., 24, 759-762.

Wessel, P., Smith, W. H. F., 1995. New version of the Generic Mapping Tools released. EOS Trans. AGU 76, 329.

Wilson, D. S., Clague D. A., Sleep, N. H., Morton, J. L., 1988. Implications of magma convection for the size and temperature of magma chambers at fast spreading ridges, J. Geophys. Res., 93, 11974-11984.

Yamaoka, K., Oikawa, J., Ida, Y., 1991. An isotropic source of volcanic tremor observations with a dense seismic network at Izu-Oshima volcano, Japan, J. Volcanol. Geoth. Res., 47, 329-336.

Zobin, V., 1999. The fault nature of the $M_s$ 5.4 volcanic earthquake preceding the 1996 subglacial eruption of Grimsvötn volcano, Iceland, J. Volcanol. Geotherm. Res., 92, 349-358.

# Appendix A
# HOTSPOT and SIL seismic networks

## HOTSPOT seismic stations

| Station | Lat (°N) | Lon (°E) | Elev (m) | Sensor type |
|---|---|---|---|---|
| HOT01 | 64.49411 | -21.16789 | 205.0 | CMG-3ESP |
| HOT02 | 64.74582 | -22.23226 | 40.0 | CMG-3ESP |
| HOT03 | 64.90760 | -23.85270 | 35.0 | CMG-40T |
| HOT04 | 65.18047 | -22.42312 | 40.0 | CMG-3ESP |
| HOT05 | 65.10969 | -21.09637 | 35.0 | CMG-3ESP |
| HOT06 | 65.70502 | -21.67787 | 25.0 | CMG-3ESP |
| HOT07 | 65.59839 | -22.50999 | 40.0 | CMG-3ESP |
| HOT08 | 65.60982 | -24.16141 | 8.0 | CMG-3ESP |
| HOT09 | 65.87388 | -23.48661 | 50.0 | CMG-3ESP |
| HOT10 | 65.92669 | -22.42822 | 7.0 | CMG-3ESP |
| HOT11 | 65.42228 | -20.72176 | 108.0 | CMG-3T |
| HOT12 | 65.67071 | -19.59965 | 38.0 | CMG-3T |
| HOT13 | 65.68600 | -18.09991 | 24.0 | CMG-3T |
| HOT14 | 65.30280 | -18.25650 | 245.0 | CMG-3ESP |
| HOT15 | 66.12100 | -15.17200 | 20.0 | CMG-3ESP |
| HOT16 | 65.54090 | -13.75350 | 5.0 | CMG-3ESP |
| HOT17 | 65.25500 | -14.50400 | 80.0 | CMG-3ESP |
| HOT18 | 65.16600 | -15.30870 | 342.0 | CMG-3ESP |
| HOT19 | 64.81200 | -14.10000 | 50.0 | CMG-3ESP |
| HOT20 | 64.28781 | -15.13921 | 15.0 | CMG-3ESP |
| HOT21 | 63.87684 | -16.64062 | 20.0 | CMG-3ESP |
| HOT22 | 63.76984 | -18.13068 | 65.0 | CMG-3ESP |
| HOT23 | 64.40670 | -17.26630 | 1730.0 | CMG-3ESP |
| HOT24 | 64.88630 | -15.35370 | 600.0 | CMG-3ESP |
| HOT25 | 65.05400 | -16.65200 | 920.0 | CMG-40T |
| HOT26 | 65.02900 | -18.33200 | 740.0 | CMG-3ESP |
| HOT27 | 65.20000 | -19.59000 | 450.0 | CMG-3ESP |
| HOT28 | 64.53220 | -19.48380 | 600.0 | CMG-40T |
| HOT29 | 65.72800 | -14.83800 | 60.0 | CMG-40T |
| HOT30 | 64.13000 | -21.90000 | 50.0 | CMG-3ESP |

## SIL seismic stations

| Station | Lat (°N) | Lon (°E) | Elev (m) | Sensor type |
|---|---|---|---|---|
| rey | 65.64697 | -16.64697 | 344.0 | BB |
| asm | 63.83397 | -20.61488 | 19.0 | SP |
| sau | 63.99013 | -20.41560 | 77.0 | SP |
| hau | 63.96885 | -19.96525 | 99.0 | BB |
| bja | 63.94622 | -21.30287 | 58.0 | SP |
| sol | 63.92930 | -20.94415 | 31.0 | SP |
| hei | 64.19998 | -21.23645 | 160.0 | BB |
| mid | 63.65833 | -19.88573 | 132.0 | BB |
| gyg | 64.28132 | -20.21540 | 113.0 | SP |
| skh | 63.45347 | -19.09453 | 70.0 | BB |
| kri | 63.87811 | -22.07623 | 130.0 | SP |
| snb | 63.73624 | -18.63043 | 230.0 | BB |
| hla | 65.94442 | -18.38722 | 41.0 | SP |
| sig | 66.13228 | -18.91483 | 16.0 | BB |
| gri | 66.54152 | -18.00951 | 36.0 | BB |
| gra | 65.91757 | -17.57812 | 25.0 | BB |
| gil | 66.07734 | -16.35131 | 141.0 | BB |
| lei | 66.40661 | -16.48956 | 45.0 | SP |
| asb | 64.74869 | -21.32614 | 110.0 | BB |
| grs | 65.63813 | -16.12409 | 390.0 | BB |
| kud | 64.31000 | -21.88000 | 30.0 | BB |
| hrn | 66.11300 | -20.11010 | 15.0 | BB |
| hve | 64.87145 | -19.55850 | 642.0 | BB |
| skr | 64.56029 | -18.38634 | 812.0 | BB |
| kro | 64.09806 | -21.11978 | 139.0 | BB |
| san | 64.05601 | -21.57013 | 208.0 | BB |
| kal | 63.94762 | -17.68699 | 83.0 | BB |
| haf | 64.04257 | -21.91870 | 70.0 | BB |
| nyl | 63.97370 | -22.73790 | 11.0 | BB |
| vog | 63.96967 | -22.39283 | 12.0 | BB |
| grv | 63.85717 | -22.45583 | 56.0 | BB |
| kra | 65.69474 | -16.77783 | 437.0 | BB |

SP: Short Period sensor

BB: BroadBand sensor

# Appendix B
# Earthquake locations using HOTSPOT arrival times

These are the locations obtained, using HOTSPOT arrival times, for events picked during the period September 29th-October 6th. The time at the beginning of each line represents the origin time for each event.

1996 Sep 29 10:48:17.068 UTC Lat: 64.66255 Lon: -17.44569 Depth: 7.295 km
1996 Sep 29 11:11:09.618 UTC Lat: 64.66818 Lon: -17.54168 Depth: 8.021 km
1996 Sep 29 11:13:30.515 UTC Lat: 64.68093 Lon: -17.62107 Depth: 0.838 km
1996 Sep 29 11:14:13.184 UTC Lat: 64.66000 Lon: -17.49138 Depth: 0.000 km
1996 Sep 29 11:14:42.426 UTC Lat: 64.66323 Lon: -17.53026 Depth: 23.428 km
1996 Sep 29 11:12:39.096 UTC Lat: 64.68860 Lon: -17.62262 Depth: 28.282 km
1996 Sep 29 11:16:16.466 UTC Lat: 64.65756 Lon: -17.60812 Depth: 9.786 km
1996 Sep 29 11:18:15.884 UTC Lat: 64.66251 Lon: -17.49877 Depth: 8.435 km
1996 Sep 29 11:22:48.864 UTC Lat: 64.65413 Lon: -17.50354 Depth: 9.446 km
1996 Sep 29 11:25:43.439 UTC Lat: 64.65592 Lon: -17.56393 Depth: 0.000 km
1996 Sep 29 11:32:10.343 UTC Lat: 64.65947 Lon: -17.58771 Depth: 9.490 km
1996 Sep 29 11:34:22.840 UTC Lat: 64.65583 Lon: -17.52652 Depth: -0.000 km
1996 Sep 29 11:36:34.258 UTC Lat: 64.65548 Lon: -17.44967 Depth: 13.513 km
1996 Sep 29 11:38:15.739 UTC Lat: 64.65257 Lon: -17.54629 Depth: 9.957 km
1996 Sep 29 11:42:17.256 UTC Lat: 64.64662 Lon: -17.57197 Depth: 13.403 km
1996 Sep 29 11:43:59.909 UTC Lat: 64.65854 Lon: -17.55435 Depth: 5.741 km
1996 Sep 29 11:46:24.150 UTC Lat: 64.66416 Lon: -17.68739 Depth: -0.000 km
1996 Sep 29 11:57:04.803 UTC Lat: 64.65877 Lon: -17.55528 Depth: 0.000 km
1996 Sep 29 12:02:14.612 UTC Lat: 64.64733 Lon: -17.53400 Depth: -0.000 km
1996 Sep 29 12:05:39.494 UTC Lat: 64.67722 Lon: -17.50581 Depth: 7.834 km
1996 Sep 29 12:10:50.616 UTC Lat: 64.67682 Lon: -17.43360 Depth: 32.426 km
1996 Sep 29 12:14:11.371 UTC Lat: 64.68209 Lon: -17.60457 Depth: 13.039 km
1996 Sep 29 12:18:56.767 UTC Lat: 64.63748 Lon: -17.50988 Depth: -0.000 km
1996 Sep 29 12:21:04.526 UTC Lat: 64.62179 Lon: -17.50517 Depth: 0.000 km
1996 Sep 29 12:22:51.852 UTC Lat: 64.62484 Lon: -17.50119 Depth: 22.249 km

1996 Sep 29 12:25:47.281 UTC Lat: 64.63832 Lon: -17.54273 Depth: 15.538 km
1996 Sep 29 12:25:46.531 UTC Lat: 64.64020 Lon: -17.56538 Depth: -0.000 km
1996 Sep 29 12:32:06.239 UTC Lat: 64.64145 Lon: -17.56852 Depth: 7.155 km
1996 Sep 29 12:38:42.723 UTC Lat: 64.62904 Lon: -17.55334 Depth: -0.000 km
1996 Sep 29 12:47:16.229 UTC Lat: 64.63501 Lon: -17.55160 Depth: 1.302 km
1996 Sep 29 12:51:29.211 UTC Lat: 64.63562 Lon: -17.57131 Depth: 13.728 km
1996 Sep 29 12:53:21.130 UTC Lat: 64.62497 Lon: -17.56174 Depth: 15.615 km
1996 Sep 29 12:57:57.372 UTC Lat: 64.62145 Lon: -17.56727 Depth: 15.467 km
1996 Sep 29 13:01:18.360 UTC Lat: 64.62595 Lon: -17.60017 Depth: 14.170 km
1996 Sep 29 13:01:59.341 UTC Lat: 64.62224 Lon: -17.55062 Depth: 8.791 km
1996 Sep 29 13:10:49.463 UTC Lat: 64.62100 Lon: -17.55558 Depth: 10.846 km
1996 Sep 29 13:12:25.303 UTC Lat: 64.61433 Lon: -17.54689 Depth: 7.410 km
1996 Sep 29 13:13:48.866 UTC Lat: 64.61020 Lon: -17.53543 Depth: -0.000 km
1996 Sep 29 13:16:47.492 UTC Lat: 64.62179 Lon: -17.53727 Depth: 8.551 km
1996 Sep 29 13:18:15.485 UTC Lat: 64.60909 Lon: -17.53245 Depth: 0.000 km
1996 Sep 29 13:21:28.552 UTC Lat: 64.61106 Lon: -17.54156 Depth: 14.796 km
1996 Sep 29 13:24:04.271 UTC Lat: 64.59716 Lon: -17.50164 Depth: -0.000 km
1996 Sep 29 13:26:11.634 UTC Lat: 64.61157 Lon: -17.53202 Depth: 5.486 km
1996 Sep 29 13:27:08.927 UTC Lat: 64.60694 Lon: -17.51134 Depth: 14.994 km
1996 Sep 29 13:28:55.621 UTC Lat: 64.61282 Lon: -17.53880 Depth: 14.003 km
1996 Sep 29 13:34:22.109 UTC Lat: 64.61211 Lon: -17.50277 Depth: 4.341 km
1996 Sep 29 13:39:13.386 UTC Lat: 64.61162 Lon: -17.52975 Depth: -0.000 km
1996 Sep 29 13:59:10.399 UTC Lat: 64.65332 Lon: -17.56138 Depth: 1.354 km
1996 Sep 29 14:00:16.219 UTC Lat: 64.60579 Lon: -17.53801 Depth: 1.281 km
1996 Sep 29 14:07:28.318 UTC Lat: 64.62944 Lon: -17.51400 Depth: 8.142 km
1996 Sep 29 14:34:24.632 UTC Lat: 64.71397 Lon: -17.55209 Depth: 0.000 km
1996 Sep 29 14:38:10.428 UTC Lat: 64.62903 Lon: -17.50599 Depth: -0.000 km
1996 Sep 29 14:49:19.614 UTC Lat: 64.64500 Lon: -17.37144 Depth: 8.022 km
1996 Sep 29 15:13:33.747 UTC Lat: 64.66630 Lon: -17.35655 Depth: 1.409 km
1996 Sep 29 15:40:37.408 UTC Lat: 64.63493 Lon: -17.38087 Depth: 7.748 km
1996 Sep 29 15:40:36.446 UTC Lat: 64.62655 Lon: -17.35824 Depth: 0.000 km
1996 Sep 29 16:05:46.620 UTC Lat: 64.64911 Lon: -17.36272 Depth: 0.002 km
1996 Sep 29 16:05:46.544 UTC Lat: 64.64562 Lon: -17.36337 Depth: 0.000 km
1996 Sep 29 16:51:58.495 UTC Lat: 64.65153 Lon: -17.35695 Depth: -0.000 km

1996 Sep 29 17:23:15.160 UTC Lat: 64.64189 Lon: -17.36268 Depth: 5.796 km
1996 Sep 29 19:20:08.566 UTC Lat: 64.61816 Lon: -17.40880 Depth: 19.517 km
1996 Sep 29 19:41:16.321 UTC Lat: 64.57558 Lon: -17.26265 Depth: 16.096 km
1996 Sep 29 19:54:40.702 UTC Lat: 64.57762 Lon: -17.23954 Depth: -0.000 km
1996 Sep 29 19:54:42.246 UTC Lat: 64.58245 Lon: -17.29850 Depth: 15.682 km
1996 Sep 29 20:22:49.103 UTC Lat: 64.59874 Lon: -17.27540 Depth: 13.033 km
1996 Sep 29 20:50:50.835 UTC Lat: 64.60316 Lon: -17.26089 Depth: 10.733 km
1996 Sep 29 20:50:50.842 UTC Lat: 64.60025 Lon: -17.25567 Depth: 7.427 km
1996 Sep 29 22:06:52.058 UTC Lat: 64.59988 Lon: -17.30278 Depth: 7.203 km
1996 Sep 29 22:13:23.673 UTC Lat: 64.65205 Lon: -17.38455 Depth: 14.559 km
1996 Sep 29 22:21:38.546 UTC Lat: 64.59287 Lon: -17.29022 Depth: 0.000 km
1996 Sep 29 22:29:54.269 UTC Lat: 64.63178 Lon: -17.24288 Depth: 8.580 km
1996 Sep 29 22:36:23.534 UTC Lat: 64.58620 Lon: -17.31856 Depth: 0.000 km
1996 Sep 29 22:46:12.818 UTC Lat: 64.56355 Lon: -17.28902 Depth: -0.000 km
1996 Sep 29 23:11:18.952 UTC Lat: 64.58111 Lon: -17.29277 Depth: 0.660 km
1996 Sep 29 23:35:35.511 UTC Lat: 64.55392 Lon: -17.31863 Depth: 0.000 km
1996 Sep 29 23:39:34.329 UTC Lat: 64.56170 Lon: -17.27883 Depth: 3.499 km
1996 Sep 29 23:41:36.842 UTC Lat: 64.55837 Lon: -17.30316 Depth: -0.000 km
1996 Sep 29 23:45:56.253 UTC Lat: 64.61556 Lon: -17.36498 Depth: 0.000 km
1996 Sep 29 23:48:43.068 UTC Lat: 64.56501 Lon: -17.50966 Depth: 0.000 km
1996 Sep 29 23:54:39.241 UTC Lat: 64.54120 Lon: -17.29930 Depth: -0.000 km
1996 Sep 29 23:55:14.723 UTC Lat: 64.59152 Lon: -17.30086 Depth: 0.000 km
1996 Sep 29 23:55:15.469 UTC Lat: 64.59257 Lon: -17.30184 Depth: 6.194 km
1996 Sep 30 00:11:52.711 UTC Lat: 64.51020 Lon: -17.30303 Depth: 8.384 km
1996 Sep 30 00:17:46.190 UTC Lat: 64.54996 Lon: -17.26940 Depth: 0.000 km
1996 Sep 30 00:19:51.288 UTC Lat: 64.53433 Lon: -17.27040 Depth: 0.000 km
1996 Sep 30 00:19:51.840 UTC Lat: 64.53186 Lon: -17.31014 Depth: 4.894 km
1996 Sep 30 00:51:56.371 UTC Lat: 64.53716 Lon: -17.30532 Depth: 8.321 km
1996 Sep 30 01:18:20.303 UTC Lat: 64.68561 Lon: -17.40658 Depth: 20.646 km
1996 Sep 30 01:21:27.770 UTC Lat: 64.58991 Lon: -17.29215 Depth: 1.144 km
1996 Sep 30 01:23:10.391 UTC Lat: 64.61741 Lon: -17.64725 Depth: -0.000 km
1996 Sep 30 01:33:19.553 UTC Lat: 64.53133 Lon: -17.35515 Depth: 0.000 km
1996 Sep 30 01:39:57.181 UTC Lat: 64.48945 Lon: -17.41016 Depth: 7.549 km
1996 Sep 30 01:53:24.599 UTC Lat: 64.49677 Lon: -17.26531 Depth: 4.517 km

1996 Sep 30 02:03:19.818 UTC Lat: 64.54459 Lon: -17.30554 Depth: 1.447 km
1996 Sep 30 02:04:24.688 UTC Lat: 64.53745 Lon: -17.30460 Depth: 0.000 km
1996 Sep 30 02:08:59.852 UTC Lat: 64.54037 Lon: -17.29260 Depth: 8.643 km
1996 Sep 30 02:29:30.337 UTC Lat: 64.50258 Lon: -17.32927 Depth: 0.000 km
1996 Sep 30 02:35:20.469 UTC Lat: 64.58645 Lon: -17.29314 Depth: 3.070 km
1996 Sep 30 02:54:59.676 UTC Lat: 64.50073 Lon: -17.22784 Depth: 6.487 km
1996 Sep 30 02:54:58.783 UTC Lat: 64.50611 Lon: -17.20522 Depth: -0.000 km
1996 Sep 30 03:14:15.200 UTC Lat: 64.45433 Lon: -17.45725 Depth: 0.000 km
1996 Sep 30 03:23:35.645 UTC Lat: 64.68305 Lon: -17.41224 Depth: 12.201 km
1996 Sep 30 04:03:21.688 UTC Lat: 64.50685 Lon: -17.31721 Depth: 0.000 km
1996 Sep 30 04:26:49.620 UTC Lat: 64.47011 Lon: -17.37030 Depth: -0.000 km
1996 Sep 30 04:31:32.838 UTC Lat: 64.50274 Lon: -17.43928 Depth: 1.384 km
1996 Sep 30 05:08:34.206 UTC Lat: 64.51969 Lon: -17.34252 Depth: 5.464 km
1996 Sep 30 05:22:05.162 UTC Lat: 64.75429 Lon: -17.30719 Depth: 15.828 km
1996 Sep 30 05:45:48.196 UTC Lat: 64.58100 Lon: -17.28502 Depth: -0.000 km
1996 Sep 30 05:45:49.271 UTC Lat: 64.58357 Lon: -17.29693 Depth: 8.699 km
1996 Sep 30 06:14:02.850 UTC Lat: 64.50554 Lon: -17.36778 Depth: 6.030 km
1996 Sep 30 06:41:49.079 UTC Lat: 64.45827 Lon: -17.76640 Depth: 14.682 km
1996 Sep 30 06:48:17.840 UTC Lat: 64.59690 Lon: -17.31013 Depth: 7.336 km
1996 Sep 30 07:03:54.064 UTC Lat: 64.60484 Lon: -17.29985 Depth: 10.515 km
1996 Sep 30 07:05:55.571 UTC Lat: 64.51112 Lon: -17.38407 Depth: 5.670 km
1996 Sep 30 08:09:24.576 UTC Lat: 64.44202 Lon: -17.29657 Depth: 10.004 km
1996 Sep 30 08:13:36.462 UTC Lat: 64.47899 Lon: -17.34415 Depth: 0.000 km
1996 Sep 30 08:18:28.632 UTC Lat: 64.49906 Lon: -17.35926 Depth: -0.000 km
1996 Sep 30 08:22:22.086 UTC Lat: 64.59090 Lon: -17.28720 Depth: 5.873 km
1996 Sep 30 08:51:14.999 UTC Lat: 64.50259 Lon: -17.33841 Depth: -0.000 km
1996 Sep 30 09:01:08.393 UTC Lat: 64.51424 Lon: -17.32505 Depth: 1.040 km
1996 Sep 30 09:07:25.265 UTC Lat: 64.50108 Lon: -17.37828 Depth: 0.000 km
1996 Sep 30 09:06:02.265 UTC Lat: 64.58422 Lon: -17.27483 Depth: 27.740 km
1996 Sep 30 09:16:26.201 UTC Lat: 64.51630 Lon: -17.35884 Depth: 7.382 km
1996 Sep 30 09:39:33.280 UTC Lat: 64.48504 Lon: -17.38191 Depth: 5.269 km
1996 Sep 30 09:54:11.555 UTC Lat: 64.48119 Lon: -17.35380 Depth: 0.000 km
1996 Sep 30 09:58:45.221 UTC Lat: 64.50226 Lon: -17.36456 Depth: 6.502 km
1996 Sep 30 10:12:38.111 UTC Lat: 64.59168 Lon: -17.30862 Depth: -0.000 km

1996 Sep 30 10:19:34.124 UTC Lat: 64.47698 Lon: -17.37644 Depth: 0.000 km
1996 Sep 30 10:20:07.501 UTC Lat: 64.51344 Lon: -17.29188 Depth: 3.729 km
1996 Sep 30 10:20:06.593 UTC Lat: 64.49544 Lon: -17.31609 Depth: 0.000 km
1996 Sep 30 10:32:46.627 UTC Lat: 64.47600 Lon: -17.38772 Depth: 0.555 km
1996 Sep 30 10:37:19.235 UTC Lat: 64.48887 Lon: -17.37354 Depth: 0.134 km
1996 Sep 30 10:47:37.267 UTC Lat: 64.69078 Lon: -17.55322 Depth: 18.158 km
1996 Sep 30 11:06:08.298 UTC Lat: 64.50692 Lon: -17.40130 Depth: -0.000 km
1996 Sep 30 11:14:40.344 UTC Lat: 64.48941 Lon: -17.40011 Depth: 0.001 km
1996 Sep 30 11:23:29.067 UTC Lat: 64.50856 Lon: -17.38977 Depth: 0.000 km
1996 Sep 30 11:44:23.122 UTC Lat: 64.48960 Lon: -17.37947 Depth: 0.000 km
1996 Sep 30 12:05:19.914 UTC Lat: 64.44644 Lon: -17.27619 Depth: 4.732 km
1996 Sep 30 12:05:19.368 UTC Lat: 64.46804 Lon: -17.19843 Depth: 3.539 km
1996 Sep 30 12:09:53.484 UTC Lat: 64.47410 Lon: -17.35987 Depth: 2.660 km
1996 Sep 30 12:06:16.492 UTC Lat: 64.54290 Lon: -17.30083 Depth: 12.146 km
1996 Sep 30 12:09:53.621 UTC Lat: 64.48928 Lon: -17.39054 Depth: 3.824 km
1996 Sep 30 12:36:44.616 UTC Lat: 64.53379 Lon: -17.19447 Depth: 8.452 km
1996 Sep 30 12:37:22.064 UTC Lat: 64.53950 Lon: -17.29580 Depth: 5.253 km
1996 Sep 30 13:05:13.644 UTC Lat: 64.48412 Lon: -17.31366 Depth: -0.000 km
1996 Sep 30 13:15:16.655 UTC Lat: 64.47442 Lon: -17.38919 Depth: 0.115 km
1996 Sep 30 13:15:16.542 UTC Lat: 64.47237 Lon: -17.40207 Depth: 0.386 km
1996 Sep 30 13:46:42.127 UTC Lat: 64.53748 Lon: -17.28461 Depth: 1.247 km
1996 Sep 30 13:58:32.075 UTC Lat: 64.49546 Lon: -17.37643 Depth: -0.000 km
1996 Sep 30 13:59:26.694 UTC Lat: 64.48302 Lon: -17.38635 Depth: 1.692 km
1996 Sep 30 14:29:58.150 UTC Lat: 64.48279 Lon: -17.39693 Depth: -0.000 km
1996 Sep 30 14:29:58.264 UTC Lat: 64.48983 Lon: -17.38594 Depth: -0.000 km
1996 Sep 30 14:45:08.596 UTC Lat: 64.49939 Lon: -17.40193 Depth: 7.081 km
1996 Sep 30 14:45:07.630 UTC Lat: 64.49116 Lon: -17.38938 Depth: 0.000 km
1996 Sep 30 14:50:56.845 UTC Lat: 64.67801 Lon: -17.32112 Depth: 0.000 km
1996 Sep 30 15:10:41.187 UTC Lat: 64.53518 Lon: -17.31414 Depth: 7.986 km
1996 Sep 30 15:11:43.855 UTC Lat: 64.47562 Lon: -17.38056 Depth: 0.791 km
1996 Sep 30 15:10:40.525 UTC Lat: 64.53217 Lon: -17.30985 Depth: 1.135 km
1996 Sep 30 15:33:00.144 UTC Lat: 64.57464 Lon: -17.42182 Depth: 4.132 km
1996 Sep 30 15:39:08.229 UTC Lat: 64.61246 Lon: -17.32275 Depth: 9.355 km
1996 Sep 30 15:55:12.499 UTC Lat: 64.52930 Lon: -17.28382 Depth: 1.309 km

1996 Sep 30 15:55:12.199 UTC Lat: 64.52656 Lon: -17.28390 Depth: -0.000 km
1996 Sep 30 16:01:29.508 UTC Lat: 64.51887 Lon: -17.36482 Depth: -0.000 km
1996 Sep 30 16:22:01.847 UTC Lat: 64.54060 Lon: -17.30255 Depth: 11.237 km
1996 Sep 30 16:47:01.004 UTC Lat: 64.51796 Lon: -17.38972 Depth: -0.000 km
1996 Sep 30 16:52:29.653 UTC Lat: 64.49408 Lon: -17.39019 Depth: -0.000 km
1996 Sep 30 17:19:58.938 UTC Lat: 64.49158 Lon: -17.39164 Depth: 1.038 km
1996 Sep 30 17:19:59.015 UTC Lat: 64.48950 Lon: -17.40000 Depth: 1.695 km
1996 Sep 30 17:59:13.517 UTC Lat: 64.53140 Lon: -17.32409 Depth: 0.005 km
1996 Sep 30 18:08:55.088 UTC Lat: 64.56788 Lon: -17.29452 Depth: 7.002 km
1996 Sep 30 18:19:33.076 UTC Lat: 64.48968 Lon: -17.40465 Depth: 3.059 km
1996 Sep 30 18:22:05.323 UTC Lat: 64.53267 Lon: -17.30602 Depth: 4.540 km
1996 Sep 30 18:38:15.928 UTC Lat: 64.62274 Lon: -17.39702 Depth: 5.558 km
1996 Sep 30 18:46:40.267 UTC Lat: 64.50456 Lon: -17.39291 Depth: 0.000 km
1996 Sep 30 19:18:03.086 UTC Lat: 64.54168 Lon: -17.29240 Depth: 4.795 km
1996 Sep 30 19:41:08.782 UTC Lat: 64.48062 Lon: -17.32077 Depth: 10.372 km
1996 Sep 30 19:44:13.728 UTC Lat: 64.59072 Lon: -17.36416 Depth: 11.637 km
1996 Sep 30 20:04:34.385 UTC Lat: 64.53528 Lon: -17.27497 Depth: 3.442 km
1996 Sep 30 20:28:35.656 UTC Lat: 64.50664 Lon: -17.25620 Depth: 6.588 km
1996 Sep 30 20:34:17.042 UTC Lat: 64.53499 Lon: -17.30793 Depth: 14.214 km
1996 Sep 30 20:35:07.812 UTC Lat: 64.54928 Lon: -17.29926 Depth: 0.005 km
1996 Sep 30 20:49:04.334 UTC Lat: 64.51149 Lon: -17.36766 Depth: -0.000 km
1996 Sep 30 20:58:31.654 UTC Lat: 64.48766 Lon: -17.39151 Depth: 3.779 km
1996 Sep 30 21:05:26.131 UTC Lat: 64.56255 Lon: -17.28888 Depth: 7.438 km
1996 Sep 30 21:13:16.847 UTC Lat: 64.49741 Lon: -17.38909 Depth: 0.000 km
1996 Sep 30 21:19:53.816 UTC Lat: 64.65742 Lon: -17.38606 Depth: 0.545 km
1996 Sep 30 21:22:15.102 UTC Lat: 64.53079 Lon: -17.39938 Depth: 8.742 km
1996 Sep 30 21:31:32.688 UTC Lat: 64.54752 Lon: -17.29500 Depth: 9.181 km
1996 Sep 30 21:38:11.488 UTC Lat: 64.48151 Lon: -17.40194 Depth: 0.000 km
1996 Sep 30 21:47:33.355 UTC Lat: 64.68235 Lon: -17.44263 Depth: 19.019 km
1996 Sep 30 22:02:52.628 UTC Lat: 64.48399 Lon: -17.40113 Depth: 5.930 km
1996 Sep 30 22:14:06.670 UTC Lat: 64.48353 Lon: -17.38398 Depth: -0.000 km
1996 Sep 30 22:48:50.842 UTC Lat: 64.60641 Lon: -17.31653 Depth: 0.572 km
1996 Sep 30 23:29:23.624 UTC Lat: 64.54603 Lon: -17.36212 Depth: 9.273 km
1996 Sep 30 23:50:17.093 UTC Lat: 64.76133 Lon: -17.76063 Depth: 5.975 km

1996 Sep 30 23:58:06.494 UTC Lat: 64.54341 Lon: -17.30686 Depth: -0.000 km
1996 Oct 1 00:04:30.642 UTC Lat: 64.56538 Lon: -17.28145 Depth: 6.202 km
1996 Oct 1 00:09:19.019 UTC Lat: 64.48402 Lon: -17.41022 Depth: 1.356 km
1996 Oct 1 00:23:40.562 UTC Lat: 64.52984 Lon: -17.29793 Depth: 4.712 km
1996 Oct 1 01:58:45.511 UTC Lat: 64.57758 Lon: -17.29730 Depth: 3.907 km
1996 Oct 1 02:28:47.389 UTC Lat: 64.70954 Lon: -17.39849 Depth: 10.038 km
1996 Oct 1 02:31:16.720 UTC Lat: 64.70438 Lon: -17.37687 Depth: 0.000 km
1996 Oct 1 02:53:41.416 UTC Lat: 64.66895 Lon: -17.26224 Depth: 10.382 km
1996 Oct 1 03:04:27.250 UTC Lat: 64.59013 Lon: -17.27024 Depth: 9.911 km
1996 Oct 1 03:58:39.115 UTC Lat: 64.55904 Lon: -17.27838 Depth: 8.120 km
1996 Oct 1 04:57:09.352 UTC Lat: 64.59732 Lon: -17.31460 Depth: 0.000 km
1996 Oct 1 05:07:48.789 UTC Lat: 64.59880 Lon: -17.39387 Depth: 26.030 km
1996 Oct 1 05:43:49.662 UTC Lat: 64.54725 Lon: -17.27651 Depth: 0.001 km
1996 Oct 1 05:57:51.177 UTC Lat: 64.53627 Lon: -17.28988 Depth: 1.770 km
1996 Oct 1 06:00:33.494 UTC Lat: 64.68660 Lon: -17.75820 Depth: 0.000 km
1996 Oct 1 06:06:14.955 UTC Lat: 64.69023 Lon: -17.37650 Depth: 0.000 km
1996 Oct 1 06:22:21.154 UTC Lat: 64.56175 Lon: -17.28859 Depth: 10.740 km
1996 Oct 1 06:41:10.891 UTC Lat: 64.53123 Lon: -17.30081 Depth: 10.248 km
1996 Oct 1 07:51:34.559 UTC Lat: 64.55217 Lon: -17.30370 Depth: 4.801 km
1996 Oct 1 08:03:24.414 UTC Lat: 64.67002 Lon: -17.49797 Depth: 3.482 km
1996 Oct 1 08:17:49.465 UTC Lat: 64.53076 Lon: -17.30242 Depth: 16.822 km
1996 Oct 1 08:26:45.543 UTC Lat: 64.62194 Lon: -17.40575 Depth: 3.688 km
1996 Oct 1 08:29:06.221 UTC Lat: 64.62144 Lon: -17.43957 Depth: 8.091 km
1996 Oct 1 08:24:56.979 UTC Lat: 64.66742 Lon: -17.42217 Depth: -0.000 km
1996 Oct 1 08:56:57.993 UTC Lat: 64.69857 Lon: -17.40725 Depth: 6.991 km
1996 Oct 1 09:09:40.692 UTC Lat: 64.56987 Lon: -17.27926 Depth: 4.493 km
1996 Oct 1 09:09:39.977 UTC Lat: 64.57692 Lon: -17.30440 Depth: 0.000 km
1996 Oct 1 09:18:25.289 UTC Lat: 64.57423 Lon: -17.28625 Depth: 3.082 km
1996 Oct 1 09:56:58.578 UTC Lat: 64.67194 Lon: -17.44032 Depth: 12.148 km
1996 Oct 1 09:59:56.569 UTC Lat: 64.66997 Lon: -17.41535 Depth: 10.285 km
1996 Oct 1 09:59:56.836 UTC Lat: 64.66731 Lon: -17.38879 Depth: 17.074 km
1996 Oct 1 10:11:52.506 UTC Lat: 64.55253 Lon: -17.30488 Depth: 9.620 km
1996 Oct 1 10:50:24.597 UTC Lat: 64.68663 Lon: -17.44506 Depth: 9.211 km
1996 Oct 1 10:59:58.810 UTC Lat: 64.53198 Lon: -17.29129 Depth: 8.159 km

1996 Oct 1 10:59:57.766 UTC Lat: 64.51475 Lon: -17.29301 Depth: 0.001 km
1996 Oct 1 11:49:57.780 UTC Lat: 64.50686 Lon: -17.32686 Depth: 59.997 km
1996 Oct 1 12:44:05.957 UTC Lat: 64.52081 Lon: -17.27468 Depth: 18.537 km
1996 Oct 1 13:21:24.367 UTC Lat: 64.54275 Lon: -17.31835 Depth: 11.096 km
1996 Oct 1 14:19:53.160 UTC Lat: 64.67910 Lon: -17.42590 Depth: -0.000 km
1996 Oct 1 14:47:48.420 UTC Lat: 64.66347 Lon: -17.49479 Depth: 14.704 km
1996 Oct 1 14:50:47.946 UTC Lat: 64.48764 Lon: -17.41980 Depth: 1.601 km
1996 Oct 1 15:13:36.794 UTC Lat: 64.57219 Lon: -17.34804 Depth: 0.000 km
1996 Oct 1 15:17:45.642 UTC Lat: 64.62230 Lon: -17.48578 Depth: 0.000 km
1996 Oct 1 15:41:39.469 UTC Lat: 64.53164 Lon: -17.30580 Depth: 4.414 km
1996 Oct 1 15:55:29.295 UTC Lat: 64.53752 Lon: -17.28100 Depth: 6.405 km
1996 Oct 1 15:55:29.440 UTC Lat: 64.53825 Lon: -17.28041 Depth: 12.587 km
1996 Oct 1 16:01:17.369 UTC Lat: 64.57586 Lon: -17.26051 Depth: 20.506 km
1996 Oct 1 16:16:19.680 UTC Lat: 64.56097 Lon: -17.28585 Depth: 0.001 km
1996 Oct 1 17:10:55.009 UTC Lat: 64.56280 Lon: -17.27805 Depth: 0.000 km
1996 Oct 1 17:52:33.952 UTC Lat: 64.73054 Lon: -17.46601 Depth: 29.210 km
1996 Oct 1 18:31:47.700 UTC Lat: 64.54328 Lon: -17.31358 Depth: 12.117 km
1996 Oct 1 18:35:49.228 UTC Lat: 64.49461 Lon: -17.38992 Depth: 1.061 km
1996 Oct 1 18:37:34.157 UTC Lat: 64.51998 Lon: -17.37526 Depth: 7.388 km
1996 Oct 1 19:58:49.921 UTC Lat: 64.54773 Lon: -17.32544 Depth: 0.000 km
1996 Oct 1 20:26:02.240 UTC Lat: 64.53462 Lon: -17.32152 Depth: -0.000 km
1996 Oct 1 20:36:44.796 UTC Lat: 64.53529 Lon: -17.28325 Depth: -0.000 km
1996 Oct 1 20:44:09.885 UTC Lat: 64.68566 Lon: -17.40213 Depth: 0.000 km
1996 Oct 1 22:25:16.103 UTC Lat: 64.66853 Lon: -17.35650 Depth: 3.690 km
1996 Oct 1 23:15:16.165 UTC Lat: 64.70266 Lon: -17.35740 Depth: 7.284 km
1996 Oct 1 23:33:57.481 UTC Lat: 64.49084 Lon: -17.37889 Depth: 5.808 km
1996 Oct 1 23:34:51.016 UTC Lat: 64.67953 Lon: -17.27327 Depth: 6.740 km
1996 Oct 2 00:02:59.473 UTC Lat: 64.54285 Lon: -17.32256 Depth: 0.000 km
1996 Oct 2 00:55:11.502 UTC Lat: 64.68993 Lon: -17.43956 Depth: 9.742 km
1996 Oct 2 01:27:55.926 UTC Lat: 64.68636 Lon: -17.42677 Depth: 13.489 km
1996 Oct 2 01:39:09.664 UTC Lat: 64.54745 Lon: -17.35834 Depth: 3.143 km
1996 Oct 2 02:36:55.942 UTC Lat: 64.62098 Lon: -17.38446 Depth: 5.948 km
1996 Oct 2 04:15:52.891 UTC Lat: 64.68671 Lon: -17.40788 Depth: 0.000 km
1996 Oct 2 04:23:53.026 UTC Lat: 64.67422 Lon: -17.41377 Depth: 14.858 km

1996 Oct 2 06:05:09.152 UTC Lat: 64.64859 Lon: -17.37447 Depth: 0.000 km
1996 Oct 2 07:24:14.956 UTC Lat: 64.62905 Lon: -17.41925 Depth: 0.000 km
1996 Oct 2 07:30:10.697 UTC Lat: 64.55034 Lon: -17.38577 Depth: 0.717 km
1996 Oct 2 07:30:11.454 UTC Lat: 64.55300 Lon: -17.35526 Depth: 8.957 km
1996 Oct 2 08:02:16.423 UTC Lat: 64.66879 Lon: -17.46980 Depth: -0.000 km
1996 Oct 2 09:40:12.806 UTC Lat: 64.63472 Lon: -17.34262 Depth: 5.431 km
1996 Oct 2 11:07:18.674 UTC Lat: 64.70864 Lon: -17.38888 Depth: 0.000 km
1996 Oct 2 11:26:03.306 UTC Lat: 64.68993 Lon: -17.33995 Depth: 0.000 km
1996 Oct 2 11:42:08.824 UTC Lat: 64.65160 Lon: -17.52400 Depth: 1.765 km
1996 Oct 2 12:32:56.052 UTC Lat: 64.68048 Lon: -17.34522 Depth: -0.000 km
1996 Oct 2 13:16:58.013 UTC Lat: 64.68216 Lon: -17.42906 Depth: 17.200 km
1996 Oct 2 13:17:22.700 UTC Lat: 64.67516 Lon: -17.42541 Depth: 13.435 km
1996 Oct 2 17:50:45.364 UTC Lat: 64.65578 Lon: -17.58963 Depth: 0.000 km
1996 Oct 2 20:19:20.100 UTC Lat: 64.68135 Lon: -17.40999 Depth: 12.269 km
1996 Oct 2 20:59:58.774 UTC Lat: 64.66412 Lon: -17.47290 Depth: 0.001 km
1996 Oct 2 20:59:59.712 UTC Lat: 64.68466 Lon: -17.43683 Depth: 4.317 km
1996 Oct 2 22:11:10.426 UTC Lat: 64.67771 Lon: -17.33853 Depth: 8.394 km
1996 Oct 3 00:11:28.670 UTC Lat: 64.67869 Lon: -17.40591 Depth: 1.200 km
1996 Oct 3 00:33:12.860 UTC Lat: 64.65511 Lon: -17.59764 Depth: 0.000 km
1996 Oct 3 00:55:59.709 UTC Lat: 64.68052 Lon: -17.25674 Depth: 0.000 km
1996 Oct 3 01:47:08.956 UTC Lat: 64.62561 Lon: -17.43776 Depth: 12.834 km
1996 Oct 3 03:54:38.249 UTC Lat: 64.51143 Lon: -17.75938 Depth: 12.234 km
1996 Oct 3 04:00:06.854 UTC Lat: 64.66683 Lon: -17.41338 Depth: 14.872 km
1996 Oct 3 05:38:33.041 UTC Lat: 64.69355 Lon: -17.43771 Depth: 2.533 km
1996 Oct 3 06:17:17.755 UTC Lat: 64.67926 Lon: -17.49253 Depth: 11.174 km
1996 Oct 3 13:08:20.512 UTC Lat: 64.67298 Lon: -17.39666 Depth: 5.517 km
1996 Oct 3 13:57:30.656 UTC Lat: 64.54508 Lon: -17.36875 Depth: 14.316 km
1996 Oct 3 14:15:03.442 UTC Lat: 64.68177 Lon: -17.51854 Depth: 9.794 km
1996 Oct 3 18:15:14.161 UTC Lat: 64.55052 Lon: -17.42040 Depth: 13.498 km
1996 Oct 3 18:42:33.664 UTC Lat: 64.66484 Lon: -17.51513 Depth: 7.510 km
1996 Oct 3 18:48:55.575 UTC Lat: 64.71879 Lon: -17.45324 Depth: 17.112 km
1996 Oct 4 00:10:09.490 UTC Lat: 64.54669 Lon: -17.43252 Depth: 5.203 km
1996 Oct 4 00:10:09.198 UTC Lat: 64.54701 Lon: -17.34654 Depth: 12.280 km
1996 Oct 4 02:05:18.335 UTC Lat: 64.68209 Lon: -17.41511 Depth: 0.000 km

1996 Oct 4 02:53:41.708 UTC Lat: 64.62791 Lon: -17.44398 Depth: 3.319 km
1996 Oct 4 03:51:53.612 UTC Lat: 64.54120 Lon: -17.46900 Depth: 5.700 km
1996 Oct 4 07:34:29.066 UTC Lat: 64.52488 Lon: -17.37058 Depth: 7.717 km
1996 Oct 4 07:39:32.013 UTC Lat: 64.67352 Lon: -17.41861 Depth: 6.578 km
1996 Oct 4 08:25:15.863 UTC Lat: 64.67635 Lon: -17.42930 Depth: 4.282 km
1996 Oct 4 13:45:17.446 UTC Lat: 64.68038 Lon: -17.26786 Depth: 3.783 km
1996 Oct 4 14:28:37.553 UTC Lat: 64.84067 Lon: -17.47222 Depth: 28.195 km
1996 Oct 4 15:38:38.191 UTC Lat: 64.69089 Lon: -17.46715 Depth: 13.098 km
1996 Oct 4 18:43:57.082 UTC Lat: 64.51641 Lon: -17.38561 Depth: 17.742 km
1996 Oct 4 20:10:53.557 UTC Lat: 64.66197 Lon: -17.61695 Depth: 1.366 km
1996 Oct 4 21:51:59.016 UTC Lat: 64.73267 Lon: -17.51110 Depth: 0.000 km
1996 Oct 5 01:29:59.583 UTC Lat: 64.52342 Lon: -17.39182 Depth: 0.000 km
1996 Oct 5 01:36:36.324 UTC Lat: 64.54773 Lon: -17.41361 Depth: 8.837 km
1996 Oct 5 03:00:29.552 UTC Lat: 64.70099 Lon: -17.89499 Depth: 23.586 km
1996 Oct 5 03:00:29.551 UTC Lat: 64.71579 Lon: -17.89253 Depth: 15.535 km
1996 Oct 5 07:08:26.034 UTC Lat: 64.46442 Lon: -17.31488 Depth: 0.000 km
1996 Oct 5 07:17:55.844 UTC Lat: 64.69899 Lon: -17.44315 Depth: 7.430 km
1996 Oct 5 08:24:30.311 UTC Lat: 64.70962 Lon: -17.81250 Depth: 0.483 km
1996 Oct 5 08:32:25.032 UTC Lat: 64.72008 Lon: -17.79955 Depth: 0.000 km
1996 Oct 5 10:10:35.119 UTC Lat: 64.82447 Lon: -17.90653 Depth: 23.395 km
1996 Oct 5 10:51:29.653 UTC Lat: 64.79782 Lon: -17.89701 Depth: 6.894 km
1996 Oct 5 12:25:18.120 UTC Lat: 64.79656 Lon: -17.91437 Depth: -0.000 km
1996 Oct 5 17:04:29.973 UTC Lat: 64.68058 Lon: -17.41516 Depth: 10.996 km
1996 Oct 5 17:35:24.103 UTC Lat: 64.64879 Lon: -17.49377 Depth: 18.535 km
1996 Oct 5 20:18:30.206 UTC Lat: 64.68453 Lon: -17.46991 Depth: 23.358 km
1996 Oct 5 21:26:13.871 UTC Lat: 64.68949 Lon: -17.66356 Depth: 37.594 km
1996 Oct 5 22:54:45.530 UTC Lat: 64.89665 Lon: -17.74201 Depth: -0.000 km
1996 Oct 6 00:36:51.020 UTC Lat: 64.76979 Lon: -17.73856 Depth: 19.912 km
1996 Oct 6 02:21:10.232 UTC Lat: 64.76386 Lon: -17.47805 Depth: 0.000 km
1996 Oct 6 02:52:27.352 UTC Lat: 64.89925 Lon: -17.67205 Depth: 13.873 km
1996 Oct 6 03:06:10.603 UTC Lat: 64.51813 Lon: -17.38693 Depth: 4.733 km
1996 Oct 6 03:25:18.273 UTC Lat: 64.65487 Lon: -17.50571 Depth: -0.000 km
1996 Oct 6 03:44:58.151 UTC Lat: 64.86529 Lon: -17.69858 Depth: 0.354 km
1996 Oct 6 03:54:28.632 UTC Lat: 64.65198 Lon: -17.45908 Depth: -0.000 km

1996 Oct 6 03:56:56.038 UTC Lat: 64.62585 Lon: -17.48625 Depth: 8.854 km

1996 Oct 6 03:57:32.192 UTC Lat: 64.61537 Lon: -17.45088 Depth: 0.000 km

1996 Oct 6 05:09:27.739 UTC Lat: 64.80678 Lon: -17.80987 Depth: 2.964 km

1996 Oct 6 06:02:10.659 UTC Lat: 64.53848 Lon: -17.42205 Depth: 5.316 km

1996 Oct 6 10:12:22.765 UTC Lat: 64.86150 Lon: -17.52234 Depth: 1.744 km

1996 Oct 6 13:02:16.999 UTC Lat: 64.78187 Lon: -17.46496 Depth: 9.299 km

1996 Oct 6 17:07:04.618 UTC Lat: 64.47402 Lon: -17.37156 Depth: -0.000 km

1996 Oct 6 18:56:02.802 UTC Lat: 64.50030 Lon: -17.45545 Depth: 11.173 km

# Appendix C
# Relative locations using HOTSPOT arrival times

Relative locations of the earthquakes picked during the period September 29th-October 6th were calculated using the master-event method. This method is based on two assumptions: (a) most of the travel time residuals of an earthquake are due to differences between the true velocity structure and the model used to locate the earthquake; and (b) the earthquakes have similar raypaths and similar travel time residuals.

For each day, the best recorded earthquake (the one with the most measured arrival times) was used as the 'master' event. The residuals calculated for this earthquake, using the one-dimensional velocity model (Chapter 2), were subtracted from the arrival times measured for other earthquakes around it, and these earthquakes were located using the adjusted travel times. The C program *correctpicks*, written by the author of this thesis, was used to do this job. *correctpicks* first reads a file master.ev that contains the master event residuals, and then subtracts these values from the earthquake arrival times. All results were written to separate files (named like the originals for each event, with the suffix '.cor' at the end) in the binary format required by *qloc*.

The relative locations obtained in this way are shown in the figures that follow, with the master event used in each case indicated by a star. Even though clusters of epicentres look tighter, compared to the absolute locations, there was no substantial difference in the location of individual events. This might be the result of the fact that for many of the relocated events the assumption of similar raypaths probably breaks down, as there are many events scattered over the whole area of northwest Vatnajökull.

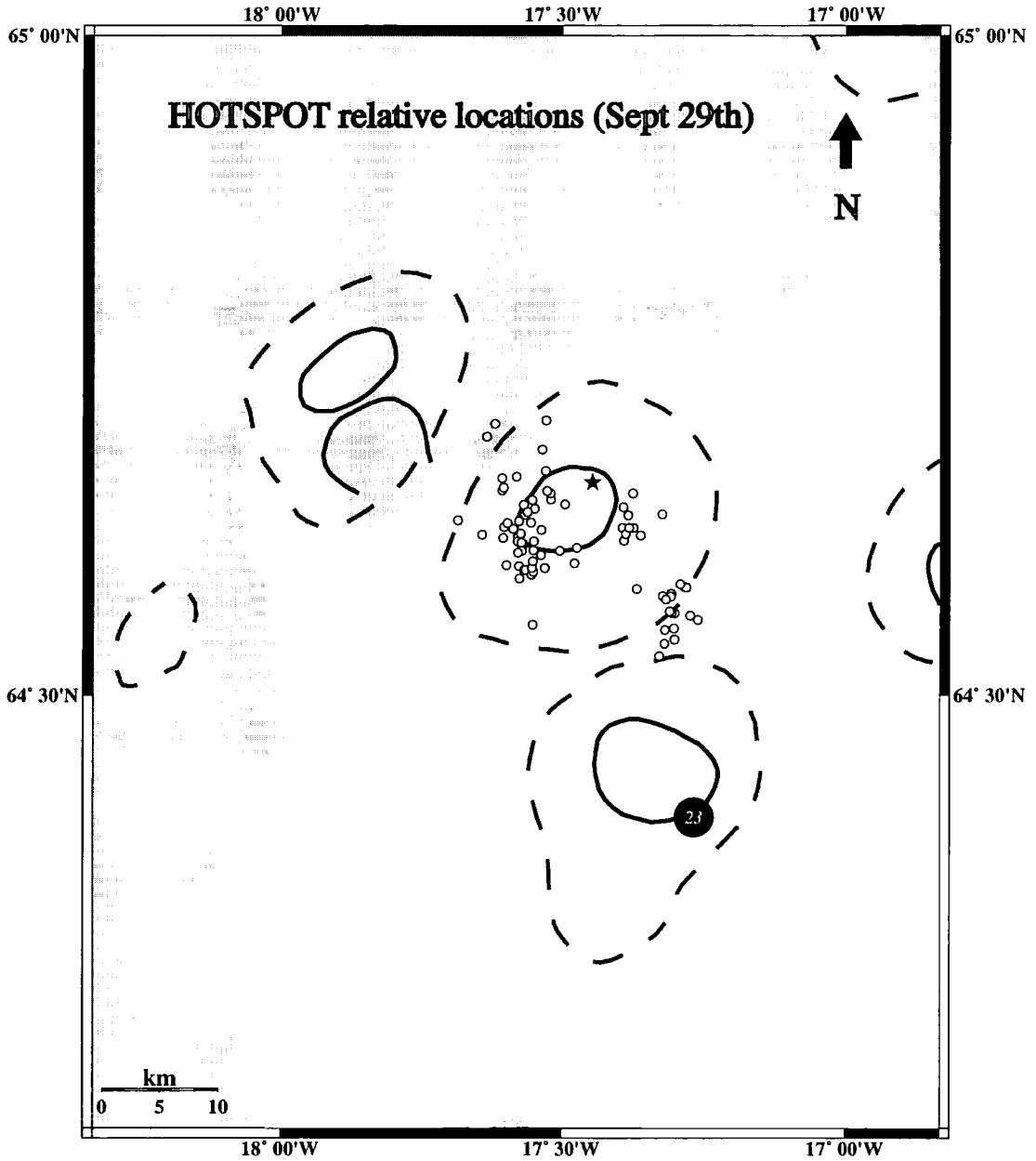
18° 00'W
17° 30'W
17° 00'W
65° 00'N
HOTSPOT relative locations (Sept 29th)
N
64° 30'N
23
km
0 5 10

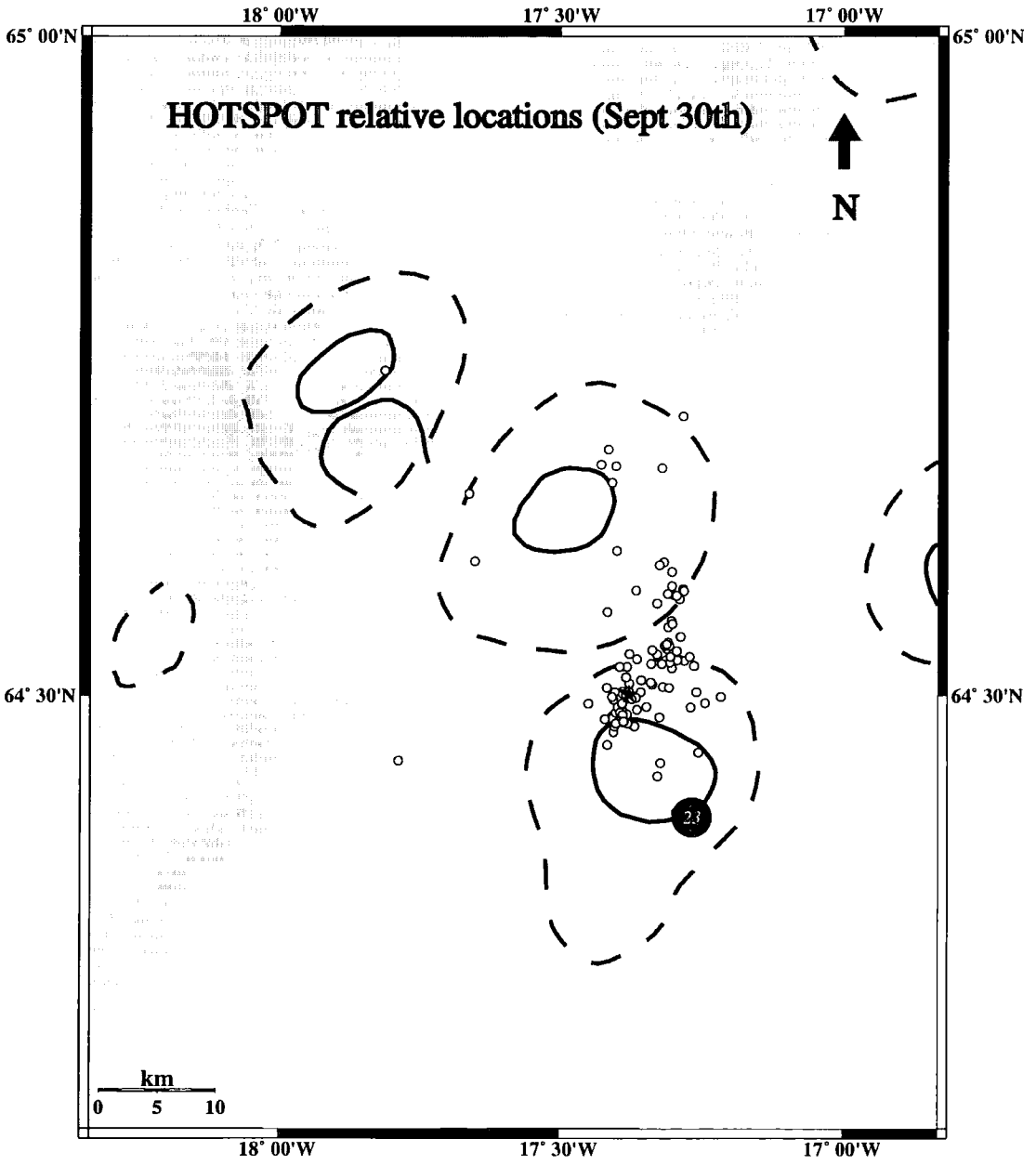
18° 00'W
17° 30'W
17° 00'W
65° 00'N
64° 30'N
HOTSPOT relative locations (Sept 30th)
N
23
km
0 5 10

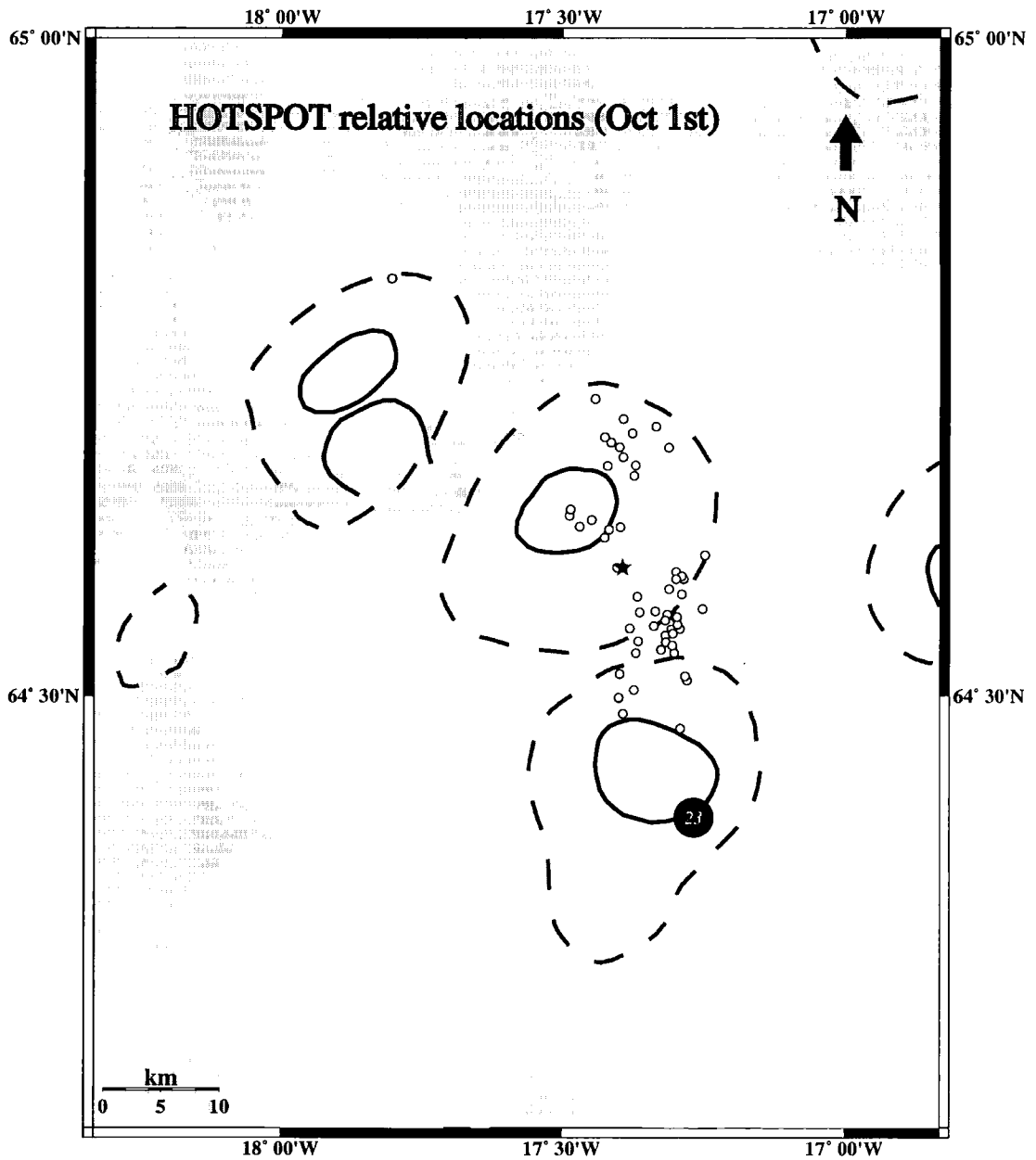
HOTSPOT relative locations (Oct 1st)
N
18° 00'W
17° 30'W
17° 00'W
65° 00'N
64° 30'N
km
0 5 10
23

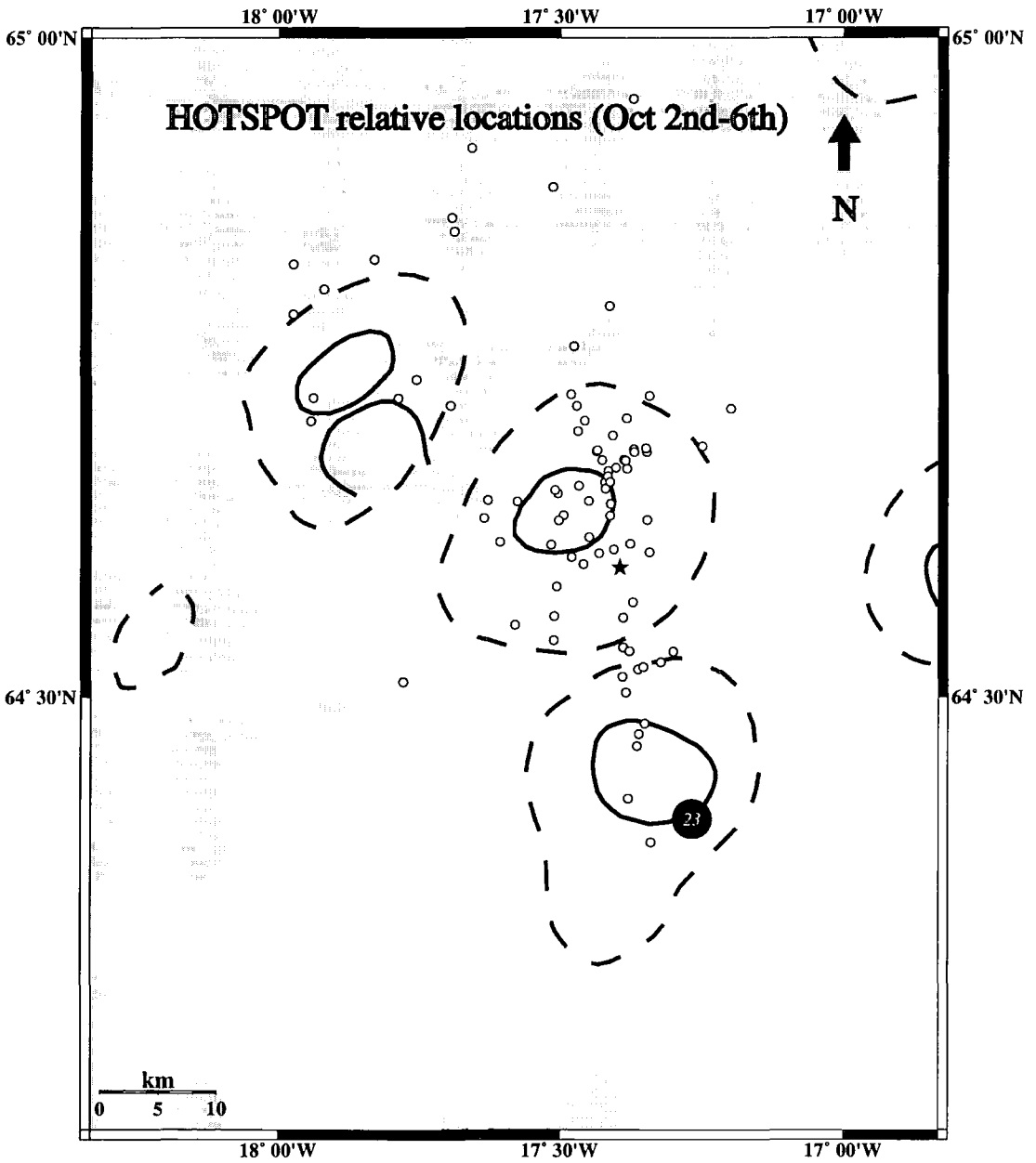
18° 00'W
17° 30'W
17° 00'W
65° 00'N
64° 30'N
HOTSPOT relative locations (Oct 2nd-6th)
N
23
km
0 5 10

# Appendix D
# Catalogue of SIL database discrepancies

The following is a catalogue of all the discrepancies found in the SIL database during the period September 29th-October 6th. The origin time for each event is the one given in each entry in the database.

### September 29th

| origin time | remark |
|---|---|
| 11:11:19.039 | nothing visible on seismograms in HOT23 |
| 11:34:30.997 | nothing visible on seismograms in HOT23 |
| 13:13:40.318 | nothing visible on seismograms in HOT23 |
| 13:59:25.795 | nothing visible on seismograms in HOT23 |
| 14:01:43.602 | nothing visible on seismograms in HOT23 |
| 23:39:01.589 | nothing visible on seismograms in HOT23 |

### September 30th

| origin time | remark |
|---|---|
| 02:59:48.707 | origin time late in station HOT23 |
| 03:59:47.052 | nothing visible on seismograms in HOT23 |
| 11:20:22.275 | earthquake visible only on seismograms in HOT23-21-25 |
| 11:25:31.532 | earthquake visible only on seismograms in HOT23-21 |
| 12:49:45.641 | nothing visible on seismogram in HOT23 |
| 13:41:28.957 | origin time 13s early in station HOT23 |

| | |
|---|---|
| 18:15:49.112 | nothing visible on seismogram in station HOT23 |
| 20:07:58.978 | origin time 5s late in station HOT23 |
| 20:39:06.981 | origin time 7s early in station HOT23 |
| 21:39:10.925 | visible in HOT25-27-28 but not HOT23 |
| 22:23:00.922 | visible only on station HOT27 |

**October 1st**

| **origin time** | **remark** |
|---|---|
| 00:25:30.146 | nothing visible on seismograms in HOT23-21-22 |
| 02:05:56.092 | nothing visible on seismogram in HOT23 |
| 02:25:26.989 | nothing visible on seismogram in HOT23 |
| 02:34:07.803 | earthquake visible only on seismogram in HOT23-21 |
| 08:05:52.988 | nothing visible on seismogram in HOT23-21 |
| 09:18:40.298 | origin time 15s late in station HOT23 |
| 11:39:17.305 | nothing visible on seismogram in HOT23 |
| 13:46:47.766 | nothing visible on seismogram in HOT23 |
| 20:44:21.107 | origin time 12s late in station HOT23 |

**October 2nd**

| **origin time** | **remark** |
|---|---|
| 02:47:23.329 | nothing visible on seismograms in HOT23-25 |
| 03:34:45.897 | nothing visible on seismograms in HOT23-25 |
| 04:58:05.442 | nothing visible on seismograms in HOT23-25 |
| 18:19:10.002 | nothing visible on seismograms in HOT23-25 |

**October 3rd**

| **origin time** | **remark** |
|---|---|
| 05:05:52.077 | nothing visible on seismograms in HOT23-25 |

**October 4th**

| **origin time** | **remark** |
|---|---|
| 05:27:09.141 | earthquake visible only on seismogram in HOT23 |

**October 5th**

| **origin time** | **remark** |
|---|---|
| 08:25:19.776 | earthquake visible only on seismogram in HOT23 |
| 23:03:24.711 | earthquake visible only on seismogram in HOT23 |
| 23:19:45.405 | earthquake visible only on seismogram in HOT23 |

**October 6th**

| **origin time** | **remark** |
|---|---|
| 09:09:34.894 | earthquake visible only on seismogram in HOT23 |
| 11:33:44.050 | earthquake visible only on seismogram in HOT23 |

# Appendix E
# Example of a SIL pickfile

The following is a typical SIL pickfile for an event that occurred September 30th:

origin time 96 09 30 03h 23m 35.5s ± 0.96s

latitude 64.636 ± 0.063 deg.

longitude -17.418 ± 0.058

focal depth 5.4 ± 0.0 km

| sta | phase | arr. time | res. | weight | dist | azi |
|---|---|---|---|---|---|---|
| grs | p | 03h 23m 54.95s | -0.01 | 21.7 | 127.3 | 28.0 |
| gra | p | 03h 23m 57.19s | -0.02 | 19.1 | 143.2 | 357.1 |
| gra | s | 03h 24m 14.25s | 0.07 | 1.1 | 143.2 | 357.1 |
| hla | p | 03h 23m 58.67s | 0.10 | 17.7 | 152.9 | 343.3 |
| sig | p | 03h 24m 2.30s | -0.21 | 6.4 | 181.0 | 338.0 |
| sig | s | 03h 24m 23.25s | -0.37 | 0.4 | 181.0 | 338.0 |

ELSEVIER

Journal of Volcanology and Geothermal Research 102 (2000) 169–187

Journal of volcanology and geothermal research

www.elsevier.nl/locate/jvolgeores

# Seismic phenomena associated with the 1996 Vatnajökull eruption, central Iceland

K.I. Konstantinou[a,*], G. Nolet[b], W.J. Morgan[b], R.M. Allen[b], M.J. Pritchard[a]

[a]*Department of Geological Sciences, University of Durham, South Road, Durham DH1 3LE, UK*
[b]*Department of Geosciences, Guyot Hall, Princeton University, Princeton, NJ 08544, USA*

Received 15 September 1999; received in revised form 23 February 2000; accepted 23 February 2000

**Abstract**

During late September 1996, a major eruption took place at the NW part of the Vatnajökull glacier in central Iceland. The eruption was preceded by intense seismic activity, which began with a $M_w = 5.6$ earthquake two days previously. Two very active volcanic systems, Bárdarbunga and Grimsvötn, are situated in that area underneath the permanent ice cap. The volcanoseismic phenomena associated with the eruption were recorded on both temporary (HOTSPOT) and permanent (SIL) seismic networks, covering most parts of the country. The recorded events were categorised, according to their waveform shape and frequency content, into three groups: (1) low-frequency events; (2) mixed-frequency events; and (3) volcanic tremor. The large earthquake at Bárdarbunga volcano, which initiated the seismic activity before the eruption, was located inside the caldera and had the characteristics of a non-double couple event. The epicentres of the earthquake swarm that followed it initially delineated the caldera rim and then migrated towards Grimsvötn, possibly indicating lateral movements of magma from a shallow chamber beneath Bárdarbunga. The eruption affected an area much larger than that between these two volcanoes, since seismic activity was also observed at distances 20 km away, at the Tindafjallajökull volcanic system. The spectral analysis of tremor, recorded at the nearest station to the eruption site, revealed its existence before the onset of the eruption in five narrow frequency bands (0.5–0.7, 1.6, 2.2, 2.8, 3.2 Hz) representing fundamental frequencies with their half- and quarter-subharmonics. This pattern continued until the last day of the eruption. It is believed that the eruption was caused by a dyke injection that had been going on beneath the Vatnajökull area for a period of 10 years. 

*Keywords*: Vatnajökull glacier; low-frequency events; mixed-frequency events; volcanic tremor; non-double couple event; dyke injection

## 1. Introduction

The NW part of the Vatnajökull glacier (Fig. 1) has been the centre of intense volcanic and seismic activity in historical times (Einarsson and Brandsdóttir, 1984; Björnsson and Einarsson, 1990; Gudmundsson and Björnsson, 1991) and is also suggested by geophysical (Einarsson, 1954; Tryggvason et al., 1983;) and geochemical studies (Sigvaldasson et al., 1974) as the centre of the Icelandic hotspot. The fact that the area is covered by a thick ice layer and that it is tens of kilometres away from the inhabited south coast has made it difficult to resolve structural details of the volcanic systems that lie underneath the ice cap. Two of these volcanic systems, responsible for much of the observed activity, are Bárdarbunga and Grimsvötn. Each is characterised by an elliptical shape caldera structure and it is generally believed that the fissure swarms that appear outside the ice cap

* Corresponding author. Fax: + 44-191-374-2510.
*E-mail address:* konstantinos.konstantinou@durham.ac.uk (K.I. Konstantinou).

0377-0273/00/$ - see front matter 
PII: S0377-0273(00)00187-6

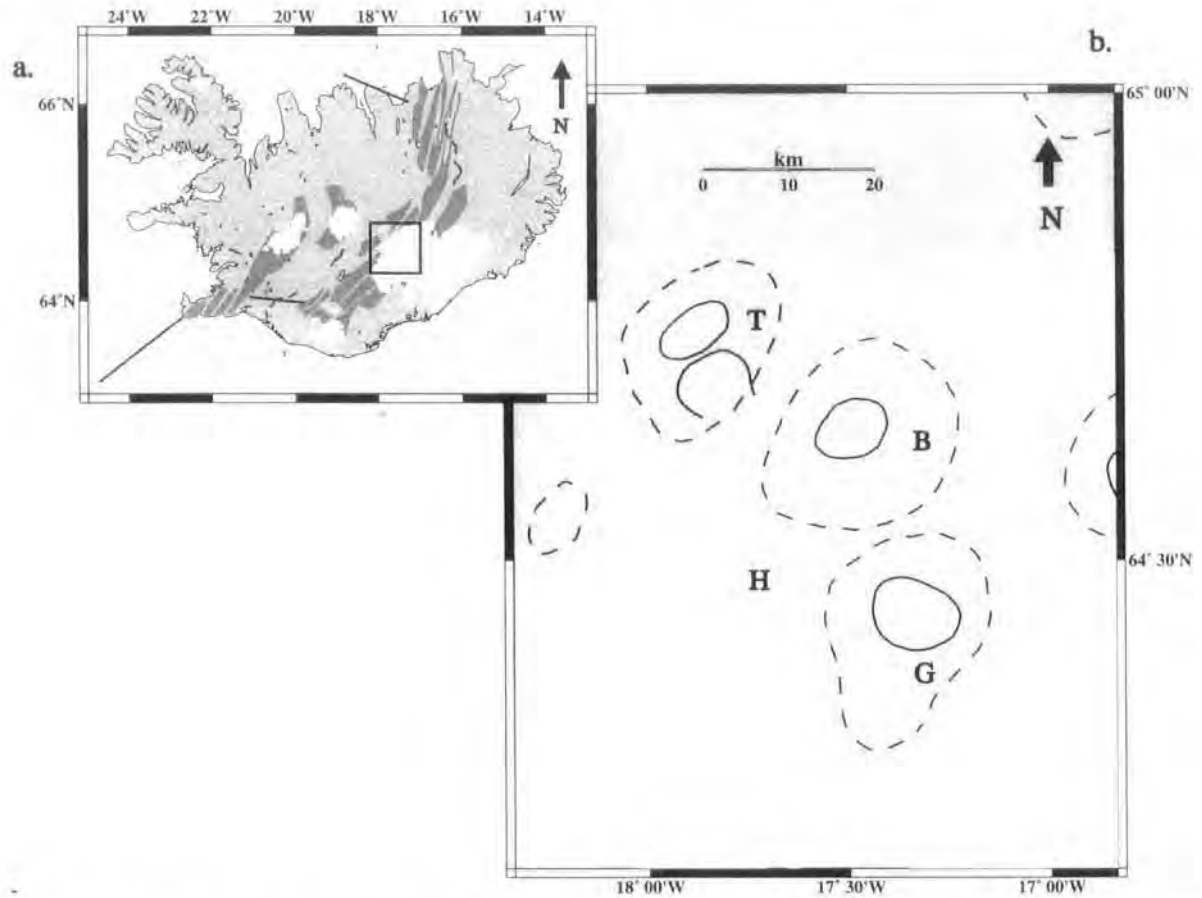


Fig. 1. (a) Map of the neovolcanic and fracture zones in Iceland. The square shows the area where the Vatnajökull eruption took place. White areas indicate permanent glaciers. (b) Map of the NW part of the Vatnajökull glacier. Solid lines represent the outline of calderas, dashed lines represent the outlines of central volcanoes. T: Tindafjallajökull; B: Bárdarbunga; G: Grimsvötn; H: Hamarinn.

are connected to these volcanic systems (Sæmundsson, 1979, 1980; Jakobsson, 1979, 1980).

Over the last 1100 years, the volcanoes beneath Vatnajökull are believed to have erupted 80 times, with 63 eruptions considered as certain, of which the number of eruptions at Grimsvötn has been estimated between forty and fifty (Gudmundsson and Björnsson, 1991). During this century, Grimsvötn

Table 1
Eruptions in the Grimsvötn area over the last century (after Gudmundsson and Björnsson, 1991)

| Year | Duration | Associated phenomena | Volume erupted ($km^3$) |
|---|---|---|---|
| 1934 | $\geq$ 2 weeks | Depressions in the ice, jökulhlaup | 0.03–0.04 |
| 1938 | 1–5 weeks | 7–8 km fissure, jökulhlaup | 0.3–0.5 |
| 1983 | 5–6 days | Depression in the ice | 0.01 |
| 1984 | 1 h? | Volcanic tremor recorded | ? |
| 1996 | 2 weeks | 9 km fissure, jökulhlaup | 0.4 |
| 1998 | 10 days | Depressions in the ice | ? |

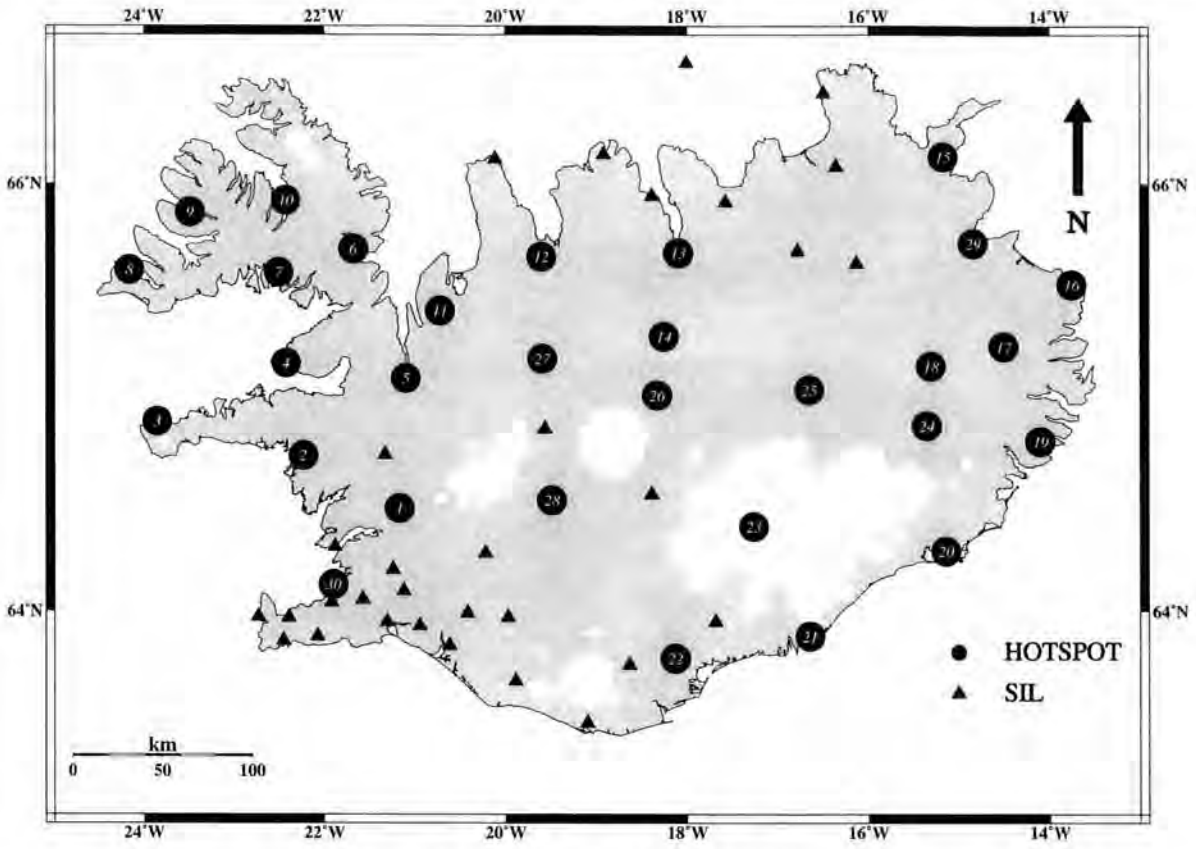


Fig. 2. Map of the HOTSPOT and SIL seismic networks.

has erupted six times (Table 1), including the latest eruption on 18 December 1998, after the large eruption in 1996. Most of the information that we have about the eruptive activity in Grimsvötn come from aerial photographs of the area. Such observations show openings in the ice shelf or depressions in the ice at the eruption site, filled with meltwater produced by the interaction of magma with ice. Accumulation of meltwater in the Grimsvötn caldera and its subsequent drainage underneath the glacier to the south coast has caused in the past catastrophic floods, that are described in the literature with the term "jökulhlaup" (meaning flooding from the glacier). However, jökulhlaups cannot be considered as definite indicators of eruptions, since the high geothermal heat flux may also cause excessive production of meltwater (Björnsson, 1988).

Several geophysical studies have been carried out in the Grimsvötn area, including radio echo-sounding (Björnsson and Einarsson, 1990) and seismic reflection surveys (Joset and Holtzscherer, 1954; Gudmundsson, 1989). They revealed an ice thickness of 240–260 m and a permanent subglacial caldera lake covering an area of 10 $km^2$ with a water depth of 40–90 m. The caldera floor was found to be covered by sediments in the northern and eastern parts and with lava flows in its southern part (Gudmundsson, 1989).

The first eruption in Grimsvötn to be detected by an increase in the level of seismicity was that of 1983, when a seismic network of 35 stations throughout the country was fully operational. The eruption was preceded by an intense earthquake swarm, believed to have been caused by the failure of the magma chamber walls and subsequent migration of magma in the surface (Einarsson and Brandsdóttir, 1984). Volcanic tremor was also recorded and it was most intense during the first 12 h of the eruption. Tremor

was observed again one year later, on 21 August 1984 for only 1 h and was interpreted as a small eruption that did not reach the surface of the ice (Björnsson and Einarsson, 1990).

Unlike Grimsvötn, Bárdarbunga was identified as an active volcano only recently, when aerial photographs revealed its elliptical shaped caldera (Einarsson, 1991). There are no historical records of volcanic activity in Bárdarbunga, even though tephrochronological and geochemical studies suggest that it may have been active in the early centuries of historical times (Larsen, 1984). Since 1974, the Bárdarbunga area has been the centre of unusual seismic activity with the occurrence of ten large earthquakes ($M_w \geq 5.1$), the latest having occurred prior to the large volcanic eruption in September 1996 (Einarsson, 1991; Nettles and Ekström, 1998). The epicentres are located around the Bárdarbunga caldera and their focal mechanisms appear to deviate from the double-couple source model.

In this paper, we present the results of the analysis of data recorded during the main phase (September 29–October 6) of the 1996 eruption, by a temporary (HOTSPOT) and a permanent seismic network (SIL). Our study starts with the location of the events and their spatial and temporal distribution, using all available data from both networks. We then examine the nature of the recorded seismic signals in the time and frequency domain in an effort to correlate them with the evolution of the eruption. Of particular interest is the occurrence of volcanic tremor before the main phase of the eruption, as well as its spectral characteristics, indicating again the potential importance of tremor in volcanic hazard assessment (Aki, 1992).

## 2. Data collection and analysis

In the summer of 1996, the HOTSPOT network was installed in Iceland as a joint project of Princeton and Durham Universities, the Icelandic Meteorological Office and the US Geological Survey. The primary purpose of the project was to obtain high quality data of local and teleseismic events in order to study the crustal and mantle structure, as well as to monitor the volcanic and high-seismicity zones. HOTSPOT consisted of 30 stations (Fig. 2) equipped with broadband three-component CMG3-ESP instruments, that had a flat velocity response in the frequency range of 0.03–20 Hz and Refraction Technology 72a-02 16-bit data loggers recording continuously at a rate of 20 samples $s^{-1}$. Absolute timing was provided by GPS receivers. The data were stored on disks which were changed every 1–4 months. HOTSPOT remained in operation until August 1998. Throughout the main phase of the 1996 eruption, all the HOTSPOT stations were operational except from HOT26. The SIL (South Iceland Lowlands) network (Stefánsson et al., 1993) is a permanent network consisting of 30 stations with broadband or short period sensors, recording data using a triggering mechanism. It is operated by the Icelandic Meteorological Office and its stations are mainly concentrated on the South Iceland Seismic Zone and the Tjörnes fracture zone in the north, where the seismic hazard is higher.

Table 2
Crustal model used to locate events

| Layer thickness (km) | $P$ wave velocity (km $s^{-1}$) |
|---|---|
| 1.00 | 3.53 |
| 2.00 | 4.47 |
| 3.00 | 5.16 |
| 4.00 | 5.60 |
| 6.00 | 5.96 |
| 9.00 | 6.50 |
| 20.00 | 6.73 |
| 32.00 | 7.20 |
| 90.00 | 7.40 |

We started analysing the HOTSPOT data first by identifying events that were recorded by at least five stations, with a good azimuthal coverage around the eruption site and with high signal-to-noise ratio. Arrival times were manually picked and each pick was assigned a quality value, which was in most cases 1 for a P wave and 3 for an S wave pick (using 0 as best quality and 4 as worst). In this way, our final dataset for the eight days period consisted of 339 events. Earthquakes were located using the program qloc (B.R. Julian, pers. commun., 1998), which performs an iterative, damped inversion of arrival time data from each recording station to minimise the sum of the travel time residuals. The one-dimensional (1D) crustal model (Table 2) we used is based on the results of the tomographic study of Iceland by Bjarnason et al. (1993).

Arrival times from the SIL stations were added to

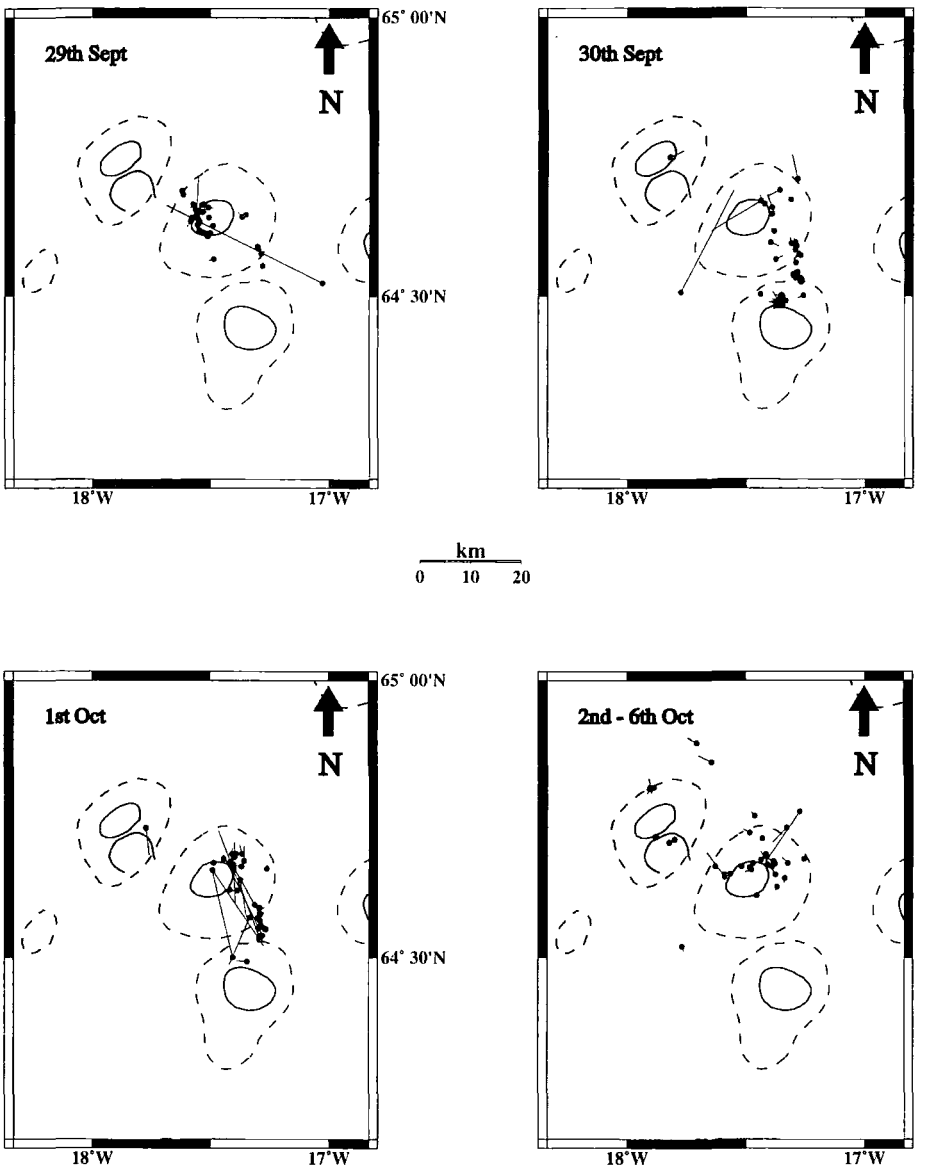


Fig. 3. Maps of events relocated using both HOTSPOT and SIL arrival times. The relocation vector has a direction from the location obtained with HOTSPOT arrival times to the new location obtained with HOTSPOT and SIL arrival times (black circle).

the HOTSPOT picked times, doubling the number of picks for each event, thus giving us the opportunity to estimate error bounds in our initial locations. However, due to the difference in detection thresholds, this was possible only for the events recorded by both networks. The relocation map for these events (Fig. 3) shows for most cases a difference in the epicentre locations of $\pm 1$ km. Larger differences are the result of the difficulty in picking small events with very emergent P onsets, introducing larger errors in the measurement of the arrival times. Residual values were usually less than 0.5 and 0.8 s for the P and S picks, respectively.

As in previous studies of the seismicity of the

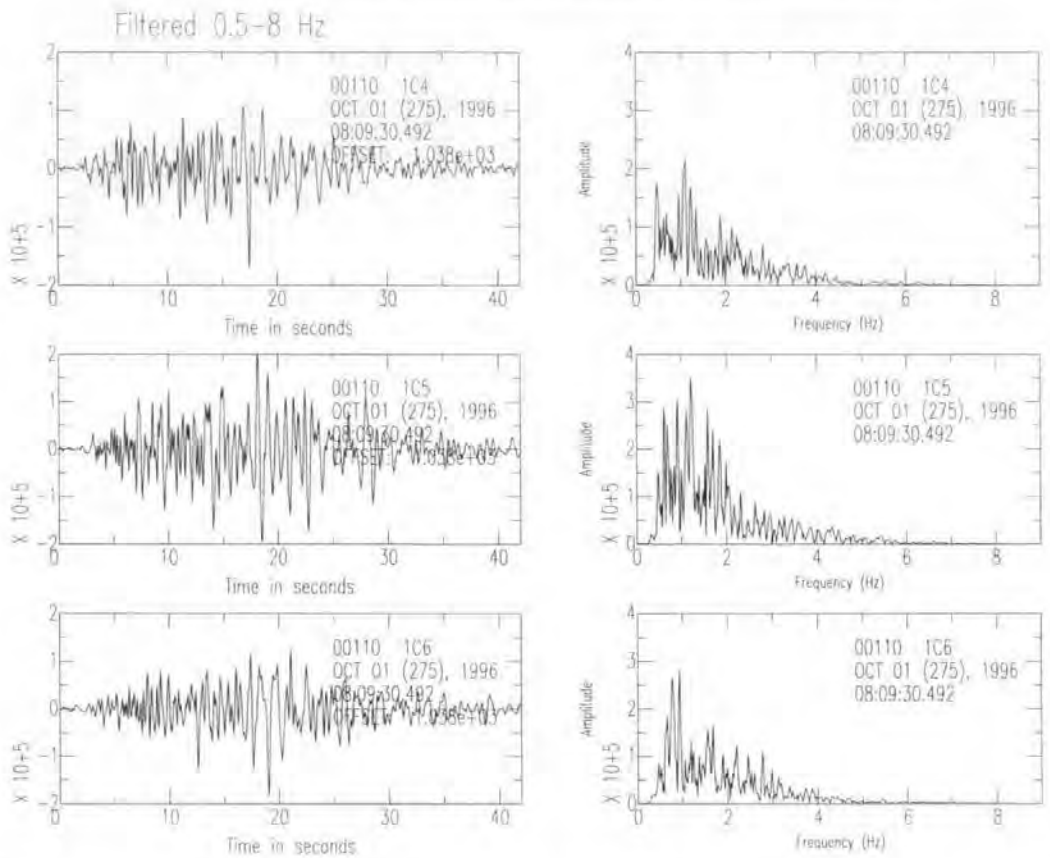


Fig. 4. Velocity waveforms and amplitude spectra of a low-frequency event recorded after the onset of the subglacial eruption (October 1) at station HOT23 by a three-component seismometer. The amplitude scales are normalised to the largest value of the three components. 1C4: vertical component, 1C5: north–south component, 1C6: east–west component.

area (Einarsson and Brandsdóttir, 1984), we had a difficulty in constraining the hypocentral locations for a large number of events. The main reason for this is the poor knowledge of the strongly heterogeneous Icelandic crust, which cannot be represented by a 1D velocity model. Currently, efforts are under way to determine a 3D model for the Iceland crust, using surface waves (Allen et al., 1999) and receiver functions (Z.J. Du, pers. commun., 1998) and may solve this problem in the future. A secondary reason is the lack of clear S phases from most of the events. Taking into account the thinning of the upper crust beneath Vatnajökull, as indicated by seismic refraction studies (Darbyshire et al., 1998), we have chosen to include only those hypocentres which are located no deeper than 8 km.

## 3. Description of seismic signals

Most of the seismic signals recorded during the eight-day period of the main eruption were categorised into groups based on waveform appearance and frequency content. Many classification schemes for volcanoseismic phenomena (e.g. Lahr et al., 1994) try to utilise these two criteria to interpret source processes. However, this can be a very difficult task, taking into account the complicated and poorly known velocity structure of most volcanic areas around the world, that can distort many features of the original waveform. In order to avoid this complicating factor, we group events using terms that are descriptive of the waveform and amplitude spectrum and not of the underlying source process. We summarise below the characteristics of each of these groups.

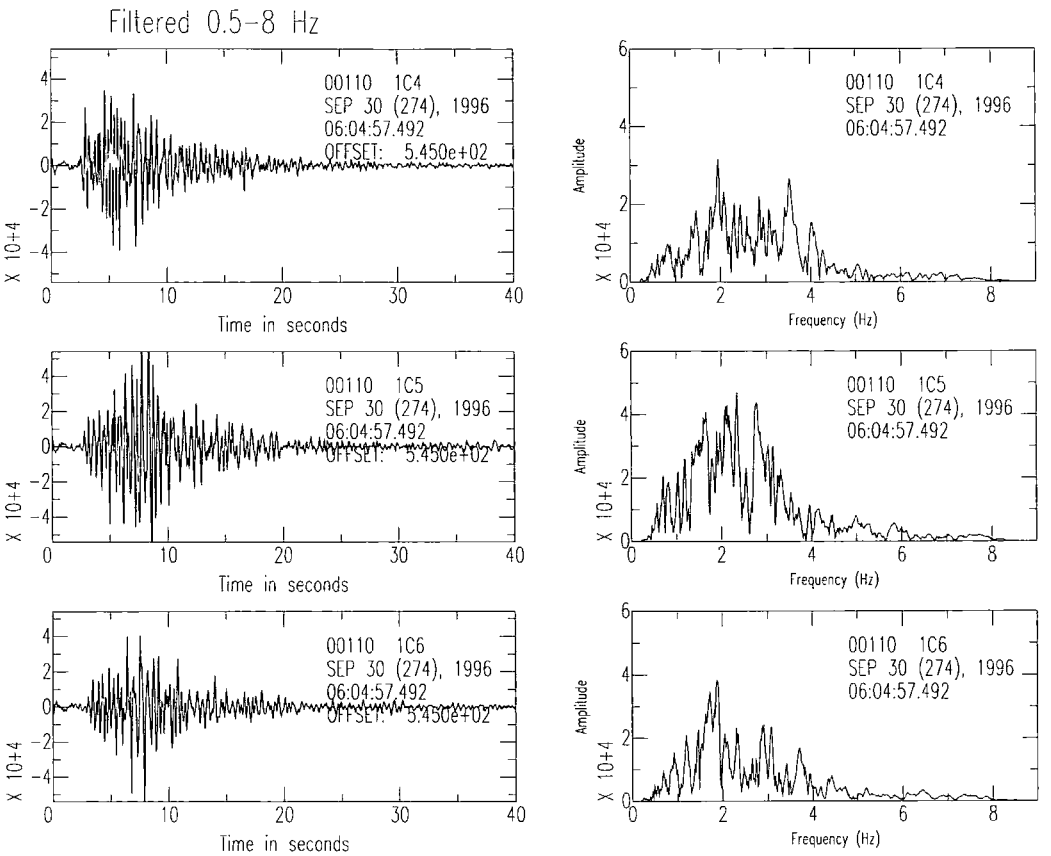


Fig. 5. Same as in Fig. 4, for a mixed-frequency event, recorded before the onset of the eruption. Note the impulsive high-frequency onset and how the coda decays exponentially with time, decreasing the duration of the signal, to about half of that of the low-frequency event in the previous figure.

*Low-frequency events.* The waveform is characterised by an emergent onset of the P wave and lack of clear S phases. The coda decays very slowly with time, increasing the duration of the signal up to 1 min. The energy in the spectrum is mostly in the range 0.5–2 Hz, with multiple sharp peaks (Fig. 4). In many cases, two or more of these events are clustered together forming a continuous wavetrain.

*Mixed-frequency events.* The waveform is characterised by a high frequency, impulsive P wave onset followed by a coda that decays almost exponentially with time. There is considerable energy in the range 1–2 Hz, but energy at higher frequencies is also present (Fig. 5).

*Volcanic tremor.* Following the start of the eruption, wavetrains with small amplitudes form continuous background tremor. Tremor bursts with larger amplitudes and variable duration are superimposed on it (Fig. 6). Energy is concentrated in the frequency range 0.5–3.9 Hz.

## 4. Spatio-temporal variations of seismicity

At 10:48 h GMT on the morning of September 29, an earthquake of magnitude $M_w = 5.6$ took place near the northern rim of the Bárdarbunga caldera (Fig. 7). It was followed by a swarm of other earthquakes about 20 min later. All of these earthquakes may be characterised as low-frequency events and their epicentres

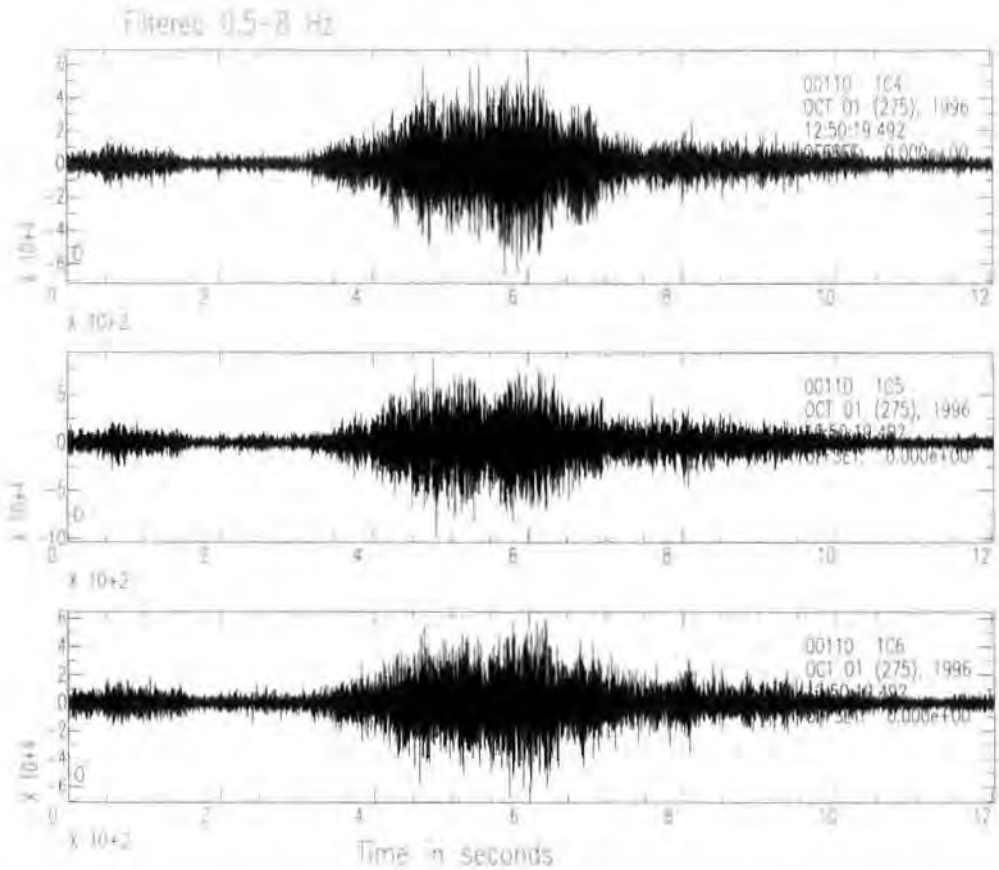


Fig. 6. Waveforms of high-amplitude tremor superimposed on the background tremor, recorded after the subglacial eruption (October 1) at station HOT23

delineate the caldera rim. Between 14:10 and 17:20 h, the activity decreased and resumed again in the evening of the same day. This time the epicentres were located to the SE of the Bárdarbunga caldera and 15 km away from the area where the seismic activity first started. The spectra of these events exhibit energy at higher frequencies but the coda decays slowly, like those of low-frequency events.

In the early hours of morning, the seismic activity continued at the same area, slowly migrating southwards towards Grímsvötn during the day (Fig. 8). The resulting earthquake cluster that is formed is elongated in the NNE–SSW direction and covers the same area where the eruptive fissure and depressions on the ice were observed later. Meanwhile, the Bárdarbunga area was relatively quiet, with only a few events occurring at the NE caldera rim. Almost all of these earthquakes are mixed-frequency events that have a coda decaying exponentially with time. Later that evening (22:00) continuous volcanic tremor started being visible above the ambient background noise at the nearest station (HOT23), indicating that the subglacial eruption was imminent.

On October 1, the activity persisted in the northern part of Grímsvötn, forming a smaller elongated cluster of epicentres, while at the same time another cluster formed at the NE part of the Bárdarbunga area (Fig. 9). Early in the morning of that day, the fissure and depressions in the ice were observed from an aeroplane. Most of the earthquakes recorded subsequently are typical low-frequency events, superimposed on the background tremor. On October 2, the eruption broke through the ice and became subaerial, but the

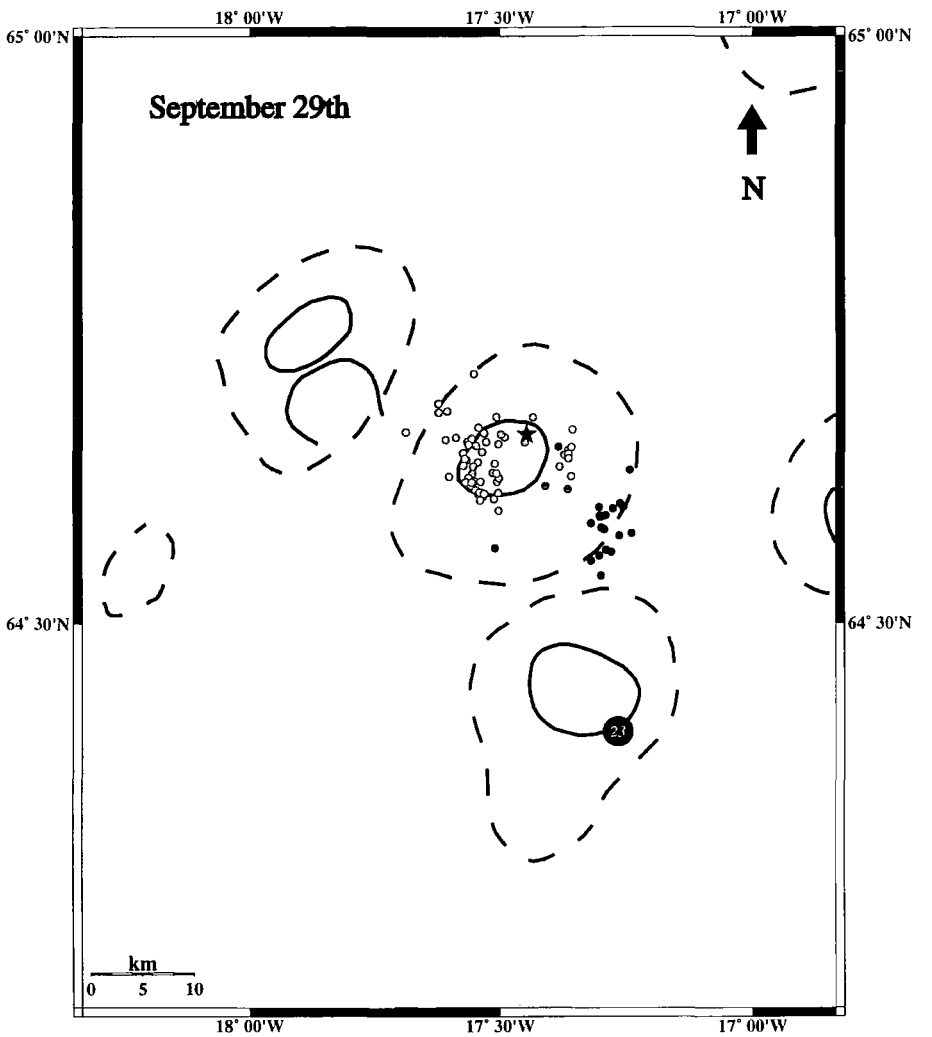


Fig. 7. Map of events located by HOTSPOT for September 29. The star indicates the epicentre of the magnitude $M_w = 5.6$ event at Bárdarbunga. The grey circles indicate epicentres of low-frequency events, while the black indicate epicentres of mixed-frequency events.

seismic activity decreased considerably. The Grimsvötn area was quiet and most of the events were located in the NE part of the Bárdarbunga caldera (Fig. 10). On subsequent days (October 3–6), low-frequency events continued to take place in the NE of Bárdarbunga and inside its caldera. However, a small number of earthquakes was located to the north and inside Tindafjallajokull volcanic system, up to 20 km away from the Bárdarbunga caldera (Fig. 11). Cross-sections of the hypocentres for the whole period are shown in Fig. 12.

## 5. Spectral analysis of volcanic tremor

Volcanic tremor was first observed at the nearest station to the eruption site (HOT23) in the evening of September 30 and was recorded continuously for 14 days, until the afternoon of October 13. Our study of the spectral characteristics of tremor covers the whole of this period, in an effort to check whether there was any substantial seismic activity shortly before the main eruption. In order to be able to observe better the temporal variations in the

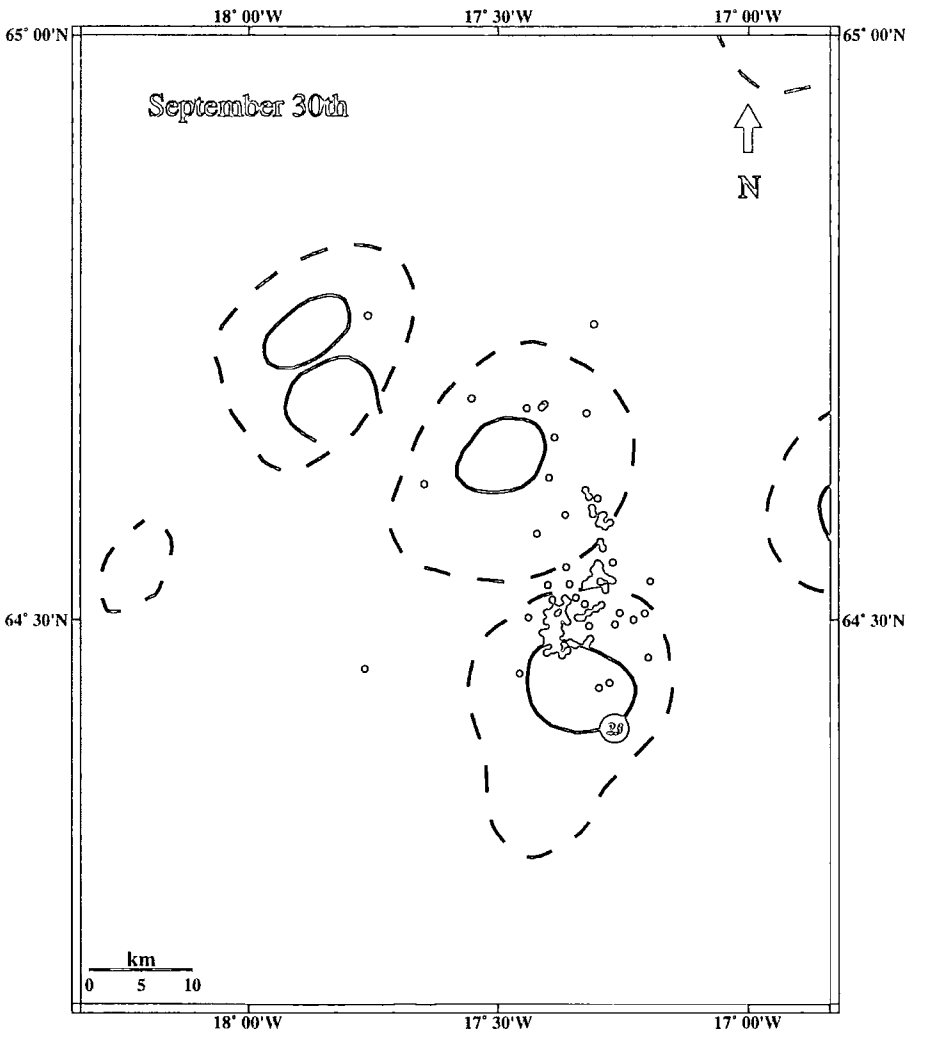


Fig. 8. Same as Fig. 7, for September 30.

frequency content of tremor, we created spectrograms for each of the three components of station HOT23 over successive time intervals of 12 h. A spectrogram is simply a 2D representation of the variations of spectral energy and frequency of the observed signal as time elapses.

The spectrograms for the first day revealed the existence of a seismic signal around five narrow frequency bands of 0.5–0.7, 1.6, 2.2, 2.8 and 3.2 Hz, not clearly visible on all three components (Fig. 13). This signal continued to be present in the spectrogram of the next day but there was an abrupt reduction in amplitude about 5 h before the large earthquake at Bárdarbunga occurred (Fig. 14). It is interesting to note the numerical relationship of the above values: there are peaks at fundamental frequencies of 3.2, 2.8 and 2.2 Hz with corresponding subharmonics at 1.6, 0.7 and 0.55 Hz, respectively. For the following day (September 30), it is quite difficult to decipher any of these frequency bands, due to the large number of earthquakes occurring in the same range of frequencies. For the remaining period up to the day that tremor was last recorded (October 13), the same pattern is observed,

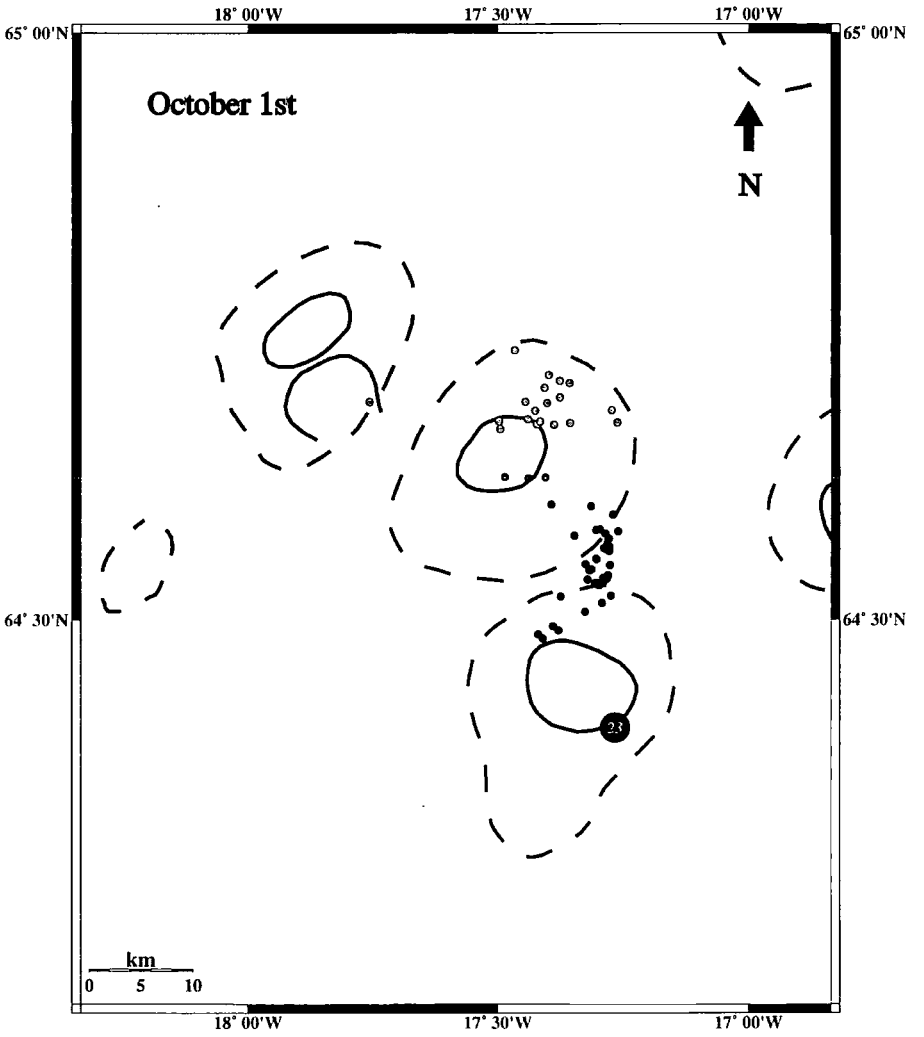


Fig. 9. Same as Fig. 7, for October 1.

with the appearance of the same fundamental frequencies and their half- and quarter-subharmonics (Fig. 15).

Such behaviour, where the period of the tremor signal is doubled, has also been observed at other volcanoes, e.g. in Hawaii (Aki and Koyanagi, 1981), Mt Semeru, Indonesia (Schlindwein et al., 1995) and Arenal volcano, Costa Rica (Barquero et al., 1992) and is believed to be the result of increasing nonlinearity in the source. This nonlinear process can be modelled numerically considering the flow of magmatic fluids through a constricted channel with deformable walls (Julian, 1994). Depending on the physical properties of the fluid-walls system and the variations of the fluid pressure, there can be either steady flow with no wall oscillations or cycles of opening and closing of the channel walls, responsible for the phenomenon of period doubling.

## 6. Discussion

The 1996 eruption at the Vatnajökull glacier was accompanied by a variety of seismic and volcanic

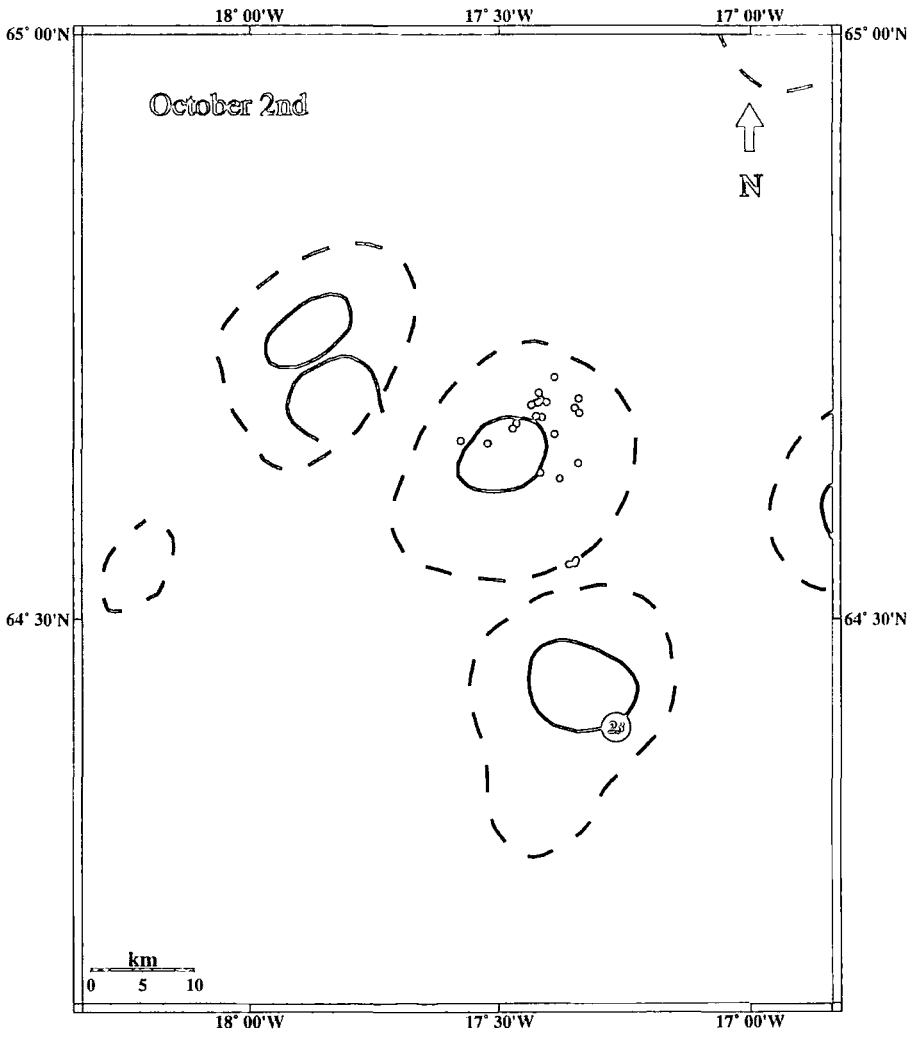


Fig. 10. Same as Fig. 7, for October 2.

phenomena, affecting a much larger area than just the area between Bàrdarbunga and Grimsvötn and more than one volcanic system. While other volcanoes in Iceland may erupt without any precursory activity, e.g. the Hekla eruptions in 1970, 1980, 1981 and 1991 (Brandsdóttir and Einarsson, 1992), this eruption was preceded by a series of remarkable precursory phenomena. Examination of the seismicity of this area for a period of four and a half years before the eruption (Fig. 16a) revealed a considerable increase in seismic activity during the first half of 1996 in the nearby Hamarinn volcano. This is in accordance with earlier observations, which indicate that seismic activity in Hamarinn may affect Bàrdarbunga and vice versa (Björnsson and Einarsson, 1990).

Our analysis also revealed short-term precursors, in the form of volcanic tremor signals, approximately two days before the main eruption and just before the onset of the episodic earthquake swarm that preceded it (Fig. 16b). Based on the spectral characteristics of the signals, we can interpret them as evidence of flow of magma from a deeper source to a shallow magmatic chamber beneath Bardarbunga. Studies of the crustal structure beneath other Icelandic

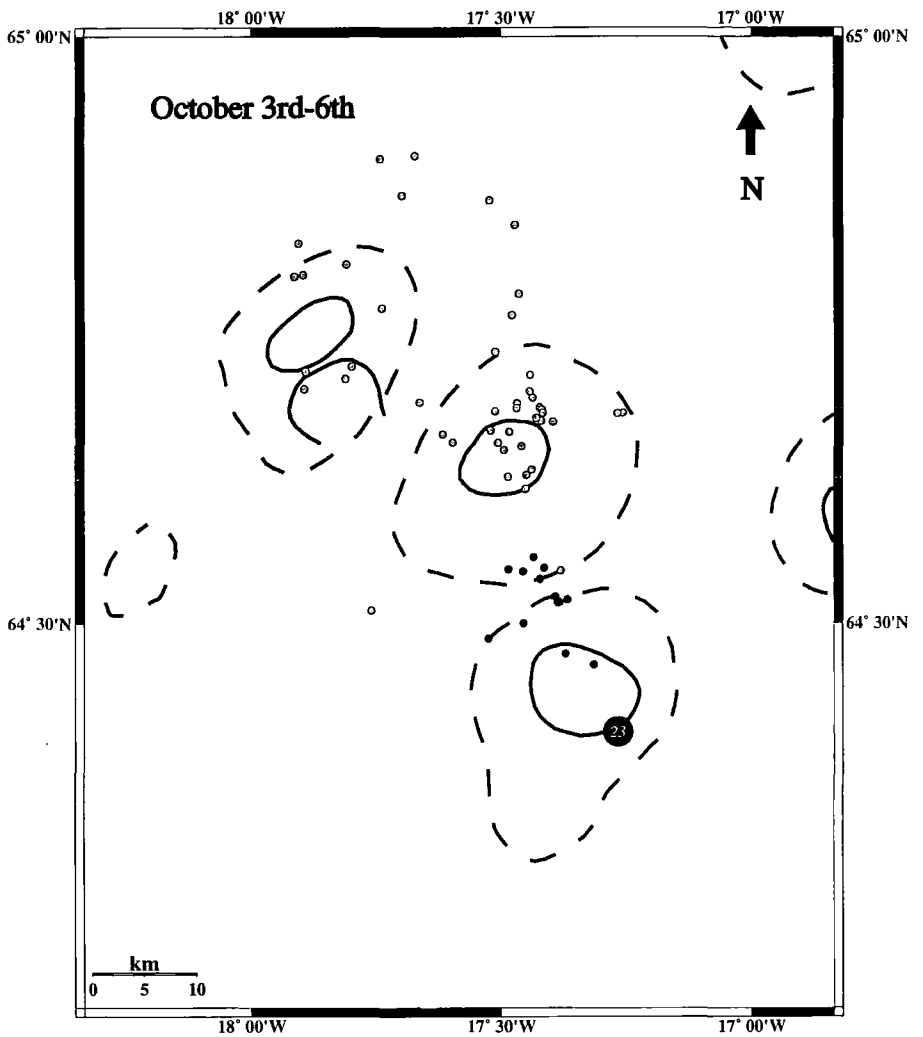


Fig. 11. Same as Fig. 7, for the period October 3–6.

volcanoes have revealed that magma chambers, filled with partially molten material, exist at depths of 1–3 km (Einarsson, 1978; Gudmundsson et al., 1994; Gudmundsson, 1995).

The large earthquake that followed the pre-eruptive tremor signals had all the characteristics of a typical low-frequency event and its focal mechanism showed a large deviation from the conventional double couple model. Nettles and Ekström (1998) obtained the centroid moment tensor solution for this event, using teleseismic data. They interpreted its non-double couple nature as the result of thrust motion on planes of varying strike that form an outward dipping cone-shaped ring fault beneath the Bárdarbunga caldera. The fact that the epicentres of the earthquakes that followed form a curved line along the western caldera rim (Fig. 7) may be evidence for such a rupture process. Numerical studies of the stress field around shallow magma chambers indicate that the initiation of ring faults is possible for sill-like magma chambers affected by doming of an area much larger than that of their caldera (Gudmundsson et al., 1997). This agrees well with the observations of early activity in Hamarinn and the shifting of

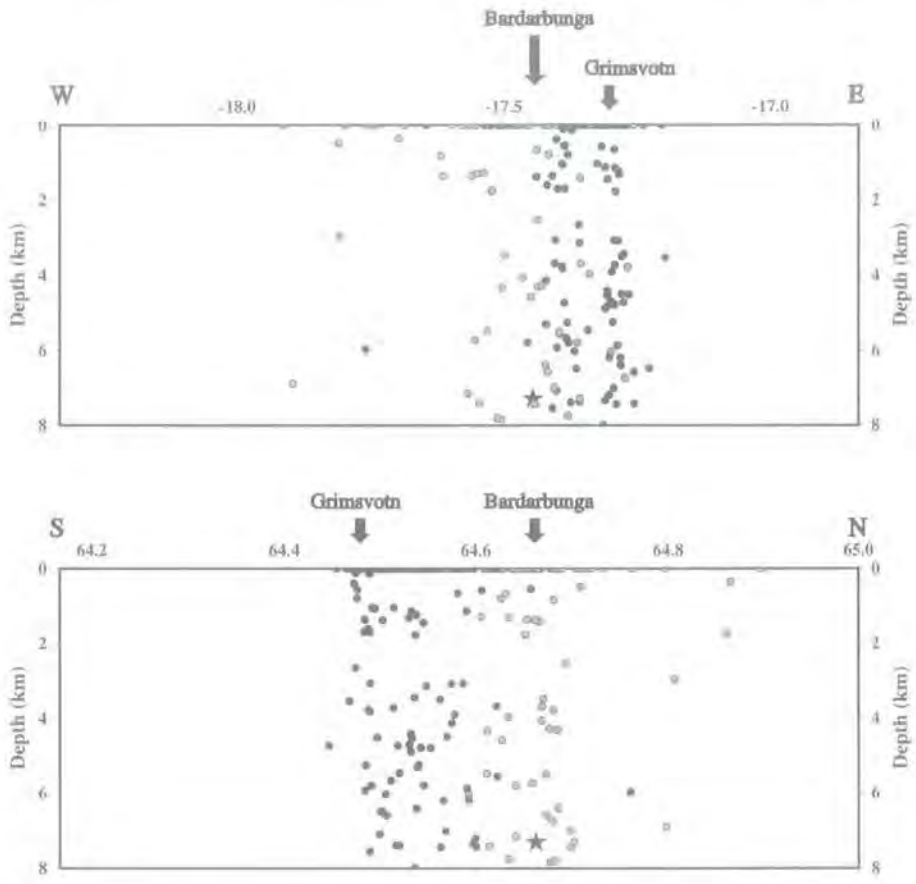


Fig. 12. East–west and north–south depth cross-sections of events for the period September 29–October 6. Symbols as in Figs. 7–11.

seismicity towards Tindafjallajökull during October 3–6. Also the shift of the epicentres that we observed in September 29–30 towards Grimsvötn and the formation of a fissure at the same place may suggest a lateral migration of magma from the shallow chamber underneath Bárdarbunga.

An alternative explanation for a non-double couple mechanism and for the course of events during the eruption, is that of a dyke injection below an area close to the eruptive site (R. Stefánsson, personal communication, 1999). It is believed that such a process had been going on in that area for a period of approximately 10 years and that the earthquakes were releasing compressive stress caused by dyke injection below the Vatnajökull area. Similar processes are believed to have taken place in other volcanoes around the world, accompanied by such anomalous earthquakes, as in Long Valley caldera (Julian, 1983) and at the Izu-Oshima volcano, Japan (Ukawa and Ohtake, 1987). In the case of Icelandic volcanoes a well-documented example of long-term dyke intrusion is the rifting episode at Krafla volcano in 1975–1984 (Brandsdóttir and Einarsson, 1979). Earthquakes with non-double couple characteristics are the result of concentrated tensile stress in the area where magma is forcing its way to the upper parts of the crust. Research is under way to obtain more focal mechanism solutions of earthquakes following the large event at Bárdarbunga that will allow a more thorough assessment of the physical mechanism of the eruption than it is possible with the analysis presented here.

Volcanoseismic phenomena have not previously been so well recorded in such an active area as NW

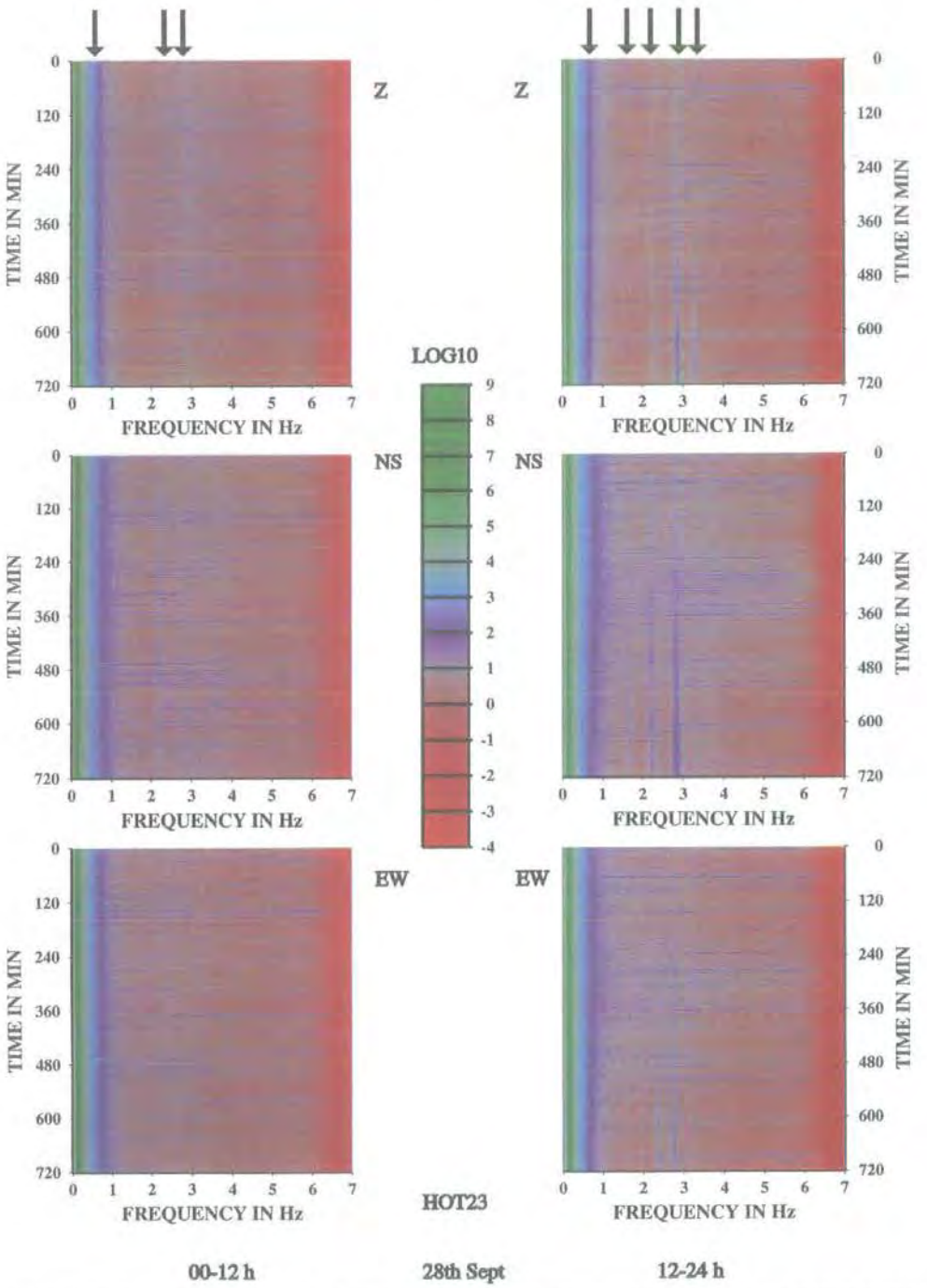


Fig. 13. Tremor spectrograms for September 28. Each plot represents 12 h of data for the three components of station HOT23. The colour scale for the amplitude is logarithmic. Vertical arrows show the frequency bands observed. The high-amplitude signal below 0.3 Hz represents ocean microseismic noise.

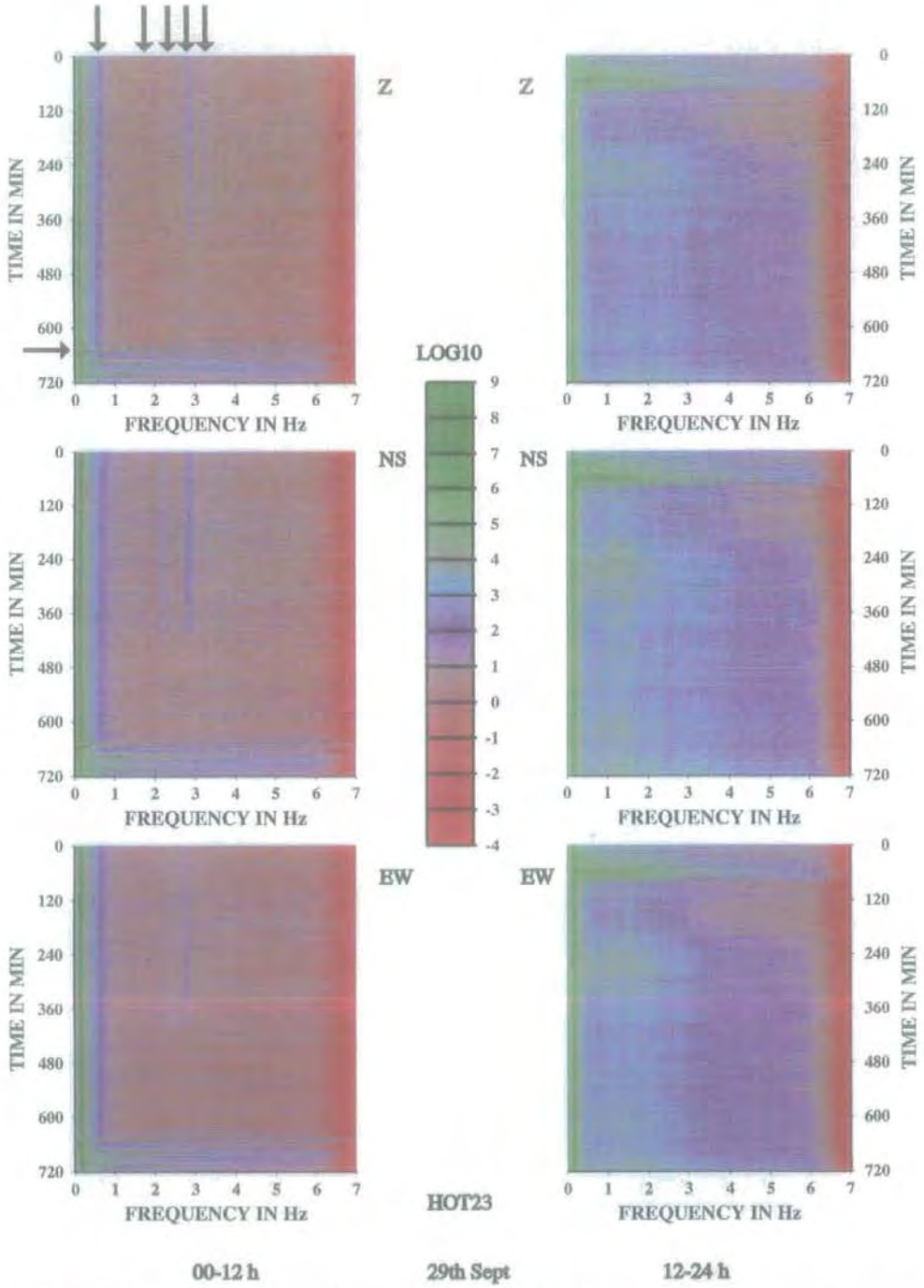


Fig. 14. Same as Fig. 13, for September 29. Horizontal arrow shows the onset of the large event at Bardarbunga and the swarm that followed it.

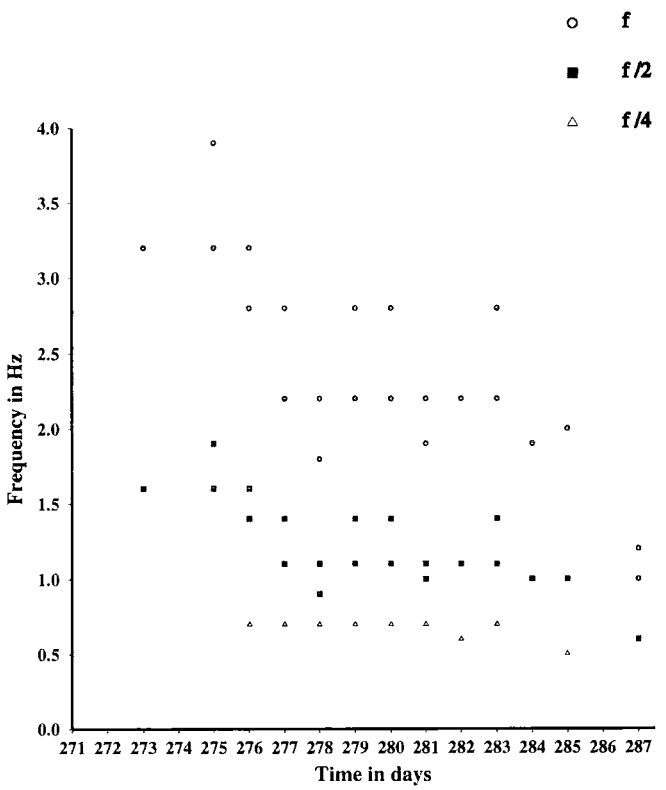


Fig. 15. Diagram of frequency versus time, showing the fundamental frequencies and their half- and quarter-subharmonics for each day, from September 28 (272) to October 13 (287).

Vatnajökull. The scientific observations described in this paper show once again the significant role that seismic monitoring of active volcanoes can play in the successful identification of eruption precursors. However, apart from the social benefit of eruption forecasting, seismic monitoring also provides an opportunity of obtaining a more thorough understanding of the processes inside active volcanoes.

## Acknowledgements

We would like to thank Neil Goulty, Vera Schlindwein, Prof. Roger Searle and an anonymous reviewer for reading this manuscript and contributing many helpful suggestions. We would also like to thank Ragnar Stefansson, members of staff at the Icelandic Meteorological Office and Kristin Vogfjörd for useful discussions and for sharing data and information with us. Christine Peirce kindly provided financial support for the reproduction of coloured figures 13–14. The HOTSPOT project was funded by the National Environmental and Research Council (NERC) grants GST/02/1238 and GR3/10727 held by G.R. Foulger, NSF grant EAR 9417918 and supported by the US Geological Survey. We thank IRIS/PASSCAL for technical support and assistance in running the network. All the maps and diagrams in this paper were plotted using the GMT software package (Wessel and Smith, 1995), the figures containing waveforms and spectra were produced using SAC2000 (Goldstein et al., 1998) and the software used to create the spectrograms was written by B.R. Julian. More information about the 1996 and 1998 eruptions in Vatnajökull, as well as a database containing preliminary determined parameters of earthquakes located by the SIL network, can be found at the Icelandic Meteorological Office webpage: http://www.vedur.is

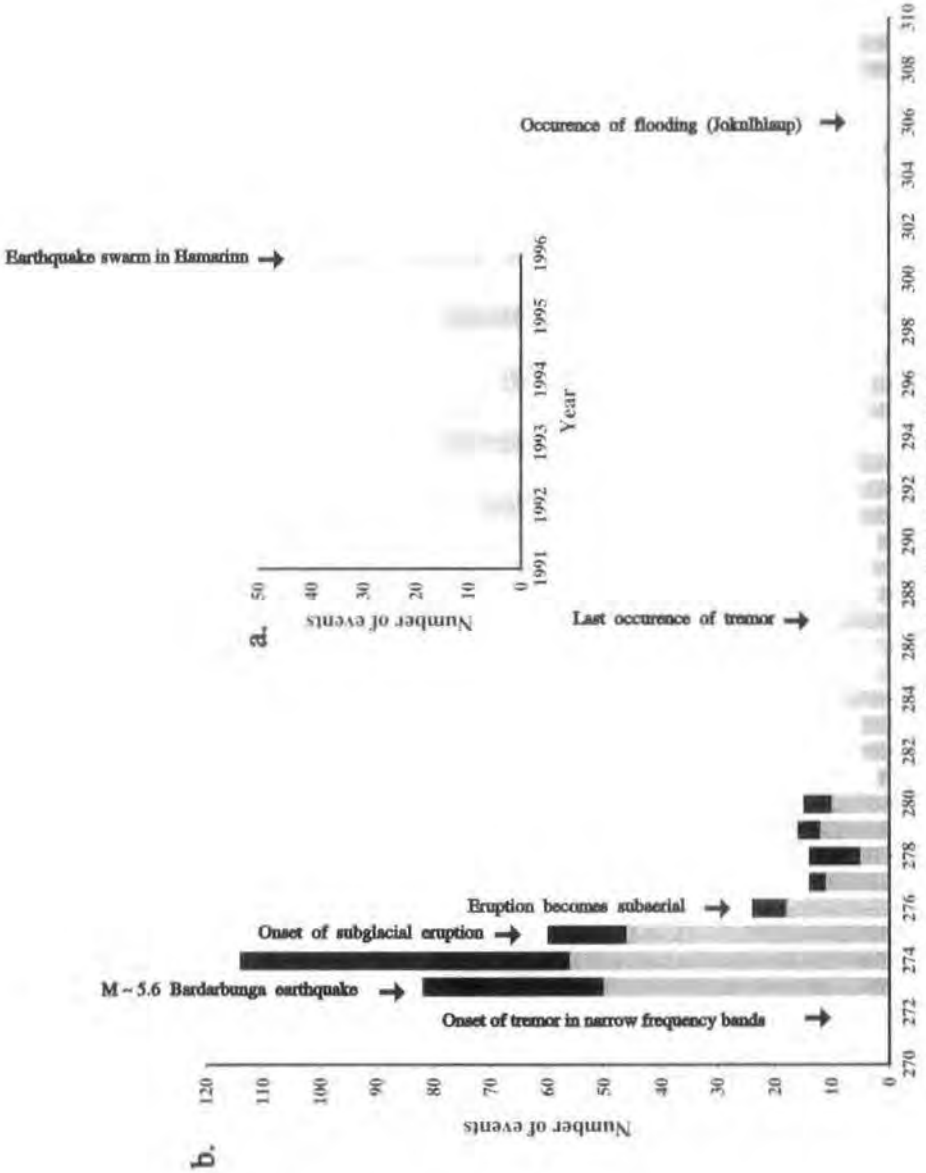


Fig. 16. (a) Annual seismicity levels from 1992 to September 1996 (numbers were obtained from the SIL network database) (b) Histogram showing the distribution of located events during the whole period of the eruption. Black bars: events located using only HOTSPOT data, grey bars: events located using only SIL data.

## References


Aki, K., 1992. State of the art in volcanic seismology. In: Gasparini, P., Scarpa, R., Aki, K. (Eds.), Volcanic Seismology. IAVCEI Proceedings in Volcanology, vol. 3, pp. 3–10.

Aki, K., Koyanagi, R.Y., 1981. Deep volcanic tremor and magma ascent mechanism under Kilauea, Hawaii. J. Geophys. Res. 86, 7095–7110.

Allen, R.M., et al., 1999. Toward a 3D crustal S-velocity model for Iceland. EOS Trans. AGU 80 (17), S220 (Spring Meet suppl.).

Barquero, R., Alvarado, G.E., Matumoto, T., 1992. Arenal volcano (Costa Rica) premonitory seismicity. In: Gasparini, P., Scarpa, R., Aki, K. (Eds.), Volcanic Seismology. IAVCEI Proceedings in Volcanology, vol. 3, pp. 3–10.

Brandsdóttir, B., Einarsson, P., 1979. Seismic activity associated with the September deflation of the Krafla central volcano in NE Iceland. J. Volcanol. Geotherm. Res. 6, 197–212.

Brandsdóttir, B., Einarsson, P., 1992. Volcanic tremor and low-frequency earthquakes in Iceland. In: Gasparini, P., Scarpa, R., Aki, K. (Eds.), Volcanic Seismology. IAVCEI Proceedings in Volcanology, vol. 3. , pp. 212–222.

Bjarnasson, I.T., Menke, M., Flóvenz, O.G., Caress, D., 1993. Tomographic image of the Mid-Atlantic plate boundary in southwestern Iceland. J. Geophys. Res. 98, 6607–6622.

Björnsson, H., 1988. Hydrology of ice caps in volcanic regions. Soc. Sci. Isl. Reykjavik 45, 139.

Bjornsson, H., Einarsson, P., 1990. Volcanoes beneath Vatnajökull, Iceland: evidence from radio echo-sounding, earthquakes and jökulhlaups. Jökull 40, 147–167.

Darbyshire, F.A., Bjarnason, I.T., White, R.S., Flóvenz, O.G., 1998. Crustal structure above the Iceland mantle plume imaged by the ICEMELT refraction profile. Geophys. J. Int. 135, 1131–1149.

Einarsson, T., 1954. A survey of gravity in Iceland. Visindafelag Isl. Rit. 30, 22.

Einarsson, P., 1978. S-wave shadows in the Krafla caldera in NE-Iceland: evidence for a magma chamber in the crust. Bull. Volcanol. 41, 1–9.

Einarsson, P., 1991. Earthquakes and present-day tectonism in Iceland. Tectonophysics 189, 261–279.

Einarsson, P., Brandsdóttir, B., 1984. Seismic activity preceding and during the volcanic eruption Grimsvötn, Iceland. Jökull 34, 13–23.

Goldstein, P., Dodge, D., Firpo, M., Ruppert, S., 1998. What's new in SAC2000? Enhanced processing and database access. Seismol. Res. Lett. 69, 202–205.

Gudmundsson, A., 1995. Infrastructure and mechanics of volcanic systems in Iceland. J. Volcanol. Geotherm. Res. 64, 1–22.

Gudmundsson, M.T., 1989. The Grimsvötn caldera, Vatnajökull: subglacial topography and structure of caldera infill. Jökull 39, 1–20.

Gudmundsson, M.T., Björnsson, H., 1991. Eruptions in Grimsvötn, Vatnajökull, Iceland, 1934–1991. Jökull 41, 21–42.

Gudmundsson, O., Brandsdóttir, B., Menke, M., Sigvaldason, G.E., 1994. The crustal magma chamber of the Katla volcano in south Iceland revealed by 2-D seismic undershooting. Geophys. J. Int. 119, 277–296.

Gudmundsson, A., Marti, J., Turon, E., 1997. Stress fields generating ring faults in volcanoes. Geophys. Res. Lett. 24, 1559–1562.

Jakobsson, S., 1979. Petrology of recent basalts of the eastern volcanic zone, Iceland. Acta Nat. Isl. 26, 103.

Jakobsson, S., 1980. Outline of the petrology of Iceland. Jökull 29, 57–73.

Joset, A., Holtzscherer, J.J., 1954. Expedition Franco-Islandaise au Vatnajökull Mars–Avril 1951, Resultats des sondages seismic. Jökull 4, 1–32.

Julian, B.R., 1983. Evidence for dyke intrusion earthquake mechanisms near Long Valley caldera, California. Nature 303, 323–325.

Julian, B.R., 1994. Volcanic tremor: nonlinear excitation by fluid flow. J. Geophys. Res. 99, 11 859–11 877.

Larsen, G., 1984. Recent volcanic history of the Veidivötn fissure swarm, southern Iceland—an approach to volcanic risk assessment. J. Volcanol. Geotherm. Res. 22, 33–58.

Lahr, J.C., Chouet, B.A., Stephens, C.D., Powers, J.A., Page, R.A., 1994. Earthquake classification, location, and error analysis in a volcanic environment: implications for the magmatic system of the – eruptions at Redoubt volcano, Alaska. J. Volcanol. Geotherm. Res. 62, 137–151.

Nettles, M., Ekström, G., 1998. Faulting mechanism of anomalous earthquakes near Bárdarbunga volcano, Iceland. J. Geophys. Res. 103, 17 973–17 983.

Schlindwein, V., Wasserman, J., Scherbaum, F., 1995. Spectral analysis of harmonic tremor signals. Geophys. Res. Lett. 22, 1685–1688.

Sigvaldasson, G.E., Steinthorsson, S., Oskarsson, N., Imsland, P., 1974. Compositional variation in recent Icelandic tholeiites and the Kverkfjöll hotspot. Nature 251, 579–582.

Stefánsson, R., Bödvarsson, R., Slunga, R., Einarsson, P., Jakobsdóttir, S., Bungum, H., Gregersen, G., Havskov, J., Hjelme, J., Korhonen, H., 1993. Earthquake prediction research in the south Iceland seismic zone and the SIL project. Bull. Seismol. Soc. Am. 83, 696–716.

Sæmundsson, K., 1979. Fissure swarms and central volcanoes of the neovolcanic zones of Iceland. Geol. J. 19, 415–432.

Sæmundsson, K., 1980. Outline of the Geology of Iceland. Jökull 29, 7–28.

Tryggvason, K., Husebye, E.S., Stefánsson, R., 1983. Seismic image of the hypothesized Icelandic hotspot. Tectonophysics 100, 97–118.

Ukawa, M., Ohtake, M., 1987. A monochromatic earthquake suggesting deep-seated magmatic activity beneath the Izu-Oshima volcano, Japan. J. Geophys. Res. 92, 12649–12663.

Wessel, P., Smith, W.H.F., 1995. New version of the Generic Mapping Tools released. EOS Trans. AGU 76, 329.

# ADVANCE GEOPHYSICAL dg13kk ramesses

## FIELD PARAMETERS

```
Date Recorded:
Shots/km:
Shot Interval:
Record Length:
Sample Rate:
Low Cut Filter:
High Cut Filter:
Low Cut Slope:
High Cut Slope:
Notch Filter:
Notch Frequency:
Notch Bandwidth:
Gain Type:
Gain Value:
Instrument:
Format:
Spread Type:
Number Channels:
```

## PROCESSING SEQUENCE

```
PCAN -> read raw data -> Sun May 13 13:53:42 2001
  SEGY_Input  input_raw_data  Auto Trace: 0
  SEGY_Input  input_raw_data  Auto Trace: 0

PCAN -> do_strip -> Thu May 10 15:31:39 2001
  Strip Trace Headers  Strip Trace Headers  Strip Trace: 0
    Strip Trace Headers
    Strip Trace Headers                          No
    Keep 1 in x Traces                           10
    Keep Traces                                  No
    Strip Trace Headers parameter file           Strip_Data
    Strip Trace Headers
    Retain Trace Headers                         Yes 0
    Strip Trace Headers                          No
    Keep Traces                                  No
    Strip Trace Headers parameter file           Strip_Data
    Strip Trace Headers
    Retain Trace Headers                         Yes 0
    Strip Trace Headers parameter file           Read_Traces

PCAN -> inst_geom(2) -> Wed May 02 15:26:45 2001
  Inst_Geom  Instrument Geometry  Auto Trace: 0
    Primary Header no source processes           (FFID)
    Primary Header no receiver processes         (CHAN)
    Primary Header no cmp processes              (CDP)
    Write Trace with Null Elevation Headers?     No
    Write Trace with Null Elevation Headers?     No
    Write Trace with Null Elevation Headers?     No

PCAN -> do_static(a_header) -> Fri Jun 15 09:19:10 2001
  Static Header  Static Header  Auto Trace: 0
    Use Map Line Geometry?                       Default
    Use Header Geometry?                         Header
    Header trace validity to be treated as       No
    Header trace validity to be treated as       No
    Apply Refraction Statics?                    No
    Apply Residual Statics?                      No
    Apply Surface Consistent Statics?            Yes
    Surface consistent statics parameter file    Statics_2820_2830_2900_3780_3070_4430_3730_4760_2820_3070
    Apply surface consistent statics?            Yes
    Surface consistent statics parameter file    Statics_2820_2830_2900_3780_3070_4430_3730_4760_2820_3070
```